Compensation of Impairments in Millimeter-Wave/Sub-THz Power Amplifier and Frequency Multiplier Based Transmitters

by

Ahmed Ben Ayed

A thesis
presented to the University of Waterloo
in fulfillment of the
thesis requirement for the degree of
Doctor of Philosophy
in
Electrical and Computer Engineering

Waterloo, Ontario, Canada, 2024

© Ahmed Ben Ayed 2024

Examining Committee Membership

The following served on the Examining Committee for this thesis. The decision of the Examining Committee is by majority vote.

External Examiner:	Anding Zhu Professor, Dept. of Electrical and Computer Engineering, University College Dublin
Supervisor(s):	Slim Boumaiza Professor, Dept. of Electrical and Computer Engineering, University of Waterloo
	Patrick Mitran Professor, Dept. of Electrical and Computer Engineering, University of Waterloo
Internal Member:	John Long Professor, Dept. of Electrical and Computer Engineering, University of Waterloo
Internal Member:	Zhou Wang Professor, Dept. of Electrical and Computer Engineering, University of Waterloo
Internal-External Member:	Baris Fidan Professor, Dept. of Mechanical and Mechatronics Engineering, University of Waterloo

Author's Declaration

This thesis consists of material all of which I authored or co-authored: see Statement of Contributions included in the thesis.

This is a true copy of the thesis, including any required final revisions, as accepted by my examiners.

I understand that my thesis may be made electronically available to the public.

Statement of Contributions

Ahmed Ben Ayed was the sole author of Chapters 1, 2, and 6 which were written under the supervision of Dr. Slim Boumaiza and Dr. Patrick Mitran and were not written for publication.

This thesis consists in part of seven manuscripts written for publication. Exceptions to sole authorship of material are as follows:

Research presented in Chapters 3:

Publications I: This research was conducted at the University of Waterloo by Ahmed Ben Ayed under the supervision of Dr. Slim Boumaiza and Dr. Patrick Mitran. Ahmed Ben Ayed drafted the manuscript and each author provided intellectual input on manuscript drafts. Ahmed Ben Ayed submitted the manuscript.

A. Ben Ayed, P. Mitran and S. Boumaiza, "Novel Algorithm to Synthesize the Tapering Profile for Enhanced Linearization of RF Beamforming Arrays Over a Wide Steering Range," in IEEE Transactions on Microwave Theory and Techniques, vol. 71, no. 8, pp. 3691-3700, Aug. 2023, doi: 10.1109/TMTT.2023.3248151.

Publications II: This research was conducted at the University of Waterloo by Ahmed Ben Ayed under the supervision of Dr. Slim Boumaiza and Dr. Patrick Mitran. Ahmed Ben Ayed contributed to the problem statement formulation, theoretical derivation, design of the measurement setup, data collection, and analysis. Ifrah Jaffri contributed to the theoretical derivation and data collection and analysis. Mahitab Eladwy contributed to electromagnetic simulation and provided data used in the simulation. Ali Darwish was a co-investigator on the grant and is a co-author on any publications related to this work. Ahmed Ben Ayed and Ifrah Jaffri co-wrote the draft manuscripts, to which all co-authors contributed intellectual input. Ahmed Ben Ayed submitted the manuscript.

A. Ben Ayed, I. Jaffri, M. ElAdwy, A. M. Darwish, P. Mitran and S. Boumaiza, "Analysis and Linearization of Frequency-Multiplier-Based RF Beamforming Transmitters Over a Wide Steering Range," in IEEE Transactions on Microwave Theory and Techniques, vol. 70, no. 8, pp. 3987-4001, Aug. 2022, doi: 10.1109/TMTT.2022.3186340.

Research presented in Chapters 4:

Publications III: This research was conducted at the University of Waterloo by Ahmed Ben Ayed under the supervision of Dr. Slim Boumaiza and Dr. Patrick Mitran. Ahmed Ben Ayed contributed to the problem statement formulation, theoretical derivation, design of the measurement setup, data collection, and analysis. Yushi Cao contributed to the

design of the array used in the experiments and provided electromagnetic simulated scattering parameter data used for simulation. Ahmed Ben Ayed wrote the draft manuscripts, to which all co-authors contributed intellectual input. Ahmed Ben Ayed submitted the manuscript.

A. Ben Ayed, Y. Cao, P. Mitran and S. Boumaiza, "Digital Predistortion of Millimeter-Wave Arrays Using Near-Field Based Transmitter Observation Receivers," in IEEE Transactions on Microwave Theory and Techniques, vol. 70, no. 7, pp. 3713-3723, July 2022, doi: 10.1109/TMTT.2022.3174857.

Publications IV: This research was conducted at the University of Waterloo by Ahmed Ben Ayed under the supervision of Dr. Slim Boumaiza and Dr. Patrick Mitran. Ahmed Ben Ayed contributed to the problem statement formulation, theoretical derivation, design of the measurement setup, data collection, and analysis. Huixin Jin contributed to the design of the near-field probe and the array used in the experiments. Bernard Tung contributed to the design of the Wilkinson distribution network in the array. Ahmed Ben Ayed wrote the draft manuscripts, to which all co-authors contributed intellectual input. Ahmed Ben Ayed submitted the manuscript.

A. Ben Ayed, H. Jin, B. Tung, P. Mitran and S. Boumaiza, "Array Calibration and Digital Predistortion Training Using Embedded Near-Field Feedback Probes and Orthogonal Coding for Enhancing the Performance of Millimeter-Wave Beamforming Arrays," in IEEE Microwave and Wireless Technology Letters, vol. 33, no. 6, pp. 891-894, June 2023, doi: 10.1109/LMWT.2023.3264877.

Research presented in Chapters 5:

Publications V: This research was conducted at the University of Waterloo by Ahmed Ben Ayed under the supervision of Dr. Slim Boumaiza and Dr. Patrick Mitran. Ahmed Ben Ayed contributed to the problem statement formulation, theoretical derivation, design of the measurement setup, data collection, and analysis. Ifrah Jaffri contributed to the initial data collection and analysis. Ali Darwish was a co-investigator on the grant and is a co-author on any publications related to this work. Ahmed Ben Ayed wrote the draft manuscripts, to which all co-authors contributed intellectual input. Ahmed Ben Ayed submitted the manuscript.

A. Ben Ayed, I. Jaffri, A. M. Darwish, P. Mitran and S. Boumaiza, "Digital Predistortion of Frequency Multiplier-Based Vector Signal Sources with Constrained Transmitter and Observation Receiver Bandwidth," in IEEE Transactions on Microwave Theory and Techniques (Accepted).

Publications VI: This research was conducted at the University of Waterloo by Ahmed Ben Ayed under the supervision of Dr. Slim Boumaiza and Dr. Patrick Mitran. Ahmed

Ben Ayed contributed to the problem statement formulation, theoretical derivation, design of the measurement setup, data collection, and analysis. Ahmed Ben Ayed wrote the draft manuscripts, to which all co-authors contributed intellectual input.

A. Ben Ayed, P. Mitran and S. Boumaiza, "Novel Digital Predistortion Method for Linearization of High-Order Frequency Multipliers Driven by Wideband Modulated Signals," in IEEE Transactions on Microwave Theory and Techniques (Submitted).

Publications VII: This research was conducted at the University of Waterloo by Ahmed Ben Ayed under the supervision of Dr. Slim Boumaiza and Dr. Patrick Mitran. Ahmed Ben Ayed contributed to the problem statement formulation, theoretical derivation, design of the measurement setup, data collection, and analysis. Ahmed Ben Ayed wrote the draft manuscripts, to which all co-authors contributed intellectual input. Ahmed Ben Ayed submitted the manuscript.

A. Ben Ayed, P. Mitran and S. Boumaiza, "Millimeter-Wave Device Characterization Under Wideband Modulated Signals Using Vector Network Analyzer Frequency Extenders," in IEEE Microwave and Wireless Technology Letters, doi: 10.1109/LMWT.2024.3383335.

As the lead author of these six chapters, my contributions included formulating the problem statement, developing theoretical frameworks, designing the measurement setup, collecting and analyzing data, and drafting and submitting manuscripts. Throughout each stage of the research process, my co-authors offered valuable guidance and provided valuable feedback.

Abstract

The ever-growing demand for increased network capacity and higher data rates has instigated, in recent years, a shift towards harnessing millimeter-wave (MMW) and sub-Terahertz (sub-THz) frequency bands, offering abundant and untapped spectrum resources. Nevertheless, transmitting wideband signals at these frequencies faces formidable challenges due to significant propagation path loss and the limitations of semiconductor devices. This doctoral thesis adopts a comprehensive approach to tackle these challenges by integrating advanced modeling and analysis methodologies with the development of innovative system-level architectures and leveraging advanced signal processing techniques and algorithms.

To mitigate the significant path loss challenge inherent to MMW/sub-THz wireless links, beamforming arrays are commonly employed, where a high count of closely spaced antenna elements are used to achieve high effective radiated power. These arrays are deliberately operated within their optimal operational range to maximize radiated power while concurrently promoting environmentally sustainable communication links. Yet, the deployment of closely spaced antenna elements brings forth new challenges e.g., antenna mutual coupling, which precipitates a degradation in array linearity. This thesis introduces a seminal closed-form analysis elucidating the nuanced interplay between array nonlinearity and array beam steering. Building upon this theoretical foundation, a novel optimization algorithm is formulated to meticulously design tapering coefficients aimed at minimizing variation in the array nonlinearity, due to antenna mutual coupling, across a wide range of array beam steering angles. Comprehensive numerical and experimental validation are provided, substantiating the capacity of the proposed scheme to enhance the linearizability of beamforming arrays when beam steering.

The thesis further addresses the challenge of implementing the transmitter observation receiver (TOR) in beamforming arrays needed for array calibration and linearization training. Traditionally, the TOR feedback mechanisms in single-antenna systems have been reliant on couplers situated at the output of power amplifiers (PAs). However, the integration of such couplers within MMW/sub-THz beamforming transmitters presents formidable technical hurdles. This thesis propounds a pioneering paradigm shift, advocating for the utilization of near-field (NF) probes intricately embedded within the array architecture itself. Different algorithms are presented in this thesis that enable harnessing the information received from these NF probes, enabling accurate estimation and compensation of the array's linear and nonlinear impairments. The proposed TOR and enabling algorithms, facilitate in-situ calibration and/or digital-predistortion training, thereby engendering a marked enhancement in system performance. Furthermore, the thesis proposed an active

array calibration scheme that leverages the signals received from the NF probes to enable simultaneous calibration of the array without resorting to element-wise sequential calibration or a far-field receiver. Extensive experimental validation on two beamforming arrays operating at 28 GHz and 39 GHz are presented showcasing the capacity of the proposed schemes.

The generation of wideband vector-modulated signals in the MMW/sub-THz bands poses a formidable technical challenge, especially at frequencies where PA based transmitters have limited performance. This thesis endeavors to surmount this obstacle through the exploration of frequency multipliers (FXs), which are characterized by the capacity to generate signals that can surpass the transistor unity-power-gain frequency (f_{max}). The thesis presents linearization algorithms that can mitigate the inherent nonlinearity associated with FXs thereby enabling the generation of wideband vector-modulated signals with significantly increased bandwidths compared to existing methods. Furthermore, the thesis delves into the scalability of these linearization algorithms for FX-based array systems, thereby underscored by their inherent resilience to antenna mutual coupling vis-a-vis PA-based arrays. These algorithms and findings are validated in simulation and experimentally on different single channel FXs and FX-based arrays with different multiplication orders and operation frequencies.

In tandem with these innovations, this thesis introduces a pioneering novel measurement system tailored for comprehensive testing of components and systems operating at sub-THz frequencies. Leveraging frequency extenders traditionally reserved for continuous-wave (CW) characterization, the proposed measurement system enables components and systems under both CW and modulated signal excitation conditions. The enabling algorithms used by the proposed measurement system are also developed and presented. Specifically, an iterative learning control linearization algorithm and a receiver signal stitching algorithm that enable the linearization and capture of wideband signals using narrowband receivers, are presented. The efficacy of the proposed measurement system and associated algorithms are rigorously substantiated through experimental validation.

In summary, this thesis represents a seminal contribution toward mitigating hardware limitations endemic to MMW/sub-THz radio frequency systems. By espousing a holistic approach that seamlessly integrates advanced modeling and analysis techniques, novel system-level architectures, and state-of-the-art signal processing techniques, this work lays the groundwork for the development of future-proof, high-capacity, and high-data-rate radio systems poised to thrive within these transformative frequency bands.

Acknowledgments

This thesis would not have been possible without the unwavering support of many individuals. I am particularly grateful to my parents, Slim and Moufida, for their enduring love, unwavering encouragement, and faith in me. Their support has been the cornerstone upon which I could achieve this milestone.

I am also deeply indebted to my siblings, Brahim and Farah, for their support and words of encouragement throughout this journey.

I am fortunate to have been a member of an exceptional research group at the University of Waterloo. I would like to thank all my colleagues, especially Bernard, Huixin, Hoda, Ifrah, Giovanni, Yushi, and Ziran, for their invaluable insights, stimulating discussions, and camaraderie. Their support, both intellectual and emotional, has been instrumental in my success.

Finally, I extend my sincere gratitude to Professor Slim Boumaiza and Professor Patrick Mitran for their guidance and support throughout my academic journey.

This journey has been a truly enriching and rewarding experience, and I am profoundly grateful to everyone who has played a part in it.

Table of Contents

Examining Committee Membership ii

Author's Declaration iii

Statement of Contributions iv

Abstract vii

Acknowledgments ix

List of Figures xiv

List of Tables xxiv

List of Abbreviations xxv

1 Introduction 1

1.1 Motivation 1

1.2 Thesis Objectives 4

1.3 Thesis Contributions and Organization 5

2 Background and Literature Review 7

2.1 Single Channel Transmitter Architectures 7

2.1.1 Overview . . . 8
2.1.2 Power Amplifier Based Transmitter Architecture . . . 9
2.1.3 Frequency Multiplier Based Transmitter Architecture . . . 14
2.2 Beamforming Architectures . . . 18
2.2.1 Digital Beamforming . . . 19
2.2.2 Analog Beamforming . . . 20
2.2.3 Hybrid Beamforming . . . 21
2.3 Antenna Mutual Coupling . . . 21
2.3.1 Antenna Spacing . . . 21
2.3.2 Antenna Active Reflection Coefficient . . . 23
2.4 Nonlinear Behavioral Modeling . . . 24
2.4.1 Forward modeling . . . 24
2.4.2 Digital Predistortion . . . 26
2.5 Important Metrics . . . 28
2.5.1 Adjacent-Channel-Power-Ratio . . . 29
2.5.2 Out-of-Band Unwanted Emissions . . . 30
2.5.3 Error Vector Magnitude . . . 30
2.6 Linearization of Power Amplifier-Based Beamforming Transmitters: State-Of-The-Art . . . 31
2.6.1 RF Beamforming Transmitters . . . 31
2.6.2 Hybrid Beamforming Transmitters . . . 38
2.6.3 Digital Beamforming Transmitters . . . 40
2.7 Calibration Techniques for Beamforming Arrays: State-Of-The-Art . . . 46
2.7.1 Element-Wise Array Calibration . . . 46
2.7.2 Active Array Calibration . . . 47
2.8 Linearization of Frequency Multipliers: State-Of-The-Art . . . 47
2.8.1 Seminal Works . . . 48
2.8.2 Phase Unwrapping and Two-Stage DPD Training . . . 49
2.8.3 Additive Error Model and Single-Stage DPD Training . . . 52

3 Linearization of RF Beamforming Arrays in the Presence of Antenna Mutual Coupling 54

3.1 Nonlinear Distortion Modeling of RF Beamforming Arrays 55

3.1.1 Angle-Independent DISO Forward Model Formulation 55

3.1.2 Angle-Dependent SISO Forward Model Formulation 59

3.2 Tapering Profile Synthesis Algorithm 63

3.2.1 Problem Formulation 63

3.2.2 Numerical Analysis 65

3.2.3 Experimental Validation 68

3.3 Effect of Antenna Mutual Coupling on FM Nonlinearity 73

3.3.1 Problem Formulation 74

3.3.2 Numerical Analysis 76

3.3.3 Experimental Validation 79

4 Near-Field-Based Transmitter Observation Receiver for Beamforming Arrays Calibration and Linearization 90

4.1 Array Linearization Using Near-Field Based Transmitter Observation Receiver and Assuming Flat Coupling 91

4.1.1 Problem Formulation 91

4.1.2 Experimental Validation 102

4.2 Active Array Calibration and Linearization Using Near-Field Based Transmitter Observation Receiver and Assuming Frequency Selective Coupling . 109

4.2.1 Problem Formulation 110

4.2.2 Experimental Validation 113

5 Linearization of Frequency Multiplier Based Transmitters Driven with Wideband Vector Modulated Signals 118

5.1 Linearization of Frequency Multipliers under Constrained Transmitter and Observation Receiver Bandwidths 119

5.1.1 Problem Formulation 119

5.1.2 Numerical Analysis . . . 126
5.1.3 Experimental Validation . . . 130
5.2 Linearization of Frequency Multipliers based on Nonlinear Deviations in Frequency Multipliers from the Ideal Power Function . . . 139
5.2.1 Problem Formulation . . . 139
5.2.2 Numerical Analysis . . . 145
5.2.3 Experimental Validation . . . 146
5.3 Device Characterization Under Wideband Modulated Signals using Vector Network Analyzer Frequency Extenders . . . 155
5.3.1 Problem Formulation . . . 157
5.3.2 Experimental Validation . . . 163

6 Thesis Summary and Future Work **171**
6.1 Thesis Summary . . . 171
6.2 Future Work . . . 173
6.2.1 Extending the Framework to Advanced Array Architectures . . . 173
6.2.2 DPD for Frequency Multipliers . . . 174
6.2.3 Additional Areas of Exploration . . . 174

References **174**

List of Figures

1.1 Global mobile network data traffic [1]. 2

2.1 (a) Last stage PA-based transmitter, (b) harmonic mixer-based transmitter architecture, (b) FX-based transmitter architecture. 8

2.2 Block diagram of a single-transistor PA. 10

2.3 Gain distortion (Left) and AM-PM (Right) of a non-ideal PA exhibiting nonlinear behavior. 12

2.4 PSD (Left) and constellation (Right) of a non-ideal PA exhibiting nonlinear behavior. 13

2.5 Block diagram of a transistor-based frequency doubler. 15

2.6 Gain (Left) and phase (Right) distortion of a non-ideal FX exhibiting nonlinear behavior. 17

2.7 PSD of the signals at the FX input and output, without (Left) and witht (Right) Dth root function applied: a) at the FX input, b) expected output from an ideal doubler and c) practical output for non-ideal doublers. 18

2.8 Block diagram of different mm-wave MIMO beamforming architectures: (a) digital beamforming; (b) analog beamforming; (c) hybrid beamforming. . . 19

2.9 Example of antenna array grids: (a) uniformly spaced rectangular antenna grid; (b) triangular antenna grid; (c) multi-ring antenna grid. 22

2.10 Block diagram of an RF beamforming array in the presence of antenna cross-coupling. 23

2.11 Block diagram of a SISO antenna Transmitter augmented with a DPD module: (a) PA-based transmitter; (b) FX-based transmitter. 26

2.12 Block diagram of an RF beamforming array augmented with a SISO DPD module and couplers at the PA outputs for DPD training. 32
2.13 Block diagram of a single dual-polarized antenna system augmented with the DPD scheme in [2]. 36
2.14 Block diagram of a partially-connected hybrid array augmented with a SISO DPD module per sub-array. 38
2.15 Block diagram of a partially-connected hybrid array augmented with a DISO-DPD module per sub-array. 39
2.16 Block diagram of a fully-connected hybrid array augmented with a MIMO DPD module. 41
2.17 Block diagram of a digital beamforming array augmented with a DISO DPD module per antenna. 43
2.18 Block diagram of the first attempted DPD scheme for linearizing FX-based transmitters [3]. 48
2.19 Block diagram of the DPD scheme incorporating phase unwrapping [4]. . . 49
2.20 Block diagram of the DPD scheme using a cascade of three modules [5]. . . 51
2.21 Block diagram of the DPD scheme using fractional power bases in [6]. . . . 53

3.1 Block diagram of RF beamforming transmitter with L FXs driving L-element antenna array. The dotted arrows depict, for illustration, the coupling to channel 1 from all other channels. 55
3.2 Array antenna element active reflection coefficients versus steering angle for $\theta \in [-50°, 50°]$: a) with uniform tapering; b) with synthesized tapering obtained from the proposed optimization with $q = 1$ and $AF = 57$ (i.e., overall array gain reduction of 1 dB); The inset highlights the variation in the antenna active reflection coefficients of three selected antenna elements when the array is steered. 65
3.3 Synthesized tapering coefficients magnitude in dB (a) and phase in degrees (b) obtained from the proposed optimization with $q = 1$ and $AF = 57$ (i.e., overall array gain reduction of 1 dB). 66
3.4 Simulated normalized array radiation pattern using uniform tapering profile and the synthesized profile obtained from the proposed optimization with $q = 1$ and $AF = 57$ (i.e., overall array gain reduction of 1 dB). 67

3.5 Variation Metric Ratio (VMR) of the antenna elements representing the reduction (in dB scale) in the antenna active reflection coefficient variation versus steering angle when the synthesized tapering profile obtained from the proposed optimization with $q = 1$ and $G = 57$ (i.e., overall array gain reduction of 1 dB) is applied. 68

3.6 Functional block diagram (Left) and picture (Right) of the measurement setup. 69

3.7 Measured spectrum results captured at the FF when the array is steered at broadside: (a) before DPD with uniform tapering applied; (b) before DPD with synthesized tapering applied; (c) after DPD with uniform tapering applied; (d) after DPD with synthesized tapering applied. 69

3.8 Measured gain distortion (Left) and AM-PM (Right) at the FF when the array is steered at broadside: (a) before DPD with uniform tapering applied; (b) before DPD with synthesized tapering applied; (c) after DPD with uniform tapering applied; (d) after DPD with synthesized tapering applied. . . 70

3.9 Measured radiated power in H-plane with the array steered at broadside: (a) in-band power with uniform tapering applied; (b) in-band power with synthesized tapering applied; (c) out-of-band power before DPD with uniform tapering applied; (d) out-of-band power before DPD with synthesized tapering applied; (e) out-of-band power after DPD with uniform tapering applied; (f) out-of-band power after DPD with synthesized tapering applied. 71

3.10 Measured UE-ACPR (Left) and EVM (Right)versus steering angle: (a) before DPD with uniform tapering applied; (b) before DPD with synthesized tapering applied; (c) after DPD with uniform tapering applied; (d) after DPD with synthesized tapering applied. 72

3.11 (a) Simplified circuit schematic of an FET-based FX; (b) Circuit-inspired conceptual block diagram of an FX. 74

3.12 Simulated results of: (a) Load impedances extracted from the 8×8 array when steered from $-50°$ to $50°$; (b) Gain and AM-PM plots of a 39 GHz class AB PA terminated with the load impedances given in (a); (c) Gain and AM-PM plots of a 60 GHz doubler in stacked push-push configuration terminated with the load impedances given in (a). 77

3.13 Simulated results of: (a) The forward model coefficients of a 39 GHz class AB PA plotted in the complex plane when terminated with the load impedances given in Fig. 3.12 (a); (b) The forward model coefficients of a 60 GHz doubler in stacked push-push configuration plotted in the complex plane when terminated with the load impedances given in Fig. 3.12 (a); (c) The CV of the PA and doubler forward model coefficients in (a) and (b) versus coefficient index. 78

3.14 Simulated EVM and UE-ACPR of DPD linearized PA/doubler terminated with variable load. DPD is trained when the PA/doubler are terminated with a load that results in a VSWR of 1.07. 80

3.15 Functional block diagram of the measurement setup. 81

3.16 Picture of the measurement setup. 81

3.17 Measured output spectra of FX-based 2×2 RF beamforming transmitter driven with 400 MHz wide modulated signal, when DPD is trained using FF probing antenna, with either square-root only ($\sqrt{(.)}$) or cascade of square-root and proposed DPD ($\sqrt{(.)}$ + DPD) as predistorter. 82

3.18 Simulated S-parameters of the 2×2 patch antenna array. 83

3.19 Measured output spectra of FX-based 2×2 RF beamforming transmitter driven with 400 MHz wide modulated signal, when DPD is trained using output of single-FX-channel, with either square-root only ($\sqrt{(.)}$) or cascade of square-root and proposed DPD ($\sqrt{(.)}$ + DPD) as predistorter. 85

3.20 Measured UE-ACPR and EVM versus steering angle (θ) for FX-based 2×2 RF beamforming transmitter driven with 100 MHz wide modulated signal and DPD function trained at $\theta = 0°$. 87

3.21 Measured UE-ACPR and EVM versus steering angle (θ) for FX-based 2×2 RF beamforming transmitter driven with 400 MHz wide modulated signal and DPD function trained at $\theta = 0°$. 88

3.22 Measured in-band and out-of-band radiated powers versus steering angle under 400 MHz wide modulated input signal. 89

4.1 Block diagram of RF beamforming array using FF-TOR DPD training. The effective signal radiated towards the UE, $r(t)$, is the superposition of the individual antenna outputs, $y_i(t), i = 1, \ldots, K$. 92

4.2 Block diagram of RF beamforming array using proposed NF-TOR DPD training. The signal captured by the m^{th} NF probe, $r_m^{\mathrm{NF}}(t)$, is the superposition of the individual antenna outputs, $y_i(t)$, scaled by the NF channel coefficient, $\beta_{m,i}$, for $i = 1...K$. 94

4.3 Flowchart of the proposed NF-TOR DPD training approach. 100

4.4 Picture of measurement setup with 16-element RF beamforming array (inset). 102

4.5 EM simulated S-Parameters of the 4x4 antenna under test. 103

4.6 EM simulated magnitude of the coupling between the 16 radiating antenna elements and one NF probe versus frequency. The four radiating antennas nearest to the NF probe of interest are circled as group A. 104

4.7 EM simulated phase of the coupling between the 16 radiating antenna elements and one NF probe versus frequency. The four radiating antennas nearest to the NF probe of interest are circled as group A. 105

4.8 Measured UE-ACPR (left axis) and EVM (right axis) at the FF reference antenna versus EIRP values: (a) before DPD; (b) after DPD trained using FF-TOR; (c) after DPD trained using proposed NF-TOR. 106

4.9 Spectrum results captured at the FF reference antenna: (a) before DPD; (b) after DPD trained using FF-TOR; (c) after DPD trained using proposed NF-TOR. 106

4.10 Spectrum results after applying DPD trained using proposed NF-TOR: (a) measured at NF probe 1; (b) estimated FF received signal; (c) measured FF received signal. 107

4.11 Measured radiation pattern versus steering angle at FF reference antenna positioned at boresight: (a) in-band power; (b) out-of-band power before DPD; (c) out-of-band power after DPD trained using FF-TOR; (d) out-of-band power after DPD trained using proposed NF-TOR. 108

4.12 Measured UE-ACPR (left axis) and EVM (right axis) versus steering angle with beam electrically steered to maximize received power at FF reference antenna positioned at broadside: (a) before DPD; (b) after DPD trained using FF-TOR; (c) after DPD trained using proposed NF-TOR. 109

4.13 Block diagram of RF beamforming array with embedded NF probes for array calibration and DPD training. 110

4.14 OTA test setup for experimental validation. 113

4.15 Measured RMS magnitude (Left) and phase (right) errors versus phase shifter settings (8-bits): (a) before calibration, (b) after proposed calibration using NF probes, and (c) after element-wise calibration using a FF probe. . 114

4.16 Measured radiation pattern with the array driven with a 400 MHz OFDM signal and the beam electrically steered from $-90°$ to $90°$: (a) before calibration, (b) after proposed calibration using NF probes, and (c) after element-wise calibration using a FF probe. 115

4.17 Measured UE-ACPR and EVM at the FF probe versus EIRP when the array is fed with a 400 MHz OFDM signal: (a) prior to DPD, (b) after DPD trained at the FF in the main beam direction, and (c) after DPD rained using NF assuming flat coupling. 116

4.18 Measured UE-ACPR and EVM at the FF probe versus EIRP when the array is fed with a 400 MHz OFDM signal: (a) prior to DPD, (b) after DPD trained at the FF in the main beam direction, and (c) after proposed DPD trained using NF probes. 117

5.1 Block diagram of proposed direct learning DPD with constrained transmitter and observation bandwidths. 119

5.2 Illustration of the resulting error due to constraining the Dth root function bandwidth on the output of an ideal doubler. 120

5.3 Simulated ideal doubler output spectrum with different constrained square-root function bandwidth input signals: (a) with ideal square-root function; (b)-(i) with square-root function bandwidth constrained from $\mathrm{BW_{TX}} = 9 \times$ BW down to $\mathrm{BW_{TX}} = 2 \times$BW with a step of $1 \times$BW. The inset in the figure denotes the bandwidth of the transmitter limiting filter. 126

5.4 Simulated ideal doubler spectrum plots: (a) ideal square-root function; (b) square-root function constrained to a bandwidth of $5 \times$ BW; (c) doubler output when the input is (a); (d) doubler output when the input is (b) and with receiver filter applied with bandwidth $4 \times$ BW. 127

5.5 Simulated NMSE at an ideal multiplier output with Dth root function bandwidth constrained to $\mathrm{BW_{TX}} = 5 \times$ BW versus different multiplier multiplication orders: (a) before and (b) after receiver filter applied with $\mathrm{BW_{RX}} = 4 \times$ BW. 128

5.6 Output spectra of a simulated frequency-doubler driven with 200 MHz OFDM signal: (a) before DPD with ideal square-root function applied; (b)-(j) After proposed DPD with BW_{TX} and BW_{RX} varied from $BW_{TX} = 10 \times BW$ and $BW_{RX} = 9 \times BW$ down to $BW_{TX} = 2 \times BW$ and $BW_{RX} = 1 \times BW$, respectively with a step of $1 \times BW$. The inset in the figure denotes the bandwidth of the transmitter limiting filter. 129

5.7 Measured output spectra of frequency-doubler (SpaceK) driven with 200 MHz OFDM signal: (a) before DPD with square-root function applied, $BW_{TX} = 10 \times BW$, and $BW_{RX} = 10 \times BW$; (b)-(j) After proposed DPD with BW_{TX} and BW_{RX} varied from $10 \times BW$ and $9 \times BW$ down to $2 \times BW$ and $1 \times BW$, respectively with a step of $1 \times BW$. The inset in the figure denotes the bandwidth of the transmitter limiting filter. 132

5.8 Measured output spectra of frequency-doubler (SpaceK) driven with 400 MHz OFDM signal: (a) before DPD with square-root function applied, $BW_{TX} = 8 \times BW$, and $BW_{RX} = 8 \times BW$; (b)-(h) After proposed DPD with BW_{TX} and BW_{RX} varied from $8 \times BW$ and $7 \times BW$ down to $2 \times BW$ and $1 \times BW$, respectively with a step of $1 \times BW$. The inset in the figure denotes the bandwidth of the transmitter limiting filter. 133

5.9 Measured gain distortion (Left) and phase distortion (Right) of the frequency-doubler (SpaceK) driven with 400 MHz OFDM signal: (a) before linearization with square-root applied, $BW_{TX} = 8 \times BW$, and $BW_{RX} = 8 \times BW$; (h) After proposed DPD with BW_{TX} and BW_{RX} set to $2 \times BW$ and $1 \times BW$, respectively. 134

5.10 Measured output spectra of frequency-doubler (HMC-578) driven with 400 MHz OFDM signal: (a) before DPD with square-root function applied, $BW_{TX} = 8 \times BW$, and $BW_{RX} = 8 \times BW$; (b)-(h) After proposed DPD with BW_{TX} and BW_{RX} varied from $8 \times BW$ and $7 \times BW$ down to $2 \times BW$ and $1 \times BW$, respectively with a step of $1 \times BW$. The inset in the figure denotes the bandwidth of the transmitter limiting filter. 135

5.11 Measured output spectra of frequency-doubler (HMC-578) driven with 800 MHz OFDM signal: (a) before DPD with square-root function applied, $BW_{TX} = 3.75 \times BW$, and $BW_{RX} = 3.75 \times BW$; (b)-(g) After proposed DPD with BW_{TX} and BW_{RX} varied from $3.75 \times BW$ and $2.75 \times BW$ down to $2 \times BW$ and $1 \times BW$, respectively. The inset in the figure denotes the bandwidth of the transmitter limiting filter. 136

5.12 Measured gain distortion (Left) and phase distortion (Right) frequency-doubler (HMC-578) driven 800 MHz OFDM signal: (a) before linearization with square-root applied, $BW_{TX} = 3.75 \times BW$, and $BW_{RX} = 3.75 \times BW$; (g) After proposed DPD with BW_{TX} and BW_{RX} set to $2 \times BW$ and $1 \times BW$, respectively. 137

5.13 Measured constellation at the frequency-doubler (HMC-578) output driven with 800 MHz OFDM signal: (Red) before DPD with square-root function applied, $BW_{TX} = 3.75 \times BW$, and $BW_{RX} = 3.75 \times BW$; (Blue) After proposed DPD with BW_{TX} and BW_{RX} set to $2 \times BW$ and $1 \times BW$, respectively. . . 138

5.14 Functional block diagrams illustrating: (a) DPD method of [7]; (b) proposed DPD method. 140

5.15 Detailed system block diagram of an FX-based transmitter equipped with the proposed DPD scheme. 141

5.16 Simulated output spectra of the 60 GHz frequency-doubler driven with 400 MHz OFDM signal: (a) before DPD with square-root function applied; (b) after DPD in [7]; (c) after proposed DPD. 145

5.17 Test and measurement setup to validate the proposed DPD scheme for a frequency doubler-based vector signal generation system 146

5.18 Picture of the measurement setup conducted on an octupler with output frequency centered around 58 GHz. 147

5.19 Measured output spectra of the 14 GHz frequency-doubler driven with 400 MHz OFDM signal: (a) before DPD with square-root function applied; (b) after DPD in [7]; (c) after proposed DPD. 148

5.20 Measured output spectra of 25 GHz frequency-doubler driven with 800 MHz OFDM signal: (a) before DPD with square-root function applied; (b) after DPD in [7]; (c) after proposed DPD. 149

5.21 Measured output spectra of the 62 GHz frequency-doubler driven with 400 MHz OFDM signal: (a) before DPD with square-root function applied; (b) after DPD in [7]; (c) after proposed DPD. 150

5.22 Measured output spectra of the 62 GHz frequency-doubler driven with 800 MHz OFDM signal: (a) before DPD with square-root function applied; (b) after proposed DPD. 151

5.23 Measured constellation of the 62 GHz frequency-doubler driven with 800 MHz OFDM signal: (a) before DPD with square-root function applied; (b) after proposed DPD. 152

5.24 Measured output spectra of the 28 GHz frequency-quadrupler driven with 400 MHz OFDM signal: (a) before DPD with square-root function applied; (b) after DPD in [7]; (c) after proposed DPD. 153

5.25 Measured output spectra of the 58 GHz frequency-octupler driven with 200 MHz OFDM signal: (a) before DPD with eighth-root function applied; (b) after DPD in [7]; (c) after proposed DPD. 154

5.26 Measured gain distortion (Left) and phase distortion (Right) of the 58 GHz frequency-octupler driven with 256-QAM 200 MHz OFDM signal: a) before linearization with eighth-root applied; (b) after DPD in [7]; (c) after proposed DPD. 154

5.27 System block diagram of the proposed measurement system for component level characterization under CW and modulated signal excitation. 156

5.28 Proposed system block diagram. 158

5.29 a) Image signal overlapping onto the desired signal. b) Select LO at 3/4 of the signal tones, the image signal tones will fall in between the desired signal tones. 158

5.30 Block diagram illustrating; (Left) the PA-based ILC algorithm extended to FXs; (Right) the proposed FX-based ILC algorithm. 161

5.31 Measurement setup using the OML VNA extenders. 163

5.32 Picture of the measurement setup using the OML VNA extenders. 164

5.33 Measured PSD (Left) and constellation (Right) at OML's frequency quadrupled output when driven with 256-QAM 400 MHz OFDM signal: a) before linearization with Dth-root applied; b) with PA-based ILC applied; c) with proposed FX-based applied. 165

5.34 Measured gain distortion (Left) and phase distortion (Right) at OML's frequency quadrupled output when driven with 256-QAM 400 MHz OFDM signal: a) before linearization with Dth-root applied; b) with PA-based ILC applied; c) with proposed FX-based applied. 165

5.35 Measured PSD (Left) and constellation (Right) at OML's frequency quadrupled output when driven with 256-QAM 800 MHz OFDM signal: a) before linearization with Dth-root applied; b) with PA-based ILC applied; c) with proposed FX-based applied. 166

5.36 Measured gain distortion (Left) and phase distortion (Right) at OML's frequency quadrupled output when driven with 256-QAM 800 MHz OFDM signal: a) before linearization with Dth-root applied; b) with PA-based ILC applied; c) with proposed FX-based applied. 167

5.37 Measurement setup for the D-Band doubler. 168

5.38 Picture of the measurement setup for the D-Band doubler. 168

5.39 Measured PSD (Left) and constellation (Right) at the D-band frequency doubler output when driven with 256-QAM 800 MHz OFDM signal: a) before linearization with Dth-root applied; b) with PA-based ILC applied; c) with proposed FX-based applied. 169

5.40 Measured PSD (Left) and constellation (Right) at the D-band frequency doubler output when driven with 256-QAM 1200 MHz OFDM signal: a) before linearization with Dth-root applied; b) with PA-based ILC applied; c) with proposed FX-based applied. 169

List of Tables

3.1 Simulated EVM and UE-ACPR of DPD linearized PA/doubler terminated with variable load. DPD is trained when the PA/doubler are terminated with a load that results in a VSWR of 1.07. 79

3.2 EVM and UE-ACPR With and Without DPD When DPD is Trained Using a Far-Field Probing Antenna 84

3.3 EVM and UE-ACPR With and Without DPD When DPD is Trained Using the Output of a Single FX in the beamforming transmitter array 86

4.1 Comparison of Recent Digital Predistortion Schemes at Millimeter-Wave . 107

5.1 Linearization results for the frequency doubler (SpaceK) with output frequency centered around 25 GHz 131

5.2 Linearization results for the frequency doubler (HMC578) with output frequency centered around 28 GHz 134

5.3 Summary of state-of-the-art DPD schemes for FXs 137

List of Abbreviations

f_{max} unity-power-gain frequency viii, 4, 8, 9, 14

ACPR adjacent channel power ratio xvi–xix, xxiv, 29–32, 35, 44, 45, 72, 73, 78–80, 84–88, 104–109, 115–117, 130, 132–138, 145, 146, 148–153, 155, 164, 166, 167, 169

ADC analog-to-digital-converter 119, 122, 128

ADS advanced design system 77, 129, 145

AM-AM amplitude-to-amplitude 13, 48, 78, 129, 132, 134, 136, 137, 145

AM-PM amplitude-to-phase xiv, xvi, 12, 13, 48, 70, 71, 77, 78, 129, 132, 134, 136, 137, 145

AUT antenna-under-test 69, 102, 103, 113, 114

AWG arbitrary waveform generator 68, 79, 102, 113, 130, 147–150, 152, 163, 164, 167

BPF bandpass filters 74, 80

BW signal bandwidth 29

CBBE discrete-time complex baseband 25–28, 55–60, 91, 92, 139, 160

CRV complexity-reduced Volterra 26, 92, 100

CV coefficient of variation xvii, 77, 78

CW continuous-wave viii, xxii, 5, 15, 155–157, 172

DAC digital-to-analog-converter 27, 52, 119

DC direct current 11

DDR dynamic deviation reduction 26

DE drain efficiency 11, 12

DISO dual-input-single-output xv, 37–39, 42–44, 59

DNN deep neural network 36

DPD digital-predistortion vii, xv–xxii, xxiv, 3–7, 12, 18, 24, 26–29, 31–53, 59, 62, 65, 68–73, 76, 78–80, 82–88, 91, 92, 94, 96, 98, 100–110, 112–120, 122, 123, 125–127, 129–157, 172–174

DUT device-under-test 80, 84, 135, 146, 148–151, 153, 156, 157, 167

EIRP effective isotropic radiated power xviii, xix, 30, 71, 105, 106, 115–117

EM electromagnetic xviii, 77, 98, 103–105, 111, 126, 129

EP equal power 43, 44

EVM error vector magnitude xvi–xix, xxiv, 13, 18, 29, 30, 35, 50, 72, 73, 78–80, 84–88, 105–109, 115–117, 130, 132–138, 145, 148–153, 155, 164, 166, 167, 169

FET field-effect transistor xvi, 74

FF far-field viii, xvi–xix, 4–6, 21, 33, 34, 37–40, 46, 47, 58, 62, 69–73, 80, 82–88, 90, 92–94, 96–98, 100, 102, 104–110, 113–117, 172

FMCW frequency-modulated continuous-wave 14, 48

FR1 frequency range 1 29

FR2 frequency range 2 29, 30

FWA fixed wireless access 1

FX frequency multiplier viii, xiv–xvii, xxi–xxiv, 4–9, 14–19, 22–28, 47–62, 73–79, 82–88, 118–123, 126, 127, 129, 130, 134, 136–141, 144, 146, 155, 157, 160–172, 174

Gbps Gigabits per second 1, 2, 9, 170

GMP generalized memory polynomial 26

GSG ground-signal-ground 151

IC integrated circuit 22, 103, 111, 114

IF intermediate frequency 8, 14, 20, 68, 70, 79, 80, 102, 113, 130, 131, 147–150, 152, 153, 155, 159, 164

ILC iterative learning control viii, xxii, xxiii, 6, 118, 155–157, 160–169, 173

IMN input matching network 10–12, 74, 76

ITU international telecommunication union 29

KPI key performance indicators 8–10

LO local oscillator xxii, 8, 9, 15, 20, 70, 79, 80, 102, 113, 130, 131, 148, 149, 151, 152, 158, 159, 164, 167, 169, 170

LoS line-of-sight 19, 20, 45, 57, 58, 92, 93, 95

LPF lowpass filter 79, 130

LUT look-up-table 78, 129, 145

Mbps Megabits per second 1

MIMO multiplier-input-multiple-output xv, 1, 40–45

MISO multiple-input-single-output 39–41

MMSE minimum mean square error 43

MMW millimeter-wave vii, viii, 1–5, 7, 9, 18–21, 30, 31, 33, 34, 37, 57, 90, 92, 155, 171–174

MP memory polynomial 36

MRT maximum ratio combining 40, 43, 45

NF near-field vii, viii, xviii, xix, 5, 6, 34, 46, 47, 90, 91, 94–117, 172, 173

NLoS non-line-of-sight 19

NMSE normalized mean square error xix, 35, 128, 129

NN neural network 36, 42, 44

OBUE out-of-band unwanted emissions 29, 30

OFDM orthogonal frequency division multiplexing xix–xxiii, 14, 16, 19, 30, 50, 51, 70, 82, 87, 102, 103, 114–117, 129, 131–138, 145, 146, 148–155, 164–167, 169, 172, 173

OMN output matching network 10–12, 74, 76

OTA over-the-air xviii, 36, 37, 113

PA power amplifier vii, viii, xiv–xvii, xxii–xxiv, 3–5, 7–14, 16, 17, 19, 20, 22–28, 31–35, 37–45, 51–63, 68, 72, 76–80, 90–93, 96–98, 101, 104, 110–112, 126, 156, 161–167, 169

PAE power added efficiency 11, 12

PAPR peak-to-average power ratio 11, 16, 18, 35, 70, 103, 114, 130, 131, 147

PCB printed-circuit-board 20, 22, 33

PD predistortion 120, 121, 125, 126, 144

PM-PM phase-to-phase 48, 49

PSD power spectral density xiv, xxii, xxiii, 13, 18, 71, 105, 107, 130–132, 135, 136, 148, 150–153, 155, 164–169

QAM quadrature amplitude modulation xxii, xxiii, 31, 70, 82, 103, 114, 130–132, 134, 137, 138, 145, 146, 148, 150–155, 164–167, 169, 173

QPSK quadrature phase shift keying 31

REV rotating element electric field vector 46

RF radio frequency xiv, xv, xvii, xviii, 3–6, 9–11, 15, 16, 19–21, 23–25, 29, 31–34, 36, 37, 39, 40, 43, 44, 46, 47, 52–55, 57, 59, 60, 65, 68, 77, 79, 80, 82, 83, 85–88, 91, 92, 94, 98, 99, 102, 110–113, 151, 155, 157–159, 163, 164, 167, 171–173

RMS root-mean-square xix, 114

S-Parameter scattering-parameter 59

S-Parameters scattering-parameters xviii, 23, 59, 61, 65, 98, 101, 103

SISO single-input-single-output xv, 26, 31–33, 35–38, 40, 41, 44, 59, 62, 68, 73, 76, 79, 84–87, 91, 108

SNR signal-to-noise-ratio 19

sub-THz sub-Terahertz vii, viii, 1–5, 7, 9, 18–21, 30, 31, 57, 90, 171–174

SVD singular value decomposition 35

Tbps Terabits per second 1, 2

TDD time-division duplex 19, 37

TOR transmitter observation receiver vii, xvii, xviii, 3, 5, 6, 27, 33, 34, 37, 52, 82–84, 86, 87, 90–92, 94, 97, 98, 100–102, 104–109, 118, 119, 157, 172, 173

TRP total radiated power 29–32, 35, 44, 45, 73, 84, 86, 88, 104, 107

UE user equipment xvi–xix, xxiv, 30–33, 35, 37, 39, 72, 73, 78–80, 84–88, 92, 105–109, 115–117

VNA vector network analyzer xxii, 5, 6, 113, 118, 148, 155–157, 160, 162–164, 170, 173

VSWR voltage standing wave ratio xvii, xxiv, 24, 66, 77–80

XPI cross-polarization interference 37

ZF zero-forcing 43, 44

Chapter 1

Introduction

1.1 Motivation

The rapid evolution of wireless radio technology has been a defining feature of recent decades, marked by the successive deployment of new mobile communication systems, each generation offering transformative capabilities. Initially, 1G/2G networks provided basic tetherless speech services, setting the stage for a revolutionary shift. Within two decades, the advent of 3G/4G technologies ushered in an era of broadband internet access, bringing wireless data rates of up to 100 Megabits per second (Mbps) to the palm of our hands. This remarkable leap in performance was primarily enabled by the adoption of spectrally efficient signals and the implementation of pioneering techniques such as multiplier-input-multiple-output (MIMO) transceivers, significantly enhancing system capacity.

The relentless demand for higher data rates driven by data-intensive applications shows no signs of abating. While upcoming releases of 5G standards promise data rates of up to 20 Gigabits per second (Gbps), projections indicate a future landscape where peak data rates could reach into the Terabits per second (Tbps) realm by the 2030s. Illustrating this exponential growth, global mobile data traffic surged to an impressive 97 exabytes per month in 2022. Projections suggest a staggering increase to 403 exabytes per month by 2029, representing a remarkable 315% rise from 2022 [1]. When factoring in fixed wireless access (FWA), this projection escalates to an anticipated 563 exabytes per month by the end of 2029, as depicted in Fig. 1.1. These figures underscore the urgent imperative for network infrastructure to evolve in tandem with this escalating demand.

With the insatiable demand for data pushing current wireless networks to their limit, millimeter-wave (MMW)/sub-Terahertz (sub-THz) frequencies (30-300 GHz) emerge as

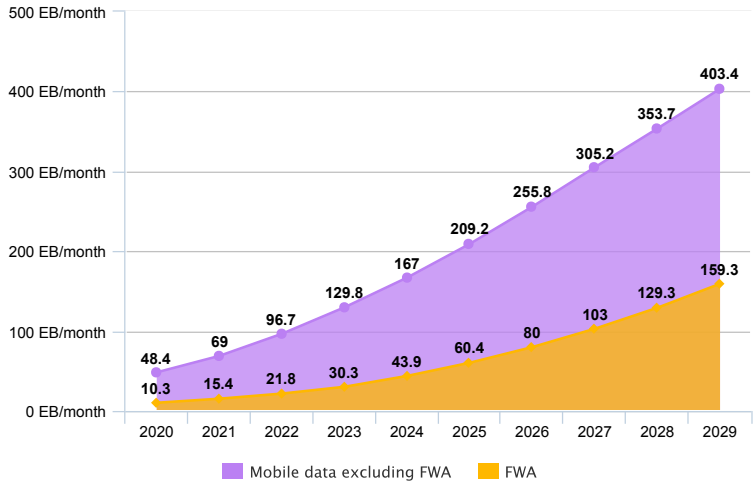


Figure 1.1: Global mobile network data traffic [1].

the future cornerstone for ultra-high data rates. Accessing this vast spectrum will unlock the transmission of multi-GHz bandwidth signals and unleash the potential for spatial multiplexing techniques through the use of advanced beamforming architectures, promising significant capacity gains. While sub-6 GHz frequencies will retain their significance for ubiquitous coverage, MMW spectra below 50 GHz will target Gbps wireless access for fixed and semi-fixed applications and frequencies above 50 GHz in the sub-THz bands are poised to revolutionize fixed links with Tbps data rates. However, while MMW and sub-THz frequency bands hold immense promise, they also introduce unique challenges that must be addressed to fully realize their potential.

The primary challenge in MMW and sub-THz frequency bands lies in their propagation characteristics. Unlike lower frequencies (sub-6 GHz) that offer good signal penetration and range, MMW and sub-THz signals suffer from increased free-space path loss, resulting in a rapid weakening of the radiated signal as it travels through space and consequently limiting coverage range. Beamforming techniques present a solution to this path loss challenge by utilizing large antenna arrays with hundreds or even thousands of elements to focus the signal toward specific users. However, extending the coverage range of these beamformers requires careful consideration of the radio hardware design. One viable strategy involves operating the radio hardware within these arrays in their efficient yet nonlinear region to maximize radiated power and enhance the deployment economics of beamforming systems. While this approach holds the potential to boost signal strength and reduce wasted power dissipation, thereby improving heat management and potentially reducing the carbon foot-

print, it also introduces complexities. The nonlinear operation introduces distortions and unwanted signal components, ultimately leading to system performance degradation.

To address this challenge, recent research has delved into the utilization of digital-predistortion (DPD) to improve the efficiency-linearity trade-off of MMW/sub-THz radio hardware and hence the coverage of beamforming arrays operating at these frequencies. While DPD techniques for sub-6 GHz systems are well-studied and typically rely on couplers at the power amplifier (PA)-antenna interface to serve a transmitter observation receiver (TOR), extending their applicability to beamforming arrays presents significant challenges. For instance, the high level of integration required in MMW/sub-THz beamforming arrays, prohibits the use of couplers at the PA-antenna to serve as TORs for DPD function training. Furthermore, the close proximity of antennas in beamforming arrays leads to a phenomenon known as antenna mutual coupling. This occurs when the radiated signals from one antenna couples to its neighboring antennas. In sub-6 GHz systems, isolators are typically used at the PA-antenna interface to mitigate antenna mutual coupling. However, due to feasibility constraints, isolators are not suitable for MMW/sub-THz applications. The combined effect of circuit nonlinearities and antenna mutual coupling creates unique system nonlinearities that differ fundamentally from those experienced in sub-6 GHz systems. To address these challenges, researchers have explored DPD techniques tailored for MMW/sub-THz beamforming arrays. However, these efforts have often either employed unrealistic PA models, overlooked issues associated with implementing the DPD TOR, or proposed computationally complex solutions validated on low antenna count systems.

While DPD techniques can potentially compensate for the nonlinearity exhibited by MMW/sub-THz antenna systems and improve their linearity-efficiency tradeoff, beamforming antenna systems also require the deployment of calibration techniques to compensate for the linear errors exhibited between their different RF chains and ensure their proper functioning (e.g., minimize user spatial interference and maximizing link capacity). Different array calibration techniques have been discussed in the literature. These can be classified into two categories; i) element-wise array calibration and ii) active array calibration. Using element-wise calibration, the array's RF chains are calibrated sequentially one antenna at a time with the remaining elements disabled. Such an approach however does not calibrate for antenna mutual coupling, current loading, and thermal grading effects experienced by large-count antenna systems. Conversely, using active array calibration, the array's RF chains are calibrated simultaneously. While active array calibration can account for current loading and thermal effects, the existing solutions in the literature yield a sub-optimal calibration solution when the number of RF inputs to the array is less than the number of antennas. Moreover, most of the calibration techniques rely on a receiver

located in the far-field (FF) to acquire the feedback signal and hence are not suitable for in-field testing. The development of in-field array calibration techniques tailored for large-count antenna systems that can combine the benefits of passive and active calibration is extremely desirable and is an active area of research with interest from both academia and industry.

Another challenge MMW/sub-THz wireless radio systems arises when operating at carrier frequencies approaching the transistor's unity-power-gain frequency (f_{max}). At these frequencies, signal generation and achievable amplification using conventional PA-based beamforming arrays become limited. This is exacerbated by the low performance of semiconductor devices and passive structure yielding low power efficiency and low output power at the transmitters. Hence, the viable deployment of commercial high-frequency radio hardware operating close to the transistor's f_{max} necessitates the rethinking of the conventional transceiver architectures. To that end, frequency multiplier (FX) -based architectures have been recently identified as a promising solution as they allow for a frequency of operation that approaches the transistor's f_{max} and reduce the design complexity of the circuitry that precede them as the latter are operated at a lower frequency. These architectures, however, are inherently nonlinear and hence require the use of spectrally non-efficient constant envelope signals or the deployment of linearization techniques. Nevertheless, existing linearization techniques discussed in the literature have only been demonstrated on narrowband signals. To accommodate the high data rates envisioned for these high-frequency systems, developing effective linearization techniques capable of mitigating nonlinearities in FX-based transmitters driven with wideband modulated signals is crucial.

1.2 Thesis Objectives

Building upon the identified challenges, this thesis aims to contribute to the advancement of high-performance MMW/sub-THz radio systems through the following objectives:

1. Modeling Nonlinear Effects in MMW/sub-THz Beamforming Arrays [**Publications I, II**]: Develop a comprehensive modeling framework that captures the impact of antenna mutual coupling and other nonidealities on the nonlinear behavior of RF beamforming arrays.

2. Mitigating the Impact of Mutual Coupling on MMW/sub-THz Beamforming Arrays Nonlinear Behavior During Beam Steering [**Publications I**]: Design a novel signal processing algorithm specifically tailored for MMW/sub-THz beamforming arrays to mitigate the detrimental effects of antenna mutual coupling on system nonlinearities and thus enhance the DPD linearization performance across a wide range of steering angles.

3. Overcoming TOR Feedback Challenges in MMW/sub-THz Beamforming Arrays [**Publications III, IV**]: Develop a novel near-field(NF) -based TOR and associated enabling algorithms for array calibration and DPD training that overcomes limitations associated with traditional FF feedback acquisition methods, enabling practical implementation in real-world scenarios.

4. Developing Linearization Algorithms for FXs driven with Wideband Modulated Signals [**Publications V, VI**]: Design computationally efficient DPD techniques capable of linearizing high-order FXs driven by wideband modulated signals and minimizing the bandwidth complexity requirements of both the transmitter and the TOR in these systems.

5. Characterization of High-Frequency Components/Systems [**Publications VII**]: Design a measurement system and associated signal processing algorithms specifically tailored for characterizing high-frequency components and systems driven by wideband modulated signals using vector network analyzer (VNA) frequency extenders traditionally only used of continuous-wave (CW) measurements.

1.3 Thesis Contributions and Organization

The articles within this thesis are organized as follows:

Chapter 3 presents the contributions from [**Publications I, II**]. It starts with a theoretical analysis and modeling approach to investigate the intricate interplay among array nonlinearity, antenna mutual coupling, and steering angles [**Publications I, II**]. This analysis yields a closed-form equation encapsulating these relationships [**Publications I**]. Subsequently, an optimization algorithm is developed to synthesize tapering coefficients to mitigate the array's nonlinear behavior dependency on beam-steering, particularly in the presence of antenna mutual coupling [**Publications I**]. These findings are validated through simulations and experiments conducted on a 64-element PA-based RF beamforming array. Additionally, a circuit-inspired analysis explores the impact of antenna mutual coupling on FXs nonlinearity [**Publications II**]. This investigation reveals that FX-based arrays exhibit greater resilience to antenna mutual coupling compared to PA-based arrays, with validation provided through simulation and experimental results obtained from a four-element FX-based beamforming array.

Chapter 4 delves into the contributions outlined in [**Publications III, IV**]. It introduces the concept of using NF-based TORs for array calibration and linearization. First, the chapter introduces a NF-based DPD formulation under the assumption of flat frequency coupling between the antenna elements and NF probes [**Publications III**]. This

includes the development of a NF to FF transformation, NF channel identification, and DPD function training. Experimental validations illustrate the efficacy of the proposed NF-based DPD in linearizing a 16-element 28 GHz RF beamforming array. Subsequently, the chapter introduces active array calibration and linearization algorithms tailored to address phase-dependent beamforming errors and nonlinearity in beamforming arrays using NF-based TORs, particularly in the presence of frequency-selective coupling between the NF probes and the radiating antenna elements [**Publications IV**]. Experimental validations of these algorithms are conducted on a 16-element RF beamforming array operating at 39 GHz.

Chapter 5 focuses on the contributions from [**Publications V, VI, VII**]. It begins with a DPD formulation aimed at linearizing FXs under limited transmitter and TOR bandwidths [**Publications V**]. Experimental validations demonstrate improved linearization performance under these constraints. Subsequently, a novel DPD formulation is introduced to mitigate deviations of multipliers from an ideal power function, showcasing resilience to calibration inaccuracies in the transmitter chain and suitability for linearizing high multiplication order FXs [**Publications VI**]. Experimental results exhibit significant improvements in linearization performance compared to state-of-the-art techniques, validated across various multiplication orders ranging from 2 to 8 and output frequencies ranging from 14 GHz to 62 GHz. Finally, a measurement system for high-frequency component/system characterization is presented, leveraging VNAs frequency extenders for modulated signal testing [**Publications VI**]. An iterative learning control (ILC) and a receiver stitching algorithms are proposed that are leveraged to linearize FXs within these frequency extenders, with experimental validation conducted using an OML VNA frequency extender operating at 58 GHz and on a custom-designed frequency doubler operating at 120 GHz.

Chapter 2

Background and Literature Review

In this chapter, a comprehensive exploration of the foundational concepts and contemporary research surrounding beamforming arrays in wireless radio systems is presented. Beamforming arrays stand as pivotal technologies for bolstering signal transmission and reception efficiency, particularly within the challenging MMW/sub-THz frequency bands, where heightened free-space propagation path loss poses significant obstacles. To cultivate a profound understanding of beamforming arrays and their practical ramifications, we delve into the fundamental principles underpinning various transmitter and beamforming architectures tailored for high-frequency signal generation and transmission, encompassing both PA and FX based beamformers. Our inquiry extends to scrutinizing the formidable challenges engendered by nonlinear behavior within these systems, along with the multifaceted strategies deployed to mitigate such challenges, including the application of DPD techniques. Furthermore, we undertake an in-depth examination of antenna mutual coupling, an omnipresent phenomenon within array configurations that exerts a substantial impact on system performance. Through an exhaustive review of pertinent literature, our objective is to lay a robust groundwork for our research endeavors while identifying pivotal areas for further investigation. This chapter serves as an essential gateway to unraveling the intricacies and subtleties inherent in beamforming arrays, thereby priming the stage for the subsequent exploration of our contributions and insights within this domain.

2.1 Single Channel Transmitter Architectures

In this section, we delve into different transmitter architectures discussed in the literature tailored for MMW and sub-THz signal generation and transmission.

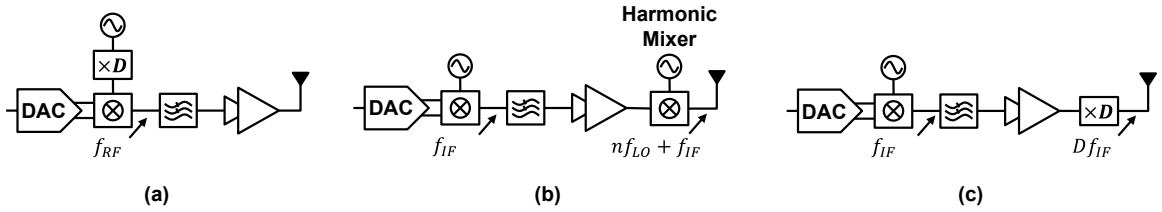


Figure 2.1: (a) Last stage PA-based transmitter, (b) harmonic mixer-based transmitter architecture, (b) FX-based transmitter architecture.

2.1.1 Overview

The intricate task of transmitter design necessitates the seamless integration of multiple components working harmoniously to meet application-specific requirements, encompassing linearity, output power, signal integrity, and various key performance indicators (KPI). Broadly speaking, a transmitter can be conceptualized through three primary building blocks: the data converter, the frequency converter block, and the signal amplification block. As operational frequencies increase and demands for wider signal bandwidths grow, the design of these building blocks becomes progressively challenging, often demanding innovation at both the component and system levels. Additionally, at high frequencies, critical system considerations come to the forefront. Factors such as transmitter chain noise figure, local oscillator (LO) phase noise, and modulation schemes, with their interdependencies, require careful attention. To address these complexities, diverse transmitter architectures have emerged in the literature, each offering distinct advantages, facing unique challenges, and addressing different applications. Fig. 2.1 illustrates three exemplary transmitter architectures reported in the literature.

In this thesis, particular emphasis is placed on the last-stage PA-based and FX-based transmitter architectures depicted in Fig.2.1 (a) and 2.1 (c) respectively. Nevertheless, before proceeding, it is imperative to briefly discuss the harmonic mixer-based transmitter architecture shown in Fig.2.1 (b). This architecture employs a heterodyne or homodyne fundamental mixer-based upconverter to translate the baseband signal to an intermediate frequency (IF). Subsequently, the output of the fundamental mixer undergoes processing through filters and signal amplification blocks before being fed to a harmonic mixer to yield modulated signals at the desired high frequency. This approach allows the frequency ceiling of the generated modulated signals to closely approach the transistor's f_{max}. This configuration has been implemented in seminal works such as [8] and [9], showcasing the generation of digitally modulated signals with carrier frequencies extending up to 300 GHz

and achieving a data rate of 105 Gbps. While this technique holds promise, literature recognizes intrinsic challenges in its design. Notable issues include severely limited output power and a pronounced presence of unwanted spurious frequencies near the desired frequency due to the harmonic mixing process. Addressing such challenges would necessitate high-order analog filters to suppress these spurious products which would yield high losses. Moreover, the architecture's susceptibility to the mixer's nonlinearity presents an additional hurdle, requiring careful compensation to avoid degraded signal quality that may fall short of meeting regulatory requirements. We next provide an overview of PA-based and FX-based transmitter architectures.

2.1.2 Power Amplifier Based Transmitter Architecture

Last-stage PA-based transmitters (see Fig.2.1(a)) have gained widespread adoption for generating radio frequency (RF) signals with exceptional signal integrity. This architecture typically incorporates a heterodyne or homodyne fundamental mixer-based upconverter to generate the RF signal. The signal is then amplified using a cascade of driver amplifiers and PAs before being radiated by the antenna. In this configuration, components following the mixer, including filters, driver amplifiers, and PAs, operate at RF frequencies. To minimize the design complexity associated with implementing a high-frequency LO source, FXs are commonly integrated into this architecture. FXs help generate a high-frequency LO from a low-noise, low-frequency high-performance LO source, which is then employed to drive the mixer LO port.

While last-stage PA-based signal sources/transitters are highly effective in generating RF signals tailored to meet the system's KPIs in terms of output power and efficiency, their operational frequency is constrained by the transistor f_{max} [10, 11]. Consequently, at MMW and sub-THz frequencies, unless sophisticated and expensive transistor technologies are adopted, the use of this architecture becomes less suitable. For example, attempts have been made to implement last-stage PA-based architectures at frequencies above 100 GHz. However, the reported performance in terms of power, efficiency, linearity, and bandwidth were limited. This restricted most reported results to modest signal modulation schemes with constant or minimally varying envelope profiles [10–20]. Furthermore, the signal quality produced is limited by the LO source phase noise, the FX's multiplication order, and the linearity characteristics of the PA, which is typically operated nonlinearly to maximize output power and enhance system efficiency. These limitations have prompted the development of alternative transmitter architectures in the literature, particularly for systems that need to operate at frequencies above 100 GHz.

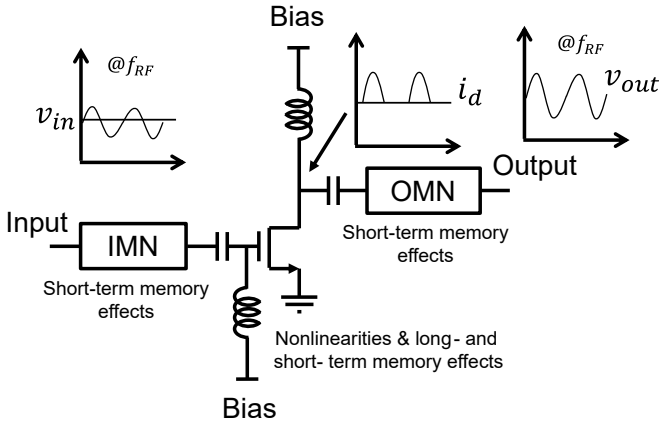


Figure 2.2: Block diagram of a single-transistor PA.

Basic Principle

Unlike driver amplifiers, which prioritize gain and linearity, PAs are typically the final stage in a transmitter and are designed for efficiency. Fig. 2.2 shows a simplified block diagram of a single-transistor PA. To determine optimal biasing voltages, various system KPIs such as gain, efficiency, and linearity need to be considered.

PAs can be biased in different classes of operation, which are determined based on the conduction angle, representing the portion of the RF signal cycle during which the transistor conducts current. Class A and Class B (push-pull) PAs are considered linear classes of operation, i.e., the fundamental output power is linearly proportional to the PA input power. In Class A, the transistor is biased to be "ON" throughout the entire input signal cycle, resulting in a theoretical peak efficiency of 50% and a 360° conduction angle. Conversely, Class B PAs bias the transistor to conduct for only half the input signal cycle (ideally 180° conduction angle), achieving a theoretical peak efficiency of approximately 78%. A smaller conduction angle generally leads to higher PA efficiency but comes at the cost of lower gain and increased nonlinearity due to signal clipping when the transistor is not conducting. Class AB and class C are nonlinear classes of operation and have conduction angles between 360° and 180° for class AB PAs and lower than 180° for class C PAs. Note, class AB PAs are linear is back-off while class C PAs are nonlinear across the entire range of input powers.

Once the gain-efficiency trade-off is determined, and the biasing is selected, the input matching network (IMN) and output matching network (OMN) for the transistor can be

designed. The OMN is designed to show a load impedance at the transistor drain theoretically chosen based on the load line to maximize the power transferred to the load. In practice, a process called load-pull is used to sweep the load impedance seen by the transistor in simulation to find the optimal load for maximum efficiency and output power while accounting for transistor parasitics. On the other hand, the IMN is typically designed for a conjugate match to maximize power transfer from the driver stage to the PA. A significant drawback of Class A, B, AB, and C operating modes is that their efficiency typically drops at lower input power levels. This is particularly problematic for communication signals with a high peak-to-average power ratio (PAPR). If the PA is operated such that the input signal's peak aligns with the PA's peak efficiency, the average efficiency of the PA (which is experienced by the average power of the signal) will be significantly lower.

At its core PAs transform direct current (DC) power into RF power. The efficacy of this power conversion mechanism can be quantified using the drain efficiency (DE) metric, defined as,

$$\eta_D = \frac{P_{out}}{P_{DC}}, \tag{2.1}$$

where P_{out} is the output power at the fundamental frequency and P_{DC} is the DC power. In order to quantify the efficiency of a PA at amplifying an input RF signal with power P_{in}, the power added efficiency (PAE) is commonly used and is defined as follows,

$$\begin{aligned}\eta_{PAE} &= \frac{(P_{out} - P_{in})}{P_{DC}} \\ &= \eta_D(1 - \frac{1}{G}),\end{aligned}$$

where G is the PA power gain.

Distortion in RF Power Amplifiers

An ideal linear amplifier is assumed to have an input power independent gain, G, defined as,

$$G = \frac{P_{out}}{P_{in}}, \tag{2.2}$$

While this equation holds true for small signal operation (i.e., within the linear region), it's not achievable for PAs when the input power is varied over a wide range. When the PA is operated outside the linear region (nonlinearly), its gain becomes a function of the input power. Furthermore, when the input power is increased beyond a certain point,

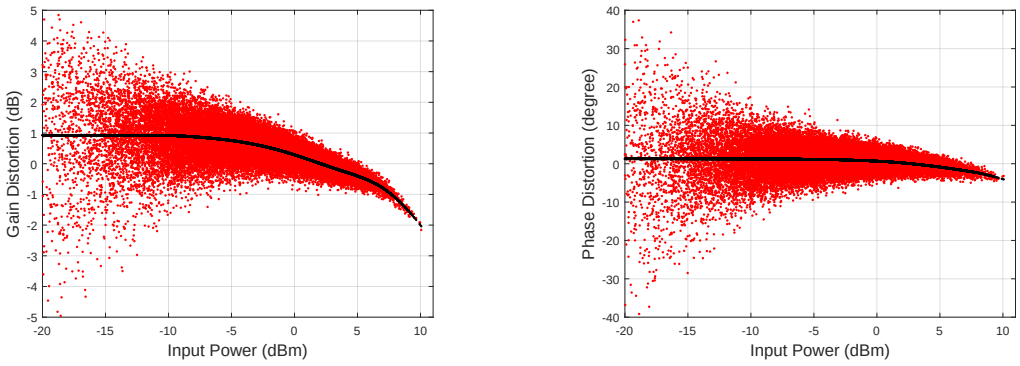


Figure 2.3: Gain distortion (Left) and AM-PM (Right) of a non-ideal PA exhibiting nonlinear behavior.

the PA output power no longer increases proportionally, and this is commonly referred to as the saturation region. For most PA designs, the nonlinear behavior can be mitigated by operating the PA in the back-off region where the gain is more power-independent. However, this approach comes at the expense of degraded DE/PAE and reduced output power. System designers must carefully consider this trade-off when selecting the operating point and back-levels the PA is to be operated based on the application needs. While back-off is a common technique, DPD is another approach to manage nonlinearities and is discussed in a subsequent section.

The PA nonlinearities significantly impact signal fidelity. These nonlinearities can be classified into static (memoryless) and dynamic (memory-based) categories. Static nonlinearities, caused by factors like transistor characteristics and clipping, are independent of the input signal's history. They can be modeled with simple polynomials, as follows,

$$y(t) = \alpha_0 + \alpha_1 x(t) + \alpha_2 x^2(t) + \alpha_3 x^3(t) + ..., \tag{2.3}$$

where $x(t)$ and $y(t)$ are the PA input and output signals respectively and α_k are the polynomial coefficents. Dynamic nonlinearities, on the other hand, depend on the past values of the input signal. These can be further divided into short-term and long-term memory effects. Short-term memory effects, influenced by the immediate past values of the signal, arise from factors such as the PA IMN and OMN non-flat frequency responses and the transistor's parasitics. Long-term memory effects, impacted by a longer time constant of the signal past values, can be caused by the transistor trapping effects [21]. Modeling

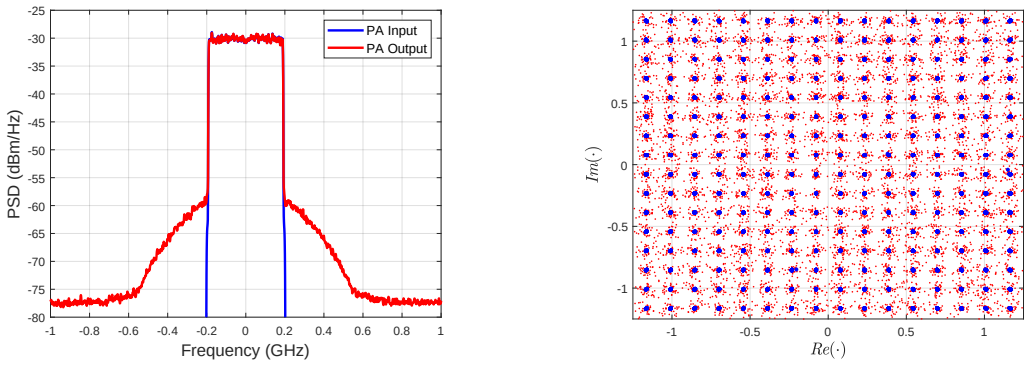


Figure 2.4: PSD (Left) and constellation (Right) of a non-ideal PA exhibiting nonlinear behavior.

dynamic nonlinearities requires more complex approaches like augmented Weiner or Hammerstein models that account for memory [22, 23]. Both static and dynamic distortions contribute to spectral regrowth, intermodulation distortion, and adjacent channel interference, all of which degrade PA performance. Understanding the type of nonlinearity present (static vs. dynamic, short-term vs. long-term) is crucial for selecting appropriate mitigation techniques.

Gain or amplitude-to-amplitude (AM-AM) and amplitude-to-phase (AM-PM) distortion plots are visual tools used to quantify the PA's nonlinear behavior. In the gain distortion plot, the PA's power gain is plotted versus the input power. For PAs that exhibit nonlinear behavior, the gain distortion curve shows a gain drop as the input power increases. Similarly, in the AM-PM plot, the phase response of the power gain is plotted versus input power. The AM-PM plot illustrates the power-dependent phase distortion created by the PA. An example of the gain and phase distortion curves of a nonlinear PA driven by modulated signals is shown in Fig. 2.3. The scattering behavior shown in the gain and AM-PM plots in Fig. 2.3 (Red) showcase the memory in the system which may be due to linear or nonlinear behavior in the PA. If the PA is memoryless, the gain and AM-PM plots in Fig. 2.3 would not experience this scattering behavior and would yield the curves shown black. Additionally, these nonlinearities lead to out-of-band spectral regrowth, expanding the occupied spectrum and potentially interfering with neighboring channels as shown in power spectral density (PSD) plot in Fig. 2.4 (Left). The nonlinearity also degrades the error vector magnitude (EVM), a metric for signal constellation quality

in communication systems (see Fig. 2.4 (Right)). Minimizing these detrimental effects through proper PA design, bias optimization, and pre-distortion techniques is essential for achieving high-fidelity signal amplification and maximizing the outputted power.

2.1.3 Frequency Multiplier Based Transmitter Architecture

An alternative architecture to PA-based transmitters, which exhibit limited performance at operating frequencies approaching the transistor f_{max}, are FX-based transmitters, as depicted in Fig.2.1(c) where FXs are inserted as last stage before the antenna. These have recently garnered attention for signal generation and transmission tailored for high frequencies. FX-based transmitters not only enable operation at frequencies surpassing the transistor's f_{max} but also relaxes the design constraints on components preceding the FX, which now operate at IF with enhanced performance. In radar applications, for instance, FX-based transmitters are commonly adopted to up-convert frequency-modulated continuous-wave (FMCW) signals to the desired radar operational frequency. While this architecture holds considerable advantages, its predominant application has been confined to scenarios where generated signals exhibit constant envelope characteristics, coupled with low spectral efficiency. This limitation stems from the intrinsic nonlinearity of FXs resulting in varying power gains depending on the instantaneous signal envelope input power. Consequently, when applying this approach to generate signals with varying envelopes, such as orthogonal frequency division multiplexing (OFDM) signals, the produced signal suffers from significant nonlinear distortions that cannot be corrected using linear equalizers at the receiver.

To overcome this challenge, pioneering research in [24] and [25] introduced the concept of outphasing FX-based transmitters. In this approach, the non-constant envelope modulated input signal is divided into two constant envelope signals, subsequently fed to two multipliers, with their outputs combined to reconstruct the desired modulated signal. While this method successfully facilitates the generation of OFDM signals using FX-based transmitters, the inherent bandwidth expansion introduced by outphasing brings forth intricate challenges. These complexities complicate the design of the constituent components of the transmitter and heighten sensitivity to imbalances among different branches, rendering this approach challenging for the generation of wideband, high-quality modulated signals, and thus limiting its adoption to communication systems in the literature. We now proceed to discuss the basic principle behind FXs design and will then investigate their nonlinear characteristics.

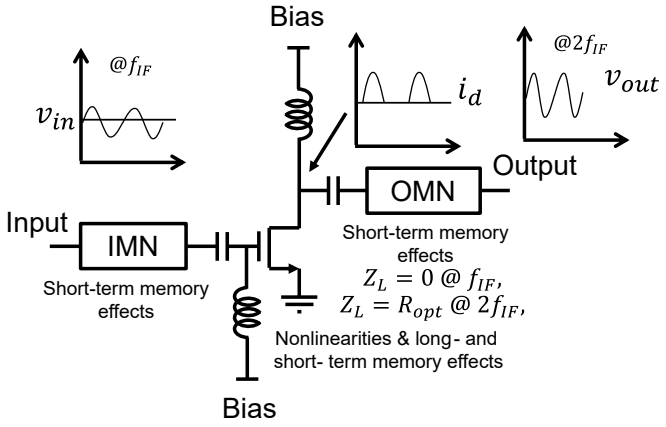


Figure 2.5: Block diagram of a transistor-based frequency doubler.

Basic Principle

FXs at their core are nonlinear devices that enable frequency translation of an input CW signal to a higher frequency proportional to $D\times$ the input signal frequency and where D is the multiplier multiplication order. Contrary to mixers, that also allow frequency translation operation by multiplying an input signal centered at f_{IF} with a CW LO signal with frequency f_{LO}, resulting in an output frequency at $f_{IF} + f_{LO}$, FXs on the other hand performer a power operation on the input signal resulting in an output frequency centered $D \times f_{IF}$ and does not require an LO signal. FXs can be classified into two categories: passive and active. Passive FXs are typically implemented using diodes [26] [27]. They can achieve good fundamental suppression and wide RF bandwidth but suffer from high conversion loss. On the other hand, active FXs, in addition to frequency translation, they can be designed to have a power gain, higher output power, and improved efficiency. Various circuit topologies have been proposed in the literature for the realization of active frequency doublers and triplers, with higher frequency multiplication orders achieved through cascading multiple stages of these components. For instance, [28, 29] proposed Gilbert-cell mixer-based topologies that achieved high conversion and good fundamental suppression at the expense of increased power consumption. This approach relies on feeding the input signal to the mixer's input and LO ports resulting in the doubling operation. Other studies, such as [30–40], focused on exploiting the nonlinearity in the transistor transconductance to design frequency doublers with improved power efficiency. For instance, if the transistor is biased in a nonlinear class of operation such as class C, it is possible to leverage the harmonic signals generated to achieve the frequency translation operation.

Fig. 2.5 shows a high-level diagram of a transistor-based doubler. In order to maximize the second harmonic transistor transconductance at the doubler output, the transistor can biased in deep Class C mode with a conduction angle of 126° [41]. While class C PAs are commonly not used for communication systems due to their nonlinearity and limited input power range, for FXs this nonlinearity is harnessed to achieve the frequency translation operation. Furthermore, as we will see later, linearizing FXs would require the use of a Dth root function which interns limits the modulated signal PAPR to a lower value, typically for OFDM signals the PAPR is around 8-12 dB after taking the square root, for instance, this is reduced to 3-6 dB which further motive the use of class C FXs for such applications given the lower requirement on the input signal power range. The output matching network in Fig. 2.5 is chosen ideally to provide the optimal impedance for power transfer at the second harmonic derived from the load line and provides a short at the other frequencies. Furthermore, the input matching network is typically designed for the conjugate match at the fundamental and provides a short at the second harmonic for doublers.

Distortion in Frequency Multipliers

An ideal FX is designed to provide the power function and can be expressed as follows,

$$y(t) = G_{FM} x^D(t), \tag{2.4}$$

where G_{FM} is the FX conversion gain. The RF signal $x(t)$ can also be expressed as a function of its complex baseband $\tilde{x}(t)$ as follows,

$$x(t) = \frac{1}{2}\left(\tilde{x}(t)e^{i\omega_{IF}t} + \tilde{x}^*(t)e^{-i\omega_{IF}t}\right), \tag{2.5}$$

where ω_{IF} is the signal's angular frequency. Substituting (2.5) in (2.4) and assuming the FX is designed to show a short impedance at the fundamental and harmonic output frequencies other than the desired harmonic at $D \times f_{IF}$, we have the following,

$$y(t) = G_{FM}\frac{1}{2}\left(\tilde{x}^D(t)e^{iD\omega_{IF}t} + \tilde{x}^{*D}(t)e^{-iD\omega_{IF}t}\right). \tag{2.6}$$

From (2.6) we clearly see that if the desired out signal is to be

$$d(t) = \frac{1}{2}\left(\tilde{d}(t)e^{iD\omega_{IF}t} + \tilde{d}^*(t)e^{-iD\omega_{IF}t}\right), \tag{2.7}$$

This can be achieved by setting $\tilde{x}(t) = \sqrt[D]{\tilde{d}(t)}$. In practice, ideal FX behavior is hard to design for and more importantly even if possible would not be maintained at higher input

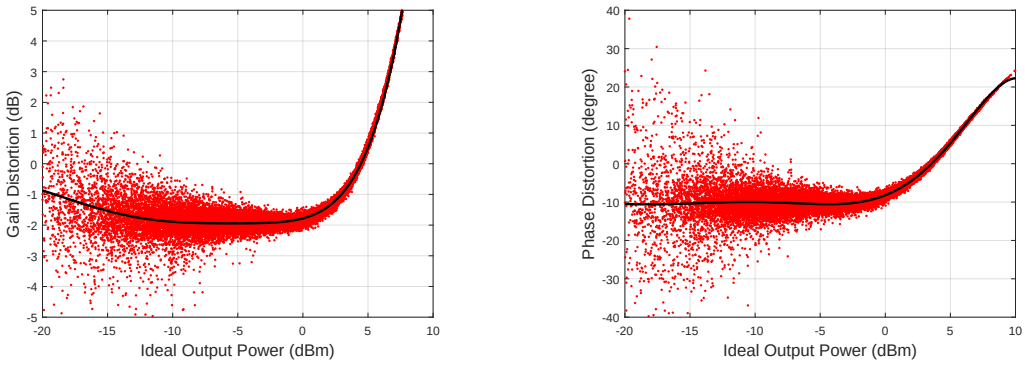


Figure 2.6: Gain (Left) and phase (Right) distortion of a non-ideal FX exhibiting nonlinear behavior.

powers where the transistor exhibits intrinsic nonlinearity other than those imposed by the conduction angle.

In a manner akin to PAs, FXs also manifest both static and dynamic nonlinear behavior. However, the characterization of gain and phase distortions differs slightly for FXs. Rather than evaluating the ratio between output and input signal magnitudes and phases to determine gain and phase distortion with respect to varying input power, for FXs, we consider the ratio between the output signal and the ideal output signal, the latter being what an ideal multiplier with a gain of one would produce [42]. Fig. 2.6 depicts the gain (Left) and phase (Right) distortion of a frequency doubler driven with modulated signals. Notably, these plots demonstrate an expansion behavior, a hallmark trait often observed in FXs, underscoring their pronounced nonlinear behavior.

Similar to the case with PAs, the nonlinear distortions exhibited by FXs result in out-of-band regrowth. Fig. 2.7 (Left) illustrates the spectrum at a doubler's input and output when driven with modulated signals: a) input signal, b) expected output from an ideal doubler, and c) output of a non-ideal doubler. Applying a Dth root function to the baseband signal (desired to be transmitted) can linearize an ideal FX. However, residual distortion persists due to internal nonlinearities within the FX. Fig. 2.7 (Right) portrays the spectrum at a doubler's input and output when a Dth root function is applied to the baseband signal before driving the doubler: a) input signal to the doubler with the Dth root function applied, b) expected output from an ideal doubler, and c) output of a

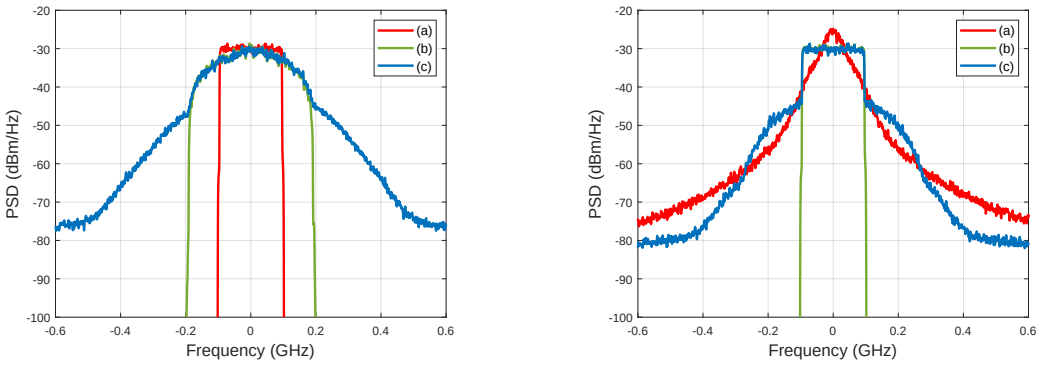


Figure 2.7: PSD of the signals at the FX input and output, without (Left) and witht (Right) Dth root function applied: a) at the FX input, b) expected output from an ideal doubler and c) practical output for non-ideal doublers.

non-ideal doubler. From Fig. 2.7 (Right), it's evident that a practical doubler exhibiting nonlinear behavior demonstrates out-of-band regrowth at its output even when a Dth root function is applied. This regrowth can lead to interference with users on adjacent channels and signal distortion and would deteriorate the EVM. Consequently, the implementation of effective DPD schemes to mitigate these nonlinearities is imperative for the feasible deployment of FX-based transmitters.

It's worth noting that applying the Dth root function to the signal in Figure 2.7 (Left) (a) transforms it into the signal depicted in Figure2.7 (Right) (a), which has a lower PAPR but broadened bandwidth. While a lower PAPR is a desirable signal characteristic, the bandwidth expansion attributed to the Dth root function may impose additional constraints on data converters during signal synthesis. More details regarding this point are discussed in subsequent chapters.

2.2 Beamforming Architectures

MMW and sub-THz frequencies will play a crucial role in future-generation wireless communication systems and will be instrumental in addressing the current challenge of bandwidth shortage in sub-6 GHz frequency bands. The migration to higher frequencies, however, brings forth challenges associated with severe propagation path loss, penetration loss,

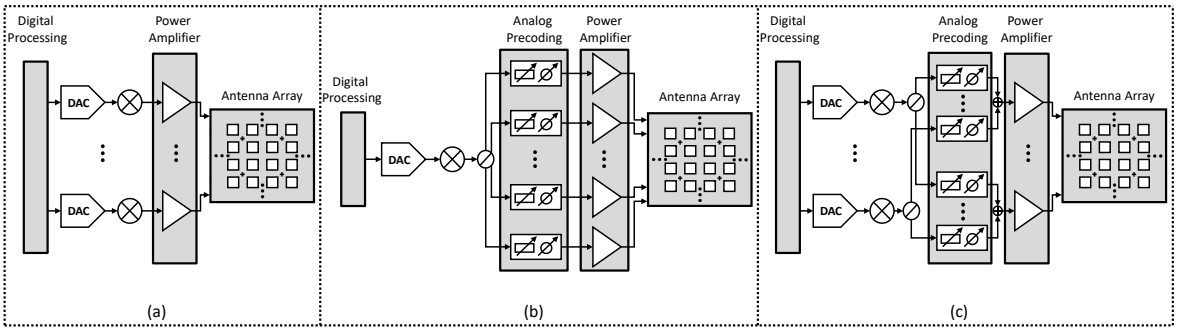


Figure 2.8: Block diagram of different mm-wave MIMO beamforming architectures: (a) digital beamforming; (b) analog beamforming; (c) hybrid beamforming.

and rain fading as compared to signals in sub-6 GHz frequencies. This is exacerbated by the limited PA/FX output power at MMW/sub-THz frequencies. These challenges have motivated the shift from the single antenna to multiple antenna systems which allows for spatial multiplexing (spatial diversity) and directional beamforming.

2.2.1 Digital Beamforming

Different beamforming architectures for MMW/sub-THz antenna systems have been discussed in the literature. These are shown in Fig. 2.8. At sub-6 GHz frequencies, digital beamforming arrays shown in Fig. 2.8 (a) is the preferred architecture where each antenna in the array has its own RF chain and data converters. During downlink operation, the base-station precodes the user's signals to counteract channel fading and ensure that each terminal receives its intended signal with adequate signal-to-noise-ratio (SNR). Digital beamforming allows for the most flexibility as it can serve multiple users simultaneously under line-of-sight (LoS) or non-line-of-sight (NLoS) channel conditions. Moreover, when combined with OFDM signals, it is able to translate the frequency selective channel into small flat-fading sub-channels to simplify precoding and help achieve high channel capacity and high data throughput. The channel matrix used to generate the precoder is estimated for both the uplink and downlink channels. These channels are equivalent in time-division duplex (TDD) operation [43], assuming proper reciprocity calibration [44], and are estimated using the pilot signals transmitted by the terminals during the uplink phase [45].

2.2.2 Analog Beamforming

Contrary to sub-6 GHz bands, at higher carrier frequencies, there are several hardware and engineering constraints that make it challenging to implement digital beamforming with high antenna count [46, 47]. For instance, given the required high level of integration of MMW/sub-THz antenna systems, implementing dedicated front-end hardware (i.e., PA, low noise amplifier, filters, mixers, etc.) per antenna element becomes very complex [48]; this dedicated front-end hardware have to be packed behind each antenna element and within a constrained antenna spacing to avoid grating lobes. Moreover, power consumption is also an important limiting factor; a digital conversion stage per antenna leads to a large demand on digital signal processing, which increases the system's power consumption. These challenges have led to several MMW/sub-THz specific beamforming architectures to emerge where signal processing is accomplished in a mixture of analog and digital domains or where different design tradeoffs are made with respect to number of antennas or resolution of data converters.

An example of MMW/sub-THz specific beamforming architecture and one of the simplest to implement is analog beamforming shown in Fig. 2.8 (b). Analog beamforming uses a network of digitally controlled phase shifters and attenuators to perform the beamforming functionality. This enables a reduction in the number of data converters per array (only one needed) and allows for improved power consumption, simplified printed-circuit-board (PCB) routing, and an overall reduction in system complexity compared to digital beamforming. This thesis will concentrate on a specific type of analog beamforming known as RF beamforming where the precoding is performed at RF (depicted in Fig. 2.8 (b)). While RF beamforming is the prevalent implementation of analog beamforming in the literature, it's worth noting that other variations of analog beamforming exist, such as IF [49] and LO [50] beamforming, though they are less commonly employed. In analog beamforming, the beamforming weights (phase and magnitude) are adaptively adjusted using digital signal processing to steer the beam and meet a given objective (e.g., maximize received signal power, etc.). Analog beamforming and specifically RF beamforming is a cost-effective architecture for MMW/sub-THz LoS channel conditions that can achieve, in such a case, similar single-user performance as fully digital arrays [51].

RF beamforming arrays are most commonly implemented using patch antennas arranged in a uniformly spaced rectangular grid as shown in Fig. 2.9 (a) [52–55]. Assuming a single user and LoS propagation environment, the beamforming coefficients that maximize the array gain are as follows,

$$w_\ell(\theta,\phi) = e^{-i\frac{2\pi}{\lambda}\sin(\theta)\left(d_\ell^x\cos(\phi)+d_\ell^y\sin(\phi)\right)} \tag{2.8}$$

where $\theta \in [-90°, 90°]$ and $\phi \in [0°, 180°]$, are the user's location specified by the elevation and azimuth angles, respectively, $i = \sqrt{-1}$, (d_ℓ^x, d_ℓ^y) is the location of the ℓ'th antenna in the x-y plane, and λ is the wavelength. Assuming omnidirectional antenna elements, the array's FF radiation pattern for given beamforming coefficients, w_ℓ, is then given by,

$$AF(\theta, \phi) = \sum_{\ell=1}^{L} w_\ell e^{i\frac{2\pi}{\lambda}\sin(\theta)\left(d_\ell^x \cos(\phi) + d_\ell^y \sin(\phi)\right)}, \tag{2.9}$$

where L is the total number of antennas in the array and AF is the array factor.

2.2.3 Hybrid Beamforming

In order to allow for multi-user scenarios and without resorting to a complex digital beamforming architecture, hybrid beamforming shown in Fig. 2.8 (c) has been proposed in the literature as a promising solution for MMW/sub-THz antenna systems. Two hybrid structures can be identified in the literature; namely a fully connected [51,56–58], and a partially connected suture [59–62]. In a fully connected hybrid beamforming array, all the antennas can connect to each RF chain in the array (as illustrated in Fig. 2.8 (c)). Conversely, in a partially hybrid beamforming array, the array is divided into subarrays, where each subarray connects to its own individual transceiver, and the antennas in each of the subarrays are connected to a single phase shifter-attenuator pair. In addition to enabling multi-user deployments through the use of spatial multiplexing (multiple simultaneous beams), an advantage of the hybrid approach is that the digital precoder/combiner can correct for lack of precision in the analog precoder, for example, to cancel residual multi-beam interference.

2.3 Antenna Mutual Coupling

2.3.1 Antenna Spacing

When deciding the antenna spacing to used in the beamforming array, the desired steering range and the concept of grating lobes need to be considered. Grating lobes are copies of the main beam (same magnitude) that appear when the array is steered outside of a given steering range and are due to spatial aliasing effects. From the receiver's perspective, grating lobes can cause plane waves incident to the array from visible angles other than the desired direction to be coherently added, hence causing interference with the desired

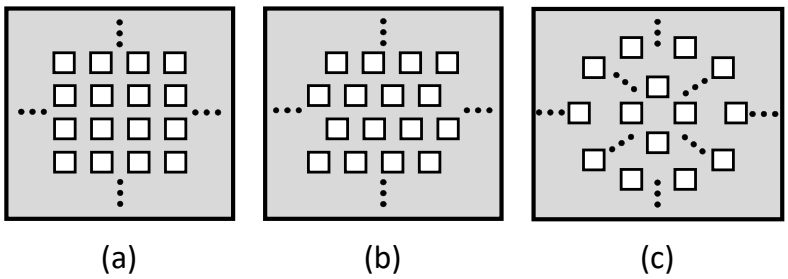


Figure 2.9: Example of antenna array grids: (a) uniformly spaced rectangular antenna grid; (b) triangular antenna grid; (c) multi-ring antenna grid.

received signal that can significantly deteriorate the system performance in terms of achievable data rates. For uniformly spaced rectangular grid arrays, grating lobes can be avoided by spacing the antenna elements $\lambda_m/2$ apart where λ_m is the wavelength corresponding to the highest frequency the array is to be operated at. In practice, the $\lambda_m/2$ requirement can be relaxed and the maximum antenna spacing that avoids grating lobes can be selected based on the maximum desired steering angle range (i.e., $\theta \in [-\theta_{max}, \theta_{max}]$) and is given by the following equation,

$$d_{max} = \frac{\lambda_m}{1 + \sin\theta_{max}}. \tag{2.10}$$

Note, (2.10) is only valid for uniformly spaced rectangular grid arrays.

The choice of antenna spacing also affects the antenna mutual coupling levels (i.e., the isolation between the antenna elements). Higher antenna mutual coupling levels can impact the performance of the active components connected to the antennas in the array (i.e., the PAs/FXs). In order to minimize the problem of antenna mutual coupling while avoiding grating lobes, it is possible to resort to other antenna grids that allow for larger antenna spacing. For instance, a triangular antenna grid shown in Fig. 2.9 (b) allows for a maximum antenna spacing of $0.577\lambda_m$ for $\theta \in [-90°, 90°]$ while a multi-ring antenna grid shown in Fig. 2.9 (c) does not suffer from grating lobes. The antenna grids in Fig. 2.9 (b)-(c), however, impose non-negligible challenges on the PCB routing as most ICs are designed to work in a rectangular grid. Moreover, different antenna grids have different radiation pattern characteristics (i.e., beam-width, side-lobe levels, etc.) which need to be considered for optimal system performance.

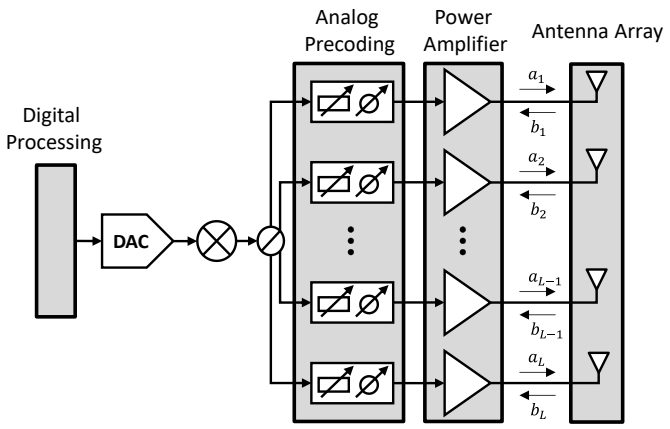


Figure 2.10: Block diagram of an RF beamforming array in the presence of antenna cross-coupling.

2.3.2 Antenna Active Reflection Coefficient

In order to quantify the extent of antenna mutual coupling in an array, the active reflection coefficient is commonly used and is defined for the n'th antenna element in the array as follows,

$$\Gamma_A^{(n)}(f) = \sum_{m=1}^{L} S_{nm}(f) \frac{a_m(f)}{a_n(f)}, \tag{2.11}$$

where $a_n(f)$ is the incident wave at the n'th antenna element, $S_{nm}(f)$ are the array's antenna scattering-parameters (S-Parameters), and f is the frequency of the incident waves at the antenna ports. In the absence of antenna mutual coupling (i.e., $S_{nm}(f) = 0,\ \forall\, n \neq m$), (2.11) simplifies to $\Gamma_A^{(n)}(f) = S_{nn}(f)$. In practice due to antenna mutual coupling, the active reflection coefficient at the n'th antenna element in (2.11) will depend on the incident waves to adjacent antenna elements in the array (i.e., $a_m,\ \forall\ n \neq m$). The presence of antenna mutual coupling causes the active reflection coefficient (and consequently the nonlinear behavior of PAs/FXs in the array) to exhibit dependency on the analog/digital pre-coding. For instance, consider the case of an PA-based RF beamforming array with antenna mutual coupling shown in Fig. 2.10 and assume, for simplicity, that the PA outputs reflection coefficients, $\Gamma_{out}^{(n)}(f)$, are zero (i.e., the PA outputs are matched). Then the incident wave to the n'th PA can be expressed as a function of the analog pre-coding coefficients, w_n, as follows,

$$a_n(f) = G w_n(f), \tag{2.12}$$

where G is the PA gain (all PAs in the array are assumed to have the same gain G for convenience). Substituting (2.12) in (2.11), we then have,

$$\Gamma_A^{(n)}(f) = \sum_{m=1}^{L} S_{nm}(f) \frac{w_m(f)}{w_n(f)}. \tag{2.13}$$

Finally, using the analog pre-coding in (2.8), (2.13) can be rewritten as follows,

$$\Gamma_A^{(n)}(\theta, \phi, f) = \sum_{m=1}^{L} S_{nm}(f) e^{-i\frac{2\pi}{\lambda}\sin(\theta)\left[(d_m^x - d_n^x)\cos(\phi) + d_(m^y - d_n^y)\sin(\phi)\right]}. \tag{2.14}$$

Note, it is clear from (2.14) that the active reflection coefficient in the case of RF beamforming is steering angle dependent. This variation in the active reflection coefficient causes significant challenges for the active devices that have to be designed to withstand large variations in voltage standing wave ratio (VSWR). The steering angle range and frequency of operation of an antenna array can be defined in terms of the active reflection coefficient (e.g., a −6 dB active reflection coefficient threshold is commonly referenced in the literature for defining the steering range of beamforming arrays).

2.4 Nonlinear Behavioral Modeling

Accurate modeling of the nonlinear behavior of PAs and FXs is crucial for mitigating the impact of their nonlinearities on signal fidelity. Behavioral modeling offers a powerful approach for this task, as it allows for the creation of mathematical relationships between the input and output signals of these devices without requiring detailed knowledge of their internal circuitry. This significantly simplifies and expedites the model development process, compared to approaches that rely on in-depth circuit analysis. Furthermore, behavioral models play a vital role in designing DPD techniques, which rely on accurate modeling to achieve effective linearization. To this end, this section presents behavioral models for FMs and PAs that can capture both static nonlinearities and dynamic effects, furthermore, an overview of DPD as used in sub-6 GHz systems is provided.

2.4.1 Forward modeling

A memoryless (static) nonlinear behavior produces distortions that do not depend on the input signal past values and, hence, can be modeled in discrete-time passband using a

simple polynomial model as follows,

$$y[n] = \alpha_0 + \alpha_1 x[n] + \alpha_2 x^2[n] + \alpha_3 x^3[n] + ..., \tag{2.15}$$

where $x[n]$ and $y[n]$ are the PA/FX input and output discrete-time signals, respectively, and α_j are the model coefficients. Conversely, dynamic nonlinear behavior (nonlinear memory) generates distortions that depend on the input signal past values. PA/FX exhibiting nonlinear memory can be modeled using a Volterra series [7, 63] that can be described in discrete-time passband as follows,

$$y[n] = \sum_{p=0}^{N} \sum_{\mathbf{m} \in \mathcal{B}^p} \eta_{\mathbf{m}}^{p} \prod_{i=1}^{p} x[n - m_i], \tag{2.16}$$

where N is the nonlinearity order, M is the memory depth, $\eta_{\mathbf{m},\ell}^{p}$ are the passband Volterra forward model coefficients and $\mathcal{B} = \{0, 1, 2, \ldots, M\}$. The expression in (2.16) contains harmonic components centered around integer multiples of the input signal carrier frequency ω_{RF}. Assuming that frequency components other than at $D \times \omega_{RF}$ are filtered out by the PA/FX output matching network where $D = 1$ is the PA case, $D > 1$ denotes the FX multiplication order, and ω_{RF} the input signal RF angular frequency. Consequently, in (2.16) we are only interested in the terms appearing at $D \times \omega_{RF}$. To that end, we first express $x[n]$ as a function of its discrete-time complex baseband (CBBE) signal, $\tilde{x}[n]$ as follows,

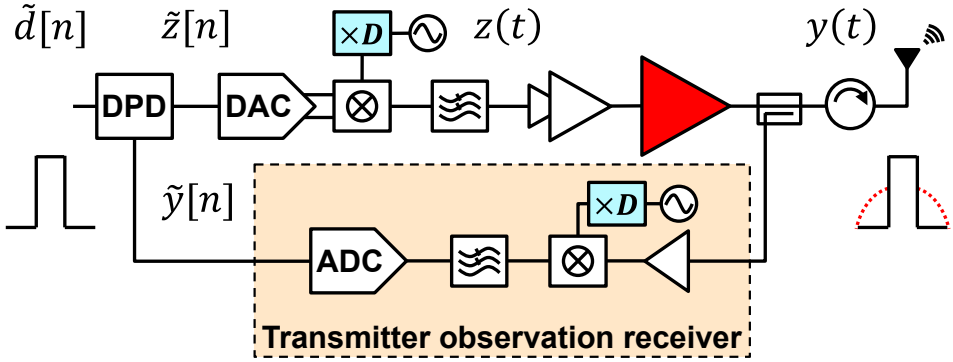
$$x[n] = 2\Re\left\{\tilde{x}[n] e^{i\omega_{RF} n}\right\} = \tilde{x}[n] e^{i\omega_{RF} n} + \tilde{x}^*[n] e^{-i\omega_{RF} n}. \tag{2.17}$$

Substituting (2.17) in (2.16) and only keeping the terms appearing around the carrier frequency ω_{RF}, we get the following CBBE Volterra series of the PA,

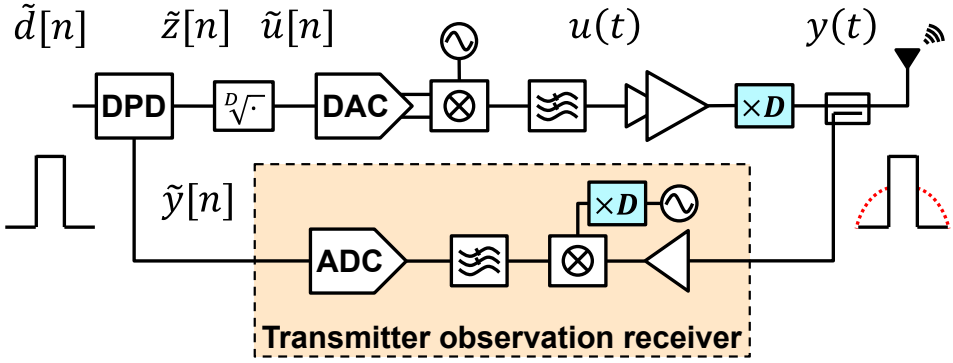
$$\tilde{y}[n] = \sum_{p=0}^{N} \sum_{\mathbf{m} \in \mathcal{B}^p} \sum_{\bar{\mathbf{m}} \in \mathcal{B}^{p+1}} \tilde{\eta}_{\mathbf{m},\bar{\mathbf{m}}}^{p} \prod_{i=1}^{p} \tilde{x}^*[n - \mathbf{m}_i] \prod_{j=1}^{p+D} \tilde{x}[n - \bar{\mathbf{m}}_j], \tag{2.18}$$

where $\tilde{x}[n]$ and $\tilde{y}[n]$ are the CBBE of the PA/FX input and output signals, respectively, $2N + D$ is the PA/FX nonlinearity order, and $\tilde{\eta}_{\mathbf{m},\bar{\mathbf{m}}}^{p}$ are the PA/FX model CBBE Volterra series coefficients. In the absence of memory effects, i.e. $M = 0$, the PA/FX CBBE model in (2.18) simplifies to,

$$\tilde{y}[n] = \sum_{p=0}^{N} \tilde{\eta}_p \tilde{x}^D[n] \left|\tilde{x}[n]\right|^{2p}, \tag{2.19}$$



(a)



(b)

Figure 2.11: Block diagram of a SISO antenna Transmitter augmented with a DPD module: (a) PA-based transmitter; (b) FX-based transmitter.

which corresponds to the CBBE model of the discrete-time passband polynomial model in (2.3). Note, due to the complexity and large number of bases used in the CBBE Volterra model in (2.18), various attempts have been made to reduce its number of bases by pruning some of its parameters. Some of the popular pruned Volterra models for PAs are the complexity-reduced Volterra (CRV) model presented in [64], the generalized memory polynomial (GMP) proposed in [65], and the dynamic deviation reduction (DDR) in [66].

2.4.2 Digital Predistortion

Fig. 2.11 shows a single-input-single-output (SISO) transmitter incorporating a SISO-DPD module for linearization. Fig. 2.11 (a) shows a PA-based transmitter and Fig. 2.11 (b)

illustrates an FX-based transmitter. A coupler is used at the PA/FX output to serve as a TOR when training the DPD function coefficients. Additionally, Fig. 2.11 (a) employs a circulator at the PA output to isolate the PA from potential antenna-received interferences.

The fundamental principle behind DPD is to use a nonlinear function that pre-distorts the desired signal to be transmitter so that the tandem cascade of the DPD module and the nonlinear system approximates an ideal linear behavior. It's important to note that for FXs, the predominant approach in the literature treats the cascaded system of the Dth root function and the FX nonlinearity as the entity to be linearized, which is different from the PA case where no Dth root function is needed. The DPD in FX case is then used to mitigate the deviation of the latter cascade system from an ideal frequency translation plus gain function. Generally speaking the DPD CBBE output can be expressed as follows,

$$\tilde{z}[n] = \sum_{b=1}^{K} \gamma_b \tilde{\psi}_b\big(\tilde{\mathbf{d}}(n)\big), \tag{2.20}$$

where $\tilde{d}[n]$ is the desired transmitted signal, $\tilde{\mathbf{d}}(n) = (\tilde{d}[n], ..., \tilde{d}[n-M])$, M is the DPD function memory depth, K is the total number of bases $\tilde{\psi}_b$, and γ_b is the b'th DPD basis coefficient. In the FX case the DPD output is further processed through a Dth root function such that, the CBBE at the digital-to-analog-converter (DAC) input, $\tilde{u}[n]$ is expressed as follows,

$$\tilde{u}[n] = \sqrt[D]{\tilde{z}[n]}. \tag{2.21}$$

Note: to avoid introducing a discontinuity in the phase of $\tilde{u}[n]$, the Dth roots of the complex-valued signal $\tilde{z}[n]$ i.e.,

$$\sqrt[D]{\tilde{z}[n]} = |\tilde{z}[n]|^{\frac{1}{D}} \exp\left(\frac{j\phi(\tilde{z}[n])}{D}\right), \tag{2.22}$$

is computed using the unwrapped phase, $\phi(\tilde{z}[n])$, which is required to ensure that the wrapped phase remains bounded in the interval of $[-\pi, \pi)$ rather than $[-\frac{\pi}{D}, \frac{\pi}{D}]$ [67] .

The DPD nonlinear bases in (2.20) can be obtained from the CBBE Volterra series in (2.18) for PAs or the CBBE Volterra series with factional power bases appended [7] for FXs. Alternatively, to lower the computation complexity associated with estimating a large number of coefficients, a pruned version of these models can also be adopted. In order to identify the DPD function coefficients, two approaches are commonly adopted, namely indirect and direct learning [68]. The indirect learning approach assumes that the PA (or the Dth root function FX cascade) pre-inverse and post-inverse are identical such that,

$$\tilde{f}^{-1}_{PA/FA}\big(\tilde{\mathbf{y}}(n)\big) = \tilde{z}[n] \Rightarrow \tilde{z}[n] = \tilde{f}^{-1}_{PA/FM}\big(\tilde{\mathbf{d}}(n)\big), \tag{2.23}$$

where $\tilde{f}_{PA/FM}^{-1}$ is the PA (or the Dth root function FX cascade) post inverse function and $\tilde{\mathbf{y}}(n) = (\tilde{y}[n], ..., \tilde{y}[n-M])$. Using indirect learning, the DPD coefficients at kth+1 iteration, $\boldsymbol{\gamma}^{k+1}$, can be estimated iteratively using the post inverse's least square solution as follows,

$$\boldsymbol{\gamma}^{k+1} = \left(\Psi^H(\tilde{\mathbf{y}}_k(n))\Psi(\tilde{\mathbf{y}}_k(n))\right)^{-1}\Psi^H(\tilde{\mathbf{y}}_k(n))\tilde{\mathbf{z}}_k(n). \tag{2.24}$$

where $\tilde{\mathbf{z}}_1(n) = \tilde{\mathbf{d}}(n)$, $\tilde{\mathbf{y}}_k(n)$ is the PA/FX output at the kth iteration, Ψ is a $N \times L$ matrix with entry in the ℓ^{th} row and b^{th} column given by

$$\left[\Psi(\tilde{\mathbf{y}}_k(n))\right]_{\ell,b} = \psi_b(\tilde{\mathbf{y}}_k(n+\ell-1)), \tag{2.25}$$

and $\tilde{\mathbf{d}}(n) = (\tilde{d}[n], ..., \tilde{d}[n-M])$.

Alternatively, direct learning can also be used to determine the DPD function coefficients iteratively. Using direct learning the PA (or the Dth root function FX cascade) nonlinearity is assumed to take the form of an additive error model such that the CBBE PA (or the Dth root function FX cascade) output, $\tilde{y}[n]$ is expressed as follows,

$$\tilde{y}[n] = G\tilde{z}[n] + \tilde{e}[n] \tag{2.26}$$

where G is the PA/FX linear gain, and $\tilde{e}[n]$ is a complex-valued additive error term that approximates the higher-order nonlinearities in the system. Using Newton's method, the DPD function coefficients can then be identified iteratively using the following update equation,

$$\boldsymbol{\gamma}^{k+1} = \boldsymbol{\gamma}^k - \mu\Delta\boldsymbol{\gamma}^k \tag{2.27}$$

where $0 < \mu < 1$ is the update step size, and $\Delta\boldsymbol{\gamma}^k$ is the update direction of the predistorter model coefficients given by,

$$\Delta\boldsymbol{\gamma}^k = \left(\Psi^H(\tilde{\mathbf{d}}(n))\Psi(\tilde{\mathbf{d}}(n))\right)^{-1}\Psi^H(\tilde{\mathbf{d}}(n))(\tilde{\mathbf{y}}_k(n) - \tilde{\mathbf{d}}(n)), \tag{2.28}$$

and $\boldsymbol{\gamma}^1$ is a vector with all elements set to zero except for the entry with index b corresponding to,

$$\left[\Psi(\tilde{\mathbf{d}}(n))\right]_{\ell,b} = \tilde{\mathbf{d}}(n+\ell-1). \tag{2.29}$$

2.5 Important Metrics

Various metrics, as defined by industry standards and prevalent in the literature, are employed for evaluating the performance of transmitters and assessing the effectiveness of

DPD techniques. In this section, we delve into the definitions of these metrics as outlined by industry standards, focusing specifically on the adjacent channel power ratio (ACPR), out-of-band unwanted emissions (OBUE), and EVM metrics in both single antenna and beamforming arrays.

As defined by the international telecommunication union (ITU), unwanted emissions consist of out-of-band emissions and spurious emissions. Out-of-band emissions, in ITU terminology, are unwanted emissions occurring immediately outside the user-allocated frequency channel, resulting from the modulation process and nonlinearity in the transmitter, but excluding spurious emissions. On the other hand, spurious emissions are caused by unwanted transmitter effects such as harmonic emission, parasitic emission, intermodulation products, and frequency conversion products, but exclude out-of-band emissions. The out-of-band emissions requirement for transmitters is specified both in terms of ACPR and OBUE. EVM is used to assess the impact of the impairments in the transmitter chain on the signal quality. Both linear and nonlinear impairments in the transmitter RF chains can impact the EVM.

2.5.1 Adjacent-Channel-Power-Ratio

In the context of single antenna systems, ACPR is defined as the ratio of the filtered mean power centered on the assigned user's channel frequency to the filtered mean power centered on an adjacent channel frequency. The filter used for these calculations is specified to be a rectangular window and has a bandwidth equal to the user's allocated signal bandwidth (BW). Furthermore, the filtered mean power centered on an adjacent channel frequency is calculated for a specified frequency offset equal to $n \times BW$, where n is an integer. In frequency range 1 (FR1) bands $n = 1, 2$ while for frequency range 2 (FR2) bands $n = 1$. For beamforming arrays, the spectral mask is defined in terms of the total radiated power (TRP) -ACPR as follows,

$$\text{TRP-ACPR [dB]} = 10 \log_{10} \frac{\text{TRP}_{\text{out-of-band}}}{\text{TRP}_{\text{in-band}}}, \tag{2.30}$$

where $\text{TRP}_{\text{in-band}}$ denotes the TRP within the assigned frequency channel, and $\text{TRP}_{\text{out-of-band}}$ is out-of-band nonlinear TRP in the frequency-channels adjacent to the frequency channel allocated by the service provider. The TRP is defined as follows,

$$\text{TRP [mW]} = \frac{\pi}{2N_A N_E} \sum_{n=0}^{N_A-1} \sum_{m=0}^{N_E-1} \text{EIRP}(\theta_n, \phi_m) \sin\theta_n, \tag{2.31}$$

where N_A and N_E are the total numbers of elevation (θ) and azimuth (ϕ) observation angles respectively, and EIRP is the effective isotropic radiated power, in the two orthogonal polarizations. Furthermore, in this thesis, in addition to ACPR and TRP-ACPR we define user equipment (UE) -ACPR which refers to the ACPR as measured at the user's location and used to assess the nonlinearity radiated by beamforming arrays in the UE direction.

For beamforming arrays operating at sub-6 GHz, the TRP-ACPR requirement (i.e., spectral mask requirement) set by the standard is 45 dB [69]. On the other hand, at MMW/sub-THz frequencies and specifically in the n257, and n258 frequency bands (i.e., from 24.25 GHz to 33.4 GHz) the TRP-ACPR requirement is more relaxed and is specified as 28 dB while at higher frequencies in the n259, and n260 (i.e., from 37 GHz to 52.6 GHz) the TRP-ACPR requirement is 24 dB [69]. Beyond 52.6 GHz, the spectral mask is not specified by the 3GPP standard release 16 [69].

2.5.2 Out-of-Band Unwanted Emissions

Unlike ACPR, which examines unwanted out-of-band distortions in adjacent channel frequencies, the OBUE requirement, specified in dBm/MHz, mandates that unwanted emissions remain below a specified value across the entire frequency band and extend beyond it up to an offset Δf_{OBUE}. In the specific case of FR2 frequencies, Δf_{OBUE} is specified to be equal to 1.5 GHz [69, p.123].

2.5.3 Error Vector Magnitude

In this subsection, we limit our definition of EVM to OFDM signals. In OFDM signals, the EVM per OFDM symbol is defined as,

$$\text{EVM } [\%] = \frac{\sum_{k=0}^{K_\text{D}} \left|\tilde{y}_\text{FFT}(v_k)W(v_k) - \tilde{d}_\text{FFT}(v_k)\right|^2}{\sum_{k=0}^{K_\text{D}} \left|\tilde{d}_\text{FFT}(v_k)\right|^2} \times 100, \tag{2.32}$$

where, $\tilde{y}_\text{FFT}$ and $\tilde{d}_\text{FFT}$ are the discrete-time Fourier transform of UE's received signal and ideal signal, respectively. Furthermore, K_D is the total number of data sub-carriers, v_k is the index of the discrete Fourier transform tone corresponding to the kth data sub-carrier, and $W(.)$ is the transfer function of the linear equalization filter which is obtained from K_P OFDM pilot sub-carriers. The standard defines EVM to be the equalized EVM and is measured overall allocated resource blocks and within a minimum length of 10 subframes (i.e., 10 ms measurement periods). The EVM requirement set by the standard is 17.5% for

quadrature phase shift keying (QPSK) modulation, 12.5% for 16- quadrature amplitude modulation (QAM), 8% for 64-QAM and 3.5% for 256-QAM [69].

2.6 Linearization of Power Amplifier-Based Beamforming Transmitters: State-Of-The-Art

Owing to its success in compensating for the nonlinearity exhibited by sub-6 GHz PAs, DPD has recently been employed to improve the linearity-efficiency tradeoff of MMW/sub-THz radio systems. In this section, we present a comprehensive review of major works on DPD for beamforming arrays.

2.6.1 RF Beamforming Transmitters

DPD techniques aimed at linearizing RF beamforming arrays have garnered significant attention in recent literature. These studies delve into the feasibility of employing DPD to linearize arrays of PAs, tackle the implementation complexities related to the feedback mechanism necessary for DPD training, and explore methods to maintain linearization performance under varying operation conditions such as beam steering and input power.

SISO-DPD

Seminal research works such as in [4, 70–76], have extensively explored the feasibility of employing DPD techniques to linearize arrays of PAs within RF beamforming architectures. In [70, 71], the authors proposed employing a SISO-DPD function trained to minimize the ℓ_2 norm of errors measured at the PAs' outputs, thereby mitigating the average nonlinear behavior exhibited by these PAs. Conversely, authors in [72–76] advocated for a SISO-DPD trained to minimize the error between the coherent sum of PA outputs and the intended transmitted signal. While the approach in [70] may achieve better TRP-ACPR, the SISO-DPD proposed in [72–76] ensures a linearized behavior at the UE and strive for improved UE-ACPR. Nevertheless, as demonstrated through simulations in [75, 76] and subsequently validated in measurements in [77], linearizing the coherent sum of the PAs' outputs, although not guaranteed, often leads to a reduction in out-of-band emissions in the sidelobe directions of the array, which translate in improved TRP-ACPR performance. The degree of sidelobe linearization hinges upon the similarity between the nonlinearities exhibited by the PAs in the array.

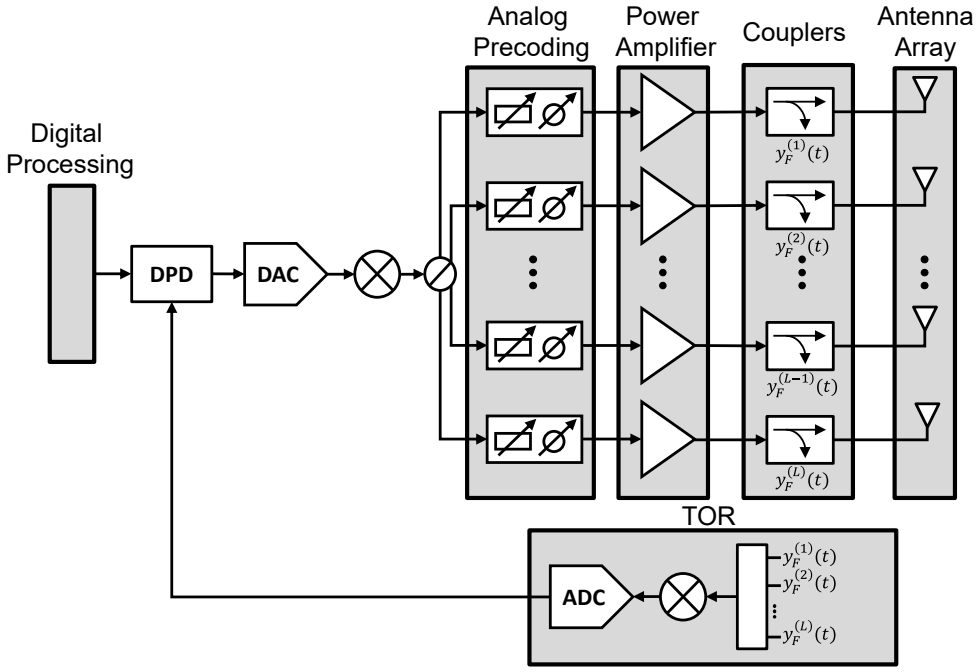


Figure 2.12: Block diagram of an RF beamforming array augmented with a SISO DPD module and couplers at the PA outputs for DPD training.

Ensuring linearization across both the main beam and sidelobes is paramount for meeting the TRP-ACPR requirement and ensuring linearized behavior at the UE. In the presence of significant discrepancies between the PAs' nonlinearity, the two-stage SISO-DPD proposed by [78] holds promise for improved TRP-ACPR and UE-ACPR. This approach involves using tuning boxes, implemented in the analog domain, to compensate for differences in PA behaviors, followed by the adoption of a SISO-DPD function to linearize the coherent sum of the residual nonlinearity in the array. Validation of the scheme proposed in [78] was conducted on a 4-element tapered slot linear array driven with up to 40 MHz LTE signals centered at 27 GHz, demonstrating linearization of both the main beam and sidelobes, thereby achieving excellent TRP and UE-ACPR.

Transmitter Observation Receivers

To facilitate the acquisition of feedback signals necessary for training the SISO-DPD function, several studies including [70, 75, 76] have proposed the integration of dedicated RF

signal sampling components, typically directional couplers, between each PA and antenna element in the array. These components serve as TORs, as illustrated in Fig. 2.12. The acquisition of the coupled signals is then carried out using either i) a single time-shared TOR across all paths [70, 75], or ii) an analog anti-beamforming circuitry that enables the capture of the PA outputs coherent sum [76]. An alternative approach, proposed by [4, 79], suggests sampling the signal transmitted by a single representative PA in the array while assuming similar nonlinearity across all other PAs, effectively reducing the number of required feedback paths. The investigations conducted in [4, 70, 75, 76, 79] have demonstrated good linearization results in both simulation and measurement when applied to sub-6 GHz systems. Nevertheless, implementing couplers at the PA outputs in MMW phased arrays can pose challenges due to demanding system integration requirements and limitations imposed by the PCB fabrication process.

To limit the number of TORs required to train the DPD function in RF beamforming arrays and avoid the use of couplers at the PA outputs, researchers have explored the concept of FF TORs, as discussed in previous literature [72–74, 77, 80–82]. Using this approach, during SISO-DPD training, the array's main beam is directed towards the FF probe, which samples the coherent sum of the PA outputs needed to train the DPD function. Alternatively, to alleviate the need to direct the beam towards the FF feedback probe during DPD training, which would disrupt the communication link, researchers proposed an alternative approach in [83], further explored in subsequent works such as [84, 85], where the feedback mechanism uses a FF probing antenna positioned in a fixed location, distinct from the direction of the main beam and where the DPD training does not necessitate steering the beam towards the FF probe. In this scheme, a system of equations derived from the signals acquired from the FF probe when the main beam is steered is utilized to estimate the individual PA outputs in the array. Subsequently, the estimated PA outputs are leveraged to infer the FF-received signal at the intended UE for DPD function training. Furthermore, to relax, the requirement on the FF TOR dynamic range, [84] introduced an algorithm that synthesizes constant magnitude tapering profiles, ensuring that sidelobes in the FF feedback probe direction maintain adequate SNR when acquiring necessary data for SISO-DPD function training.

The seminal research in [83–85], while promising, comes with its own set of drawbacks. For instance, routing the sampled signals from the FF probe to the base-station would inevitably increase system deployment costs. Moreover, relying on a FF feedback mechanism may introduce sensitivity in SISO-DPD training to variations in channel conditions, such as shadowing effects, potentially altering DPD linearization performance. As an alternative to coupler-based and FF-based DPD training methods, [86] proposed the use of antenna elements in the array to serve as TORs. During SISO-DPD training, the feedback signal

at each feedback antenna is captured in different time slots, with the transmitting array's beamforming coefficients adjusted in each slot to ensure a coherent phase combining of the PA outputs at the selected feedback antenna. The acquired feedback signals are then digitally summed to generate an estimate of the FF signal, which is subsequently used to train the DPD function. However, this approach necessitates an array system where the selection of feedback antennas ensures that the sums of the magnitudes of the coupling factors between a radiating element and the feedback antenna are equal for all radiating elements. While the method was successfully validated on a sub-6 GHz linear array with four radiating elements and two feedback probes, the feasibility of extending this approach to larger arrays while maintaining the requirement on the coupling magnitudes remains uncertain. To alleviate the requirement on the coupling magnitude between the array elements and the TOR antennas in [86], the authors in [87] proposed to perform DPD training using a single transmit-receive antenna pair, with the remaining transmitting elements turned off and where an antenna element is the array is repurposed as a TOR. This approach assumes that all the PAs in the array exhibit similar nonlinearity, enabling the DPD function trained on one PA to extend its linearization to the remaining PAs in the array. While this condition is met by the array to be linearized in [87], a typical off-the-shelf MMW array will not satisfy this condition. Furthermore, using antenna elements in the array to serve as TORs for DPD training such as in [86] and [87], has the disadvantage of disturbing the uniformity in distributions of the antenna elements which affects the array's radiation pattern. Alternatively, [88] proposed a DPD training method employing NF probes positioned along the array's perimeter. This technique entails synthesizing an NF target signal, which corresponds to a distortion-free FF signal directed toward the intended user. During DPD training, the NF probes' output signals are iteratively adjusted until they converge to the pre-synthesized NF target signal. While this approach showcases the feasibility of NF-based DPD training methods, it still relies on synthesizing the desired NF target signal, which initially necessitates a FF probing antenna. While promising for DPD training, its practical deployment requires the development of a real-time methodology to derive the NF target signal solely based on information available at the transmitter side, an area of focus for this thesis.

Linearization Performance under Varying Operation Conditions

While the research in [4, 70, 72–76, 80, 83, 86, 87, 89] has effectively showcased the capacity of DPD to linearize RF beamforming arrays, maintaining their linearization performance proves challenging under varying array operation conditions. Specifically, the finite isolation between array antenna elements in typical beamforming arrays induces distinct nonlin-

ear behaviors in the PAs as the beam is steered (as discussed in sub-section 2.3.2) [90–92]. Consequently, when the beam deviates from the angle at which the SISO-DPD function was trained, the linearization performance of these arrays is significantly compromised, resulting in degraded TRP/UE-ACPR, and EVM. To address the above-mentioned challenge and improve DPD linearization performance over a wide steering range, [81] proposed using a neural network DPD model trained using data from multiple beam directions. While this approach reduced the variation in DPD performance versus steering angle, it provides sub-optimal DPD linearization in any direction. To maintain an optimal linearization performance when the beam is steered, [77, 92–95] suggested the use of multiple sets of DPD coefficients. In [77, 93], steering angles with comparable nonlinearity are grouped either based on measured UE-ACPR [77] or using a normalized mean square error (NMSE) based clustering algorithm [93]. Subsequently, a common DPD set of DPD coefficients is used for each grouping/cluster, effectively enabling linearization of the array over-wide steering range with excellent UE-ACPR and EVM. In an attempt to reduce the number of SISO-DPD coefficient sets to be identified, the authors in [92, 94] proposed using different interpolation schemes. Specifically, these works proposed to extract the SISO-DPD model coefficients for different reference steering angles. A linear interpolation model relating the antenna active reflection coefficient to the optimal DPD coefficients is then generated. Subsequently, when the array is steered, the antenna active reflection coefficient is measured using couplers at the PA outputs and the DPD model coefficients are deduced.

Alternatively, in [95, 96], building upon the foundation laid out in [97], a DPD scheme was introduced to dynamically adjust its coefficients according to the array's operational conditions such as steering angle and input power in [95] and steering angle and input signal PAPR in [96]. Recognizing the computational complexity associated with identifying a large set of coefficients for each operational condition and for each of the PAs in the array, and acknowledging that the array's nonlinearity across these conditions is correlated, the authors proposed a method to reduce complexity. Their approach involves transforming the regression matrix into a lower-dimensional form using a feature transformation matrix, selected via QR-singular value decomposition (SVD). In [95], this transformation is performed on the regression matrix used to describe the individual nonlinear behavior of the PAs in the array, while in [96], it operates on the regression matrix used to describe the aggregate nonlinearity of the array in the UE direction. This transformation allows for the identification of a reduced set of coefficients that theoretically capture the variations in the array's nonlinearity across different operational conditions. Furthermore, to further reduce the number of coefficients to be identified, the authors in [95, 96] proposed interpolation schemes that can interpolate between the identified coefficients using the proposed feature transformation and identify the required DPD coefficients for different operation condi-

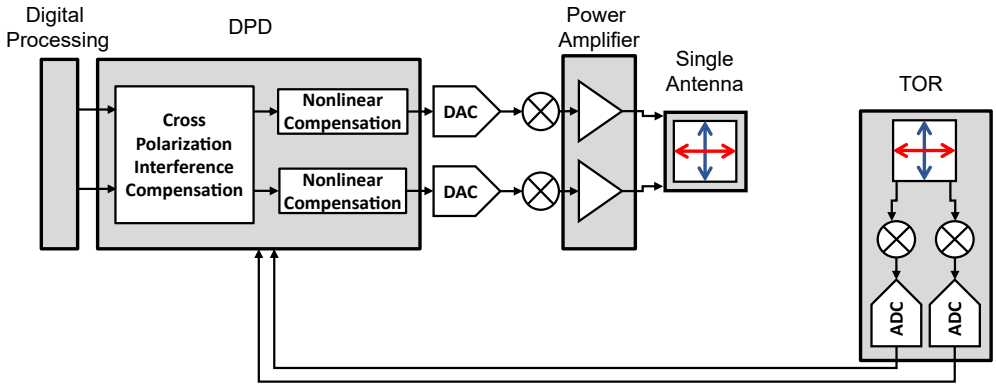


Figure 2.13: Block diagram of a single dual-polarized antenna system augmented with the DPD scheme in [2].

tions other than the ones identified during training. In [98] the authors proposed a DPD scheme that uses a memory polynomial (MP) -aided deep neural network (DNN) structure, where the neural network (NN) is used as a nonlinear mapper between the different array operation conditions and is used to generate the polynomial coefficients. Effectively, the DNN is acting as an interpolation function. The work in [98] was shown to yield excellent linearization across a wide range of steering angles and array input powers.

In addition to linearizing array behavior across different steering angles, several studies have investigated maintaining linearization behavior across various operational conditions such as bandwidth. For example, to sustain linearization performance across different bandwidth excitations without the need for full re-optimization of coefficients, [82] proposed a transfer learning-based approach. In this method, a NN-based DPD is pre-trained using a narrow-band signal, and during operation, only specific layers are retrained to adapt to changing signal bandwidth. These retrained layers are referred to as fine-tuning layers. The effectiveness of the DPD was validated through over-the-air (OTA) measurements on a 16-element array at 28 GHz, excited with signals ranging from 20 MHz to 100 MHz in bandwidth. Experimental results demonstrated a significant reduction in training time while ensuring good linearization performance. Despite the success of works such as [77, 82, 92–96, 98] in linearizing RF beamforming arrays over a wide steering range, they suffer from increased DPD training complexity and/or require substantial amounts of pre-training data. In this thesis, we aim to improve the linearization performance of SISO-DPD across various steering angles while reducing the necessity for identifying multiple sets of DPD coefficients or the need for substantial amounts of pre-training data.

Dual-Polarized RF Beamforming Transmitters

Dual-polarized MMW RF beamforming arrays have attracted significant research interest in recent years [99–101]. These arrays aim to exploit polarization diversity to transmit two independent data streams over the same carrier frequency, thereby enhancing spectrum utilization. DPD techniques have been recently applied to linearize dual-polarized arrays. For instance, in [2], the authors proposed the utilization of a SISO-DPD scheme (per polarization) preceded by a cross-polarization interference (XPI) compensation block to jointly mitigate both the nonlinearity of the PA and the XPI, which was experimentally validated on a single antenna system. While the results reported in [2] are promising, the proposed scheme is computationally complex as it requires iteratively estimating the XPI compensation block parameters during DPD function training. Moreover, in [2], the XPI is assumed to be frequency-independent, and the convergence of the proposed algorithm is not guaranteed.

More recently, in [102], the authors proposed using a dual-input-single-output (DISO) -DPD scheme (per polarization) to linearize a dual-polarized RF beamforming array in the presence of XPI, where, similarly to [2], the interference is solely attributed to the transmitter antennas. The inputs to the DISO-DPD functions are the signals intended to be radiated to the UE. However, training the DPD function to compensate for both the array's nonlinearity and the antennas' XPI is not desirable in practice. The XPI introduced by the antennas in the array is part of the channel (experienced during both up-link and down-link transmission) and should be accounted for by the precoder block. Compensating for the transmitter antennas' XPI using DPD would break channel reciprocity in TDD systems. Moreover, in both [2] and [102], the authors used a FF probe to capture the feedback signal needed to train the DPD functions. However, using FF-based TORs in dual-polarized arrays presents new challenges. For instance, relying on an FF-TOR would inevitably introduce XPI in the feedback channel. This may be due to the FF probe used, the OTA channel between the array and the FF probe, or mechanical misalignment between the transmitter antennas and the FF probe.

It's worth noting that the current literature lacks analysis of the impact of load modulation on dual-polarized arrays' nonlinearity when the array is steered and only focuses on single-user scenarios where both polarizations are steered toward the same direction. While the specific focus of this thesis does not encompass dual-polarized arrays, certain aspects of the research presented here can potentially be extended to such arrays. However, the exploration of this topic remains open for future investigation.

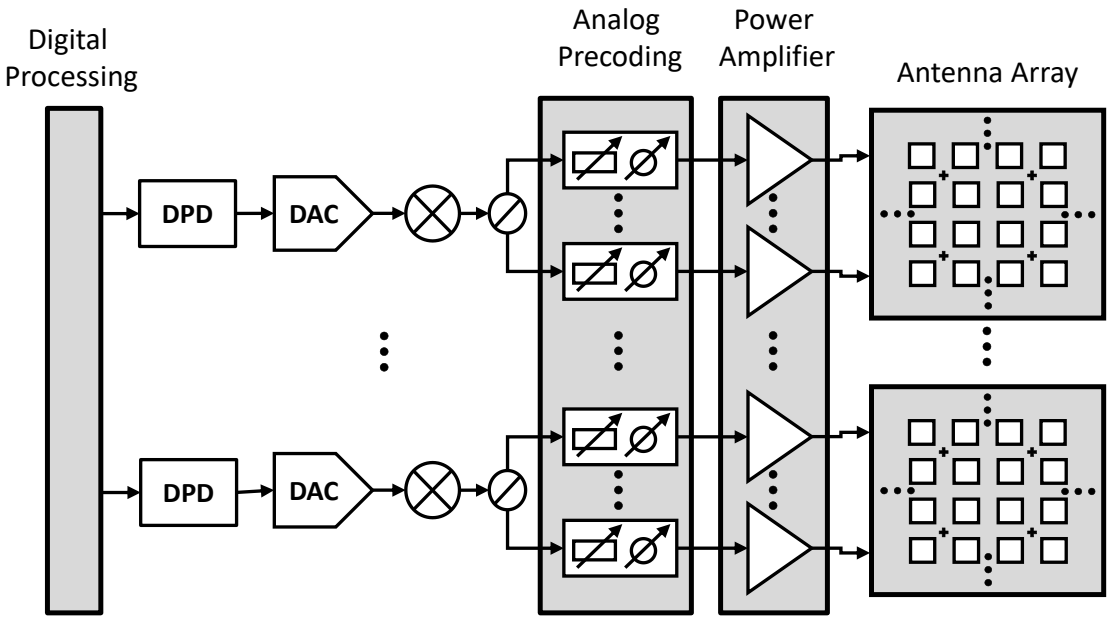


Figure 2.14: Block diagram of a partially-connected hybrid array augmented with a SISO DPD module per sub-array.

2.6.2 Hybrid Beamforming Transmitters

DPD techniques for linearizing hybrid beamforming arrays can be categorized into two groups: those tailored for partially-connected hybrid arrays and those targeting fully-connected hybrid arrays. For partially-connected hybrid arrays, researchers have proposed various approaches such as those outlined in [75,76,79,86,103,104]. These methods typically employ a SISO-DPD function per sub-array, as illustrated in Fig. 2.14. Accordingly, these sub-arrays are treated independently, and the SISO-DPD function within each sub-array is optimized to minimize the error between the desired transmitted signal and the coherent sum of the sub-array's PA outputs. In the presence of antenna mutual coupling between the sub-arrays' antennas, the work in [105] proposed to use DISO-DPD functions to linearize partially-connected hybrid arrays, as depicted in Fig. 2.15. Accordingly, one input to the DISO-DPD module represents the desired signal to be transmitted by the sub-array, while the second input provides an estimate of the impinging signal due to inter-sub-array antenna mutual coupling. It's noteworthy that in [105], the feedback signal used to train the DISO-DPD functions is obtained using a single FF feedback probe capturing the superposition of the coherent sum of the PA outputs in each sub-array. The effectiveness of this

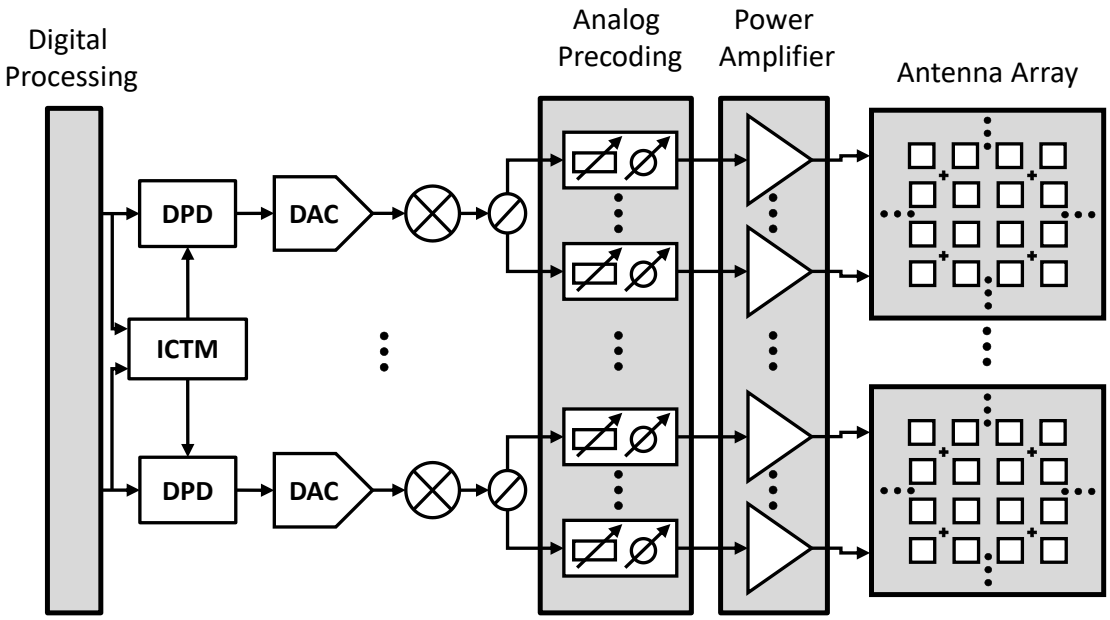


Figure 2.15: Block diagram of a partially-connected hybrid array augmented with a DISO-DPD module per sub-array.

scheme was demonstrated on a partially-connected hybrid beamforming array, which includes a three-path transmitter, with each path comprising two PA-antenna chains. These chains operate at 1.93 GHz and are driven with 20 MHz single-carrier signals.

On the other hand, for fully-connected hybrid beamforming arrays, where each RF to the array is connected to all of the array's antennas through a network of phase shifters and gain control circuitry, the DPD schemes in [75, 76, 79, 86, 103–105] are no longer applicable. This is due to the PAs in the array being driven with a linear combination of the array's input signals, which causes the nonlinear behavior at each of these PAs outputs to depend on all the array input signals. To linearize these arrays, the authors in [73, 106, 107] suggested using a multiple-input-single-output (MISO) -DPD function per RF input in the array. The DPD functions in these schemes are trained to minimize the errors radiated in the main beams' directions. The feedback signals needed to train the MISO-DPD functions are acquired using either couplers at the PAs outputs and an anti-beamformer that estimates the radiated signals in the beams' directions or using FF receivers located in the UE directions. These schemes have shown good linearization results in simulation [73, 106, 107] and in measurements on a 4-element linear hybrid array with two RF inputs

operating at 3.5 GHz [107]. Note, in [73, 106, 107], there is an underlying assumption that the number of beams generated by the analog precoder is equal to the number of RF inputs to the array and that the radiated signal in each beam is only proportional to one of the array's inputs. In practice, the number of radiated beams can differ from the number of RF inputs to the array. Moreover, in the special case where the number of beams is equal to the number of RF inputs to the array, relying on maximum ratio combining (MRT) analog precoder (as done in [73, 106, 107]) will induce interferences between the signals in the different beams and hence would break the aforementioned assumption (i.e., the radiated signal in each beam is only proportional to one of the array's inputs). To address this challenge, the authors in [108] proposed to use a feedback compensation block that maps the received signals in the directions of the beams to signals that are proportional to the array's RF inputs as shown in Fig. 2.16. The outputs of the feedback compensation block are then used to train MISO-DPD functions. The work in [108] was validated in simulation. Nevertheless, relying on couplers at the PA outputs or FF probes to capture the feedback signals needed to train the DPD functions, significantly increases the DPD complexity. Moreover, while the works in [73, 106–108] have shown promising results, the impact of beam steering on the DPD performance and analysis of the effects of load modulation experienced in large count fully-connected hybrid arrays are currently lacking in the literature and are areas of potential future investigation.

Although this thesis does not specifically address hybrid beamforming arrays, certain elements of the research presented herein may be applicable to partially connected hybrid arrays. However, the exploration of linearization techniques for both partially and fully connected hybrid beamforming arrays is an avenue for future investigation that warrants further exploration.

2.6.3 Digital Beamforming Transmitters

SISO-DPD

Numerous studies have explored DPD techniques for linearizing digital beamforming arrays operating below 6 GHz. In the absence of antenna mutual coupling, employing a SISO DPD per PA-antenna proves effective for linearizing digital beamforming arrays [109]. In such contexts, the DPD functions are trained independently, with feedback signals captured using couplers at the PA outputs. To mitigate the complexity associated with implementing a feedback path per antenna in a MIMO array, the authors in [110] proposed to train the SISO-DPDs to share a single set of coefficients, which are extracted by sampling a subset of PAs in the array. The scheme presented in [110] demonstrated exceptional linearization

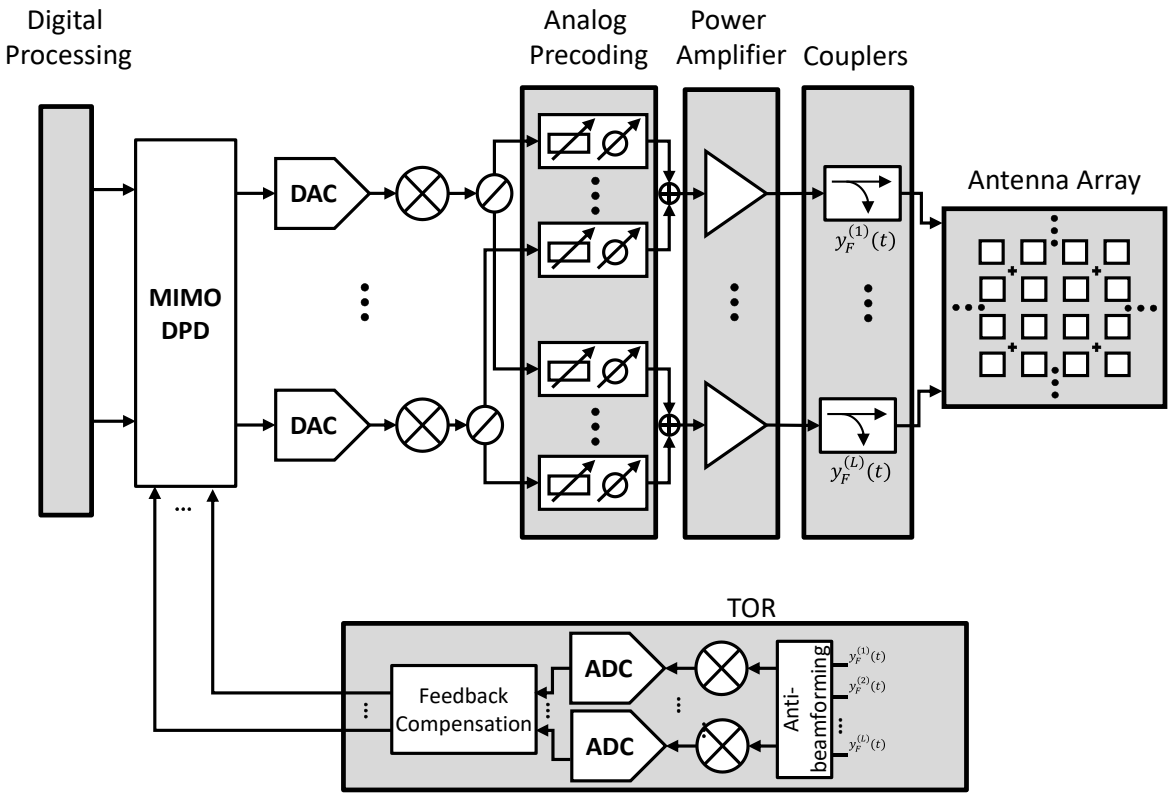


Figure 2.16: Block diagram of a fully-connected hybrid array augmented with a MIMO DPD module.

results in measurements, achieving effective linearization of an array of PAs using a single set of coefficients and trained using the outputs of a sub-set of PAs. Nevertheless, practical MIMO arrays suffer from non-negligible antenna mutual coupling, causing the PAs in the array to experience time-varying incident waves at their outputs. This phenomenon introduces non-negligible nonlinearities and hinders the capacity of SISO DPDs to linearize MIMO arrays.

MIMO-DPD

To mitigate the impact of mutual coupling on array non-linear behavior, MISO-DPD architectures have been proposed by researchers [111, 112]. In [111], a MIMO-DPD was devised using multi-input Volterra-based functions, while in [112], a MIMO-DPD based on

real-valued time-delay NN was adopted. These approaches were validated on arrays with two and three antennas, respectively. In [111], the MIMO-DPD compensated for array nonlinearity amidst mutual coupling at PA inputs, while in [112], it addressed PA nonlinearity, mutual coupling, and I/Q imbalance. While the work in [111,112] demonstrated the applicability of MIMO-DPD to linearize the impairments in MIMO arrays, implementing these methods in large array systems can be complex due to their quadratic complexity scaling with the number of antennas and the large number of DPD bases.

Pruning strategies offer a solution to mitigate MIMO-DPD complexity. For example, Pere et al. [113] proposed employing data selection and dimensionality reduction techniques to streamline MIMO-DPD complexity, reduce training time, and simplify DPD coefficient identification. Their method selects training data based on their correlation factor to the previous dataset used for training. Furthermore, they proposed two techniques to reduce MIMO-DPD basis matrix dimensionality. The first employs orthogonal least squares for model order reduction, transforming DPD bases into orthogonal bases using the Gram–Schmidt method. This transformation enables tracking the contribution of the MIMO-DPD bases to modeling accuracy, which is leveraged to reduce the size of the basis matrix while minimizing the impact on performance. The second approach uses principal component analysis to transform an original set of potentially correlated basis functions into a new, uncorrelated, and lower-dimensional orthogonal basis, known as principal components. This transformation is achieved by multiplying the basis matrix by a transformation matrix. In [114], a pruning technique for NNs was proposed, where specific coefficients and bias terms in the NN structure are zeroed based on their impact on linearization performance, determined offline. Furthermore, to enable fast identification and updates of NN-based MIMO-DPD when power to the PAs varies, the authors proposed retraining only a predefined subset of NN coefficients/bias terms. The work in [114] was successfully validated on hardware platforms.

DISO-DPD

Alternatively to MIMO-DPD, in [115] the authors proposed the use of DISO-DPD functions per PA-antenna pair to linearize digital beamforming arrays in the presence of antenna mutual coupling as shown in Fig. 2.17. The implementation complexity of the DPD scheme proposed in [115] has the advantage of scaling approximately linearly with the number of antennas [116]. In [115], the ℓ'th DISO-DPD module associated with the ℓ'th PA-antenna pair in the array is designed to have as inputs, the desired signal to be transmitted by the ℓ'th antenna and the incident wave at the ℓ'th PA output. In [115], the incident wave at the PA outputs can either be sampled using reverse couplers at the PA outputs or can

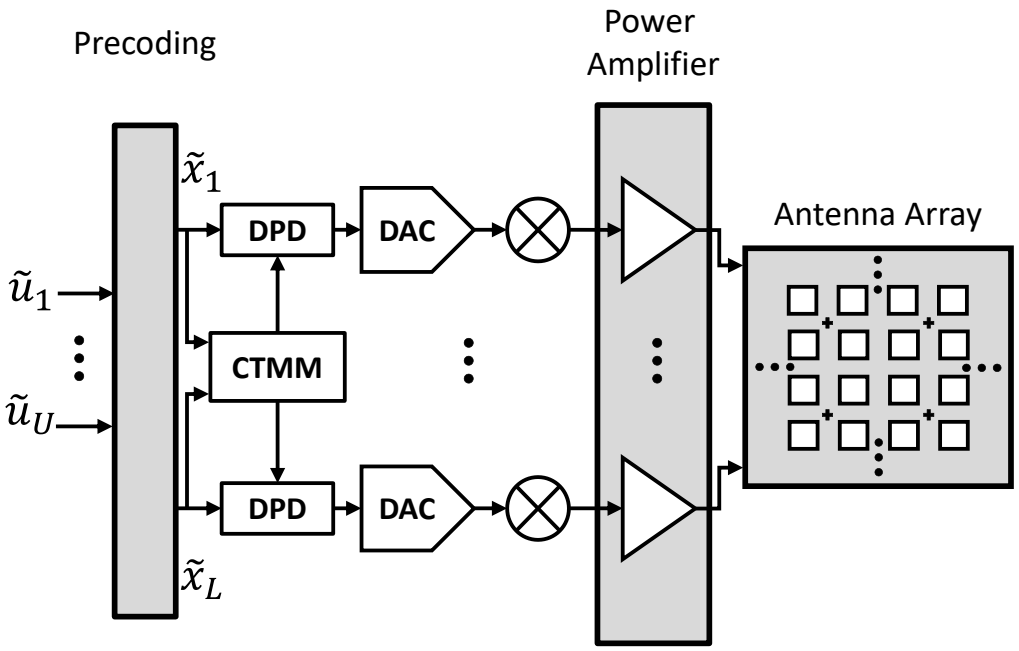


Figure 2.17: Block diagram of a digital beamforming array augmented with a DISO DPD module per antenna.

be estimated using a mutual coupling and mismatch model (CTMM). The work in [115] was validated on a digital beamforming array with four antenna elements and driven with 5 MHz signals centered at 2.12 GHz where the precoder is bypassed and the PAs are driven with equal power uncorrelated signals. While the DPDs in [111–115] proved effective in linearizing MIMO arrays, their performance is typically affected when conventional precoding schemes are applied (namely, MRT, zero-forcing (ZF), and minimum mean square error (MMSE) precoders). This is because these precoding techniques typically result in significant disparities in the average power levels across the RF chains in the array that are a function of the channel. The combined effect of precoding and antenna mutual coupling results in channel-dependent array nonlinearity where the DPD functions would need to be retrained when the precoding matrix is updated.

To address this challenge, the authors in [117] proposed to use of precoders, referred to as equal power (EP) -MRT, EP-ZF or EP-MMSE, that are optimized to minimize the disparity in radiated power between the antenna elements. Using these classes of precoders, the author then shows in simulation and in measurements, on a 4-element array operating at 3.5 GHz, driven with 100 MHz OFDM signals, that a single set of DISO-DPD coeffi-

cients trained using the approach in [115] can maintain excellent linearization performance across 200 different channel realization. While effective, "EP-precoders" do not possess a closed-form solution and are complex to synthesize in real-time which hinders their applicability in fast-changing channel conditions. In an attempt to reduce the complexity associated with synthesizing the "EP-precoders", the authors in [118, 119] proposed a ZF precoder that can be iteratively computed with relatively low complexity, compared to the optimum EP-precoder in [120], and that sub-optimally approaches the EP-ZF precoder in terms of reducing the power disparity between the antenna elements. Furthermore, to ensure better linearization performance across different channel realization, in addition to the sub-optimal EP-precoder, the authors [119] proposed a load and power-indexed DISO-DPD scheme to linearize the array. Once these coefficients are estimated (i.e., for predefined load and power indexes), depending on the channel, one of these identified sets of DPD coefficients is applied. To linearize MIMO arrays in the presence of antenna cross-coupling without resorting to the complex DISO-MIMO DPD, Yao et al. [121] proposed a combination of SISO-DPD trained to minimize distortions as received by the user (i.e., linearizing the coherent combining error) and a successive refining filtering applied to the precoding matrix to mitigate the impact of antenna mutual coupling on the user-received signal. While effective in simulation and showing improved performance compared to a conventional SISO-DPD as used in Hang et al. [109], this approach of linearizing distortions as experienced by users results in residual nonlinearity at the PAs outputs and leads to deteriorated TRP-ACPR performance compared to the previously discussed DPD schemes. Furthermore, the approach necessitates retraining of the precoder refining function and DPD coefficients when the channel is updated.

UE-MIMO-DPD

In an attempt to reduce the number of DPD functions needed to linearize digital beamforming arrays, the authors in [122, 123] suggested implementing the DPD modules before the precoding block. In doing so, the number of DPD functions needed to linearize the array becomes proportional to the number of spatially multiplexed streams or users, rather than being dependent on the number of antennas. The DPD in [122] uses a NN while in [123] the authors implemented the DPD in the frequency domain. Both approaches in [122, 123] adopt a MIMO-DPD structure. The DPD in [122] was validated in simulation while the one in [123] was validated both in simulation on a 100-element digital beamforming system and in measurements on a 64-element RF beamforming array operating at 28 GHz. Despite the promising results reported in [122, 123] in linearizing MIMO arrays and ensuring distortion-free signals at the users, positioning the DPD before the precoding block may

lead to failure in ensuring linear behavior for each of the PAs in the array. This aspect is particularly crucial in stringent applications such as in the Sub-6 GHz range, where adopting this approach may cause the DPD to fail to meet the TRP-ACPR emission mask requirement. Furthermore, the authors in [123] demonstrated that in multi-beam scenarios, higher-order nonlinearity can cause what can be visualized as inter-beam spatial mixing or beam intermodulation products, resulting in distortions adding coherently in various directions, including those towards the users. Similar phenomena are also discussed in Hemmi et al. [124]. Positioning the DPD before the precoder would leave the inter-beam products un-linearized, potentially causing interference. To address this issue, Brihuega et al. [123] proposed linearizing the MIMO array in the direction where coherent combining of the nonlinearity is achieved.

Precoding and DPD

Alternatively, in scenarios where the TRP-ACPR is relaxed, some work has investigated using precoding to cancel nonlinear distortion in specific locations in space to avoid interference without the need to deploy DPD. For instance, Kolomvakis et al. [125] proposed a null-forming precoder that nulls the distortions at user-specific locations in space while maximizing the power in the user direction. The synthesized precoder in [125] has a constant magnitude constraint that ensures that both linear and nonlinear portions of the signals are affected by the precoder similarly, guaranteeing linear and nonlinear nulling of the interference in space. Additionally, Rottenberg et al. [126, 127] proposed a family of precoders with a closed-form solution that cancels third-order nonlinear distortion in the user directions without characterizing or compensating for the PA's nonlinearity. While the scheme in [127] was successfully demonstrated in simulation, the synthesized precoders have the disadvantage of reducing the received power at the user compared to the MRT precoder. Nevertheless, the authors showed that for a large number of antennas, the gain drop tends to zero as the number of antenna elements increases. Alternatively, in an endeavor to synthesize a precoder maximizing the sum rate at the user direction in the presence of PA distortion, Sina et al. [128] proposed a method. Given the non-convex nature of the formulated optimization problems, they proposed solving the optimization problem using an iterative projected gradient ascent algorithm where the gradient of the sum rate is computed numerically. Through simulations, assuming identical PA nonlinearity, the proposed precoder outperformed conventional linear precoders. While the work in [125,127,128] have shown promise, they assume that the PA's nonlinearity in the array is identical, limiting the achievable nonlinearity spatial cancellation in practice. Furthermore, both schemes in [125, 127, 128], are limited to single-user LoS scenarios.

2.7 Calibration Techniques for Beamforming Arrays: State-Of-The-Art

Most works on DPD discussed in Section 2.6 assume that the array is calibrated a priori. Many calibration techniques for beamforming arrays have been discussed in the literature. For digital beamforming arrays, calibration schemes are used to compensate for the different time delays, phase offsets, and magnitude discrepancies in the array's RF chains. For hybrid and RF beamforming arrays, where an analog precoder is used, calibration is used to compensate for beamforming errors attributed to the phase shifters and gain control circuitry in the array as well as any other errors attributed to, among others, process variation, unequal routing, impedance variations, or positional offsets in assembly. Existing calibration methods in the literature for beamforming arrays can be classified into two categories; i) element-wise array calibration [129–136] and ii) active array calibration [137–140].

2.7.1 Element-Wise Array Calibration

Using element-wise calibration, the array's RF chains are calibrated sequentially one antenna at a time with the remaining elements typically disabled. The NF scanning probe method in [129], also known as "park and probe", is one of the most widely used element-wise calibrations in the industry. Using this approach, a robotic manipulator places an NF probe at the boresight of the antenna element to be tested and measures its relative phase and magnitude errors with respect to a reference element. The NF scanning probe method is typically performed in a controlled environment such as an anechoic chamber. In [130] the authors proposed a rotating element electric field vector (REV) method for element-wise array calibration that only relies on a power detector receiver to calibrate the array. Using this scheme, the phase and magnitude errors corresponding to the individual elements in the array can be sequentially estimated by sweeping the antenna element phase settings (one antenna at a time) and measuring the ratio between the maximum and minimum FF received powers as well as the phase setting that maximizes the FF received power. In [131] the authors proposed a REV-based calibration method that only requires three-phase measurements per element. While [129–131] are effective in calibrating beamforming arrays with a high level of accuracy, the reliance on a FF probe and an anechoic chamber limits their applicability to in-situ calibration (i.e., factory calibration). For in-field calibration, the authors in [133, 134] suggested the use of an element-wise calibration method where the calibration feedback signal is captured using an NF probe mounted on

a calibration tower in the vicinity of the array [133], or an array of NF probes embedded in the transmitting array [134]. Alternatively, the authors in [132] suggest the use of a mutual coupling method to calibrate digital beamforming arrays. Using the method in [132], the inherent mutual coupling among the array elements is used where one antenna element is operated in transmitter mode while another is used in receiver mode. The measurements between all pairs of elements in the array are then used to characterize the relative errors between the antenna elements and calibrate the array. In [135,136] the authors embedded a transmission line in the antenna array that weakly couples with all the radiating elements. The output of the transmission line is then used to sequentially calibrate an RF beamforming array in [135] and a digital beamforming array in [136]. While the works in [132–136] enable in-field calibration, they are inherently slow as they rely on element-wise calibration. Moreover, they do not account for errors due to current loading and heating effects.

2.7.2 Active Array Calibration

To mitigate the challenges associated with element-wise calibration, active array calibration has been proposed in the literature where the array's RF chains are calibrated simultaneously. In [137–140] an active array calibration method that uses orthogonal coding and a series of measurements at the FF is proposed. In [139, 140], the array was calibrated to have similar third-order inter-modulation product levels between the different RF branches in the array. Despite the promising results achieved using the methods in [137–140], the reliance on a FF probe hinders its applicability to in-field testing. Moreover, such an approach is not suitable to calibrate for phase-dependent errors.

The development of calibration schemes that merge the benefits of element-wise and FF-based active calibration methods more suitable for in-field deployment is an active area of research and is addressed in parts of this thesis.

2.8 Linearization of Frequency Multipliers: State-Of-The-Art

In this section a review of the state-of-the-art DPD schemes for linearizing FXs and FX-based transmitters are presented.

FXs play a pivotal role in radar systems, especially in scenarios requiring high-frequency resolution sources [141]. The digitally controlled oscillator in these systems is typically

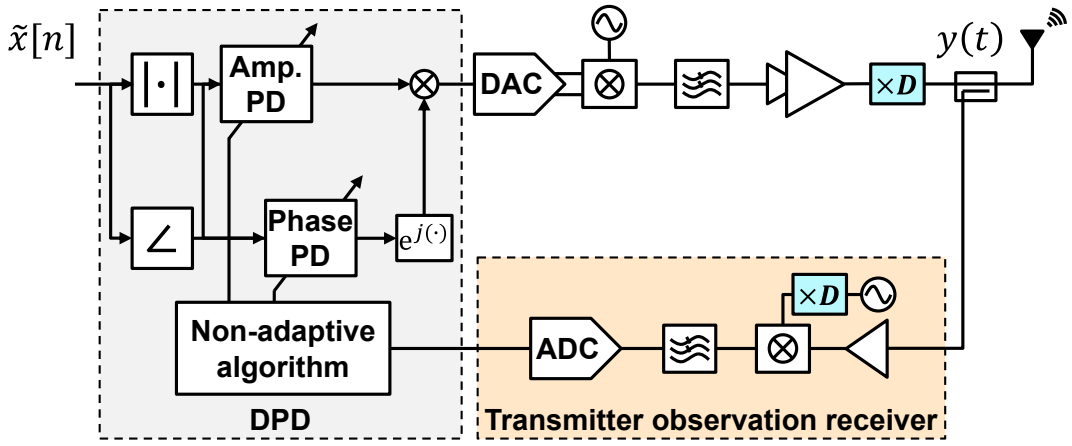


Figure 2.18: Block diagram of the first attempted DPD scheme for linearizing FX-based transmitters [3].

designed to operate at lower frequencies, ensuring superior frequency resolution. FXs then become integral components, up-converting the generated FMCW signal from these sources to the desired radar operational frequency. The incorporation of FXs as up-converters in radar systems is made feasible by the constant envelope characteristic inherent in FMCW signals, providing resilience to FX nonlinearity. However, in the context of generating distortion-free, spectrum-efficient modulated signals for communication systems using FX-based transmitters, the application of linearization techniques becomes imperative. This is essential to counteract the inherent FX nonlinearity and ensure compliance with stringent regulatory requirements.

2.8.1 Seminal Works

The pursuit of linearizing FXs finds its roots in a seminal work from 2003 by Park et al. [3]. This groundbreaking study introduced an innovative approach, modeling the nonlinearity of FXs as a composite effect of both AM-AM and AM-PM nonlinearity. Additionally, the authors incorporated a phase-to-phase (PM-PM) nonlinearity factor to account for the power function intrinsic to FXs, resulting in a phase multiplication of the input signal by the multiplication order of the FX. The proposed DPD model in this early work was non-adaptive, utilizing indirect learning. It relied on two memory-less polynomial functions to model the AM-AM and AM-PM characteristics, with their coefficients identified through least square estimation. A block diagram representation of the DPD proposed in [3] is

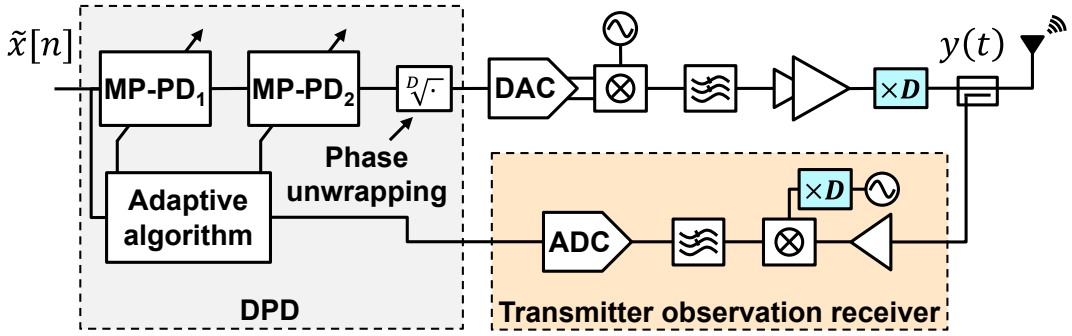


Figure 2.19: Block diagram of the DPD scheme incorporating phase unwrapping [4].

shown in Fig. 2.18. To enhance linearization performance, the authors in [142] later suggested the use of an adaptive Look-Up Table (LUT) and polynomial-based linearization schemes. These advancements built upon the initial DPD architecture proposed by Park et al. [3] and allowed for improved linearization performance.

2.8.2 Phase Unwrapping and Two-Stage DPD Training

The exploration conducted in [3, 142–145] highlighted the capability of FXs in generating modulated signals. However, the reported linearization outcomes faced constraints, particularly notable when extending the signal modulation bandwidth. This limitation stems from two primary factors. Firstly, these methodologies operated under the assumption of a memoryless model. Secondly, compensation for PM-PM nonlinearities, achieved by dividing the input signal phase by the multiplier multiplication order, introduced discontinuities in the phase of the predistorted signal. This, coupled with the inherent band-limited nature of the transmitter, led to a degradation of linearization performance. Addressing these challenges, [4] proposed an innovative DPD structure for FX linearization illustrated in Fig. 2.19. This structure comprises a cascade of two memory-polynomial functions, designed to model the FX's high nonlinearity, followed by a Dth root function. A pivotal contribution of the work lies in the authors' analysis of the impact of the phase discontinuity introduced by the Dth root function on FX linearizability in band-limited transmitters. Additionally, a phase unwrapping Dth root-based method was introduced to mitigate this challenge, resulting in significantly improved linearization performance. The proposed DPD in [4] underwent experimental validation on a frequency-quadrupler setup, enabling the generation of up to 256-QAM, 5 MHz bandwidth single carrier modulated signals with excellent linearization performance. To determine the coefficients of the DPD

functions, [4] introduced a sequential least square estimation approach. In this method, each memory polynomial function in the proposed cascaded structure is identified one at a time and iteratively. It is noteworthy that the use of phase unwrapping, pioneered by [4], became widely adopted in subsequent works in the literature, marking a crucial milestone in the field of DPD for FXs. Nevertheless, one of the major challenges in [4] lies in the complexity associated with the two-stage estimation process of the DPD coefficients and with the implementation complexity associated with implementing the Dth root function in practical hardware.

In an endeavor to simplify the signal processing complexities associated with FX-based transmitters, Nopchinda et al. proposed a novel linearization scheme in their work [146], drawing inspiration from the phase-unwrapping technique introduced in [4]. This innovative approach involves selectively altering only the phase of the input signal to the multiplier while keeping the magnitude unaltered, a technique termed as a phase-retarder by the authors. Remarkably, using this technique the author in [147] demonstrated in later work that, under the specific condition of memoryless FX nonlinearity, the use of the proposed phase-retarder ensures that the transmitted M-PSK OFDM signal constellation remains unaffected by the FX's static nonlinearity, facilitating successful demodulation of OFDM symbols. Experimental validation of these findings was conducted on a 20 GHz frequency doubler, operating with an 8-PSK OFDM signal, yielding successful demodulation with a low bit-error rate. To further enhance signal demodulation accuracy, a nonlinear equalizer at the receiver can be employed [146, 147], effectively mitigating the impact of residual nonlinearities introduced by the FX on signal integrity. While these results offer practical solutions to alleviate the digital signal processing burden associated with FX-based transmitters, it is crucial to recognize that for higher constellation OFDM signal modulation schemes, the implementation of DPD at the transmitter remains the preferred choice. This ensures superiorEVM performance and avoids imposing constraints on the modulation scheme. Additionally, it is important to note that the FX memoryless assumption, while valid for certain scenarios, may not hold for wide modulation bandwidth signals, thereby limiting the applicability of this approach.

In an effort to enhance the DPD linearization performance in FX-based transmitters operating with wideband modulated signals, Chung et al. proposed a novel modeling approach in their work [5]. The authors envisioned the FX as the cascade of three nonlinear blocks: a non-frequency-translating nonlinear block, an ideal power function, and a second non-frequency-translating nonlinear block, shown in Fig. 2.20. To establish the DPD bases, the authors initiated their modeling from a passband Volterra series, subsequently simplifying it to complex baseband to effectively capture FX nonlinearities around the carrier frequency. Moreover, in [5], the authors theoretically investigated the impact of the

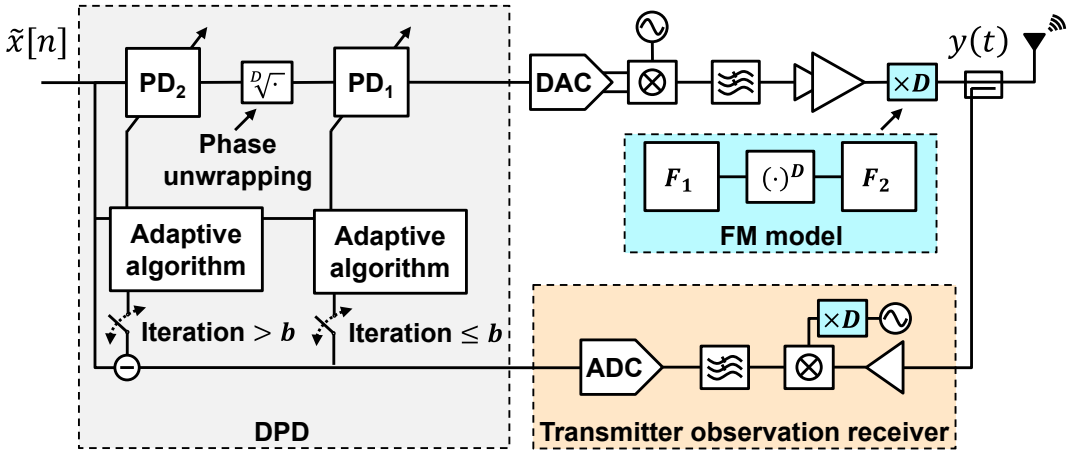


Figure 2.20: Block diagram of the DPD scheme using a cascade of three modules [5].

FX power function on quantization noise, revealing a degradation proportional to the FX multiplication factor. Similar to the approach in [4], the DPD scheme in [5] employed a two-stage DPD coefficients identification procedure, but with the distinction that the DPD Volterra functions were interspersed with a Dth root function as shown in Fig. 2.20. Experimental validation of the DPD scheme in [5] was conducted on FXs with multiplication orders up to four. Notably, it marked the first time OFDM signals with bandwidths up to 400 MHz were applied, and the system operated at frequencies reaching 63 GHz. The reported results in [5] demonstrated excellent linearization performance, with measured KPIs comparable to those achieved by DPDs applied to PA-based systems, especially for modulation bandwidths below 200 MHz. Despite these promising outcomes, three notable issues were identified. Firstly, the linearization performance appeared to deteriorate with an increase in modulation bandwidth, indicating a potential challenge with the suggested three-block modeling approach. Secondly, linearization performance seemed to decline with an increase in FX multiplication order. Finally, the use of a two-stage identification method introduces significant computational complexity and does not guarantee convergence to an optimal solution.

As the modulated signal bandwidth is widened, the application of DPD to FX-based transmitter linearization encounters practical limitations that require careful consideration. Notably, issues related to data-converter bandwidths and sampling speeds emerge as constraining factors when striving to increase signal modulation bandwidths. For instance, to facilitate the training of the DPD function, the feedback observation receiver required for sampling the FX nonlinear output typically operates at around five times the signal

bandwidth. A recent endeavor to mitigate these challenges and reduce the DPD feedback receiver bandwidth in FX-based transmitters was presented in [148]. The DPD structure utilized in [148] adopts the three-block model proposed in [5]. This innovative method incorporates spectral extrapolation and a band-divided-based DPD modeling approach to enable the training of the DPD function within the limitations of a bandwidth-limited feedback receiver. Specifically, to train the DPD function following the Dth root function, the bandwidth-limited FX output received signal undergoes forward modeling. This process estimates the out-of-band spectral content, contributing to the training of the DPD function. Similarly, for the DPD function preceding the Dth root function, a forward modeling approach, coupled with band-divided-based training, is employed. This involves using the bandwidth-limited FX output received signal to train two memory polynomial functions. These functions aid in estimating the inband and out-of-band spectral content of the received signal, facilitating the reconstruction of the full-band FX output signal and training of the associated DPD functions. The effectiveness of the proposed methodology in [148] was successfully demonstrated in the linearization of a frequency doubler. The system was driven by a 16-QAM modulated signal with a modulation bandwidth of 24 MHz, utilizing an observation bandwidth of 78 MHz—equivalent to 3.25 times the signal bandwidth. This approach showcases a promising solution to overcome the challenges associated with DPD implementation in FX-based transmitters operating with wide signal bandwidths. While the work in [148] primarily focused on reducing the TOR bandwidth, it did not tackle the challenge associated with the high-speed DACs required by FX-based transmitters. In fact, unlike non- FX-based transmitters that typically necessitate a transmitter with about five times the signal bandwidth, FM-based transmitters require approximately twice or more that bandwidth due to spectral regrowth attributed to the Dth root function. This translates into high DAC power overhead and stringent bandwidth requirements for the RF front-end. This challenge associated with the high-speed DAC requirement in FX-based transmitters will be addressed in subsequent chapters of this thesis.

2.8.3 Additive Error Model and Single-Stage DPD Training

The challenges observed in the linearization performance for ultra-wideband modulated signals, as reported in [5], prompted a reevaluation of existing approaches by the authors in [6]. Previous methodologies in the literature predominantly adapted techniques developed for linearizing nonlinear PAs and applied them to FXs. In contrast, the authors in [6] introduced an innovative additive model to characterize FX nonlinearity. Notably, this approach made no assumptions about the FX nonlinearity or the structure of the DPD system. Instead, the DPD solution was directly derived from the proposed additive

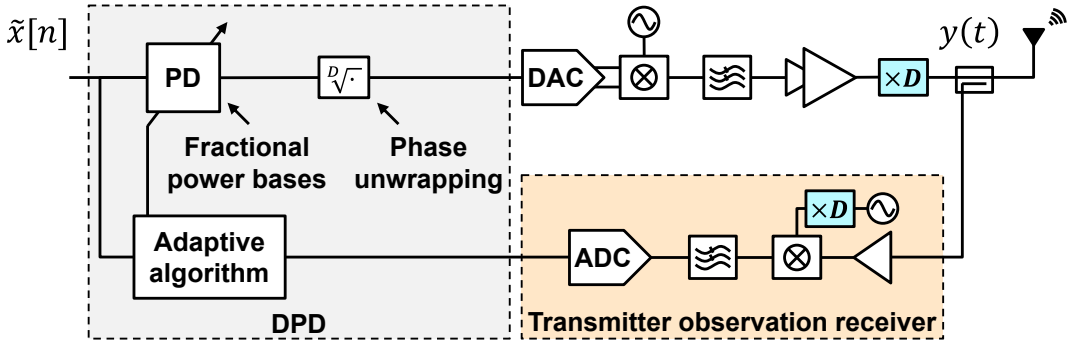


Figure 2.21: Block diagram of the DPD scheme using fractional power bases in [6].

model and hence specifically tailored to the characteristics of FXs. To establish the DPD model bases, a passband Volterra series was employed by the authors to model FX nonlinearity. Subsequently, this model was simplified to complex baseband and integrated into the derived DPD solution. Two key findings emerged from this study. First, the additive model suggested that a straightforward DPD structure, comprising a Volterra-based function followed by a Dth root function, is sufficient for FX linearization. Second, it was shown that the DPD Volterra-based function must include fractional power bases to comprehensively model FX nonlinearity, in addition to both odd and even order bases. A block diagram representation of the DPD scheme proposed in [6] is shown in Fig. 2.21. These counter-intuitive findings, deviating from PA-based solutions, were experimentally validated and compared against the results in [5]. The experimental results showcased substantial improvements in linearization performance compared to [5], utilizing a reduced number of DPD coefficients. Additionally, the proposed approach demonstrated increased resilience to changes in modulation bandwidth and multiplication orders, while not relying on computationally complex sub-optimal two-step DPD coefficients identification schemes. While the results reported in [6] are promising, the reported linearization performance is diminished when the multiplication order and linearization bandwidth are increased. Notably, this scheme is sensitive to linear errors, such as non-flat frequency response, in the transmitter's RF chains preceding the FXs. Furthermore, the use of fractional bases significantly increases DPD implementation complexity in hardware. These challenges will be addressed in subsequent chapters of this thesis.

Chapter 3

Linearization of RF Beamforming Arrays in the Presence of Antenna Mutual Coupling

In beamforming arrays, the close spatial arrangement of antennas causes the radiated signals from the antennas in the array to couple to their adjacent antennas through a mechanism known as antenna mutual coupling. The confluence of circuit nonlinearity, resulting from the active circuitry within the array being driven efficiently yet nonlinearly, and the antenna mutual coupling between the antenna elements collectively induces nonlinear behavior that exhibits variability contingent on the beamforming steering angle. This chapter presents the contributions of **Publication I** and **Publication II**. Firstly, we investigate the impact of antenna mutual coupling on the nonlinear behavior of active circuitry in PA-based (**Publication I**) and FX-based (**Publication II**) beamformers. Our analysis yields a closed-form equation capturing the interplay between array nonlinear behavior and antenna mutual coupling during beam steering. Notably, we identify the substantial influence of tapering, a radiation pattern shaping technique, on antenna mutual coupling and array nonlinear behavior. Building on these insights, we introduce an optimization algorithm to synthesize tapering coefficients, mitigating the array's nonlinear dependency on beam-steering in the presence of mutual coupling **Publication I**. Additionally, for FX-based beamformers, we demonstrate through circuit-inspired analyses that transmitter nonlinearity displays resilience to antenna mutual coupling during beam-steering **Publication II**. Simulation and experimental validation illustrate the efficacy of the proposed tapering algorithm in reducing variation in PA-based RF beamforming arrays during beam steering (**Publication I**). Furthermore, simulation and experimental evidence confirm the

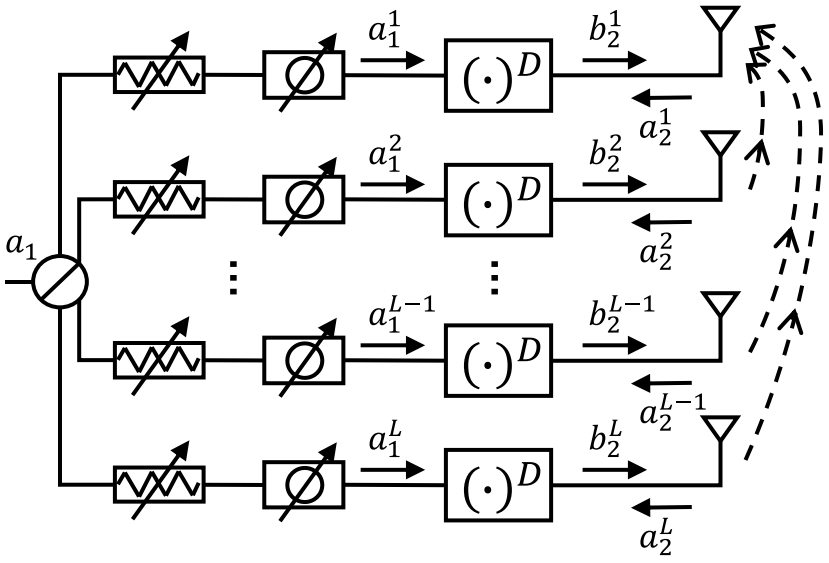


Figure 3.1: Block diagram of RF beamforming transmitter with L FXs driving L-element antenna array. The dotted arrows depict, for illustration, the coupling to channel 1 from all other channels.

resilience of FX-based beamformer nonlinearity to antenna mutual coupling effects during beam steering (**Publication II**).

3.1 Nonlinear Distortion Modeling of RF Beamforming Arrays

In this section, the nonlinear model of the nonlinear RF beamforming array depicted in Fig. 3.1 is formulated. The derivation is general and can be applied to PA-based RF beamforming arrays (i.e., with $D = 1$) or FX-based RF beamforming arrays (i.e., $D > 1$).

3.1.1 Angle-Independent DISO Forward Model Formulation

Let $a_1[n]$ be the sampled CBBE of the RF continuous time array input signal $a_1(t)$, and let $\tilde{a}_1^\ell[n]$ and $\tilde{a}_2^\ell[n]$ be the sampled CBBE of the incident wave signals at the ℓ'th PA/FX input, $a_1^\ell(t)$, and output, $a_2^\ell(t)$, ports respectively. Note here that $a_1^\ell[n]$ possesses an

angular frequency of ω_c rad/s while $b_2^\ell[n]$ and $a_2^\ell[n]$ appear at $D\omega_c$ rad/s. To derive the CBBE model for $\tilde{b}_2^\ell[n]$ in terms of $\tilde{a}_1^\ell[n]$ and $\tilde{a}_2^\ell[n]$, the passband dual-input Volterra series is used as a starting point and several signal conversions and simplifications are applied. The general form of the passband dual-input Volterra series used in this analysis is given below,

$$b_2^\ell[n] = \sum_{p_1=0}^{N} \sum_{p_2=0}^{N-p_1} \sum_{\substack{\mathbf{n}\in\mathcal{B}_1^{p_1} \\ \hat{\mathbf{n}}\in\mathcal{B}_2^{p_2}}} \eta_{\mathbf{n},\hat{\mathbf{n}}}^{p_1,p_2,\ell} \prod_{i=1}^{p_1} a_1^\ell[n-n_i] \prod_{j=1}^{p_2} a_2^\ell[n-\hat{n}_j], \tag{3.1}$$

where the set $\mathcal{B}_1 = \{0,1,2,\ldots,M_1\}$, the set $\mathcal{B}_2 = \{0,1,2,\ldots,M_2\}$, M_1 and M_2 are the maximum memory depth of a_1 and a_2 respectively, and $\eta_{\mathbf{n},\hat{\mathbf{n}}}^{p_1,p_2,\ell}$ are the passband forward model coefficients. Now, applying passband to baseband conversion and only keeping the terms appearing at output frequency $D\omega_c$, we get the following CBBE dual-input Volterra series for PAs/FXs,

$$\begin{aligned}\tilde{b}_2^\ell[n] = \sum_{p=0}^{N} \sum_{\substack{(k,k',s,s')\in\mathcal{A}(p) \\ \mathbf{m}\in\mathcal{B}_1^k,\, \hat{\mathbf{m}}\in\mathcal{B}_1^{k'} \\ \bar{\mathbf{m}}\in\mathcal{B}_2^s,\breve{\mathbf{m}}\in\mathcal{B}_2^{s'}}} & \gamma_{\mathbf{m},\hat{\mathbf{m}},\bar{\mathbf{m}},\breve{\mathbf{m}}}^{k,k',s,s',\ell} \prod_{i=1}^{k} \tilde{a}_1^\ell[n-m_i] \\ & \times \prod_{j=1}^{k'} \tilde{a}_1^{*\ell}[n-\hat{m}_j] \prod_{q=1}^{s} \tilde{a}_2^\ell[n-\bar{m}_q] \prod_{r=1}^{s'} \tilde{a}_2^{*\ell}[n-\breve{m}_r],\end{aligned} \tag{3.2}$$

where

$$\begin{aligned}\mathcal{A}(p) = \Big\{ & (k,k',s,s') \Big| (k,k',s,s') \in \mathbb{Z}^4, \\ & k \geq 0, k' \geq 0, s \geq 0, s' \geq 0, \\ & k + k' + s + s' = p, \\ & k - k' + Ds - Ds' = D \Big\},\end{aligned} \tag{3.3}$$

is the set of tuples (k,k',s,s') that result in a nonlinearity order of p and $\gamma_{\mathbf{m},\hat{\mathbf{m}},\bar{\mathbf{m}},\breve{\mathbf{m}}}^{k,k',s,s',\ell}$ are the CBBE forward model coefficients. Note, in (3.2) when D is odd (e.g., PA, tripler), the set $A(p) = \emptyset$ for p even. Consequently, for D odd, only bases with odd nonlinearity order p appear at the desired output frequency $D\omega_c$.

The beamformer in Fig. 3.1 is modeled using the beamforming weights, $w_\ell \in \mathbb{C}$ for $\ell = 1, ..., L$, such that the CBBE input of the ℓ'th PA/FX is

$$\tilde{a}_1^\ell[n] = w_\ell \tilde{a}_1[n], \tag{3.4}$$

where $\ell \in \{1, 2, ..., L\}$ and L is the number of elements in the array. Substituting (3.4) in (3.2), we get

$$\tilde{b}_2^\ell[n] = \sum_{p=0}^{N} \sum_{\substack{(k,k',s,s') \in \mathcal{A}(p) \\ \mathbf{m} \in \mathcal{B}_1^k,\, \hat{\mathbf{m}} \in \mathcal{B}_1^{k'} \\ \bar{\mathbf{m}} \in \mathcal{B}_2^s, \breve{\mathbf{m}} \in \mathcal{B}_2^{s'}}} \gamma_{\mathbf{m},\hat{\mathbf{m}},\bar{\mathbf{m}},\breve{\mathbf{m}}}^{k,k',s,s',\ell} w_\ell^D |w_\ell|^{p'-D} \prod_{i=1}^{k} \tilde{a}_1[n - m_i]$$
$$\times \prod_{j=1}^{k'} \tilde{a}_1^*[n - \hat{m}_j] \prod_{q=1}^{s} \hat{a}_2^\ell[n - \bar{m}_q] \prod_{r=1}^{s'} \hat{a}_2^{*\ell}[n - \breve{m}_r], \tag{3.5}$$

where $p' = k + k' + D(s + s')$ and

$$\hat{a}_2^\ell[n] = \frac{\tilde{a}_2^\ell[n]}{w_\ell^D}. \tag{3.6}$$

Equation (3.5) describes the ℓ'th PA/FX output, $\tilde{b}_2^\ell[n]$, as a function of the array input, $\tilde{a}_1[n]$, and the incident wave at the ℓ'th PA/FX output.

For MMW/sub-THz RF beamforming arrays, the channel can be characterized as a single LoS path. The channel coefficient, h_ℓ, between the ℓ'th antenna and the user, is approximated by a phase shift that is a function of the user location specified by the elevation and azimuth angles θ and ϕ respectively. Consequently, the LoS channel coefficient can be expressed as follows,

$$h_\ell(\theta, \phi) = e^{-i\frac{2\pi}{\lambda}\sin(\theta)\left(d_\ell^x \cos(\phi) + d_\ell^y \sin(\phi)\right)} \tag{3.7}$$
$$= e^{-i\zeta_\ell(\theta,\phi)}, \tag{3.8}$$

where $i = \sqrt{-1}$, (d_ℓ^x, d_ℓ^y) is the location of the ℓ'th antenna in the x-y plane, λ is the wavelength, and

$$\zeta_\ell(\theta, \phi) = \frac{2\pi}{\lambda}\sin(\theta)\left(d_\ell^x \cos(\phi) + d_\ell^y \sin(\phi)\right) \tag{3.9}$$

is the beamforming phase. Using (3.8), the PA/FX beamforming weights for the direction (θ, ϕ) can then be expressed as,

$$w_\ell^D(\theta,\phi) = \nu_\ell^D h_\ell^*(\theta,\phi), \tag{3.10}$$

where $(.)^*$ denotes the complex-conjugate, and ν_ℓ are steering-angle independent complex tapering coefficients. Using the LoS assumption in (3.10), (3.5) can be rewritten as,

$$\begin{aligned}\tilde{b}_2^\ell[n] = \sum_{p=0}^{N} \sum_{\substack{(k,k',s,s')\in\mathcal{A}(p)\\ \mathbf{m}\in\mathcal{B}_1^k,\, \hat{\mathbf{m}}\in\mathcal{B}_1^{k'}\\ \bar{\mathbf{m}}\in\mathcal{B}_2^s,\breve{\mathbf{m}}\in\mathcal{B}_2^{s'}}} \gamma_{\mathbf{m},\hat{\mathbf{m}},\bar{\mathbf{m}},\breve{\mathbf{m}}}^{k,k',s,s',\ell} h_\ell^*(\theta,\phi)\nu_\ell^D|\nu_\ell|^{p'-D} \\ \times \prod_{i=1}^{k} \tilde{a}_1[n-m_i] \prod_{j=1}^{k'} \tilde{a}_1^*[n-\hat{m}_j] \\ \times \prod_{q=1}^{s} \hat{a}_2^\ell[n-\bar{m}_q] \prod_{r=1}^{s'} \hat{a}_2^{*\ell}[n-\breve{m}_r].\end{aligned} \tag{3.11}$$

The CBBE FF received signal at the observation angle (θ, ϕ) with beam steering direction (θ, ϕ), denoted as $\tilde{r}[n]$, can then be written as,

$$\tilde{r}[n] = \sum_{\ell=1}^{L} h_\ell(\theta,\phi)\ \tilde{b}_2^\ell[n]. \tag{3.12}$$

Substituting (3.11) in (3.12), we have

$$\begin{aligned}\tilde{r}[n] = \sum_{\ell=0}^{L}\sum_{p=0}^{N} \sum_{\substack{(k,k',s,s')\in\mathcal{A}(p)\\ \mathbf{m}\in\mathcal{B}_1^k,\, \hat{\mathbf{m}}\in\mathcal{B}_1^{k'}\\ \bar{\mathbf{m}}\in\mathcal{B}_2^s,\breve{\mathbf{m}}\in\mathcal{B}_2^{s'}}} \alpha_{\mathbf{m},\hat{\mathbf{m}},\bar{\mathbf{m}},\breve{\mathbf{m}}}^{k,k',s,s',\ell} \prod_{i=1}^{k} \tilde{a}_1[n-m_i] \\ \times \prod_{j=1}^{k'} \tilde{a}_1^*[n-\hat{m}_j] \prod_{q=1}^{s} \hat{a}_2^\ell[n-\bar{m}_q] \prod_{r=1}^{s'} \hat{a}_2^{*\ell}[n-\breve{m}_r],\end{aligned} \tag{3.13}$$

where $\alpha_{\mathbf{m},\hat{\mathbf{m}},\bar{\mathbf{m}},\breve{\mathbf{m}}}^{k,k',s,s',\ell} = \gamma_{\mathbf{m},\hat{\mathbf{m}},\bar{\mathbf{m}},\breve{\mathbf{m}}}^{k,k',s,s',\ell}\nu_\ell^D|\nu_\ell|^{p'-D}$ and $p' = k + k' + D(s+s')$. The result in (3.13) shows a dependency of the array nonlinearity on the incident waves at the PA/FX outputs, $\tilde{a}_2^\ell[n]$. Moreover, it indicates that the received signal at the FF can be represented as a sum of the

antenna PA nonlinearities weighted by the tapering profile coefficients ν_ℓ. Subsequently, if knowledge of the incident waves $\tilde{a}_2[n]$ at the PAs/FXs outputs are available, then using (3.6) a DISO DPD can be formulated from (3.13) that accounts for the angle-dependent load mismatch.

3.1.2 Angle-Dependent SISO Forward Model Formulation

The following analysis shows that for RF beamforming TXs, (3.13) can be reduced to an angle-dependent SISO model. Moreover, we will derive the dependency of RF beamforming array nonlinearity on the tapering coefficients, the antenna active reflection coefficients, and the PAs/FXs outputs reflection coefficients. To that end, the expression in (3.13) is first written as the sum of linear terms and an additive error $\tilde{\epsilon}^\ell(\tilde{\mathbf{a}}_1^\ell[n], \tilde{\mathbf{a}}_2^\ell[n])$, as,

$$\tilde{b}_2^\ell[n] = G_\ell(\tilde{a}_1^\ell[n])^D + \beta_\ell \tilde{a}_2^\ell[n] + \tilde{\epsilon}^\ell(\tilde{\mathbf{a}}_1^\ell[n], \tilde{\mathbf{a}}_2^\ell[n]), \tag{3.14}$$

where $\ell = 1, 2, \ldots, L$, β_ℓ is the ℓ'th PA/FX output reflection coefficient, and G_ℓ is the gain of the ℓ'th branch. Note, the additive error model in (3.14) shares similarities with those used for PAs in [77] (when $D = 1$) and for FXs in [7] (when $D > 1$). However, in (3.14) the proposed model incorporates the term $\beta_\ell \tilde{a}_2^\ell[n]$ to explicitly capture the reflected wave at the ℓ'th PA/FX output port caused by the incident wave $\tilde{a}_2^\ell[n]$. Using the antenna S-Parameters, the CBBE incident wave at the ℓ'th PA/FX output port, $\tilde{a}_2^\ell[n]$, can be expressed as follows,

$$\tilde{a}_2^\ell[n] = \sum_{j=1}^{L} \tilde{b}_2^j[n] S_{\ell j}, \tag{3.15}$$

where $S_{\ell j}$ is the ℓ'th row and j'th column entry of the antenna array S-Parameter matrix $\mathbf{S}$. Note, to simplify the analysis and without loss of generality, the antenna S-Parameters are assumed to be constant versus frequency. Substituting (3.14) in (3.15), one gets,

$$\tilde{a}_2^\ell[n] = \sum_{j=1}^{L} \left(G_j(\tilde{a}_1^j[n])^D + \beta_j \tilde{a}_2^j[n] + \tilde{\epsilon}^j(\tilde{\mathbf{a}}_1^j[n], \tilde{\mathbf{a}}_2^j[n]) \right) S_{\ell j}. \tag{3.16}$$

In order to simplify the recursion in (3.16), it is assumed that the PA/FX nonlinearity deviates weakly from an ideal PA/FX such that,

$$\left| G_j(\tilde{a}_1^j[n])^D + \beta_j \tilde{a}_2^j[n] \right| \gg \left| \tilde{\epsilon}^j(\tilde{\mathbf{a}}_1^j[n], \tilde{\mathbf{a}}_2^j[n]) \right|. \tag{3.17}$$

Consequently, in (3.14) and (3.16) the rightmost terms, $\tilde{\epsilon}^j$, can be neglected. Keeping the remaining terms, we get

$$\tilde{b}_2^\ell[n] = G_\ell(\tilde{a}_1^\ell[n])^D + \beta_\ell \tilde{a}_2^\ell[n], \tag{3.18}$$

and

$$\tilde{a}_2^\ell[n] = \sum_{j=1}^{L} S_{\ell j}\big(G_j(\tilde{a}_1^j[n])^D + \beta_j \tilde{a}_2^j[n]\big). \tag{3.19}$$

Using the RF beamforming in (3.4) and the precoding in (3.10), (3.18) and (3.19) can be rewritten as a function of the array CBBE input signal, $\tilde{a}_1[n]$, as,

$$\tilde{b}_2^\ell[n] = G_\ell(\tilde{a}_1[n])^D \nu_\ell^D e^{i\zeta_\ell(\theta,\phi)} + \beta_\ell \tilde{a}_2^\ell[n], \tag{3.20}$$

and

$$\tilde{a}_2^\ell[n] = \sum_{j=1}^{L} S_{\ell j}\big(G_j(\tilde{a}_1[n])^D \nu_j^D e^{i\zeta_j(\theta,\phi)} + \beta_j \tilde{a}_2^j[n]\big). \tag{3.21}$$

In order to solve the recursion in (3.21), (3.20) and (3.21) are first expressed in matrix form. Let $\mathbf{Z}$ and $\boldsymbol{\beta}$, be $L \times L$ diagonal matrices with j'th column and j'th row entries given by $G_j e^{i\zeta_j(\theta,\phi)}$ and β_j respectively. Consequently, (3.18) and (3.21) can be expressed as,

$$\tilde{\mathbf{b}}_\mathbf{2} = \mathbf{Z}\boldsymbol{\nu}(\tilde{a}_1[n])^D + \boldsymbol{\beta}\tilde{\mathbf{a}}_\mathbf{2}, \tag{3.22}$$

and

$$\tilde{\mathbf{a}}_\mathbf{2} = \mathbf{S}\mathbf{Z}\boldsymbol{\nu}(\tilde{a}_1[n])^D + \mathbf{S}\boldsymbol{\beta}\tilde{\mathbf{a}}_\mathbf{2}, \tag{3.23}$$

respectively, where $\tilde{\mathbf{b}}_\mathbf{2} = \big[\tilde{b}_2^1[n], ..., \tilde{b}_2^L[n]\big]^T$, $\tilde{\mathbf{a}}_\mathbf{2} = \big[\tilde{a}_2^1[n], ..., \tilde{a}_2^L[n]\big]^T$ and $\boldsymbol{\nu} = [\nu_1^D, ..., \nu_L^D]^T$. Solving for $\tilde{\mathbf{a}}_\mathbf{2}$ in (3.23), the expression of the incident waves at the PA/FX outputs can be expressed as a function of the array input, $\tilde{a}_1[n]$, and the tapering coefficients, $\boldsymbol{\nu}$, as follows,

$$\tilde{\mathbf{a}}_\mathbf{2} = (\mathbf{I} - \mathbf{S}\boldsymbol{\beta})^{-1}\mathbf{S}\mathbf{Z}\boldsymbol{\nu}(\tilde{a}_1[n])^D. \tag{3.24}$$

The ℓ'th entry of $\tilde{\mathbf{a}}_\mathbf{2}$ is then given by

$$\tilde{a}_2^\ell[n] = \big[(\mathbf{I} - \mathbf{S}\boldsymbol{\beta})^{-1}\mathbf{S}\big]_\ell \mathbf{Z}\boldsymbol{\nu}(\tilde{a}_1[n])^D, \tag{3.25}$$

where $\left[(\mathbf{I}-\mathbf{S\beta})^{-1}\mathbf{S}\right]_\ell$ is the ℓ'th row of the matrix $(\mathbf{I}-\mathbf{S\beta})^{-1}\mathbf{S}$. In order to derive the expression of array antenna active reflection coefficients as a function of the tapering coefficients, (3.24) is first substituted in (3.22). Rearranging the terms, we get,

$$\tilde{\mathbf{b}}_\mathbf{2} = \left(\mathbf{Z\nu} + \boldsymbol{\beta}(\mathbf{I}-\mathbf{S\beta})^{-1}\mathbf{SZ\nu}\right)(\tilde{a}_1[n])^D. \tag{3.26}$$

The ℓ'th entry of $\tilde{\mathbf{b}}_\mathbf{2}$ is then given by

$$\begin{aligned}\tilde{b}_2^\ell[n] &= \left[\mathbf{Z\nu} + \boldsymbol{\beta}(\mathbf{I}-\mathbf{S\beta})^{-1}\mathbf{SZ\nu}\right]_\ell(\tilde{a}_1[n])^D &(3.27)\\ &= G_\ell(\tilde{a}_1[n])^D\nu_\ell^D e^{i\zeta_\ell(\theta,\phi)} + \beta_\ell\left[(\mathbf{I}-\mathbf{S\beta})^{-1}\mathbf{S}\right]_\ell\mathbf{Z\nu}(\tilde{a}_1[n])^D, &(3.28)\end{aligned}$$

where $\left[\mathbf{Z\nu} + \boldsymbol{\beta}(\mathbf{I}-\mathbf{S\beta})^{-1}\mathbf{SZ\nu}\right]_\ell$ is the entry in the ℓ'th row of the column vector $\mathbf{Z\nu} + \boldsymbol{\beta}(\mathbf{I}-\mathbf{S\beta})^{-1}\mathbf{SZ\nu}$. The active reflection coefficient seen by the ℓ'th antenna element can then be expressed as follows,

$$\Gamma_\ell = \frac{\tilde{a}_2^\ell[n]}{\tilde{b}_2^\ell[n]}. \tag{3.29}$$

Substituting (3.25) and (3.28) in (3.29), we then have,

$$\Gamma_\ell(\theta,\phi,\mathbf{\nu}) = \frac{\left[(\mathbf{I}-\mathbf{S\beta})^{-1}\mathbf{S}\right]_\ell\mathbf{Z\nu}}{G_\ell\nu_\ell^D e^{i\zeta_\ell(\theta,\phi)} + \beta_\ell\left[(\mathbf{I}-\mathbf{S\beta})^{-1}\mathbf{S}\right]_\ell\mathbf{Z\nu}}, \tag{3.30}$$

where the dependence of Γ_ℓ on θ, ϕ and $\mathbf{\nu}$ was made explicit. From (3.30), it is clear that the array antenna active reflection coefficients depend on the tapering coefficients, $\mathbf{\nu}$, the beamforming coefficients in $\mathbf{Z}$, the PA/FX output reflection coefficients in $\boldsymbol{\beta}$, and the array S-Parameters in $\mathbf{S}$. It is to note that in the special case where $\beta_\ell = 0$ (i.e., the PA/FX output reflection coefficients are zero), the expression of Γ_ℓ in (3.30), simplifies to the following,

$$\Gamma_\ell(\theta,\phi,\mathbf{\nu}) = \frac{1}{G_\ell\nu_\ell^D}\sum_{j=1}^{L} S_{\ell j}G_j\nu_j^D e^{i\left(\zeta_j(\theta,\phi)-\zeta_\ell(\theta,\phi)\right)} \tag{3.31}$$

which clearly shows the dependency of the array antenna active reflection coefficients on the tapering coefficients ν_ℓ and on the steering angle.

Returning to (3.29), the incident wave at the ℓ'th PA/FX output can be expressed as follows,

$$\tilde{a}_2^\ell[n] = \Gamma_\ell\tilde{b}_2^\ell[n]. \tag{3.32}$$

Substituting (3.20) in (3.32) and solving for $\tilde{a}_2^{\ell}[n]$ we get,

$$\tilde{a}_2^{\ell}[n] = \Gamma_\ell G_\ell(\tilde{a}_1[n])^D \nu_\ell^D e^{i\zeta_\ell(\theta,\phi)} + \Gamma_\ell \beta_\ell \tilde{a}_2^{\ell}[n] \tag{3.33}$$

$$= \frac{\Gamma_\ell G_\ell(\tilde{a}_1[n])^D \nu_\ell^D e^{i\zeta_\ell(\theta,\phi)}}{1-\Gamma_\ell\beta_\ell}. \tag{3.34}$$

Using (3.34), (3.6) can then be expressed as follows,

$$\hat{a}_2^{\ell}[n] = \frac{G_\ell\Gamma_\ell}{1-\Gamma_\ell\beta_\ell}(\tilde{a}_1[n])^D. \tag{3.35}$$

Finally, substituting (3.35) in (3.13), we get

$$\begin{aligned}\tilde{r}[n] = \sum_{\ell=1}^{L}\sum_{p=1}^{N} \sum_{\substack{(k,k',s,s')\in\mathcal{A}(p)\\ \mathbf{m}\in\mathcal{B}_1^k,\,\hat{\mathbf{m}}\in\mathcal{B}_1^{k'}\\ \bar{\mathbf{m}}\in\mathcal{B}_2^s,\check{\mathbf{m}}\in\mathcal{B}_2^{s'}}} \alpha_{\mathbf{m},\hat{\mathbf{m}},\bar{\mathbf{m}},\check{\mathbf{m}}}^{k,k',s,s',\ell} \prod_{i=1}^{k}\tilde{a}_1[n-m_i] \\ \times \prod_{j=1}^{k'}\tilde{a}_1^*[n-\hat{m}_j]\prod_{q=1}^{s}\frac{G_\ell\Gamma_\ell}{1-\Gamma_\ell\beta_\ell}(\tilde{a}_1[n-\bar{m}_q])^D \\ \times \prod_{r=1}^{s'}\frac{G_\ell^*\Gamma_\ell^*}{1-\Gamma_\ell^*\beta_\ell^*}(\tilde{a}_1^*[n-\bar{m}_r])^D.\end{aligned} \tag{3.36}$$

From (3.36), it is clear that the array behavior at the FF is nonlinearly dependent on the antenna active reflection coefficients Γ_ℓ, $\ell = 1, ..., L$. Moreover, the impact of Γ_ℓ on the array's nonlinear behavior is magnified by the PA/FX output reflection coefficients. This dependency on Γ_ℓ also causes the array to exhibit angle-dependent nonlinear behavior and hinders the capacity of a single SISO-DPD set of coefficients to linearize the array over a wide range of steering angles. Alternatively, (3.36) can also be rewritten as follows,

$$\begin{aligned}\tilde{r}[n] = \sum_{p=1}^{N} \sum_{\substack{(k,k',s,s')\in\mathcal{A}(p)\\ \mathbf{m}\in\mathcal{B}_1^k,\,\hat{\mathbf{m}}\in\mathcal{B}_1^{k'}\\ \bar{\mathbf{m}}\in\mathcal{B}_2^s,\check{\mathbf{m}}\in\mathcal{B}_2^{s'}}} \alpha_{\mathbf{m},\hat{\mathbf{m}},\bar{\mathbf{m}},\check{\mathbf{m}}}^{k,k',s,s'} \prod_{i=1}^{k}\tilde{a}_1[n-m_i] \\ \times \prod_{j=1}^{k'}\tilde{a}_1^*[n-\hat{m}_j]\prod_{q=1}^{s}(\tilde{a}_1[n-\bar{m}_q])^D \\ \times \prod_{r=1}^{s'}(\tilde{a}_1^*[n-\bar{m}_r])^D,\end{aligned} \tag{3.37}$$

where

$$\alpha^{k,k',s,s'}_{\mathbf{m},\hat{\mathbf{m}},\tilde{\mathbf{m}},\check{\mathbf{m}}} = \sum_{\ell=1}^{L} \alpha^{k,k',s,s',\ell}_{\mathbf{m},\hat{\mathbf{m}},\tilde{\mathbf{m}},\check{\mathbf{m}}} \prod_{j=1}^{k'} \tilde{a}_1^*[n-\hat{m}_j] \prod_{q=1}^{s} \frac{G_\ell \Gamma_\ell}{1-\Gamma_\ell \beta_\ell} \prod_{r=1}^{s'} \frac{G_\ell^* \Gamma_\ell^*}{1-\Gamma_\ell^* \beta_\ell^*}. \tag{3.38}$$

Note, in (3.37) the Γ_ℓ terms have been absorbed into the model coefficients $\alpha^{k,k',s,s'}_{\mathbf{m},\hat{\mathbf{m}},\tilde{\mathbf{m}},\check{\mathbf{m}}}$. These coefficients are now angle-dependent, emphasizing that the nonlinear error in the received signal $\tilde{r}[n]$ depends on the steering angle

3.2 Tapering Profile Synthesis Algorithm

In this section, an algorithm to synthesize tapering profiles that minimize the variation of $\Gamma_\ell(\theta, \phi, \mathbf{v})$ across a range of steering angles is presented. The proposed algorithm is subsequently validated numerically and experimentally on a 64-element PA-based beamforming array operating at 28 GHz.

3.2.1 Problem Formulation

In this subsection, the proposed tapering algorithm that synthesizes tapering profiles that minimize the variation of $\Gamma_\ell(\theta, \phi, \mathbf{v})$ across a range of steering angles is formulated. These optimal tapering coefficients are those that reduce the variation of $\Gamma_\ell(\theta, \phi, \mathbf{v})$ when the array is steered, i.e., are the solution to the following optimization problem,

$$\mathbf{v_{opt}} = \underset{\mathbf{v}\in\mathbb{C}^L}{\operatorname{argmin}} \quad \sum_{\substack{\theta\in\boldsymbol{\Theta}\\ \phi\in\boldsymbol{\Phi}}} \sum_{\ell=1}^{L} \left|\frac{d\Gamma_\ell}{d\theta}\right|^q + \left|\frac{d\Gamma_\ell}{d\phi}\right|^q \tag{3.39a}$$

$$\text{subject to} \quad \left|\sum_{\ell=1}^{L} v_\ell\right| \geq AF \tag{3.39b}$$

$$|v_\ell| \leq 1, \qquad \ell = 1, ..., L \tag{3.39c}$$

where $AF \leq L$ is the targeted array factor, $\boldsymbol{\Theta} \subset [-\pi/2, \pi/2]$ and $\boldsymbol{\Phi} \subset [0, \pi]$ are the sets of azimuth and elevation angles the array is to be optimized over, and $q \geq 1$ is a real number that determines how significantly large variations in an active reflection coefficient versus steering angle should be penalized. The constraint in (3.39b) ensures that the array gain

meets a minimum specified gain target value of AF. Moreover, the constraint in (3.39c) ensures that the resulting tapering coefficient magnitudes in (3.39a) do not exceed 1.

Note, the optimization problem in (3.39a) – (3.39c) is difficult to solve since the objective function in (3.39a) is non-convex and the constraint in (3.39b) is non-convex as well. We first show how the constraint in (3.39b) can be transformed into a convex constraint. Note that due to (3.30), we can apply a common phase shift $e^{i\alpha}$ to each ν_ℓ, and the Γ_ℓ remain unchanged, i.e.

$$\Gamma_\ell(\theta, \phi, \mathbf{v}) = \Gamma_\ell(\theta, \phi, e^{i\alpha}\mathbf{v})$$

Therefore, in (3.39a) – (3.39c) there is an optimal solution $\tilde{\mathbf{v}}$ such that the sum $\sum_{\ell=1}^{L} \tilde{\nu}_\ell$ is a non-negative real-number. Furthermore, this solution has its sum lie in the real interval $[AF, L]$. Hence, without loss, we may replace the constraint (3.39b) with $\left|L - \sum_{\ell=1}^{L} \nu_\ell\right| \leq L - AF$ as this latter contains the real interval $[AF, L]$.

To address the non-convexity of the objective function in (3.39a), we propose using an iterative approach. Specifically, the dependency in the denominator of $\Gamma_\ell(\theta, \phi, \mathbf{v})$ in (3.30) on the tapering coefficients $\mathbf{v}$ is removed by replacing these tapering coefficients in the $(k+1)$'th optimization iteration with the resulting tapering coefficients from the k'th optimization iteration. To that end, we define,

$$\bar{\Gamma}_\ell(\mathbf{v}, \bar{\mathbf{v}}) := \frac{\left[(\mathbf{I} - \mathbf{S}\boldsymbol{\beta})^{-1}\mathbf{S}\right]_\ell \mathbf{Z}\mathbf{v}}{G_\ell \bar{v}_\ell^D e^{i\zeta_\ell(\theta,\phi)} + \beta_\ell \left[(\mathbf{I} - \mathbf{S}\boldsymbol{\beta})^{-1}\mathbf{S}\right]_\ell \mathbf{Z}\bar{\mathbf{v}}}, \tag{3.40}$$

where $\bar{\mathbf{v}} = [\bar{v}_1^D, ..., \bar{v}_L^D]^T$. The optimization problem in (3.39a) – (3.39c) can then be solved iteratively as follows,

$$\mathbf{v}^{k+1} = \underset{\mathbf{v}\in\mathbb{C}^L}{\operatorname{argmin}} \sum_{\substack{\theta\in\boldsymbol{\Theta}\\ \phi\in\boldsymbol{\Phi}}} \sum_{\ell=1}^{L} \left|\frac{d\bar{\Gamma}_\ell(\mathbf{v}, \mathbf{v}^k)}{d\theta}\right|^q + \left|\frac{d\bar{\Gamma}_\ell(\mathbf{v}, \mathbf{v}^k)}{d\phi}\right|^q \tag{3.41a}$$

$$\text{subject to } \left|L - \sum_{\ell=1}^{L} \nu_\ell\right| \leq L - AF, \tag{3.41b}$$

$$|\nu_\ell| \leq 1, \qquad \ell = 1, ..., L \tag{3.41c}$$

where $\mathbf{v}^{k+1} = [(\nu_1^{k+1})^D, ..., (\nu_L^{k+1})^D]$, and $\mathbf{v}^1 = [1, ..., 1]$ (i.e., $\nu_\ell^1 = 1$ for $\ell = 1, ..., L$). Since in step k, $\mathbf{v}^k$ in (3.41a) is fixed, the objective is convex with respect to $\mathbf{v}$. Note, the derivatives of Γ_ℓ and $\bar{\Gamma}_\ell$ with respect of θ and ϕ in (3.39a) and (3.41a) respectively can be computed numerically. Please note that the proposed method to synthesize the tapering profile does not explicitly consider the beam shape. Nevertheless, the formulation could be extended to incorporate additional beam shape-related constraints.

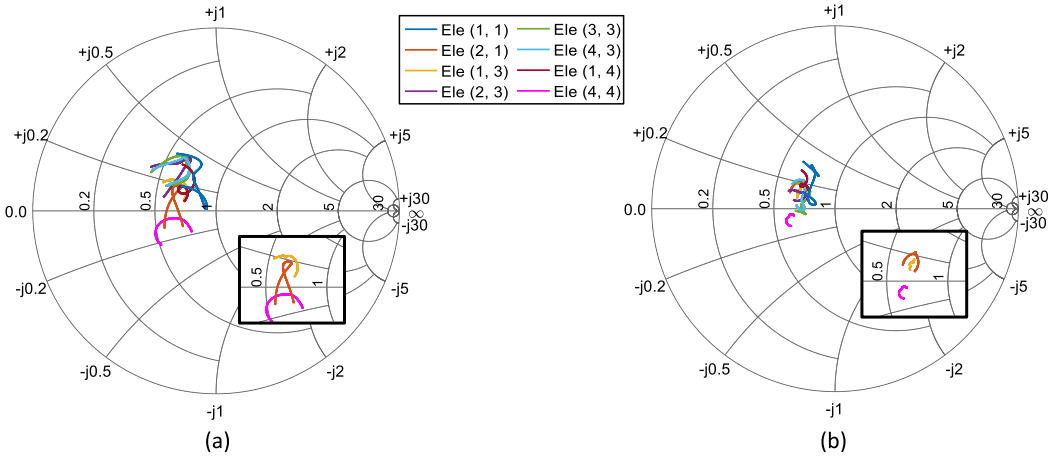


Figure 3.2: Array antenna element active reflection coefficients versus steering angle for $\theta \in [-50°, 50°]$: a) with uniform tapering; b) with synthesized tapering obtained from the proposed optimization with $q = 1$ and $AF = 57$ (i.e., overall array gain reduction of 1 dB); The inset highlights the variation in the antenna active reflection coefficients of three selected antenna elements when the array is steered.

3.2.2 Numerical Analysis

In this subsection, the performance of the proposed algorithm is validated in simulation and experimentally using an 8×8 RF beamforming array designed to operate at 28 GHz and characterized with a maximum antenna mutual coupling of -14 dB. The impact of the tapering profile obtained using the proposed optimization algorithm on the extent of variation in the antenna active reflection coefficients is evaluated in simulation using the antenna array scattering-parameters (S-Parameters). Experimental results are then presented to assess the implication of applying the synthesized tapering obtained from the proposed algorithm on the performance of DPD over a wide steering range. Note, the synthesis of the tapering profile is an offline process; hence the proposed solution does not increase the DPD complexity.

In this subsection, we evaluate in simulation the impact of the tapering profile on the variation of antenna active reflection coefficients versus steering angle. Fig. 3.2 shows the array antenna active reflection coefficients versus steering angle ($-50° \leq \theta \leq -50°$ and ϕ set to $0°$) when either the uniform (Fig. 3.2 (a)) or synthesized (Fig. 3.2 (b)) tapering profiles are applied. The synthesized tapering profile coefficients used in Fig. 3.2 (b) are shown Fig. 3.3 and are synthesized using the proposed optimization algorithm in (3.41a) –

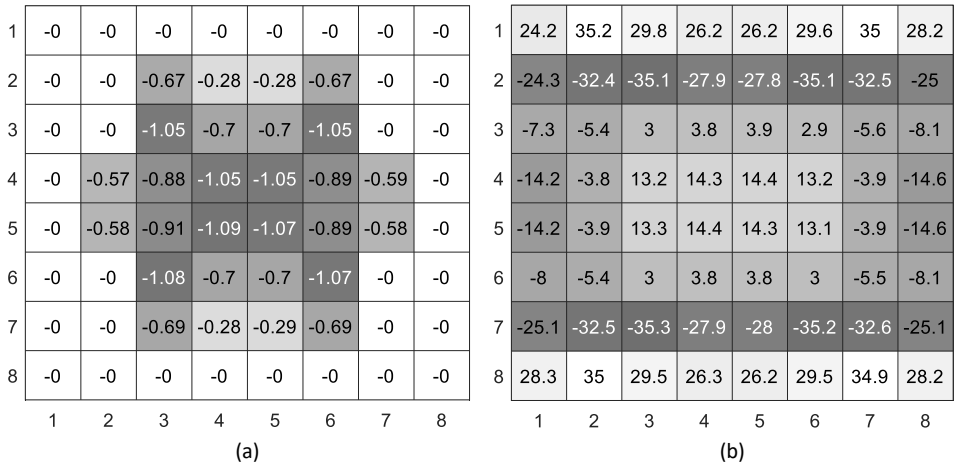


Figure 3.3: Synthesized tapering coefficients magnitude in dB (a) and phase in degrees (b) obtained from the proposed optimization with $q = 1$ and $AF = 57$ (i.e., overall array gain reduction of 1 dB).

(3.41c) with $q = 1$, $AF = 57$ (i.e., overall array gain reduction of 1 dB) and are optimized for $-50^\circ \leq \theta \leq -50^\circ$ with a step of 1° and ϕ set to 0°. The optimization problem in (3.41a) was solved using CVX (a disciplined convex solver for MATLAB) and a total of three iterations were used to generate the synthesized tapering profile used in this work. Note, the synthesized tapering obtained from the proposed optimization is fixed versus the steering angle. From Fig. 3.2, it is clear that the synthesized tapering profile reduced the variation of the antenna active reflection coefficients (both in magnitude and phase) compared to the uniform tapering profile case. For instance, the VSWR at the input of antenna element (3,3) varied by 0.9 (between 1.6 and 2.5) and 0.3 (between 1.4-1.7) when the tapering is set to uniform or synthesized profiles, respectively. Fig. 3.4 shows the normalized radiation pattern of the array when uniform or the synthesized tapering is applied. From Fig. 3.4, applying the synthesized tapering profile did not affect the array beam width but did affect the array's sidelobe levels and nulls.

In order to further analyze the impact of the synthesized tapering profile obtained from the proposed algorithm, we define a q-norm based variation metric, $\mathrm{VM}_\ell(\mathbf{v})$, that quantifies the variation of the active reflection coefficient at the ℓ'th antenna element for

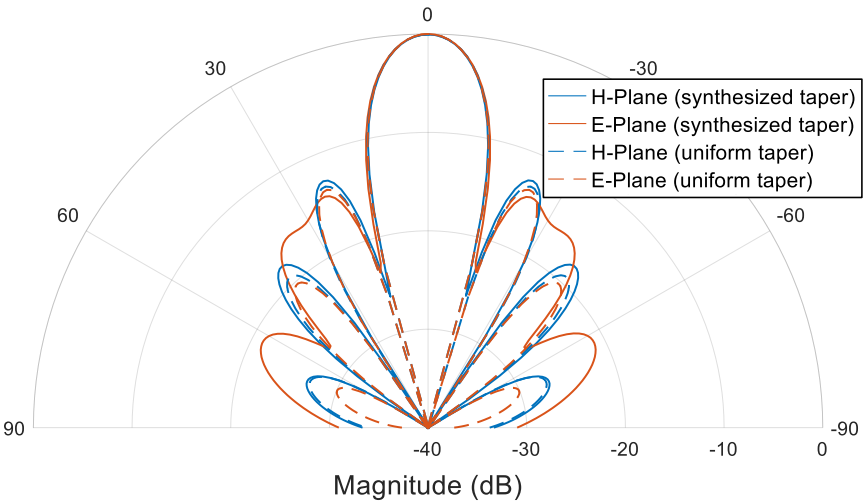


Figure 3.4: Simulated normalized array radiation pattern using uniform tapering profile and the synthesized profile obtained from the proposed optimization with $q = 1$ and $AF = 57$ (i.e., overall array gain reduction of 1 dB).

given tapering coefficients, $\mathbf{v}$, when the array is steered, as follows,

$$\mathrm{VM}_\ell(\mathbf{v}) = \left(\frac{1}{|\boldsymbol{\Theta}||\boldsymbol{\Phi}|} \sum_{\substack{\theta \in \boldsymbol{\Theta} \\ \phi \in \boldsymbol{\Phi}}} \left| \frac{d\Gamma_\ell(\theta, \phi, \mathbf{v})}{d\theta} \right|^q + \left| \frac{d\Gamma_\ell(\theta, \phi, \mathbf{v})}{d\phi} \right|^q \right)^{1/q}. \tag{3.42}$$

Note, if the applied tapering profile eliminates the variation in the antenna active reflection coefficients versus steering angle, then (3.42) reduces to $\mathrm{VM}_\ell(\mathbf{v}) = 0$ (i.e., constant active reflection coefficient versus steering angle). The extent of reduction in Γ_ℓ variation versus steering angle when a synthesized tapering profile is applied, compared to the uniform profile case, can then be defined using the variation metric ratio (VMR) as follows,

$$\mathrm{VMR}_\ell = \frac{\mathrm{VM}_\ell(\mathbf{v_{opt}})}{\mathrm{VM}_\ell(\mathbf{1_L})}. \tag{3.43}$$

Fig. 3.5 shows the VMR of all the elements of the simulated antenna array when the synthesized tapering profile obtained from the proposed algorithm is applied. From Fig. 3.5, compared to the uniform profile case, the synthesized tapering profile reduced the variation in the antenna active reflection coefficients versus steering angle by 6 dB or more for 25% of the antenna elements and had a median improvement of 3.9 dB. Moreover, only four

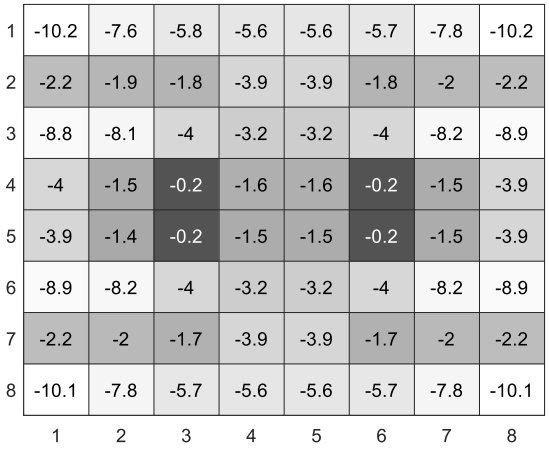


Figure 3.5: Variation Metric Ratio (VMR) of the antenna elements representing the reduction (in dB scale) in the antenna active reflection coefficient variation versus steering angle when the synthesized tapering profile obtained from the proposed optimization with $q = 1$ and $G = 57$ (i.e., overall array gain reduction of 1 dB) is applied.

antenna elements experienced an improvement below 1.4 dB. The results in Fig. 3.5 further confirm the ability of synthesized tapering profiles generated using the proposed algorithm to reduce the extent of variation in the antenna active reflection coefficients versus steering angle. Please note that the above simulation results assumed an infinite resolution for the phase and magnitude controls. Nevertheless, it was found that if the phase control is quantized to at least 4 bits and the magnitude control step size is at most 0.5 dB, then the impact of phase and magnitude control resolution is negligible.

3.2.3 Experimental Validation

In this subsection, the capacity of SISO-DPD to linearized PA-based RF beamforming arrays, the impact of antenna mutual coupling on the SISO-DPD linearization versus steering angle and the effectiveness of applying synthesized tapering obtained from the proposed algorithm to reduce the extent of the variation of the active reflection coefficients and improve the performance of SISO-DPD over a wide steering range is validated experimentally using the experimental setup shown in Fig. 3.6. The vector-modulated test signal used in the experiment was generated using a 12-bit, 12 GS/s arbitrary waveform generator (AWG) (M8121A from Keysight Technologies), with output centered at an IF of 1.75 GHz. An IQ-mixer (ADMV-1013) was used to up-convert the IF signal to a center frequency of 28

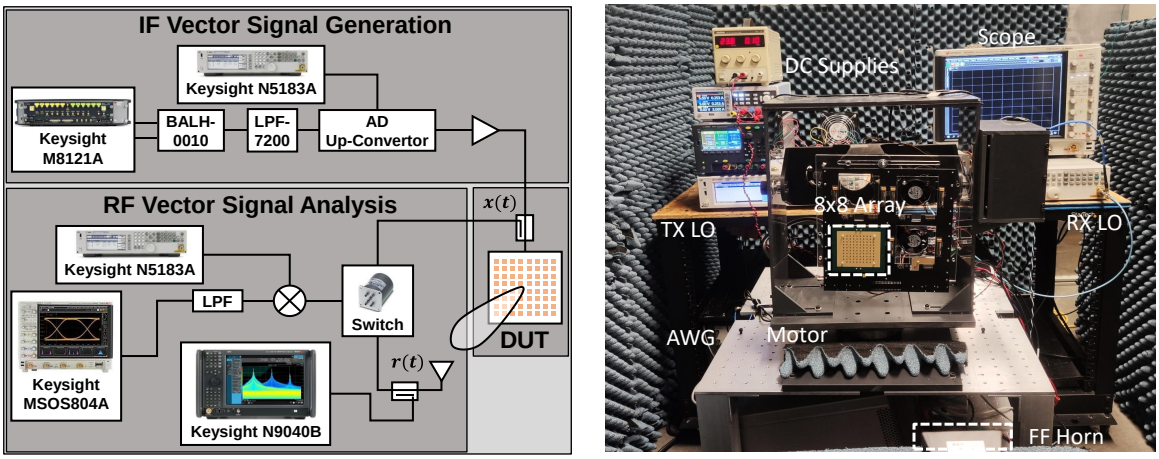


Figure 3.6: Functional block diagram (Left) and picture (Right) of the measurement setup.

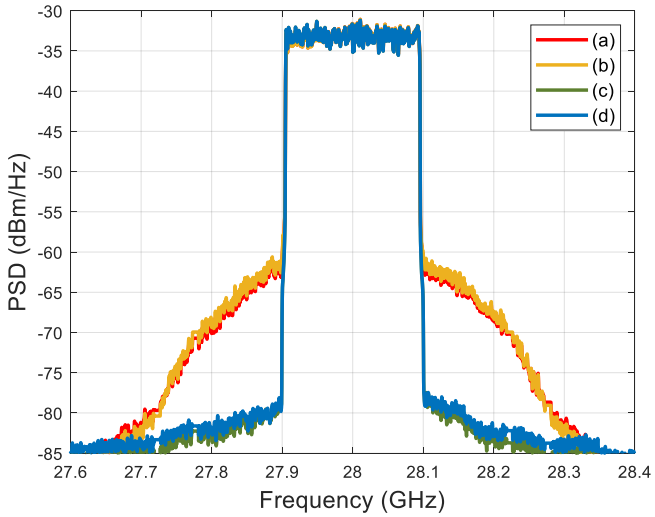


Figure 3.7: Measured spectrum results captured at the FF when the array is steered at broadside: (a) before DPD with uniform tapering applied; (b) before DPD with synthesized tapering applied; (c) after DPD with uniform tapering applied; (d) after DPD with synthesized tapering applied.

GHz. The signal was then amplified using a driver amplifier (HMC-1131) and fed to the antenna-under-test (AUT). The array uses 16 beamforming integrated circuits (BFICs; Anokiwave AWMF-0162 [149]). The BFICs allow for 4-bits (step size of 0.5 dB) gain control and 6-bits phase resolution. The AUT was mounted on a servo motor that is rotated

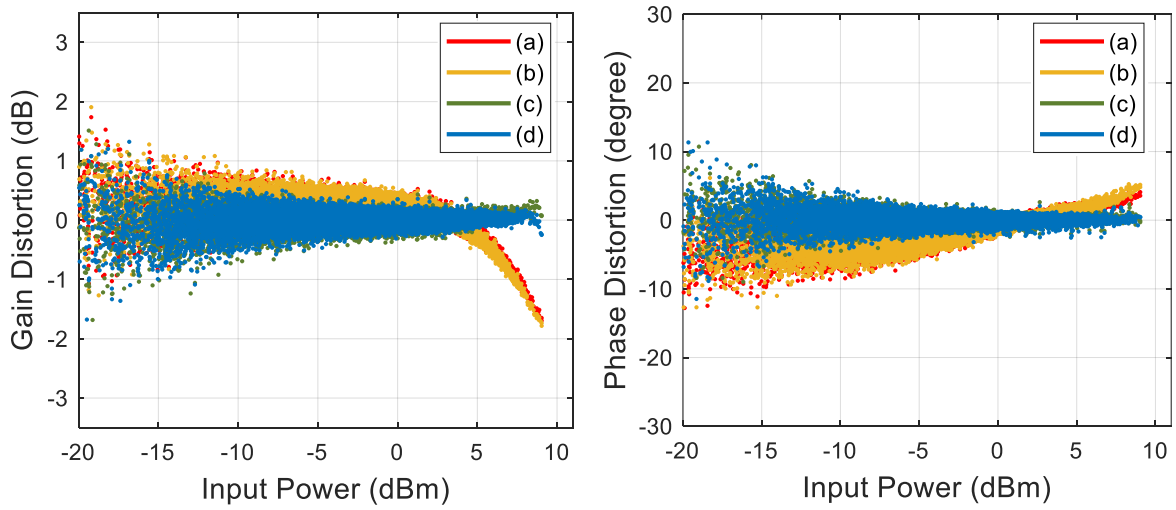


Figure 3.8: Measured gain distortion (Left) and AM-PM (Right) at the FF when the array is steered at broadside: (a) before DPD with uniform tapering applied; (b) before DPD with synthesized tapering applied; (c) after DPD with uniform tapering applied; (d) after DPD with synthesized tapering applied.

to align the beam with the receiver when electrically steering the array. A horn antenna was used to capture the FF signal and validate the DPD linearization performance. The output of the horn antenna was down-converted to an IF frequency of 2 GHz and captured using a 10-bit, 20 GS/s, 8 GHz analog bandwidth oscilloscope (MSOS804A from Keysight Technologies). LO sources (MXG-N5183B from Keysight Technologies) were used to drive the up-conversion and down-conversion mixers used in the setup.

The measurements were performed using 200 MHz OFDM signals conforming to 3GPP 5G NR downlink specifications, with sub-carriers modulated using 256-QAM, a sub-carrier spacing of 120 kHz, $K_{\mathrm{D}} = 1584$ total data sub-carriers, a fast Fourier transform size of $K_{\mathrm{FFT}} = 2048$, and characterized by a PAPR (after crest factor reduction using clipping and filtering) of 9 dB. For the DPD function, the model in [7] is adopted where the nonlinearity order, nonlinear memory depth, linear memory depth, multiplication order, and memory step were set to 9, 3, 3, 1, and 1 respectively. Moreover, the number of nonlinear memory cross-terms was limited to 3 resulting in a total of 35 coefficients. Indirect learning was used to train the DPD coefficients. The number of iterations used was fixed to 10, and 1.5×10^4 samples were used per iteration.

In order to ensure acceptable signal accuracy at the array's input, the setup was calibrated using a wideband multi-tone signal with 1 MHz tone spacing. Moreover, the array

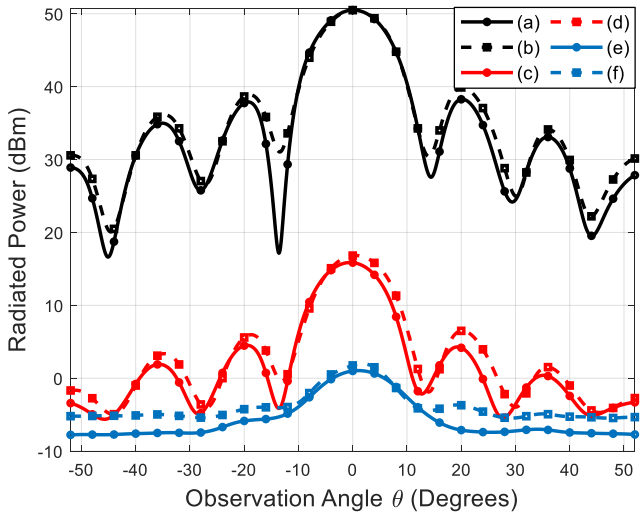


Figure 3.9: Measured radiated power in H-plane with the array steered at broadside: (a) in-band power with uniform tapering applied; (b) in-band power with synthesized tapering applied; (c) out-of-band power before DPD with uniform tapering applied; (d) out-of-band power before DPD with synthesized tapering applied; (e) out-of-band power after DPD with uniform tapering applied; (f) out-of-band power after DPD with synthesized tapering applied.

was calibrated for phase and magnitude errors using the FF horn antenna following the procedure described in [134]. The synthesized tapering profile used in the measurements was obtained from (3.41a) – (3.41c) with $q = 1$ and $AF = 57$ (i.e., overall array gain reduction of 1 dB). The input power to the array was increased when synthesized tapering was applied to maintain the EIRP and accordingly the received power at the user the same as when the uniform tapering profile was applied.

Fig. 3.7 shows the PSD of the received signal in the FF where the EIRP is set to 50.7 dBm and when the array is steered at broadside: (a) with uniform tapering profile prior to DPD, (b) with synthesized tapering profile applied prior to DPD, (c) after DPD trained with uniform taper applied, and (d) after DPD with synthesized tapering applied. Fig. 3.8 depicts the measured gain distortion (Left) and AM-PM (Right) corresponding to the signals in Fig. 3.7 (a)-(d). Note, the DPD function coefficients in Fig. 3.7 (c) and (d) are trained with the array steered at broadside (i.e., $\theta = \phi = 0$), the FF receiver positioned in the array's main beam direction and the array experiencing about 1.7-1.8 dB compression as shown in Fig. 3.8 (a) and (b). From Fig. 3.7, it is clear that applying tapering does not significantly deteriorate the DPD performance at broadside. When uniform tapering

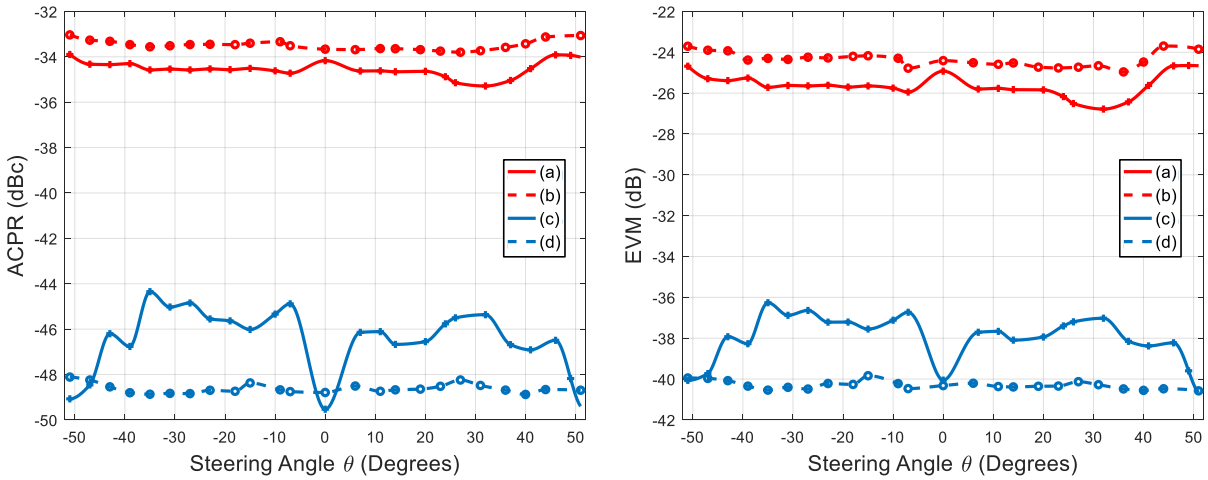


Figure 3.10: Measured UE-ACPR (Left) and EVM (Right)versus steering angle: (a) before DPD with uniform tapering applied; (b) before DPD with synthesized tapering applied; (c) after DPD with uniform tapering applied; (d) after DPD with synthesized tapering applied.

is applied, the UE-ACPR and EVM improved from −34.4/−34.0 dBc and −24.9 dB before DPD to −49.5/−49.5 dBc and −40 dB after DPD. In the case of synthesized tapering, the UE-ACPR and EVM improved from −33.8/−33.5 dBc and −24.4 dB before DPD to −48.8/−48.8 dBc and −40.3 dB after DPD. Note, the slight degradation of the UE-ACPR and EVM before and after DPD when synthesized tapering is applied as compared to the uniform tapering case, is due to the fact that array input power in the synthesized tapering case was adjusted to compensate for the reduction in array gain. This causes the PAs in the array that have a tapering coefficient of 1 to be driven at a higher compression point.

Fig. 3.9 shows the measured radiated power in the H-plane with the array steered at broadside: (a) in-band power with uniform tapering applied, (b) in-band power with synthesized tapering applied, (c) out-of-band power before DPD with uniform tapering applied, (d) out-of-band power before DPD with synthesized tapering applied, (e) out-of-band power after DPD with uniform tapering applied, and (f) out-of-band power after DPD with synthesized tapering applied. In this experiment, the FF horn remains fixed, and the measurements are conducted by mechanically rotating the array between $\theta = -52°$ and $\theta = 52°$ with the beam electrically steered at broadside. It is evident from Fig. 3.9 (e) and (f) that the linearization performance after DPD was maintained in both the main beam and in the sidelobe directions when uniform (c) or synthesized (f) tapering is

applied. Moreover, the TRP-ACPR improved from −34.3 dBc (when uniform tapering is applied) and −33.5 dBc (when synthesized tapering applied) before DPD to −46.2 dBc and −45.05 dBc for the uniform and synthesized tapering respectively after DPD.

In order to assess the generality of the DPD solution versus steering angle, a DPD function with the same coefficients used in Fig. 3.7 (c) and (d) are applied while the array is mechanically steered between $\theta = -50°$ and $\theta = 50°$. Electrical beam steering is applied to maintain alignment of the FF receiver with the direction of maximum radiation of the beam. The UE-ACPR and EVM are shown versus the steering angle in Fig. 3.10 (Left) and Fig. 3.10 (Right) respectively. From these plots, it is evident that the linearization performance of DPD in the uniform tapering profile case deteriorates when the array is steered even a few degrees away from the angle the DPD was trained at. For instance, when the array is steered to $\theta = -10°$, the UE-ACPR and EVM deteriorate from −49.5 dBc and −40 dB (at broadside) to −44 dBc and −36.4 dB, respectively. The application of the synthesized tapering profile obtained from the proposed algorithm significantly improves the DPD linearization performance versus the steering angle. The variation of the UE-ACPR and EVM after DPD is now less than ≤ 0.5 dB and ≤ 0.3 dB respectively, compared to 6 dB and 4 dB respectively when uniform tapering is applied. These results confirm the impact of tapering on the array's antenna active reflection coefficients and the capacity of synthesized tapering to enhance the SISO-DPD performance over a wide steering range.

3.3 Effect of Antenna Mutual Coupling on FM Nonlinearity

In this section, we investigate the impact of load modulation on the nonlinearity of FXs. While this investigation assumes an active FX, its outcomes can be easily extended to passive ones. Furthermore, this investigation assumes that the frequency multiplication in the active FX is dominated by the strong nonlinearity associated with the clipping of the drain current created by pinching off the channel [150–153]. Accordingly, the desired output signal of the FX is located at one of the harmonics of the input signal with the exact harmonic depending on the chosen multiplication factor. Furthermore, the undesired harmonics are assumed to be terminated with a short circuit [153].

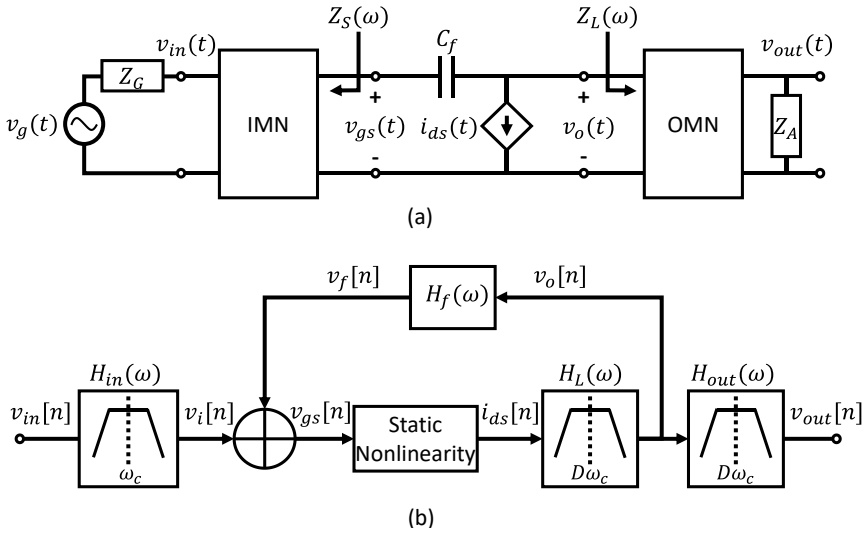


Figure 3.11: (a) Simplified circuit schematic of an FET-based FX; (b) Circuit-inspired conceptual block diagram of an FX.

3.3.1 Problem Formulation

Fig. 3.11(a) shows a generic circuit of an active FX which includes a simplified field-effect transistor (FET) model with a feedback capacitance, C_f. The drain current, $i_{ds}(t)$, is modeled using a static nonlinear function that depends on the gate-to-source voltage, $v_{gs}(t)$. This function mimics the conduction-angle dependent nonlinearity which dominates the behavior of the FX. The input matching network (IMN) and output matching network (OMN) shown in Fig. 3.11(a) are designed to produce source and load impedances, $Z_S(\omega)$ and $Z_L(\omega)$ at ω_c and $D\omega_c$ respectively, to maximize the trade-off between efficiency, output power and frequency-conversion gain assuming preset generator and termination impedances, Z_G and Z_A, respectively. The matching networks are also expected to present short-circuits at frequencies outside their passbands; i.e., outside a passband centered at ω_c (resp. $D\omega_c$) voltages at the transistor gate (resp. drain) are assumed to be zero.

The circuit in Fig. 3.11(a) is further simplified by expressing the voltages at different nodes in discrete-time with its circuit-inspired conceptual model shown in Fig. 3.11(b). In Fig. 3.11(b), the static nonlinear block is used to model the conduction-angle dependent nonlinearity of the FET output current, $i_{ds}[n]$. This output current is then fed to a transfer function, $H_L(\omega)$, that mimics the frequency selective load impedance, $Z_L(\omega)$. Note, $H_L(\omega)$ is only non-zero around $D\omega_c$. Two bandpass filterss (BPFs) centered at ω_c and $D\omega_c$ are used to account for the IMN and OMN transfer functions and are denoted by $H_{in}(\omega)$ and

$H_{out}(\omega)$, respectively. Finally, a linear feedback filter, $H_f(\omega)$, is used to account for the transfer function of the feedback capacitance C_f. The conceptual model in Fig. 3.11(b) is used hereafter to analyse the effect of the variation of the termination impedance, Z_A, and consequently the load impedance, Z_L, on the FX nonlinearity.

From Fig. 3.11(b), the discrete-time passband output of the static nonlinear block, $i_{ds}[n]$, can be expressed as follows,

$$i_{ds}[n] = \sum_{p=1}^{P} g_{m_p} v_{gs}^{p}[n], \tag{3.44}$$

where $v_{gs}[n]$ is the discrete-time passband input to the static nonlinear block, D is the FX multiplication factor, $P \geq D$ is the nonlinearity order and gm_p are the coefficients of the static nonlinear block. The output current $i_{ds}[n]$ is then fed to $H_L(\omega)$ to yield the band-limited output voltage, $v_o[n]$, around $D\omega_c$, and is expressed a follows,

$$v_o[n] = (h_L * i_{ds})[n], \tag{3.45}$$

where $h_L[n]$ is the impulse response of $H_L(\omega)$. Substituting (3.44) in (3.45), we get

$$v_o[n] = \sum_{p=1}^{P} \sum_{m=0}^{|\mathbf{h}_L|} g_{m_p} h_L[m] v_{gs}^{p}[n-m], \tag{3.46}$$

where $|\mathbf{h}_L| + 1$ is the length of the impulse response $h_L[n]$.

Based on Fig. 3.11(b), the discrete-time passband output of the feedback filter, $v_f[n]$, can be written as,

$$v_f[n] = (h_f * v_o)[n], \tag{3.47}$$

where $h_f[n]$ is the impulse response of the feedback filter, $H_f(\omega)$.

The discrete-time passband input to the static nonlinear block, $v_{gs}[n]$, can be expressed as follows,

$$v_{gs}[n] = v_i[n] + v_f[n], \tag{3.48}$$

where,

$$v_i[n] = (h_{in} * v_{in})[n], \tag{3.49}$$

$h_{in}[n]$ is the impulse response of $H_{in}(\omega)$ and $v_{in}[n]$ is the FX discrete-time passband input signal. Note, the output of the feedback filter, $v_f[n]$, at frequencies other than ω_c is assumed to be zero, due to the short circuit impedance presented by the input matching network. This is achieved by ensuring that the source impedance, $Z_S(\omega)$, is designed to show short a circuit impedance at frequencies other than ω_c. Consequently, for $D > 1$, (3.48) can be simplified as follows,

$$v_{gs}[n] = (h_{in} * v_{in})[n], \tag{3.50}$$

where the feedback voltage, $v_f[n]$, is eliminated as it does not include terms around ω_c. This simplification is only valid for FXs, i.e. $D > 1$, where the IMN and OMN are designed at different frequencies. For the PA case, as shown in [154], the feedback signal contributes to the nonlinearity at the PA output and hence cannot be ignored. Consequently, the output voltage, $v_o[n]$, of an FX is independent on the feedback signal $v_f[n]$. More importantly, given that the feedback voltage, $v_f[n]$, has no content at ω_c and the content at $D\omega_c$ is zeroed due to the short-circuit shown by the FX source impedance at the FX input, for $D > 1$, $v_f[n]$ does not affect the conduction angle of the transistor and hence does not affect the FX nonlinearity. Consequently, any variation of $Z_L(\omega)$ due to, for example, limited isolation among the antenna elements of the array only affects the FX linear response, as shown in (3.46). Furthermore, this variation does not affect the FX nonlinear behavior given that the contribution of the load-dependent feedback signal, $v_f[n]$, to the input of the FX, is forced to zero by design when $D > 1$.

Finally, substituting the expression of (3.50) in (3.46) and expressing the results in complex baseband equivalent (i.e. only keeping the terms at $D\omega_c$) results in the steering angle independent SISO Volterra model of the FX in (3.37) (see [7] for the full derivation).

Note, given that, synthesizing the matching networks in Fig. 3.11 while strictly meeting the above-mentioned short circuit source impedance at the harmonics of ω_c can be challenging, the nonlinear behavior of a practical FX may exhibit dependency to load impedance variation but to a much lesser extent than in the case of a PA. This is also validated in the simulation and measurement results shown in the following.

3.3.2 Numerical Analysis

In this subsection, we evaluate the effect of load modulation on the nonlinear behavior of both FXs and PAs in simulation. In the subsequent subsection, the ability of the proposed DPD to linearize an array of FXs will be validated experimentally.

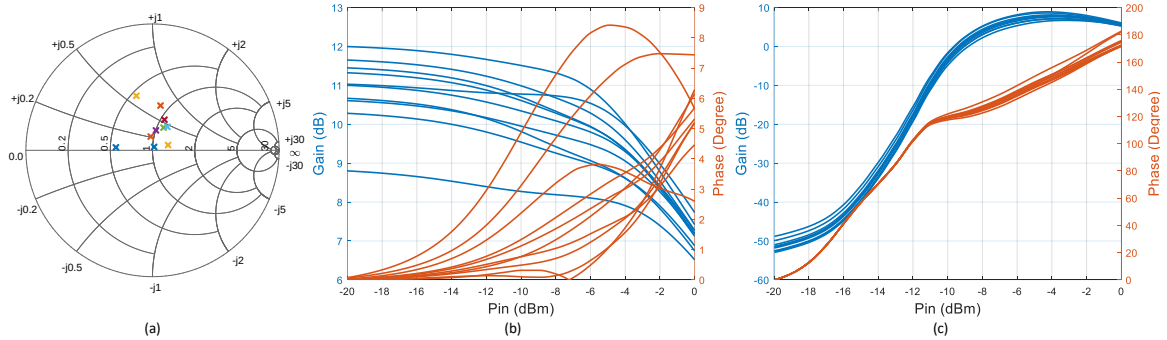


Figure 3.12: Simulated results of: (a) Load impedances extracted from the 8×8 array when steered from −50° to 50°; (b) Gain and AM-PM plots of a 39 GHz class AB PA terminated with the load impedances given in (a); (c) Gain and AM-PM plots of a 60 GHz doubler in stacked push-push configuration terminated with the load impedances given in (a).

The FX used in the simulation is a 60 GHz frequency doubler in stacked push-push configuration [155] and the PA is a 39 GHz class AB amplifier. Both the PA and the doubler are designed using 45-nm CMOS SOI technology. The designs are simulated in advanced design system (ADS) software under different load impedances to mimic the effect of load modulation in RF beamforming arrays. The impedances used in the simulations are those corresponding to an antenna element in an 8×8 electromagnetic (EM) simulated array. A total of 10 impedances were used in the simulation that were extracted at different steering angles and are characterized by a VSWR ranging from 1.07 to 2.64. These impedances are shown on a Smith chart in Fig. 3.12(a).

Fig. 3.12(b) and (c) show the simulated gain and the phase distortion versus input power under different impedance mismatches for a PA and a doubler respectively. In order to qualitatively compare the effect of the load mismatches on the PA and doubler nonlinearity, the curves of Fig. 3.12(b) and (c) were fitted using a memoryless polynomial with nonlinearity order set to 10 (i.e. 5 coefficients with only odd terms for the PA and only even terms for the doubler). The resulting model coefficients for different loads are shown in Fig. 3.13(a) and (b) for the PA case and doubler case, respectively. It is clear from Fig. 3.13(a) and (b) that the variation in complex-valued model coefficients is more significant for the PA case than for the doubler. To further illustrate this point, the coefficient of variation(CV) metric is introduced and defined as the ratio of the standard deviation, σ, to the mean, μ. Based on Fig. 3.13(c), the CV of the doubler model coefficients is an order of magnitude lower than the PA case which indicates that the effect of the load modulation on the doubler nonlinearity is less significant than the PA case.

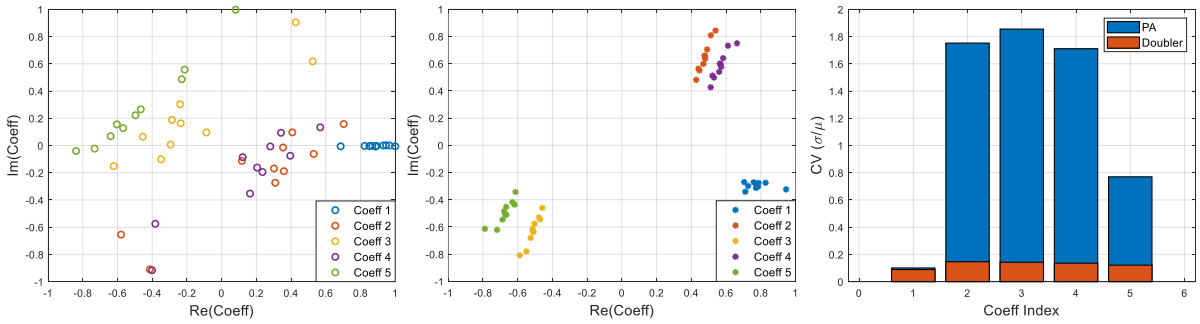


Figure 3.13: Simulated results of: (a) The forward model coefficients of a 39 GHz class AB PA plotted in the complex plane when terminated with the load impedances given in Fig. 3.12 (a); (b) The forward model coefficients of a 60 GHz doubler in stacked push-push configuration plotted in the complex plane when terminated with the load impedances given in Fig. 3.12 (a); (c) The CV of the PA and doubler forward model coefficients in (a) and (b) versus coefficient index.

Next, using the simulated AM-AM and AM-PM plots in Fig. 3.12(b) and (c), ten LUT based forward models for the PA and ten LUT based forward models for the doubler are constructed. Each of the constructed LUT models corresponds to a different load termination in Fig. 3.12(a). In order to assess the effect of load modulation on the PA and doubler nonlinearity, two DPD models (one for the PA and one for the doubler) are then trained for the case when the PA and doubler are terminated with a load of VSWR equal to 1.07. The obtained two sets of DPD coefficients are then applied to the previously constructed LUT-based forward models of the PA and doubler respectively. The PA UE-ACPR and EVM before DPD were 33.8/33.5 dBc and 4.90%, respectively. The doubler UE-ACPR and EVM before DPD (with $\boldsymbol{D}$th root applied) were 16.7/16.6 dBc and 40.3%, respectively. Table. 3.1 shows the UE-ACPR and EVM results after DPD for the PA and doubler cases when terminated with different loads in Fig. 3.12(a). For a VSWR of 1.07, the UE-ACPR and EVM results after DPD are 58.5/58.2 dBc and 0.62%, respectively for the PA case and 56.4/56.2 dBc and 0.22%, respectively for the doubler case. When the VSWR of the load is varied from 1.07 to 2.64, it is interesting to note that the linearization performance for the PA case deteriorates. For instance, the UE-ACPR for a VSWR of 2.64 is 34.4 / 34.0 dBc. For the doubler case, however, the linearization performance is maintained when the VSWR is varied from 1.07 to 2.64. The effect of varying the loads on the DPD performance can also be seen in Fig. 3.14 where the UE-ACPR (left) and EVM (right) are reported versus the different loads of Fig. 3.12(a), i.e, loads different from the one used while training the DPD. From Fig. 3.14 it is clear that the FX nonlinear behavior

Table 3.1: Simulated EVM and UE-ACPR of DPD linearized PA/doubler terminated with variable load. DPD is trained when the PA/doubler are terminated with a load that results in a VSWR of 1.07.

VSWR	$\lvert\Gamma\rvert$ (dB)	PA		FX	
		EVM (%)	UE-ACPR L/U (dBc)	EVM (%)	UE-ACPR L/U (dBc)
1.07	-29.6	0.62	58.5 / 58.2	0.22	56.4 / 56.2
1.24	-19.3	0.91	48.8 / 48.5	0.22	56.5 / 56.3
1.30	-17.7	1.82	42.6 / 42.3	0.23	56.4 / 56.2
1.38	-15.9	1.15	47.4 / 47.2	0.22	56.5 / 56.3
1.51	-13.9	1.90	43.0 / 42.9	0.22	56.5 / 56.3
1.58	-12.9	2.40	40.6 / 40.5	0.23	55.4 / 56.2
1.71	-11.6	2.44	40.5 / 40.4	0.22	56.4 / 56.2
1.81	-10.8	3.45	36.3 / 36.1	0.21	56.5 / 56.3
2.10	-9.0	3.26	36.6 / 36.1	0.22	56.4 / 56.3
2.64	-6.9	3.67	34.4 / 34.0	0.21	56.6 / 56.4

is not affected by the change in VSWR while the PA is significantly.

3.3.3 Experimental Validation

In this subsection, the ability of the proposed SISO-DPD in (3.37) to linearize an FX-based RF beamforming transmitter was experimentally validated using the measurement setup in Fig. 3.15. A picture of the measurement setup is shown in Fig. 3.16. In Fig. 3.15 four signal generators are uploaded with the same input signal except for a phase difference that is used to steer the beam towards the intended direction (θ, ϕ). The signals from each generator are centered at 1.75 GHz and are generated using 12 bit, 12 GS/s AWGs (M8190A from Keysight Technologies). Four baluns are used to convert the differential M8190A outputs to single-ended outputs and four lowpass filter (LPF) are used to remove unwanted Nyquist bands. The LPF outputs are then fed to a custom-built IF boards that contain an attenuator and a bias-T, to remove the LO leakage. The IF signals are then

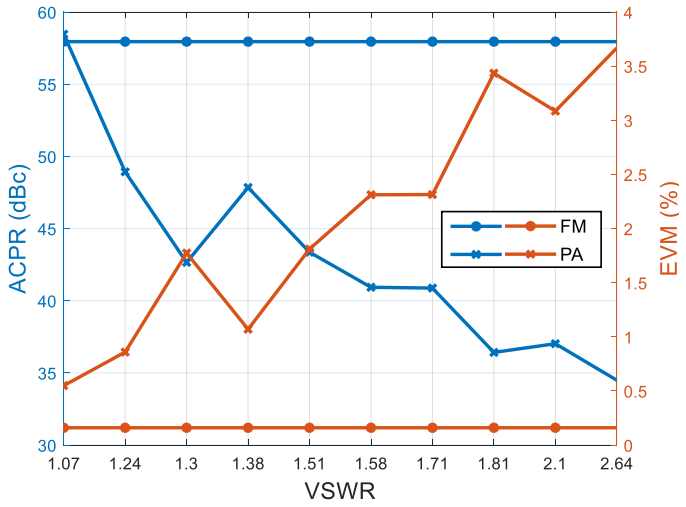


Figure 3.14: Simulated EVM and UE-ACPR of DPD linearized PA/doubler terminated with variable load. DPD is trained when the PA/doubler are terminated with a load that results in a VSWR of 1.07.

upconverted to 14 GHz using four IQ mixers (MLIQ-0416, from Marki Microwave). The IQ mixers' LO ports are driven by a 9 kHz to 40 GHz LO signal source (MXG-N5183B, from Keysight Technologies). Custom-built image rejection BPF centered at 14 GHz are then used with their outputs connected to four driver amplifiers (MAAM-011109 from MACOM). Four frequency doublers (HMC-578 from Analog Devices) form the device-under-test (DUT). Four directional couplers (from Krytar) are used to capture the signals at frequency doublers output.

The outputs from the couplers (i.e., the through ports) are fed to a 2×2 custom-built linear patch antenna array (with $\lambda/2$ antenna spacing) centered at 28 GHz. The antenna array is mounted on a servo motor that is rotated to align the beam with the receiver antenna when electrically steering the array. The FF signal is captured by a custom-built receiver horn antenna. A directional coupler (from Krytar) is placed at the horn antenna output with its coupled port connected to a spectrum analyzer (N9040B from Keysight Technologies). A 10 MHz to 70 GHz LO source (HMC-T22270 from Hittite Microwave) is used with a downconversion mixer (MM1-1140H from Marki Microwave) to downconvert the RF signal at the coupler through port output to an IF of 3 GHz. The downconverted signal is then digitized using one channel of a 4-channel, 20 GS/s, 10-bit, 8 GHz analog bandwidth oscilloscope (MSOS804A from Keysight Technologies). The second channel of the oscilloscope captures the downconverted version of the multiport RF

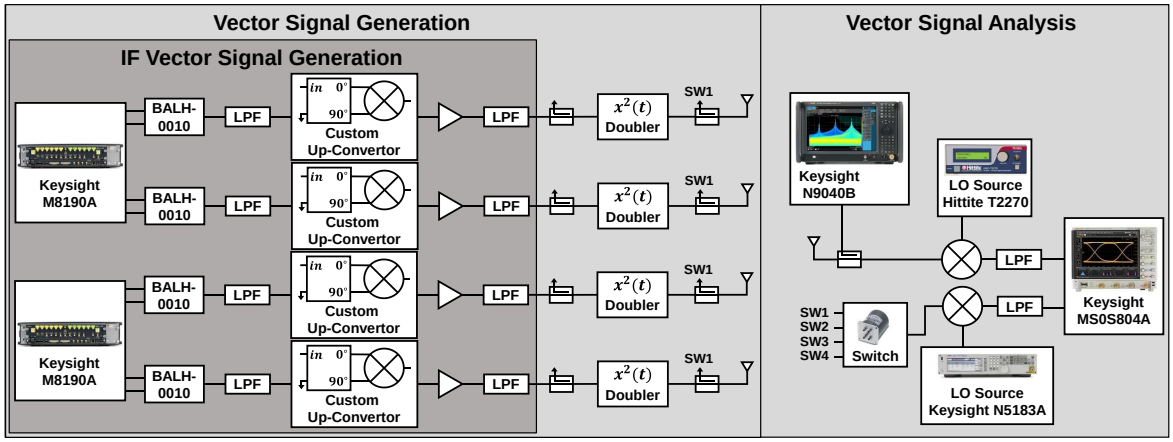


Figure 3.15: Functional block diagram of the measurement setup.

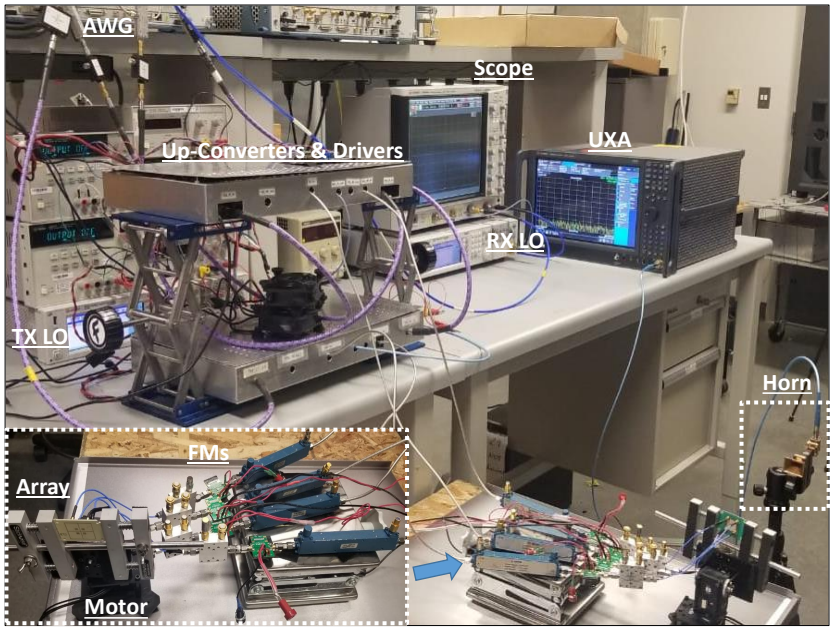


Figure 3.16: Picture of the measurement setup.

switch (87104D from Keysight Technologies) output; the switch's inputs are coupled to the doublers' outputs.

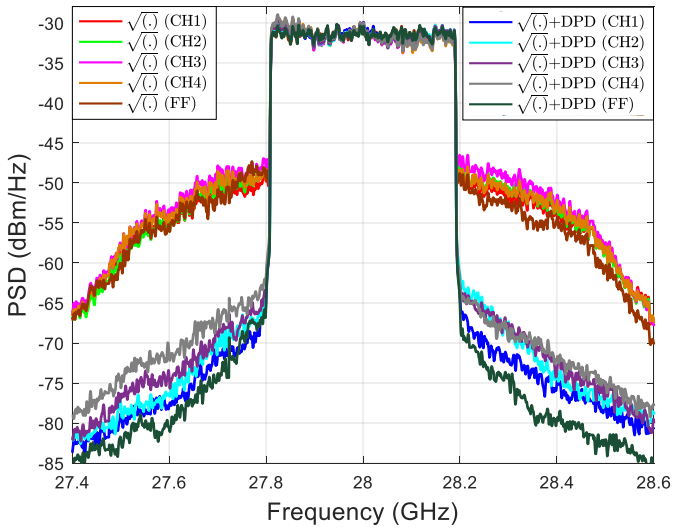


Figure 3.17: Measured output spectra of FX-based 2×2 RF beamforming transmitter driven with 400 MHz wide modulated signal, when DPD is trained using FF probing antenna, with either square-root only ($\sqrt{(.)}$) or cascade of square-root and proposed DPD ($\sqrt{(.)}$ + DPD) as predistorter.

Finally, each transmitter channel in the measurement setup was calibrated following the procedure given in [63]. A relative phase and time offset calibration between the four transmitter channels was also performed. It is worth mentioning that the phase difference between the transmitter channels was measured at the output of the FXs. Therefore, when applying the phase calibration, it was necessary to divide the measured phase by the FXs' multiplication factor, $\boldsymbol{D}$.

The test signals used were 100 MHz and 400 MHz wide OFDM signals with a sub-carrier spacing of 120 kHz and a peak-to-average power ratio of 11 dB. The 100 MHz wide signal was complex sampled at 1 GS/s with its sub-carriers modulated using 64-QAM. The 400 MHz wide signal was complex sampled at 3 GS/s with its sub-carriers modulated using 256-QAM.

For the boresight direction tests, two different TORs were used to train the DPD function. The training methods differed only in terms of the TOR employed. Each is presented and validated in this section.

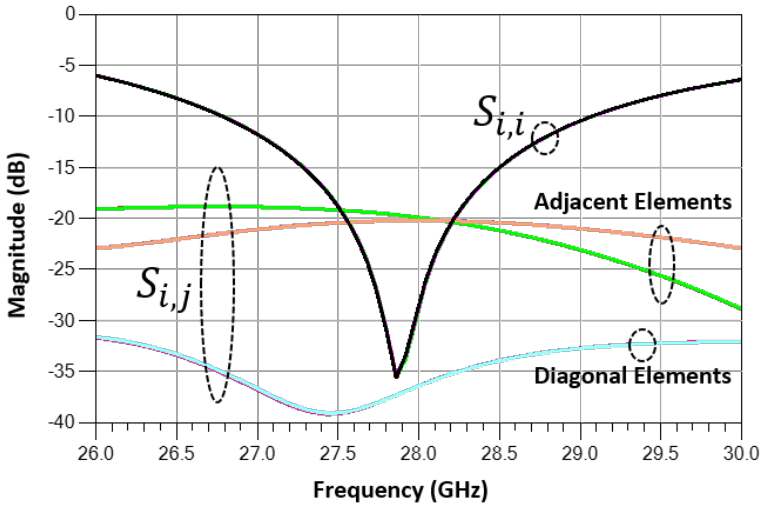


Figure 3.18: Simulated S-parameters of the 2×2 patch antenna array.

DPD Training Methods

For the boresight direction tests, two different TORs were used to train the DPD function. The training methods differed only in terms of the TOR employed. Each is presented and validated in this section.

The first method used is comprised of a FF probing antenna. In practice, this type of TOR is ideal when considering an FX-based RF beamforming scenario. While such TOR may not be feasible to implement, it is presented in this work as a reference against which the other type of TOR will be benchmarked.

The second TOR option provides a compromise between performance and complexity. This TOR is designed to capture the output of only one of the multipliers which is then used to train the DPD function (the DPD being applied to the common input of the entire array). This method is sensitive to individual FX nonlinear behavior differences that may be due to process variations or to antenna coupling. The array linearization performance also depends on which FX's output is captured. Nevertheless, this method is simple and has the potential to achieve acceptable linearization.

Fig. 3.17 shows the measured power spectral density versus frequency, at the output of each channel (i.e., FX) and in the FF (denoted by FF), when the 400 MHz signal is used with a FF probing antenna as TOR. The figure contains two sets of spectra: 1) when only a square-root function is used as predistorter (denoted as $\sqrt{(.)}$ in the legend), and 2)

Table 3.2: EVM and UE-ACPR With and Without DPD When DPD is Trained Using a Far-Field Probing Antenna

		Signal Bandwidth: 100 MHz			Signal Bandwidth: 400 MHz		
		EVM (%)	UE-ACPR L/U (dBc)	UE-TRP-ACPR L/U (dBc)	EVM (%)	UE-ACPR L/U (dBc)	UE-TRP-ACPR L/U (dBc)
Only $\sqrt{(.)}$	Ch1	22.9	21.7 / 21.7	-	27.0	22.1 / 21.7	-
	Ch2	16.5	23.9 / 24.1	-	23.4	21.8 / 21.2	-
	Ch3	27.3	19.7 / 19.6	-	24.2	20.3 / 20.0	-
	Ch4	29.5	18.9 / 18.9	-	22.8	21.1 / 21.2	-
	FF	**22.9**	**20.5 / 20.5**	**21.0 / 21.0**	**24.4**	**21.7 / 23.2**	**22.0 / 22.0**
$\sqrt{(.)}$+DPD	Ch1	3.2	41.4 / 39.2	-	4.1	41.9 / 41.2	-
	Ch2	3.9	36.6 / 36.0	-	4.7	40.3 / 38.4	-
	Ch3	1.6	44.5 / 44.5	-	3.8	39.1 / 38.5	-
	Ch4	4.2	36.0 / 35.9	-	4.8	36.7 / 37.9	-
	FF	**0.9**	**51.2 / 51.6**	**41.0 / 41.0**	**3.2**	**43.1 / 43.9**	**41.0 / 41.0**

when a cascade of a square-root function and the proposed DPD is used as the predistorter (denoted $\sqrt{(.)}$ + DPD in the legend). Table 3.2 summarizes the linearization results for the 100 MHz and 400 MHz wide test signals.

Both Table 3.2 and Fig. 3.17 show that the application of a square-root is insufficient to properly linearize the DUT, yielding an EVM of 23%, and 25% and an UE-ACPR of only 20/20 dBc and 22/23 dBc for the 100 MHz and 400 MHz signals, respectively. In order to remove the residual nonlinearity, the test signals were pre-processed with a cascade of the square-root and proposed DPD function. As a result, excellent linearization was achieved with only 44 coefficients, improving the EVM to 1% and 3% and the UE-ACPR to 51/52 dBc and 43/44 dBc for the 100 MHz and 400 MHz signals, respectively.

Table 3.2 shows that for the FF received signal, the TRP-ACPR improves from 21/21 dBc and 22/22 dBc (when only a square-root function is applied) to 41/41 dBc when the cascade of the square-root and DPD function is applied. Moreover, Table 3.2 and Fig. 3.17 also highlight an interesting observation: linearizing the FF received signal does not linearize the output of the individual channels to the same extent.

Note, similar DPD linearization results were also observed at the FF horn antenna, when the SISO-DPD function is trained using the FX output signals captured using directional couplers and summed digitally to mimic the FF combining as opposite to using a FF horn antenna as a TOR.

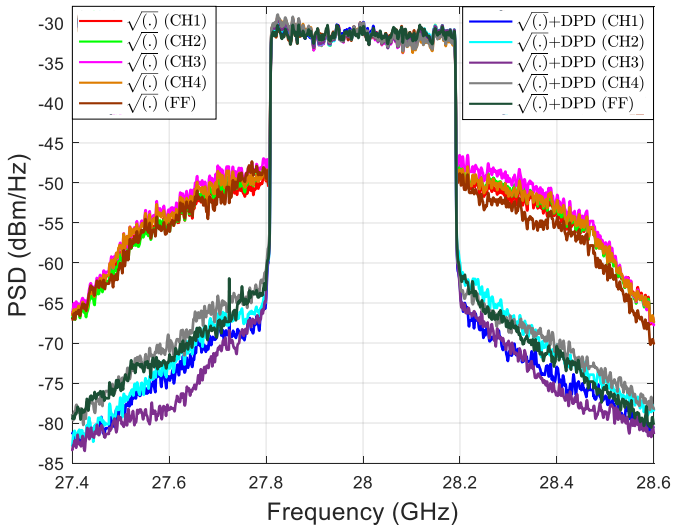


Figure 3.19: Measured output spectra of FX-based 2×2 RF beamforming transmitter driven with 400 MHz wide modulated signal, when DPD is trained using output of single-FX-channel, with either square-root only ($\sqrt{(.)}$) or cascade of square-root and proposed DPD ($\sqrt{(.)}$ + DPD) as predistorter.

The results obtained when DPD is trained using the output of one of the FXs in the beamforming transmitter array are reported in Table 3.3 and Fig. 3.19. The FX output used to train the SISO-DPD function was captured from FX number 3 (referred to as Ch-3 in Table 3.3 and Fig. 3.19). The results in Table 3.3 and Fig. 3.19 are reported under two predistorter conditions: a square-root only function, and a cascade of a square-root function with the proposed DPD. When using the square-root only function as the predistorter, the measured UE-ACPR and EVM for Ch-3 were 20/20 dBc and 27% for the 100 MHz signal and 20/20 dBc and 24% for the 400 MHz signals. At the FF horn antenna, the UE-ACPR and EVM were found to be 20/20 dBc and 23% for the 100 MHz signal and 22/23 dBc and 25% for the 400 MHz signal. Applying only a square-root function as the predistorter results in limited linearization performance and significant residual nonlinearity.

When the cascade of a square-root function and the proposed DPD scheme (with 44 coefficients) was used as the predistorter the results showed significant improvements. For the 100 MHz and 400 MHz test signals, the UE-ACPR of Ch-3 improved by 31 dBc and ~21 dBc, and the EVM improved to 1% and 4%, respectively. Note that the reported UE-ACPR and EVM results are best for Ch-3 as the output of the latter was used for DPD training. However, the actual received FF signal showed an UE-ACPR improvement

Table 3.3: EVM and UE-ACPR With and Without DPD When DPD is Trained Using the Output of a Single FX in the beamforming transmitter array

		Signal Bandwidth: 100 MHz			Signal Bandwidth: 400 MHz		
		EVM (%)	UE-ACPR L/U (dBc)	TRP-ACPR L/U (dBc)	EVM (%)	UE-ACPR L/U (dBc)	TRP-ACPR L/U (dBc)
Only $\sqrt{()}$	Ch1	22.6	21.8 / 21.8	-	26.1	22.1 / 21.8	-
	Ch2	16.3	24.1 / 24.2	-	22.9	22.2 / 21.6	-
	Ch3	**27.0**	**19.8 / 19.7**	-	**24.2**	**20.3 / 20.0**	-
	Ch4	29.2	19.0 / 19.0	-	23.3	21.1 / 21.2	-
	FF	23.9	20.3 / 20.3	21.0 / 21.0	25.7	21.6 / 23.0	22.0 / 22.0
$\sqrt{()}$+DPD	Ch1	4.1	38.4 / 36.8	-	4.3	40.1 / 40.1	-
	Ch2	4.7	34.8 / 34.5	-	4.8	38.5 / 36.3	-
	Ch3	**0.8**	**50.5 / 50.4**	-	**3.6**	**41.0 / 40.2**	-
	Ch4	3.0	38.7 / 39.4	-	4.8	35.9 / 37.0	-
	FF	3.0	38.6 / 39.3	39.0 / 39.0	4.8	35.9 / 37.0	38.0 / 38.0

of 19 dBc and 14 dBc, and the EVM improved to 3% and 5% for the 100 MHz and 400 MHz test signals, respectively. The use of the Ch-3 signal rather than the actual received FF signal allowed Ch-3 to achieve better linearization performance than the FF signal. The TRP-ACPR also showed 18 dBc and 16 dBc improvement when the cascaded predistorter was applied to the 100 MHz and 400 MHz test signals respectively. Compared to the FF TOR, training the DPD function using a single-FX can be an attractive solution as it significantly reduces the DPD TOR complexity while still maintaining acceptable linearization capacity.

Linearization Performance Versus Steering Angle

In the previous subsection we have experimentally shown that a SISO-DPD function can linearize FX-based RF beamforming TXs and that a reduced complexity TOR using the output of a single-FX can be used to linearize the FX-based array at the expense of slight deterioration in the TRP-UE-ACPR and the achievable EVM in the main beam direction. In order to assess the sensitivity of the proposed SISO-DPD to load modulation when applied to FX-based beamforming transmitter and validate the proposed theory, in this test, the same SISO-DPD function obtained at boresight, ($\theta = 0°, \phi = 0°$), with the reference FF TOR was applied while the array was electrically steered between $\theta = \pm 40°$. For each electrically steered direction, the array was physically rotated such that

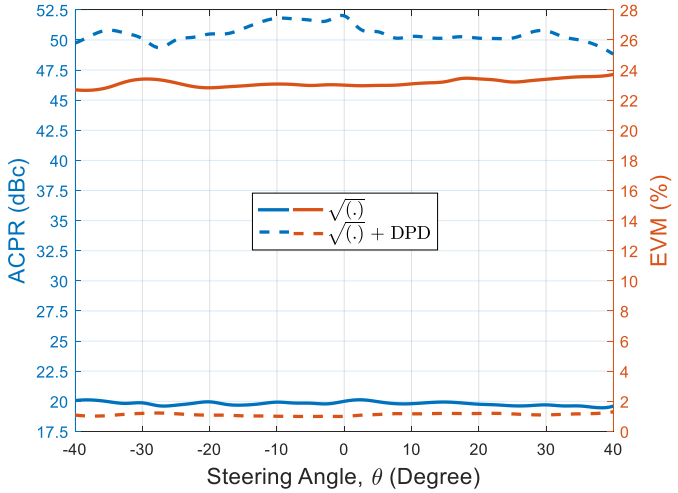


Figure 3.20: Measured UE-ACPR and EVM versus steering angle (θ) for FX-based 2×2 RF beamforming transmitter driven with 100 MHz wide modulated signal and DPD function trained at $\theta = 0°$.

the receiving horn antenna was aligned with the maximum radiation direction of the array. Figs. 3.20 and 3.21 illustrate the UE-ACPR and EVM versus steering angle, θ, when driven with both the 100 MHz and 400 MHz wide signals with the DPD function trained at $\theta = 0°$. The figures show almost negligible load modulation effects for both signal widths when the beam was steered from $-40°$ to $+40°$. When the proposed DPD approach is applied, the UE-ACPR variation is within 2 dBc while the EVM variation lies within 1%. This confirms the initial hypothesis that an FX-based array is less sensitive to load modulation effects and a single SISO-DPD model is sufficient to linearize the array over a wide range of beam steering angles.

In-band and Out-of-band Radiated Power Versus Steering Angle

In order to investigate the effect of the FF TOR DPD training on the out-of-band emissions, the in-band and out-of-band radiated powers were plotted in Fig. 3.22, when the array is driven by a 400-MHz OFDM test signal. The results with the square-root only predistorter function as well as for the cascade of the square-root function with the proposed SISO-DPD are displayed. These radiation patterns were obtained by physically rotating the motor-mounted array while the beam was fixed to boresight. The plot shows that out-of-band

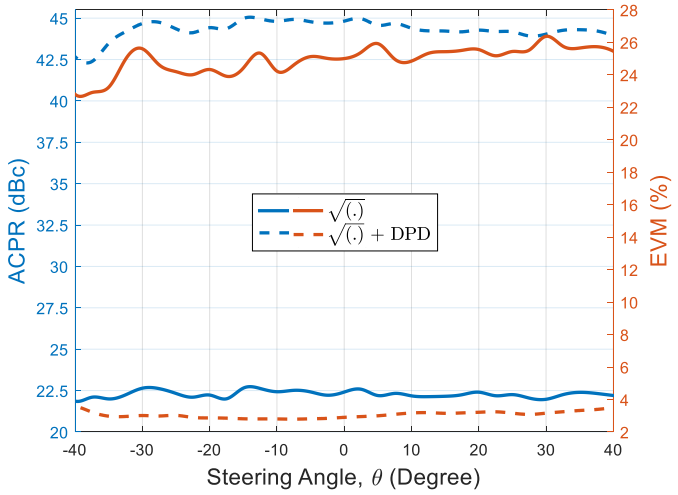


Figure 3.21: Measured UE-ACPR and EVM versus steering angle (θ) for FX-based 2×2 RF beamforming transmitter driven with 400 MHz wide modulated signal and DPD function trained at $\theta = 0°$.

emissions are reduced in directions other than that of the ($\theta = 0°, \phi = 0°$) direction where the DPD function was trained. The reduction in the DPD linearization capacity in the side lobes is in line with TRP-ACPR results reported in Table 3.2, as linearizing the FX beamforming array in the FF does not linearize the individual FXs in the array to the same extent due to process variation between the FXs.

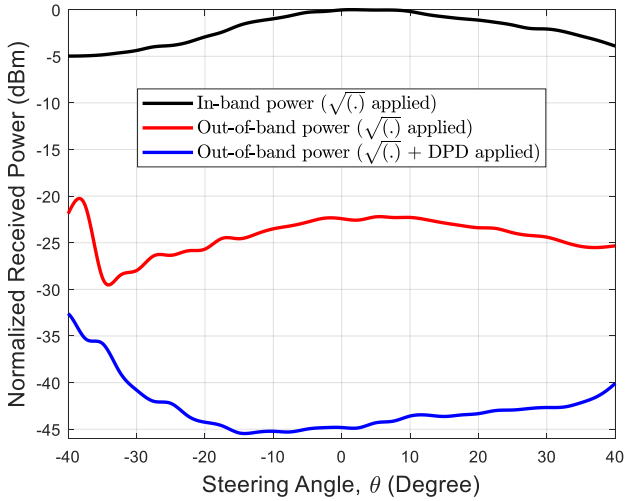


Figure 3.22: Measured in-band and out-of-band radiated powers versus steering angle under 400 MHz wide modulated input signal.

Chapter 4

Near-Field-Based Transmitter Observation Receiver for Beamforming Arrays Calibration and Linearization

To calibrate beamforming arrays or train the linearization function, it is essential to sample the radiated signals by the antennas in these arrays. In sub-6 GHz single antenna systems, this is conventionally achieved through the incorporation of couplers at the PA outputs. However, for large beamforming antenna arrays operating at MMW/sub-THz frequencies, the integration of couplers at the PA antenna interface has been demonstrated to be extremely challenging and costly. Consequently, most existing works in the literature have relied on a receiver located in the FF. While this approach proves effective in laboratory environments, the in-field deployment of external equipment such as a FF probe is often not feasible.

To address this critical challenge, this chapter introduces a NF-based TOR designed for integration within beamforming arrays. This TOR serves as feedback for in-field array calibration and linearization, offering a practical solution for real-world deployment. The associated signal processing algorithms, as proposed in **Publication III** and **Publication IV**, are also presented and discussed in detail.

4.1 Array Linearization Using Near-Field Based Transmitter Observation Receiver and Assuming Flat Coupling

In this section, the method to train the DPD function using an NF-based TOR (NF-TOR) that only relies on information/signals available at the transmitter side proposed in **Publication III** is presented. It starts by identifying the NF channel coefficients between the NF probes and the transmitting elements and then identifying the forward non-linear models that relate the NF probes output signals to the antenna array input for every captured steering angle. Subsequently, the coefficients of the identified forward non-linear models are used to deduce the individual PA forward models in the array. The SISO-DPD function is then trained using the identified PA models. The method was formulated to exploit multiple NF probes to reduce the number of required steering angles (measurements) and improve numerical stability. Extensive experiments were carried out to confirm the validity of the proposed method through the linearization of a 16-element RF beamforming array with four embedded NF probes.

4.1.1 Problem Formulation

In this subsection, the nonlinear model of the RF beamforming architecture depicted in Fig. 4.1 is formulated. For notational convenience, we express the model in the equivalent CBBE domain. Let $\tilde{x}[n]$ be the sampled CBBE of the RF continuous-time array input signal $x(t)$. The beamformer is modeled using the beamforming weights, $w_i \in \mathbb{C}$ for $i = 1, ..., K$, such that the CBBE input of the i^{th} PA is

$$\tilde{u}_i[n] = w_i \tilde{x}[n], \tag{4.1}$$

where $i \in \{1, 2, ..., K\}$ and K is the number of elements in the array.

Each of the K PAs is modeled using a baseband-equivalent nonlinear behavioral function, $f(\tilde{\mathbf{v}}(n); \boldsymbol{\mu}^{(i)})$, where

$$f(\tilde{\mathbf{v}}(n); \boldsymbol{\mu}^{(i)}) = \sum_{\ell=1}^{L} \mu_\ell^{(i)} \psi_\ell(\tilde{\mathbf{v}}(n)), \tag{4.2}$$

and $\tilde{\mathbf{v}}(n)$ denotes the block of M samples,

$$\tilde{\mathbf{v}}(n) = (\tilde{v}[n], \tilde{v}[n-1], ..., \tilde{v}[n-M+1]), \tag{4.3}$$

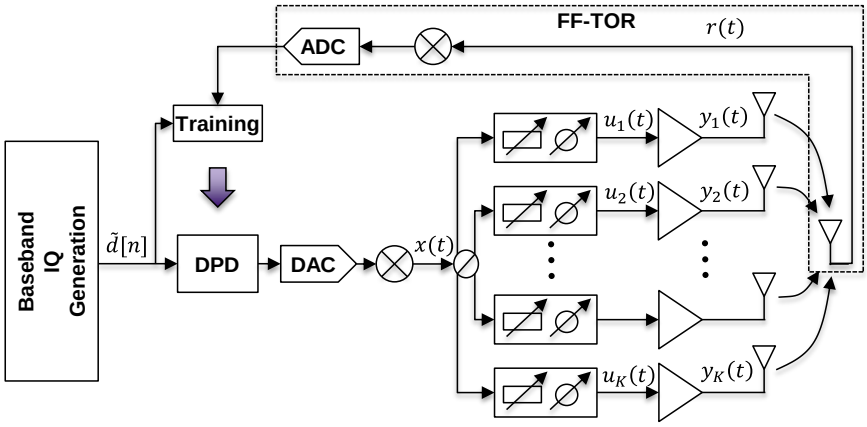


Figure 4.1: Block diagram of RF beamforming array using FF-TOR DPD training. The effective signal radiated towards the UE, $r(t)$, is the superposition of the individual antenna outputs, $y_i(t), i = 1, \ldots, K$.

M is the memory depth, $\boldsymbol{\mu}^{(i)} \in \mathbb{C}^{L\times 1}$ are the model coefficients of the i^{th} PA, $\psi_\ell(\tilde{\mathbf{v}}(n))$ is the ℓ^{th} basis, and L is the total number of basis. We note that while the behavioral model basis used in this article is built on the CRV model of [156], other nonlinear models such as the generalized memory polynomial [157] can be adopted in a straightforward manner. From (4.1) and (4.2), the CBBE output of the i^{th} PA, $\tilde{y}_i[n]$, can be written as

$$\tilde{y}_i[n] = \sum_{\ell=1}^{L} \mu_\ell^{(i)} \psi_\ell\big(\tilde{\mathbf{u}}_i(n)\big). \tag{4.4}$$

Furthermore, if the nonlinearity order of the ℓ^{th} basis function, $\psi_\ell(.)$, is $2p_\ell + 1$ then from (4.1)

$$\psi_\ell\big(\tilde{\mathbf{u}}_i(n)\big) = w_i|w_i|^{2p_\ell}\psi_\ell\big(\tilde{\mathbf{x}}(n)\big). \tag{4.5}$$

Therefore, substituting (4.5) in (4.4) we get,

$$\tilde{y}_i[n] = \sum_{\ell=1}^{L} \mu_\ell^{(i)} w_i|w_i|^{2p_\ell}\psi_\ell\big(\tilde{\mathbf{x}}(n)\big). \tag{4.6}$$

For MMW beamforming arrays, the channel is often characterized as a single LoS path. In such a case, the channel coefficient, h_i, between the i^{th} antenna and the user, can be approximated by a phase shift that is a function of the user location specified by the

elevation and azimuth angles as θ and ϕ respectively. Consequently, the normalized LoS channel coefficient can be expressed as follows,

$$h_i(\theta,\phi) = e^{-j\frac{2\pi}{\lambda}\sin(\theta)\left(d_i^x\cos(\phi)+d_i^y\sin(\phi)\right)} \tag{4.7}$$

$$= e^{-j\zeta_i(\theta,\phi)}, \tag{4.8}$$

where (d_i^x, d_i^y) is the location of the i^{th} antenna in the x-y plane, λ is the wavelength, and $\zeta_i(\theta,\phi) = \frac{2\pi}{\lambda}\sin(\theta)\left(d_i^x\cos(\phi) + d_i^y\sin(\phi)\right)$ is the beamforming phase. Note, (4.8) is general and can be applied to any configuration of one or two-dimensional arrays. Using (4.8), the beamforming weights for the direction (θ,ϕ) can be expressed as,

$$w_i(\theta,\phi) = \nu_i h_i^{\star}(\theta,\phi), \tag{4.9}$$

where $(.)^{\star}$ denotes the complex-conjugate, and ν_i is a steering-angle independent complex tapering coefficient. Substituting (4.9) in (4.6), the output of the i^{th} PA can be rewritten as

$$\tilde{y}_i(\theta,\phi)[n] = \sum_{\ell=1}^{L}\mu_\ell^{(i)}\nu_i h_i^{\star}(\theta,\phi)|\nu_i|^{2p_\ell}\psi_\ell\left(\tilde{\mathbf{x}}(n)\right) \tag{4.10}$$

$$= h_i^{\star}(\theta,\phi)\sum_{\ell=1}^{L}\alpha_\ell^{(i)}\psi_\ell\left(\tilde{\mathbf{x}}(n)\right), \tag{4.11}$$

where $\alpha_\ell^{(i)} = \mu_\ell^{(i)}\nu_i|\nu_i|^{2p_\ell}$. Consequently, the FF received signal at the observation angle (θ,ϕ), with beam-steering direction (θ,ϕ), can be written as,

$$\tilde{r}[n] = \sum_{i=1}^{K} h_i(\theta,\phi)\tilde{y}_i(\theta,\phi) \tag{4.12}$$

$$= \sum_{i=1}^{K}\sum_{\ell=1}^{L}\alpha_\ell^{(i)}\psi_\ell\left(\tilde{\mathbf{x}}(n)\right). \tag{4.13}$$

Linearizing the array in the FF at the intended user is therefore equivalent to finding the predistorter signal, $\tilde{x}[n] = \tilde{x}_{PD}[n]$, that minimizes the cost function,

$$J = \sum_{n=n_0}^{n_0+N-1}\left|\tilde{d}[n] - \tilde{r}[n]\right|^2 \tag{4.14}$$

$$= \sum_{n=n_0}^{n_0+N-1}\left|\tilde{d}[n] - \sum_{i=1}^{K}\sum_{\ell=1}^{L}\alpha_\ell^{(i)}\psi_\ell\left(\tilde{\mathbf{x}}_{PD}(n)\right)\right|^2, \tag{4.15}$$

where $\tilde{d}[n]$ is the desired output signal.

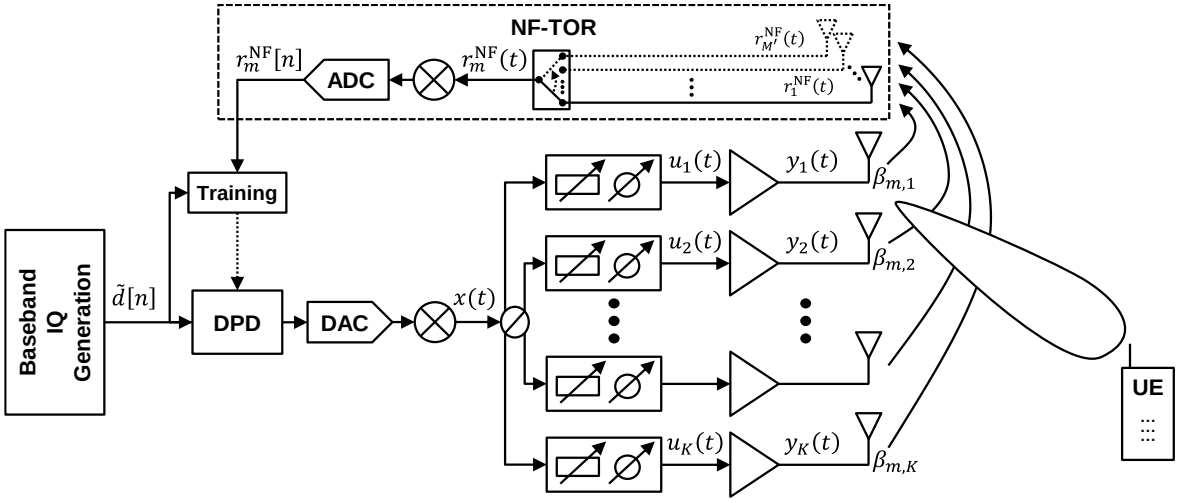


Figure 4.2: Block diagram of RF beamforming array using proposed NF-TOR DPD training. The signal captured by the m^{th} NF probe, $r_m^{\mathrm{NF}}(t)$, is the superposition of the individual antenna outputs, $y_i(t)$, scaled by the NF channel coefficient, $\beta_{m,i}$, for $i = 1...K$.

Proposed Far-Field Signal Estimation Using Near-Field Signals

In the following, a method to train the DPD function in RF beamforming arrays using signals acquired from an NF-TOR is presented. The formulation assumes that the array is calibrated a priori.

Using (4.11) the NF feedback signal, $r_m^{\mathrm{NF}}(\theta,\phi)[n]$, at the m^{th} NF receiver when the beam is steered in direction $(\theta,\ \phi)$ can be formulated as follows,

$$r_m^{\mathrm{NF}}(\theta,\phi)[n] = \sum_{i=1}^{K} \beta_{m,i}\tilde{y}_i(\theta,\phi)[n] \tag{4.16}$$

$$= \sum_{i=1}^{K} \beta_{m,i} h_i^{\star}(\theta,\phi) \sum_{\ell=1}^{L} \alpha_\ell^{(i)} \psi_\ell\big(\tilde{\mathbf{x}}(n)\big), \tag{4.17}$$

where $\beta_{m,i} \in \mathbb{C}$ is the NF channel coefficient between the i^{th} radiating element and the m^{th} NF probing antenna and $m = 1, ..., M'$ where M' is the total number of NF probes. Note, in (4.16) the coupled signal from each antenna, $\tilde{y}_i(\theta,\phi)[n]$, is subject to a different magnitude and phase before combining at the NF probe, i.e., $|\beta_{m,i}| \neq |\beta_{m,j}|$ for $i \neq j$. This is different from FF signal combining which is the result of the summation of the radiated signals by the transmitting antennas with equal magnitude combining and only phase differences.

Applying the LoS assumption in (4.8), we get

$$r_m^{\mathrm{NF}}(\theta,\phi)[n] = \sum_{i=1}^{K} \beta_{m,i} e^{-j\zeta_i(\theta,\phi)} \sum_{\ell=1}^{L} \alpha_\ell^{(i)} \psi_\ell\big(\tilde{\mathbf{x}}(n)\big) \tag{4.18}$$

$$= \sum_{\ell=1}^{L} \gamma_\ell^{(m)}(\theta,\phi)\psi_\ell\big(\tilde{\mathbf{x}}(n)\big), \tag{4.19}$$

where

$$\gamma_\ell^{(m)}(\theta,\phi) = \sum_{i=1}^{K} \beta_{m,i} e^{-j\zeta_i(\theta,\phi)} \alpha_\ell^{(i)} \tag{4.20}$$

is the coefficient of the ℓ^{th} basis of the model describing the output of the m^{th} NF probe, $r_m^{\mathrm{NF}}(\theta,\phi)[n]$. Given a block of N samples of the NF received signal at the m^{th} NF probe when the beam is steered towards the direction (θ_τ,ϕ_τ), a vector $\mathbf{r}_m^{\mathrm{NF}}(\theta_\tau,\phi_\tau)$ can be constructed as follows,

$$\mathbf{r}_m^{\mathrm{NF}}(\theta_\tau,\phi_\tau) = \begin{bmatrix} r_m^{\mathrm{NF}}(\theta_\tau,\phi_\tau)[n_\tau] \\ r_m^{\mathrm{NF}}(\theta_\tau,\phi_\tau)[n_\tau+1] \\ \vdots \\ r_m^{\mathrm{NF}}(\theta_\tau,\phi_\tau)[n_\tau+N-1] \end{bmatrix}, \tag{4.21}$$

where n_τ is the time index of the sample when the beam is steered in direction (θ_τ,ϕ_τ). Then (4.19) can be expressed in matrix form as follows,

$$\mathbf{r}_m^{\mathrm{NF}}(\theta_\tau,\phi_\tau) = \boldsymbol{\Psi}^{(\tau)}\boldsymbol{\gamma}^{(m)}(\theta_\tau,\phi_\tau), \tag{4.22}$$

where,

$$\boldsymbol{\gamma}^{(m)}(\theta_\tau,\phi_\tau) = \begin{bmatrix} \gamma_1^{(m)}(\theta_\tau,\phi_\tau) \\ \gamma_2^{(m)}(\theta_\tau,\phi_\tau) \\ \vdots \\ \gamma_L^{(m)}(\theta_\tau,\phi_\tau) \end{bmatrix} \tag{4.23}$$

and $\boldsymbol{\Psi}^{(\tau)}$ is a $N \times L$ matrix with entries in the i^{th} row and k^{th} column given by

$$\left[\boldsymbol{\Psi}^{(\tau)}\right]_{i,k} = \psi_k(\tilde{\mathbf{x}}[n_\tau + i - 1]). \tag{4.24}$$

In (4.22), $\mathbf{r}_m^{\mathrm{NF}}(\theta_\tau, \phi_\tau)$ and $\boldsymbol{\Psi}^{(\tau)}$ are known, consequently the estimate, $\hat{\boldsymbol{\gamma}}^{(m)}(\theta_\tau, \phi_\tau)$ of $\boldsymbol{\gamma}^{(m)}(\theta_\tau, \phi_\tau)$ can be calculated by means of the least squares fitting as follows,

$$\hat{\boldsymbol{\gamma}}^{(m)}(\theta_\tau, \phi_\tau) = \left(\left(\boldsymbol{\Psi}^{(\tau)}\right)^H \boldsymbol{\Psi}^{(\tau)}\right)^{-1} \left(\boldsymbol{\Psi}^{(\tau)}\right)^H \mathbf{r}_m^{\mathrm{NF}}(\theta_\tau, \phi_\tau), \tag{4.25}$$

where $(.)^H$ denotes the Hermitian-transpose. From (4.16) and (4.18) it is clear that the NF received signal at the m^{th} NF probing antenna combines the PA outputs scaled by the NF channel $\beta_{m,i}$. We can also establish from (4.19) that the NF feedback signal can be modeled using the same nonlinear basis functions, $\psi_\ell\big(\tilde{\mathbf{x}}(n)\big)$, as the FF signal and with steering angle dependent model coefficients, $\gamma_\ell^{(m)}(\theta, \phi)$, that contain information about the K PA coefficients, $\alpha_\ell^{(i)}$ for $i = 1, ..., K$. Given prior knowledge of the channel coefficients $\beta_{m,i}$, the beamforming phase ζ_i, and the tapering coefficients ν_i for $i = 1, ..., K$, it is possible to estimate the coefficients of the forward model of each PA in the array and generate the nonlinear function that describes the FF signal as a function of the array input signal in the UE direction (i.e., the coherent sum of PA outputs) needed for DPD training. This can be achieved using multiple measurements at different beamforming directions (θ_τ, ϕ_τ) and is explained in the following.

Lets assume that the transmitter steers to T different steering angles, (θ_τ, ϕ_τ) for $\tau = 1, ..., T$. Using (4.25), it is possible to generate the following $M'T \times L$ matrix of estimated NF feedback signal model coefficients,

$$\hat{\boldsymbol{\Gamma}} = \begin{bmatrix} \hat{\gamma}_1^{(1)}(\theta_1, \phi_1) & \hat{\gamma}_2^{(1)}(\theta_1, \phi_1) & \dots & \hat{\gamma}_L^{(1)}(\theta_1, \phi_1) \\ \vdots & \vdots & \ddots & \vdots \\ \hat{\gamma}_1^{(1)}(\theta_T, \phi_T) & \hat{\gamma}_2^{(1)}(\theta_T, \phi_T) & \dots & \hat{\gamma}_L^{(1)}(\theta_T, \phi_T) \\ \hat{\gamma}_1^{(2)}(\theta_1, \phi_1) & \hat{\gamma}_2^{(2)}(\theta_1, \phi_1) & \dots & \hat{\gamma}_L^{(2)}(\theta_1, \phi_1) \\ \vdots & \vdots & \ddots & \vdots \\ \hat{\gamma}_1^{(M')}(\theta_T, \phi_T) & \hat{\gamma}_2^{(M')}(\theta_T, \phi_T) & \dots & \hat{\gamma}_L^{(M')}(\theta_T, \phi_T) \end{bmatrix} \tag{4.26}$$

Consequently, (4.20) can be written in matrix for $\tau = 1, ..., T$ and $m = 1, ..., M'$ as,

$$\hat{\boldsymbol{\Gamma}} = \mathbf{BA}, \tag{4.27}$$

where $\mathbf{A}$ is the $K \times L$ matrix

$$\mathbf{A} = \begin{bmatrix} \alpha_1^{(1)} & \alpha_2^{(1)} & \dots & \alpha_L^{(1)} \\ \alpha_1^{(2)} & \alpha_2^{(2)} & \dots & \alpha_L^{(2)} \\ \vdots & \vdots & \ddots & \vdots \\ \alpha_1^{(K)} & \alpha_2^{(K)} & \dots & \alpha_L^{(K)} \end{bmatrix}, \tag{4.28}$$

and $\mathbf{B}$ is the $M'T \times K$ matrix

$$\mathbf{B} = \begin{bmatrix} \beta_{1,1} e^{-j\zeta_1(\theta_1,\phi_1)} & \dots & \beta_{1,K} e^{-j\zeta_K(\theta_1,\phi_1)} \\ \vdots & \ddots & \vdots \\ \beta_{1,1} e^{-j\zeta_1(\theta_T,\phi_T)} & \dots & \beta_{1,K} e^{-j\zeta_K(\theta_T,\phi_T)} \\ \beta_{2,1} e^{-j\zeta_1(\theta_1,\phi_1)} & \dots & \beta_{2,K} e^{-j\zeta_K(\theta_1,\phi_1)} \\ \vdots & \ddots & \vdots \\ \beta_{M',1} e^{-j\zeta_1(\theta_T,\phi_T)} & \dots & \beta_{M',K} e^{-j\zeta_K(\theta_T,\phi_T)} \end{bmatrix}. \tag{4.29}$$

The PAs model coefficients can then be estimated using least squares fit as follows,

$$\hat{\mathbf{A}} = \left(\mathbf{B}^H \mathbf{B}\right)^{-1} \mathbf{B}^H \hat{\mathbf{\Gamma}}, \tag{4.30}$$

where $\hat{\mathbf{A}} = \left[\hat{\boldsymbol{\alpha}}^{(1)}, ..., \hat{\boldsymbol{\alpha}}^{(K)}\right]^T$ is the estimate of $\mathbf{A}$, and $\hat{\boldsymbol{\alpha}}^{(i)} = \left(\hat{\alpha}_1^{(i)}, ..., \hat{\alpha}_L^{(i)}\right)^T$ are the estimate of the i^{th} PA model coefficients $\boldsymbol{\alpha}^{(i)} = \left(\alpha_1^{(i)}, ..., \alpha_L^{(i)}\right)^T$. It is worth noting that for (4.27) to have a unique solution, $M'T$ must be at least equal to K. In other words, if $M' = 1$ (i.e., only one NF probe is used) then at least $T = K$ measurements at T different steering angles need to be conducted to determine the model coefficients of all the PAs in the array. Substituting (4.30) in (4.13), the FF signal estimate in the intended UE direction, $\hat{r}[n]$, can be expressed as

$$\hat{r}[n] = \sum_{i=1}^{K} \sum_{\ell=1}^{L} \hat{\alpha}_\ell^{(i)} \psi_\ell\left(\tilde{\mathbf{x}}(n)\right). \tag{4.31}$$

Hence, together (4.25), (4.30), and (4.31) are first used to calculate the coefficients of the forward model of each PA in the array and then, from these forward models, construct the nonlinear function that describes the FF signal, in the intended user direction, as a function of the array input signal. Note, when a time-shared TOR is adopted in the implementation of the proposed method (as shown in Fig. 4.2), the above formulation does

not require the input signal samples, $\tilde{x}[n]$, to be maintained unchanged while sampling the NF probes output signal. Moreover, the proposed formulation does not require the input signal samples, $\tilde{x}[n]$, to be maintained unchanged while sampling the NF signals at different steering angles. Note, in the special case where a single feedback probe (i.e., $M' = 1$) located in the FF is used for DPD training, the channel coefficients in (4.29) can then be assumed to have constant magnitudes and only vary in phase (this assumption is not valid when the TOR is located in the NF). In such a case, the derivation above would yield similar outcomes to [83].

Proposed Near-Field Channel Identification

In order to identify the PA model coefficients using NF feedback signals, (4.30) requires prior knowledge of the NF channel coefficients, $\beta_{m,i}$. The NF channel coefficients can theoretically be calculated using the S-Parameters of the PAs and antennas. This, however, would require a full EM simulation of the array (or measurements), which may not be always possible or available. In this sub-section, we devise an approach to estimate the NF channel coefficients without the need for S-Parameters. Assuming that the array is linear (i.e., either operated in backoff or linearized a priori), the signal at the m^{th} NF probe's output, can be expressed as,

$$r_m^{\mathrm{NF}'}(\theta,\phi)[n] = \sum_{i=1}^{K} \beta_{m,i} \nu_i e^{-j\zeta_i(\theta,\phi)} \tilde{x}[n], \tag{4.32}$$

where $r_m^{\mathrm{NF}'}(\theta,\phi)[n]$ is the NF received signal at the m^{th} NF probing antenna when the array output is linear and steered to direction (θ,ϕ). Alternatively, (4.32), can be written in matrix form as follows,

$$\mathbf{r}_m^{\mathrm{RF}'}(\theta_\tau,\phi_\tau) = \mathbf{H}(\theta_\tau,\phi_\tau)\boldsymbol{\beta}^{(m)}, \tag{4.33}$$

where $\boldsymbol{\beta}^{(m)} = \left(\beta_{m,1},...,\beta_{m,K}\right)^T$ is the NF channel coefficients vector,

$$\mathbf{r}_m^{\mathrm{RF}'}(\theta_\tau,\phi_\tau) = \begin{bmatrix} r_m^{\mathrm{NF}'}(\theta_\tau,\phi_\tau)[n_\tau] \\ r_m^{\mathrm{NF}'}(\theta_\tau,\phi_\tau)[n_\tau+1] \\ \vdots \\ r_m^{\mathrm{NF}'}(\theta_\tau,\phi_\tau)[n_\tau+N'-1] \end{bmatrix}, \tag{4.34}$$

n_τ is the time index of the first sample when the beam is steered in direction (θ_τ, ϕ_τ), $N' \geq 1$ is the length of the received block of samples and $\mathbf{H}(\theta_\tau, \phi_\tau)$ is a $N' \times K$ matrix with entries in the i^{th} row and k^{th} column given by

$$\left[\mathbf{H}(\theta_\tau, \phi_\tau)\right]_{i,k} = \tilde{x}[n_\tau + i - 1]\nu_k e^{-j\zeta_k(\theta_\tau, \phi_\tau)}. \tag{4.35}$$

Now, assume that the transmitter is steered to $T \geq K$ different steering angles, (θ_τ, ϕ_τ) for $\tau = 1, ..., T$. Consequently, (4.33) can be rewritten for $\tau = 1, ..., T$ as,

$$\mathbf{r}_m^{\mathrm{RF}'} = \mathbf{H}\boldsymbol{\beta}^{(m)}, \tag{4.36}$$

where

$$\mathbf{r}_m^{\mathrm{NF}'} = \begin{bmatrix} \mathbf{r}_m^{\mathrm{NF}'}(\theta_1, \phi_1) \\ \mathbf{r}_m^{\mathrm{NF}'}(\theta_2, \phi_2) \\ \vdots \\ \mathbf{r}_m^{\mathrm{NF}'}(\theta_K, \phi_K) \end{bmatrix}, \tag{4.37}$$

and $\mathbf{H}$ is a $N'T \times K$ matrix given by,

$$\mathbf{H} = \begin{bmatrix} \mathbf{H}(\theta_1, \phi_1) \\ \mathbf{H}(\theta_2, \phi_2) \\ \vdots \\ \mathbf{H}(\theta_K, \phi_K) \end{bmatrix}. \tag{4.38}$$

In other words, $\mathbf{H}$ is obtained by stacking the matrices $\mathbf{H}(\theta_1, \phi_1), ..., \mathbf{H}(\theta_K, \phi_K)$.

The NF channel coefficients, $\boldsymbol{\beta}^{(m)}$, of the m^{th} NF probe can hence be estimated using least squares fitting as,

$$\hat{\boldsymbol{\beta}}^{(m)} = \left(\mathbf{H}^H\mathbf{H}\right)^{-1}\mathbf{H}^H\mathbf{r}_m^{\mathrm{RF}'}, \tag{4.39}$$

where $\hat{\boldsymbol{\beta}}^{(m)} = \left(\hat{\beta}_{m,1}, ..., \hat{\beta}_{m,K}\right)^T$, is the estimate of the m^{th} NF probe channel coefficients vector. Note, the NF channel coefficients do not vary over time and hence only need to be calculated once.

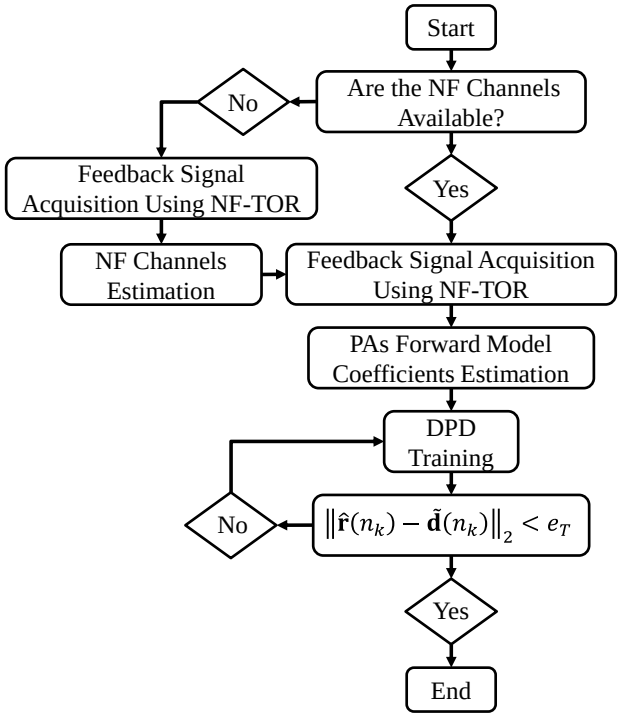


Figure 4.3: Flowchart of the proposed NF-TOR DPD training approach.

Proposed Digital Predistortion Training Procedure

In the following, the proposed DPD training procedure used in this work is presented. The proposed DPD training approach consists of minimizing the error between the DPD input signal, $\tilde{d}[n]$, and the FF signal estimate in the intended UE direction, $\hat{r}[n]$. Various behavioral models can be used to describe the DPD function. In this work, the CRV model outlined in [156] is used. The sampled complex envelope, $\tilde{x}_{PD}[n]$, of the pre-distorted signal

is expressed as,

$$\begin{aligned}\tilde{x}_{PD}[n] = &\sum_{\substack{i=0\\ \text{even}}}^{N_{NL}} \kappa_i \tilde{d}[n]\left|\tilde{d}[n]\right|^i + \sum_{m=1}^{M_L} \dot{\kappa}_m \tilde{d}[n - \mathrm{S}{\times}m] \\ &+ \sum_{\substack{i=1\\ \text{odd}}}^{N_{NL}} \sum_{m=1}^{M_{NL}} \sum_{\substack{k=2\\ \text{even}}}^{N_{NL}} \dot{\eta}_{i,m,k} \tilde{d}[n]\left|\tilde{d}[n]\right|^{i-1}\left|\tilde{d}[n - \mathrm{S}{\times}m]\right|^k \\ &+ \sum_{\substack{i=2\\ \text{even}}}^{N_{NL}} \sum_{m=1}^{M_{NL}} \sum_{\substack{k=1\\ \text{odd}}}^{N_{NL}} \ddot{\eta}_{i,m,k}\left|\tilde{d}[n]\right|^i \tilde{d}[n - \mathrm{S}{\times}m]\left|\tilde{d}[n - \mathrm{S}{\times}m]\right|^{k-1},\end{aligned} \tag{4.40}$$

where N_{NL} denotes the nonlinearity order, M_L denotes the linear memory depth, M_{NL} denotes the nonlinear memory depth, S is a memory step pruning parameter, and the model coefficients are denoted by $\{\kappa_i, \dot{\kappa}_m, \dot{\eta}_{i,m,k}, \ddot{\eta}_{i,m,k}\}$. The nonlinear memory of the higher order terms is pruned following the procedure in [5], such that the nonlinear memory basis functions are limited to those satisfying the condition $i+m+k \leq N_{NL}$. Alternatively, (4.40) can be rewritten as follows,

$$\tilde{x}_{PD}[n] = \sum_{\ell=1}^{L'} \eta_\ell \psi_\ell(\tilde{\mathbf{d}}[n]), \tag{4.41}$$

where L' is the total number of DPD bases and η_ℓ is the ℓ^{th} DPD coefficient.

Using the direct learning algorithm introduced in [158, 159], the optimal values of $\boldsymbol{\eta}$ are iteratively calculated and the coefficients are obtained using the following update equation,

$$\boldsymbol{\eta}_{k+1} = \boldsymbol{\eta}_k - \lambda\left(\left(\boldsymbol{\Psi}^{(k)}\right)^H \boldsymbol{\Psi}^{(k)}\right)^{-1}\left(\boldsymbol{\Psi}^{(k)}\right)^H\left(\hat{\mathbf{r}}(n_k) - \tilde{\mathbf{d}}(n_k)\right), \tag{4.42}$$

where $\boldsymbol{\eta}_k$ are the k^{th} iteration DPD coefficients, $\hat{\mathbf{r}}(n_k)$ is computed using (32), n_k is the time index of the first sample at the k^{th} iteration, and $\lambda \in (0, 1]$ is the step size.

Fig. 4.3 shows a flow diagram summarising the proposed NF-TOR based DPD training method, where e_T denotes the threshold error value. The proposed NF-TOR training approach requires, first, estimating the NF channel coefficients using NF measurements. Note, the NF channel coefficients depend on the PA and antenna S-Parameters and hence do not require repeated estimation whenever the DPD is retrained. Second, using the signals acquired from the NF-TOR at different steering angles, the forward model coefficients of the PAs are estimated and used to train the DPD function. The DPD training is repeated until the array is linearized and the root-mean-square error, $\left\|\hat{\mathbf{r}}(n_k) - \tilde{\mathbf{d}}(n_k)\right\|_2$, is less than e_T.

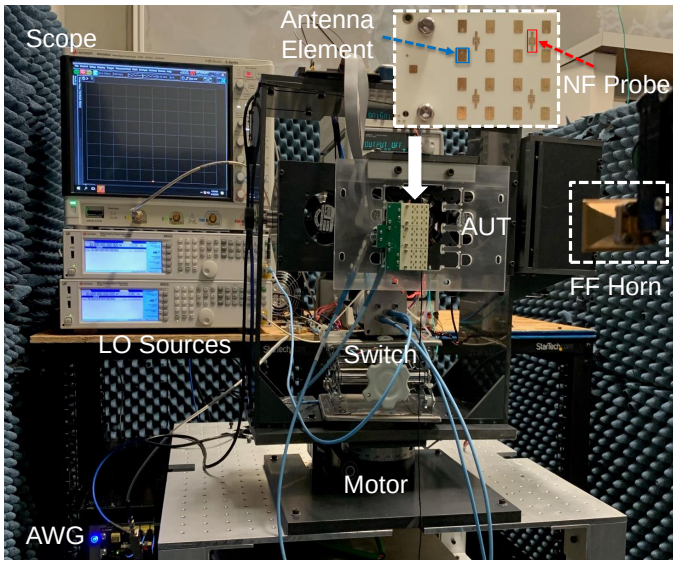


Figure 4.4: Picture of measurement setup with 16-element RF beamforming array (inset).

4.1.2 Experimental Validation

In this subsection, we provide extensive RF measurements obtained using a custom-built 16-element RF beamforming array operating at 29 GHz as the AUT. The AUT is driven with 5G NR wideband OFDM signals and the performance when the proposed NF-TOR trained DPD approach is applied is presented and discussed.

Measurement Setup

In order to demonstrate the effectiveness of the proposed DPD method to linearize RF beamforming arrays, an experimental setup, shown in Fig. 4.4, was developed. The vector-modulated test signals used in the experiment were generated using a 12-bit, 12 Gsps AWG (M8121A from Keysight Technologies), with output centered at an IF of 1.75 GHz. An IQ mixer (MMIQ 1037H from Marki Microwave) was used to up-convert the IF signal to a center frequency of 29 GHz. The signal was then amplified using a driver amplifier (MAAM-011109 from MACOM) and fed to the AUT. A horn antenna (i.e., FF reference antenna) was used to capture the FF signal and validate the DPD linearization performance. The outputs of the NF probes and the FF reference antenna were down-converted to an IF frequency of 1.75 GHz, and captured using a 10-bit, 20 Gsps, 8 GHz analog bandwidth oscilloscope (MSOS804A from Keysight Technologies). A LO source (MXG-N5183B from

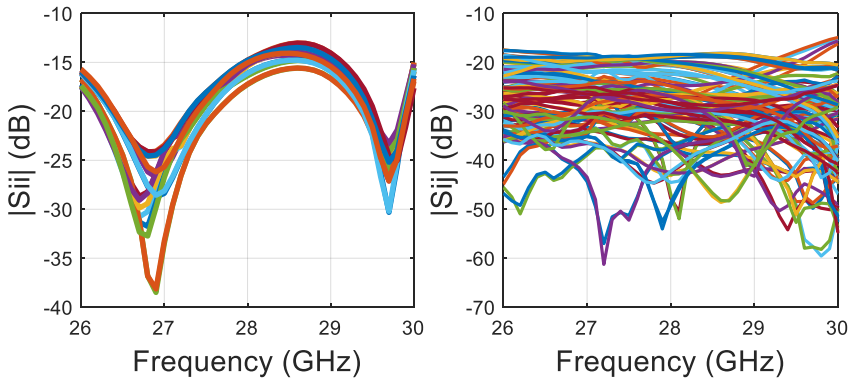


Figure 4.5: EM simulated S-Parameters of the 4x4 antenna under test.

Keysight Technologies) was used to drive the up-conversion and down-conversion mixers used in the setup.

The 4×4-element AUT, designed to operate in the 26-30 GHz frequency band, has four NF probes embedded within the array [134], four beamforming ICs (Anokiwave AWMF-0162 [149]) and utilizes anti-phase probe feeding to the antennas. Fig. 4.5 shows the S-Parameters of the 4x4 antenna array obtained using EM simulations. As per Fig. 4.5, the return loss and cross-antenna element isolation were better than 13 dB and 18 dB, respectively, across the designed band of operation. The NF probes embedded in the AUT (see magnified inset of Fig. 4.4) were designed to maximize the coupling to the four antenna elements surrounding them. Fig. 4.6 (resp. Fig. 4.7) shows the EM simulated magnitude (resp. phase) of the couplings between the 16 antennas and one of the NF probes. The four radiating antennas nearest to the NF probe of interest are circled as group A in both figures. As shown in Fig. 4.6, for the elements in group A, the magnitudes of the coupling coefficients are almost flat versus frequency. With respect to the phases shown in Fig. 4.7, these vary linearly with frequency and have average variation in group delay across the band equal to 32 ps. Together, the flat magnitude and linear phase versus frequency of the coupling coefficients confirm the validity of the assumption of a flat NF channel and the rationale for why it can be modeled with a single complex channel coefficient, $\beta_{i,j}$.

All measurements were performed using 400 MHz OFDM signals conforming to 3GPP 5G NR downlink specifications, with sub-carriers modulated using 256-QAM, sub-carrier spacing of 120 kHz, $K_{\mathrm{D}} = 3168$ total data sub-carriers, fast Fourier transform size of $K_{\mathrm{FFT}} = 4096$, and characterized by a PAPR (after crest factor reduction using clipping and filtering) of 9.5 dB. For the DPD function, the nonlinearity order, nonlinear memory depth, linear memory depth, and memory step pruning parameter were set to 9, 3, 3, and

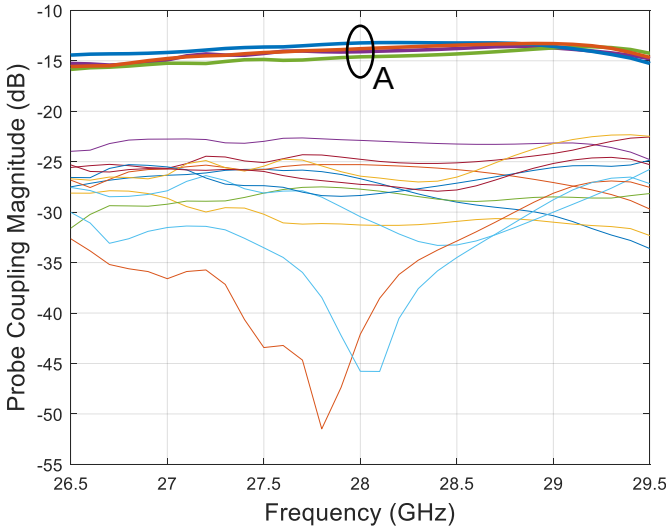


Figure 4.6: EM simulated magnitude of the coupling between the 16 radiating antenna elements and one NF probe versus frequency. The four radiating antennas nearest to the NF probe of interest are circled as group A.

4 respectively, resulting in a total of 37 coefficients. The number of iterations used to train the DPD function was fixed to 10, and 1.5×10^4 samples were used per iteration.

In order to ensure acceptable signal accuracy at the array's input, the setup was calibrated using a wideband multi-tone signal with 1 MHz tone spacing. Moreover, the array was calibrated for phase and magnitude imbalance using the FF reference antenna following the procedure described in [134].

The TRP-ACPR measurements reported in this work are computed using the signal received by a FF reference antenna while the array under test is set to radiate in the boresight and mechanically steered to vary the observation angles. Due to limitation in the experimental setup, the azimuth observation angle, ϕ, was kept to 0° while sweeping the elevation observation angle, θ, from $-48°$ to 48° with a step size of 2°.

Measurement Results and Analysis

Prior to linearizing the array using the proposed NF-TOR trained DPD, the NF channel coefficients, $\beta_{m,i}$, were identified for all four NF probes. To that end, the array was first operated in backoff, to ensure linear PA outputs. The NF channel coefficients were then

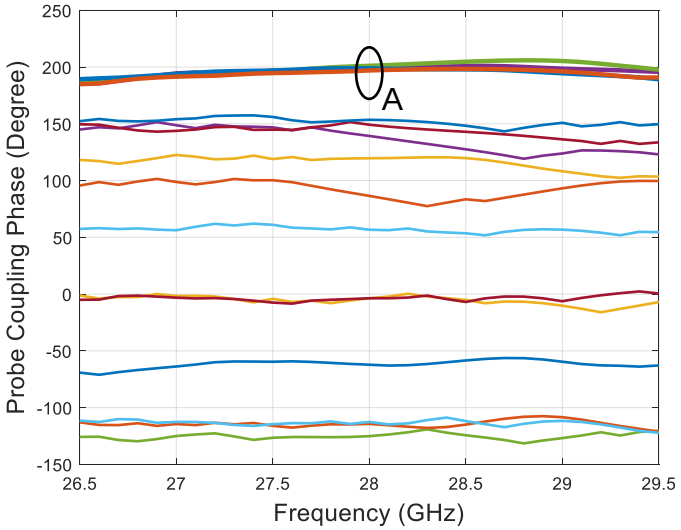


Figure 4.7: EM simulated phase of the coupling between the 16 radiating antenna elements and one NF probe versus frequency. The four radiating antennas nearest to the NF probe of interest are circled as group A.

identified using the NF received signals at the NF probes captured at 16 randomly generated steering angles. The channel coefficients were then estimated using the least squares fit of (4.39).

Fig. 4.8 shows the measured UE-ACPR and EVM of the received signal in the FF for different EIRP values: (a) prior to DPD, (b) after DPD training using FF-TOR, and (c) after DPD training using proposed NF-TOR. Note, the results corresponding to the FF-TOR based DPD are obtained using a DPD trained with a reference FF receiver located at array boresight along the main beam maximum radiation direction. Four randomly generated steering angles were used to collect the required NF signals needed to train the proposed DPD presented in Fig. 4.8 (c). The DPD functions were retrained for each backoff value and corresponding EIRP. In total, 12 backoff values were used with a step of 1 dB. From Fig. 4.8, it is evident that the NF-TOR trained DPD was able to linearize the array and achieve similar results to those obtained using an FF-TOR trained DPD. For both approaches, the EIRP improved by 5 dB (from 28.3 to 33.3 dBm) while maintaining an EVM less than 3.5%.

Fig. 4.9 shows the PSD of the received signal in the FF for an EIRP of 32.5 dBm: (a) prior to DPD, (b) after DPD trained using FF-TOR; and (c) after DPD trained using proposed NF-TOR. From Fig. 4.9 it is clear that the NF-TOR trained DPD achieves similar

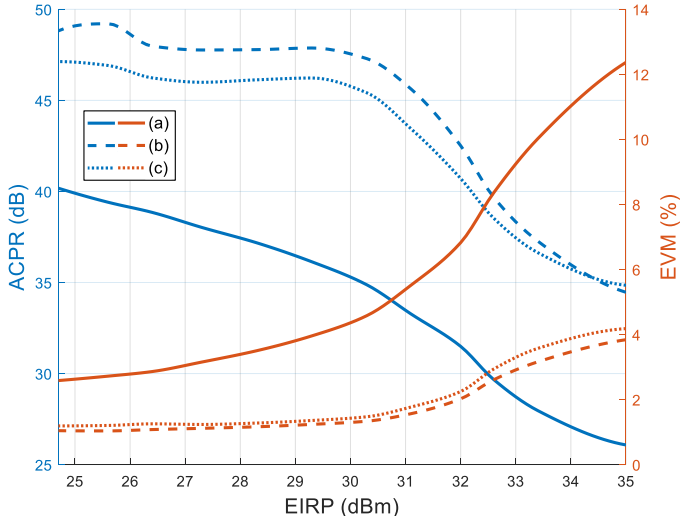


Figure 4.8: Measured UE-ACPR (left axis) and EVM (right axis) at the FF reference antenna versus EIRP values: (a) before DPD; (b) after DPD trained using FF-TOR; (c) after DPD trained using proposed NF-TOR.

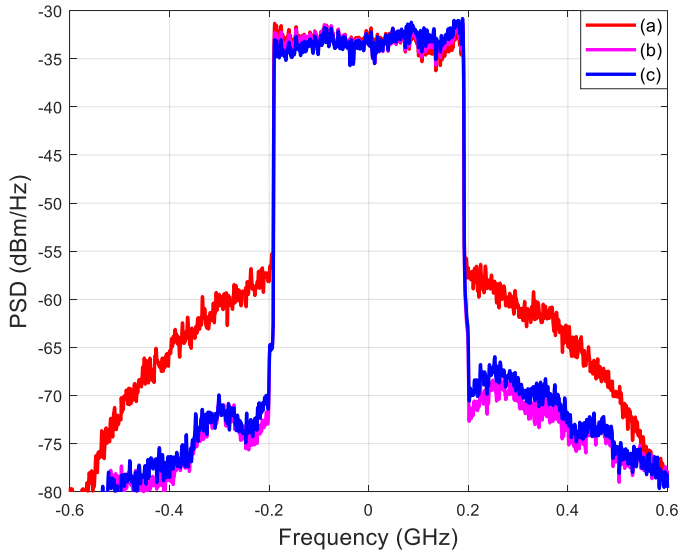


Figure 4.9: Spectrum results captured at the FF reference antenna: (a) before DPD; (b) after DPD trained using FF-TOR; (c) after DPD trained using proposed NF-TOR.

results to the FF-TOR trained DPD. The UE-ACPR and EVM improved from −29.66 dB and 8.29% before DPD to −41.03 dB and 2.12% in (b), and −40.49 dB and 2.40% in (c)

Table 4.1: Comparison of Recent Digital Predistortion Schemes at Millimeter-Wave

	# Elements	DUT	Fc (GHz)/ BW (MHz)	w/o DPD EVM (%)	w/ DPD EVM (%)	w/o DPD UE-ACPR (dB)	w/ DPD UE-ACPR (dB)	w/o DPD TRP-ACPR (dB)	w/ DPD TRP-ACPR (dB)
This Work (c)	**4×4**	**AWMF-0162**	**28 / 400**	**8.29**	**2.40**	**−29.88/−29.40**	**−42.12/−37.87**	**−29.75/−29.47**	**−41.01/−37.57**
This Work (b)	4×4	AWMF-0162	28 / 400	8.29	2.12	−29.88/−29.40	−42.33/−39.18	−29.75/−29.47	−41.11/−38.76
[160]	4×4	AWMF-0158	28 / 10	6.21	3.96	−37	−43	-	-
[80]	8×8	AWMF-0129	28 / 400	11.7	5.9	-	-	−25.5	−35.9
[161]	8×8	AWMF-0129	28 / 200	11.2	5.5	-	-	−25	−36
[83]	1×4	-	27 / 20	4.7	0.87	−37.1/−36.5	−51.7/−50.2	-	-

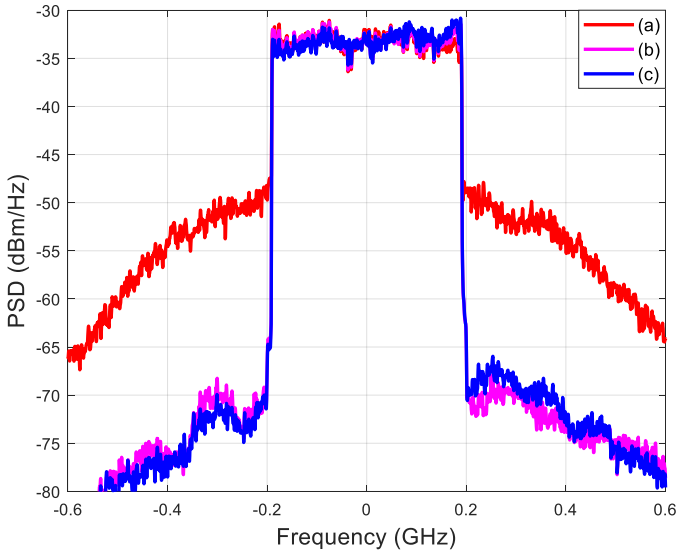


Figure 4.10: Spectrum results after applying DPD trained using proposed NF-TOR: (a) measured at NF probe 1; (b) estimated FF received signal; (c) measured FF received signal.

respectively. The TRP-ACPR also improved from −29.61 dB before DPD to −40.09 dB in (b), and −39.62 dB in (c).

Fig. 4.10 shows the PSD, after applying DPD trained using the proposed NF-TOR, of (a) the signal acquired at the first NF probe when the array is steered to broadside, (b) the FF signal estimate in the intended UE direction, and (c) the signal acquired at the FF reference antenna. Fig. 4.10 further support the results reported in [88], that training the DPD using the NF received signal, without applying the proposed data processing, will not result in a linear output at the FF reference antenna.

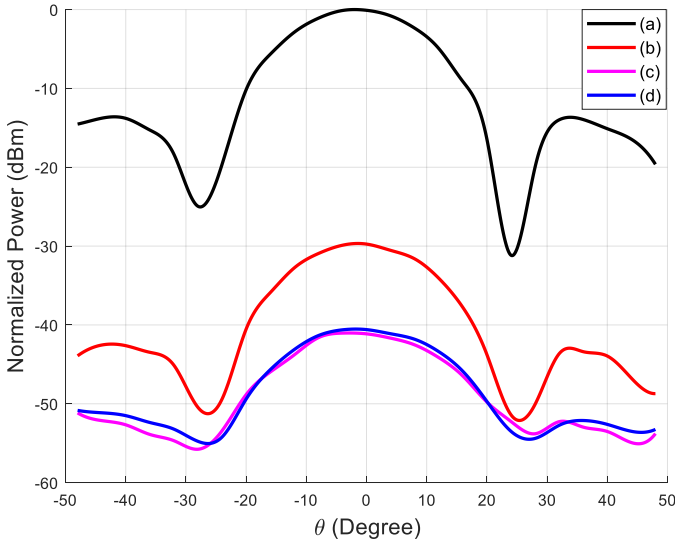


Figure 4.11: Measured radiation pattern versus steering angle at FF reference antenna positioned at boresight: (a) in-band power; (b) out-of-band power before DPD; (c) out-of-band power after DPD trained using FF-TOR; (d) out-of-band power after DPD trained using proposed NF-TOR.

Fig. 4.11 shows the measured radiation pattern of the (a) in-band power, (b) out-of-band power before DPD, (c) out-of-band power after DPD trained using FF-TOR, and (d) out-of-band power after DPD trained using proposed NF-TOR. The radiation pattern is obtained by mechanically steering the array between $\theta = -48°$ and $\theta = 48°$ while maintaining the beam at the array broadside. It is evident from Fig. 4.11 that the DPD in both (c) and (d) helped reduce the out-of-band emissions in the main beam and side lobes to the same extent.

The same SISO-DPD functions shown in Fig. 4.9 (b) and (c), and in Fig. 4.11 (c) and (d), are applied while the array is mechanically steered between $\theta = -48°$ and $\theta = 48°$. Electrical beam steering is applied to maintain alignment of the FF reference antenna with the direction of maximum radiation of the beam. The UE-ACPR and EVM are shown versus the steering angle in Fig. 4.12. From these plots, it is evident that the NF-TOR trained DPD in (c) achieves similar results to the FF-TOR trained DPD shown in (b). The variation in UE-ACPR and EVM versus steering angle is a result of the load modulation exhibited by the array due to the finite isolation between the antenna elements.

Table 4.1 compares the linearization performance of the proposed NF-TOR based DPD training approach to other works reported in the literature that use different DPD TOR

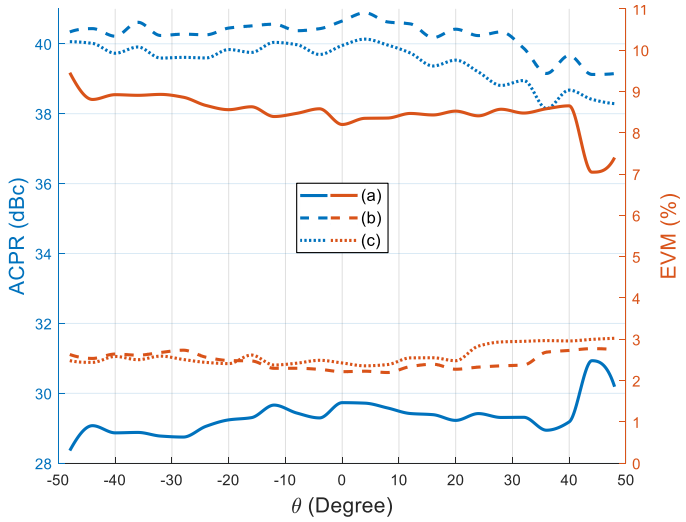


Figure 4.12: Measured UE-ACPR (left axis) and EVM (right axis) versus steering angle with beam electrically steered to maximize received power at FF reference antenna positioned at broadside: (a) before DPD; (b) after DPD trained using FF-TOR; (c) after DPD trained using proposed NF-TOR.

implementations, operating at a similar carrier frequency. The work in [80, 160] and [161] used a FF probing antenna in the main beam direction, while [83] used a FF probe located at a fixed location. The proposed work, on the other hand, uses NF-based TORs. Both [83] and the proposed NF-TOR based DPD training method require multiple measurements to train the DPD function.

4.2 Active Array Calibration and Linearization Using Near-Field Based Transmitter Observation Receiver and Assuming Frequency Selective Coupling

In the previous section, two assumptions were made. First is that the array is calibrated apriori and second is that the coupling between the NF probes and the antenna elements is flat versus frequency and has constant group delay. In this section, an NF-based array calibration and linearization that does not assume a flat coupling between the NF probes

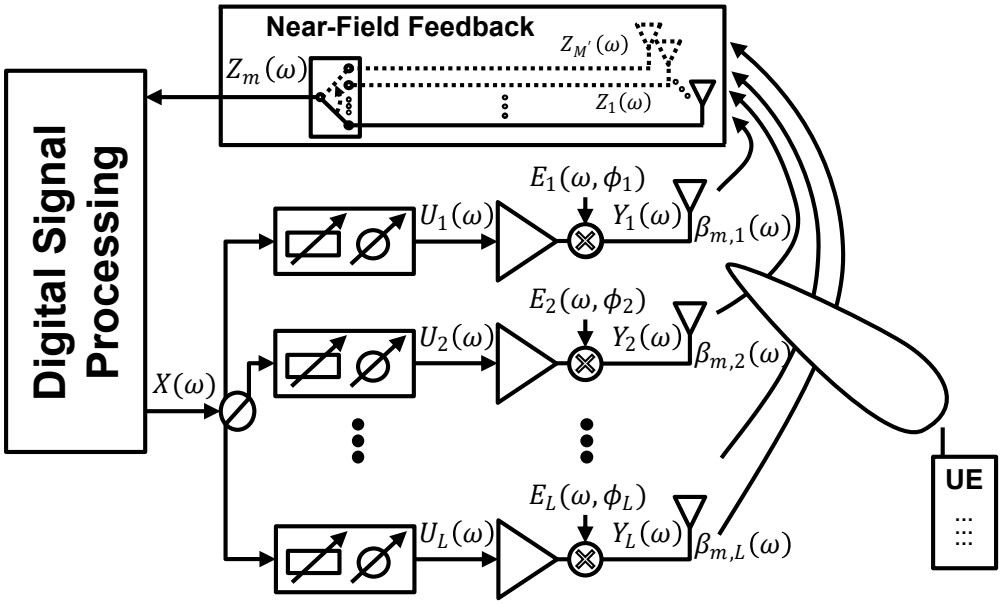


Figure 4.13: Block diagram of RF beamforming array with embedded NF probes for array calibration and DPD training.

and the beamformer antenna elements proposed in **Publication IV** are presented. Furthermore, the proposed active calibration is formulated to allow for phase-dependent error calibration as well as array linearization without resorting to element-wise calibration or FF probing. The performance of the proposed calibration and DPD training method is validated experimentally on a custom-built RF beamforming array with 16 antenna elements and four embedded NF probes. Note, for simplicity, in the following, the formulation assumes that the array is driven with a periodic input signal.

4.2.1 Problem Formulation

Fig. 4.13 shows a block diagram of an RF beamforming array with embedded NF probes. The subscript $\ell \in \{1, ..., L\}$ is used to refer to the ℓ'th RF chain in the array where L is the total number of antenna elements, while the subscript $m \in \{1, ..., M\}$ is used to refer to the m'th NF probe where M is the total number of NF probes. For simplicity, the derivation is conducted directly in the frequency domain. Let ϕ_ℓ be the beamforming phase of the ℓ'th RF chain, and let $X(\omega)$ be the array input signal where ω is the angular frequency. Assuming that the PAs are operated in their linear region (backoff), the ℓ'th PA output is

then given by,

$$Y_\ell(\omega) = GX(\omega)E_\ell(\omega, \phi_\ell)e^{j\phi_\ell}, \tag{4.43}$$

where G is the designed PA gain and $E_\ell(\omega, \phi_\ell)$ is a beamforming-phase (ϕ_ℓ) and frequency (ω) dependent complex multiplicative error corresponding to the ℓ'th RF chain in the array. Note, the error, $E_\ell(\omega, \phi_\ell)$, is assumed to be periodic in the phase ϕ_ℓ such that,

$$E_\ell(\omega, \phi_\ell) \approx E_\ell(\omega, \phi_\ell + \pi). \tag{4.44}$$

This assumption has been validated on several commercially available beamforming ICs that employ active or passive phase shifters.

The received signal by the m'th NF probe, $Z_m(\omega)$, is then given by,

$$Z_m(\omega) = \sum_{\ell=1}^{L} \beta_{m,\ell}(\omega)GX(\omega)E_\ell(\omega, \phi_\ell)e^{j\phi_\ell}, \tag{4.45}$$

where $\beta_{m,\ell}(\omega)$ is the coupling coefficient between the ℓ'th antenna element and the m'th NF probe. Rewriting (4.45) in matrix form we have,

$$Z_m(\omega) = GX(\omega)\mathbf{\Phi}\mathbf{B}_m(\omega)\mathbf{E}(\omega, \boldsymbol{\phi}), \tag{4.46}$$

where $\mathbf{\Phi}$ is the L-length row vector $\mathbf{\Phi} = [e^{j\phi_1}, \ldots, e^{j\phi_L}]$, $\mathbf{B}_m(\omega)$ is an $L \times L$ diagonal matrix with ℓ'th column and ℓ'th row entry equal to $\beta_{m,\ell}(\omega)$, and $\mathbf{E}(\omega, \boldsymbol{\phi}) = [E_1(\omega, \phi_1), ..., E_L(\omega, \phi_L)]^T$ is the error column vector.

Assuming prior knowledge of the NF coupling coefficients $\beta_{m,i}(\omega)$ (obtained, e.g., from EM simulation of the array or following the procedure described in [134]), and using a series of L/M measurements with custom phase settings applied to each chain in each measurement, the phase-dependent errors $E_\ell(\omega, \phi_\ell)$ for $\ell = 1, \ldots 1$ can be estimated. Note, these custom-selected phases need to be chosen such that the phase-dependent error, $E_\ell(\omega, \phi_\ell)$ for the ℓ'th chain, remains constant across the different measurements. To that end, the phase settings used during calibration are selected as either ϕ or $\phi + \pi$ since by (4.44) these have the same error $E(\omega, \phi)$. The choice between these two settings varies between the L/M measurements and is determined by the Walsh-Hadamard matrix, $\mathbf{H}_n$, where,

$$\mathbf{H}_n = \begin{bmatrix} \mathbf{H}_{\frac{n}{2}} & \mathbf{H}_{\frac{n}{2}} \\ \mathbf{H}_{\frac{n}{2}} & -\mathbf{H}_{\frac{n}{2}} \end{bmatrix}, \tag{4.47}$$

$\mathbf{H}_1 = 1$ and n is a power of 2. Specifically, assuming L and $M < L$ are powers of 2, then so is L/M and let $\mathbf{H}$ be the $L/M \times L$ matrix $\mathbf{H} = [\mathbf{H}_{L/M}\ \mathbf{H}_{L/M}\ \cdots\ \mathbf{H}_{L/M}]$ obtained by concatenating the Walsh-Hadamard matrix $\mathbf{H}_{L/M}$ M times. Then, the phase setting applied to the ℓ'th RF chain during the i'th measurement is determined by the entry in the i'th row and ℓ'th column of $\mathbf{H}$. If the entry is a 1, then the phase setting is $e^{j\phi}$, otherwise, the entry is -1, and the phase setting is $e^{j(\phi+\pi)} = -e^{j\phi}$. Hence, the applied phase to the ℓ'th antenna elements at the i'th measurement is given by the entry in the i'th row and ℓ'th column of $e^{j\phi}\mathbf{H}$. Consequently, if the signals received from the M NF probes are denoted as $\mathbf{Z}_m(\omega) = [Z_{m,1}(\omega), ..., Z_{m,L/M}(\omega)]^T$ where $Z_{m,i}(\omega)$ is the NF received signal at the m'th NF probe during the i'th measurement, then

$$\begin{bmatrix} \mathbf{Z}_1(\omega) \\ \vdots \\ \mathbf{Z}_M(\omega) \end{bmatrix} = GX(\omega)e^{j\phi} \begin{bmatrix} \mathbf{HB}_1(\omega) \\ \vdots \\ \mathbf{HB}_M(\omega) \end{bmatrix} \begin{bmatrix} E_1(\omega, \phi) \\ \vdots \\ E_L(\omega, \phi) \end{bmatrix}. \tag{4.48}$$

Finally, the error terms, $E_\ell(\omega, \phi)$, in (4.48) can be estimated using least-squares fit. These are then used to calibrate the array or potentially detect faulty antenna elements. With the array now calibrated and operated in its nonlinear region, the ℓ'th PA output can now be modeled as,

$$Y_\ell(\omega) = GV_\ell(\omega)e^{j\phi_\ell}, \tag{4.49}$$

where $V_\ell(\omega) = X(\omega) + N_\ell(\omega)$, and $N_\ell(\omega)$ is the ℓ'th PA nonlinear additive error. Consequently, the received signal at the m'th NF probe can be expressed as

$$Z_m(\omega) = G\mathbf{\Phi}\mathbf{B}_m(\omega)\mathbf{V}(\omega), \tag{4.50}$$

where $\mathbf{V}(\omega) = [V_1(\omega), ..., V_L(\omega)]^T$. If now a series of L/M measurements (with phase settings derived from the matrix $\mathbf{H}$) is used with $\phi = 0$, then the received signals may be expressed as

$$\begin{bmatrix} \mathbf{Z}_1(\omega) \\ \vdots \\ \mathbf{Z}_M(\omega) \end{bmatrix} = G \begin{bmatrix} \mathbf{HB}_1(\omega) \\ \vdots \\ \mathbf{HB}_M(\omega) \end{bmatrix} \mathbf{V}(\omega). \tag{4.51}$$

The PA nonlinear outputs, $\mathbf{V}(\omega)$, in (4.51) can then be estimated using least-squares fit. These are then summed and used to train the DPD function.

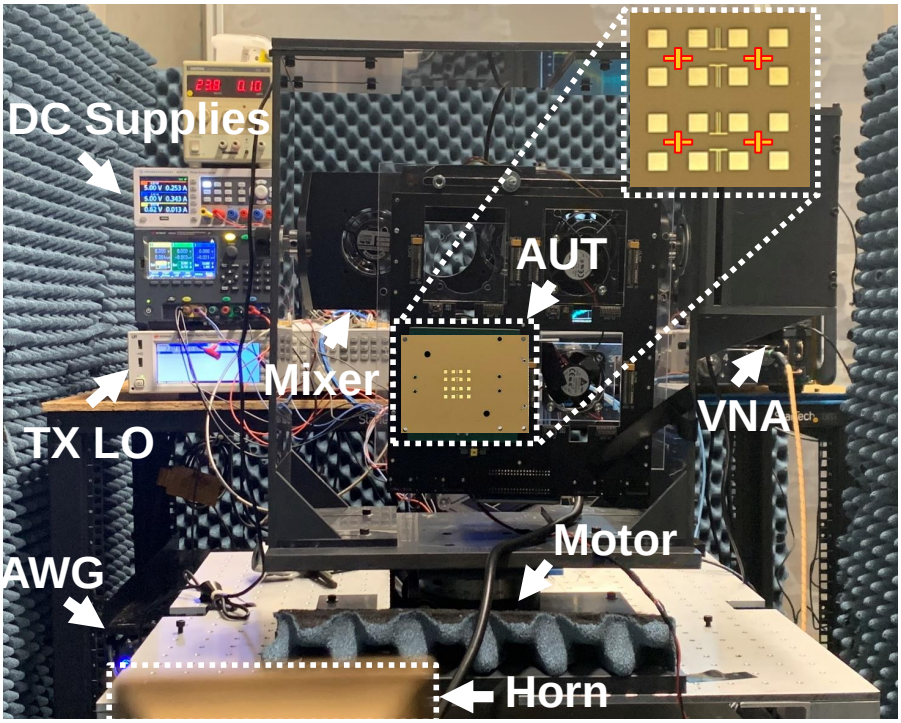


Figure 4.14: OTA test setup for experimental validation.

4.2.2 Experimental Validation

In this subsection, the performance of the proposed calibration and DPD training method is validated experimentally. Fig. 4.14 shows a picture of the measurement setup. The vector-modulated test signal used in the experiment was generated using a 12-bit, 12 Gsps AWG (M8190A from Keysight Technologies), with output centered at an IF of 2 GHz. An IQ-mixer (ADMV-1013) was used to up-convert the IF signal to a center frequency of 37.5 GHz. The signal was then amplified using a driver amplifier followed by a directional coupler and fed to the array under test (AUT). The AUT was mounted on a servo motor. A horn antenna was used to capture the FF signal. The RF output of the coupler (i.e., coupled port), the horn antenna, and the NF probes were sampled directly by a VNA. A LO source (MXG-N5183B from Keysight Technologies) was used to drive the up-conversion board used in the setup. Note, the array calibration was performed with the AUT input connected to the VNA.

The AUT used in the experiment is a 16-element array with four embedded NF probes.

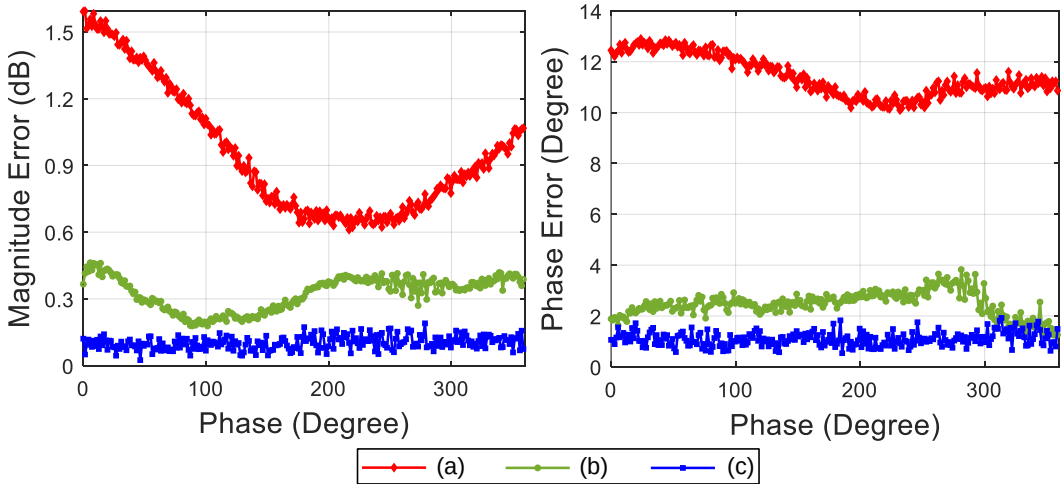


Figure 4.15: Measured RMS magnitude (Left) and phase (right) errors versus phase shifter settings (8-bits): (a) before calibration, (b) after proposed calibration using NF probes, and (c) after element-wise calibration using a FF probe.

The array was fabricated using a 13-layer printed circuit board with the NF probes located on layer 2 [162] and uses four beamforming ICs (MMW9003KC from NXP) assembled on layer 13. The inset in Fig. 4.14 shows a picture of the AUT with the location of the NF-probes highlighted in red. The modulated measurements were performed using a 400 MHz OFDM signal conforming to 3GPP 5G NR downlink specifications, with sub-carriers modulated using 256-QAM, sub-carrier spacing of 120 kHz, and characterized by a PAPR of 9 dB. For the DPD function, the nonlinearity order, nonlinear memory depth, linear memory depth, and memory step pruning parameters were set to 9, 2, 2, and 1 respectively, resulting in a total of 35 coefficients.

Fig. 4.15 shows the measured root-mean-square (RMS) error in magnitude (Left) and phase (Right) when the phase states are varied between 0° and 360° in steps of 1.4°: (a) before calibration, (b) after the proposed calibration using NF probes, and (c) after element-wise calibration using a FF probe. Note, the RMS errors in Fig. 4.15 are measured element-wise using an FF probe. Using the proposed array calibration method, the RMS error in magnitude and phase reduced by up to 1.3 dB and 10.3°, respectively, compared to before calibration. Using element-wise calibration in Fig. 4.15 (c), the magnitude and phase RMS errors are further decreased by at best 0.4 dB and 2.4°, respectively. Fig. 4.16 shows the measured array radiation pattern at the FF when the array is excited by a 400 MHz modulated signal and the beam is electrically steered from −90° to 90°: (a)

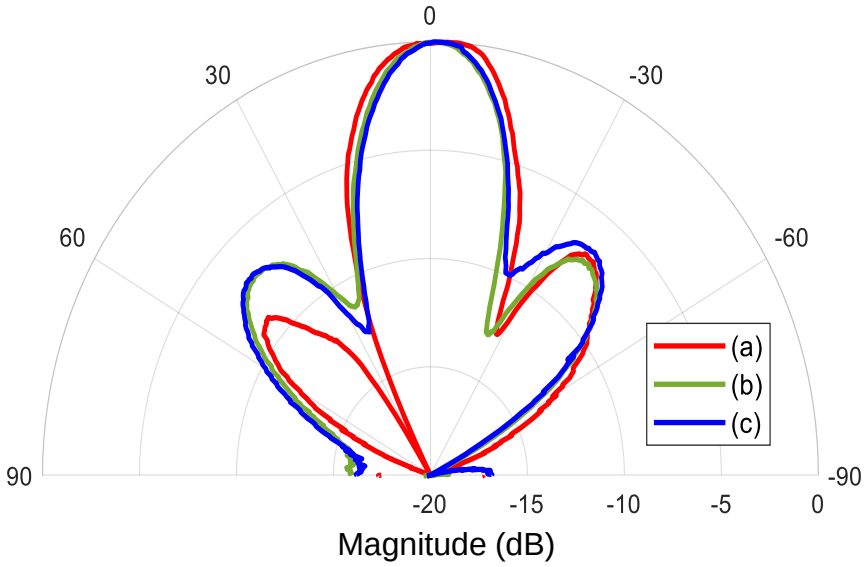


Figure 4.16: Measured radiation pattern with the array driven with a 400 MHz OFDM signal and the beam electrically steered from −90° to 90°: (a) before calibration, (b) after proposed calibration using NF probes, and (c) after element-wise calibration using a FF probe.

before calibration, (b) after proposed calibration using NF probes, and (c) after element-wise FF calibration. Using the proposed method in Fig. 4.16 (b), the imbalance in the radiation pattern sidelobes was reduced by up to 2 dB. These results are comparable to those obtained using element-wise calibration in Fig. 4.16 (c).

Fig. 4.17 and Fig. 4.18 show the UE-ACPR and EVM results at the FF probe versus the EIRP: (a) prior to DPD, (b) after DPD trained at the FF in the main beam direction, and (c) after NF-based DPD. In Fig. 4.17 the coupling between the NF probes and the antenna elements is assumed to be flat versus frequency and uses the NF-based DPD presented in the previous section. In Fig. 4.18 the NF-based DPD uses the formulation in this section with no assumption of the coupling frequency response. From Fig. 4.17 and Fig. 4.18, it is evident that the proposed DPD trained using the NF probes in Fig. 4.18 (c) using the formulation presented in this section achieves better linearization performance that when the coupling to NF probes are used to be flat versus frequency. Furthermore, from Fig. 4.18 it is clear that the proposed DPD trained using the NF probes achieves similar results to the DPD trained at the FF (b). For instance, when the EIRP is set to 34 dBm, the UE-ACPR and EVM improved from 27 dB and 8.3% before DPD, to 34.2 dB and

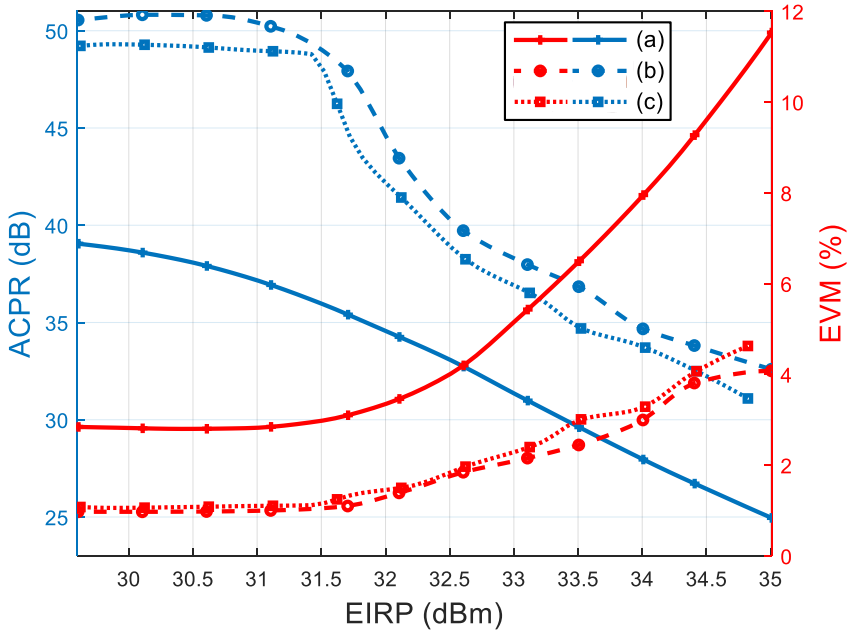


Figure 4.17: Measured UE-ACPR and EVM at the FF probe versus EIRP when the array is fed with a 400 MHz OFDM signal: (a) prior to DPD, (b) after DPD trained at the FF in the main beam direction, and (c) after DPD rained using NF assuming flat coupling.

3.1% in Fig. 4.18 (b), and 33.6 dB and 3% in Fig. 4.18 (c), respectively. Note, using DPD trained with the NF probes as feedback, the EIRP increased by 2.3 dB from 32.11 dBm to 33.4 dBm while meeting the 3GPP EVM and UE-ACPR standard of 3.5% and 26 dB requirements.

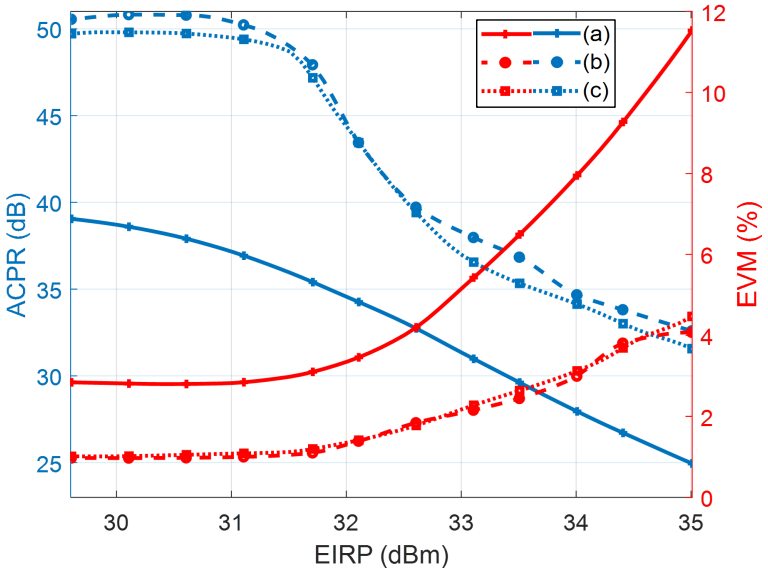


Figure 4.18: Measured UE-ACPR and EVM at the FF probe versus EIRP when the array is fed with a 400 MHz OFDM signal: (a) prior to DPD, (b) after DPD trained at the FF in the main beam direction, and (c) after proposed DPD trained using NF probes.

Chapter 5

Linearization of Frequency Multiplier Based Transmitters Driven with Wideband Vector Modulated Signals

This chapter discusses the contributions from [**Publications V, VI, VII**]. It begins with a DPD formulation aimed at linearizing FXs under limited transmitter and TOR bandwidths [**Publications V**]. Experimental validations demonstrate improved linearization performance under these constraints. Subsequently, a novel DPD formulation is introduced to mitigate deviations of multipliers from an ideal power function, showcasing resilience to calibration inaccuracies in the transmitter chain leading up to the FX and suitability for linearizing high-order multiplication FXs [**Publications VI**]. Experimental results exhibit significant improvements in linearization performance compared to state-of-the-art techniques, validated across various multiplication orders and output frequencies ranging from 14 GHz to 62 GHz. Finally, a measurement system for high-frequency component/system characterization is presented, leveraging VNAs frequency extenders for modulated signal testing [**Publications VI**]. An ILC algorithm is proposed to linearize FXs within these frequency extenders, with experimental validation conducted using an OML VNA frequency extender operating at 58 GHz and a D-band custom-build frequency doubler operating at 120 GHz.

5.1 Linearization of Frequency Multipliers under Constrained Transmitter and Observation Receiver Bandwidths

In this section, we propose a novel DPD scheme for linearizing FX-based transmitters driven by vector-modulated signals, while working within the constraints of limited transmitter and TOR bandwidths. The proposed formulation reduces the DAC and analog-to-digital-converter (ADC) sampling speeds required by conventional DPD schemes, maintaining excellent linearization performance. Specifically, the approach begins by formulating an additive error model for an FX driven by a Dth root function under bandwidth constraints. This model is then leveraged to derive the proposed DPD model expression and the underlying DPD training algorithm while reducing the required TOR bandwidth. Furthermore, this work delves into the selection of TOR bandwidth requirement and its interdependence with the Dth root function bandwidth constraint. Detailed theoretical analysis and extensive simulation experimental validations are presented.

5.1.1 Problem Formulation

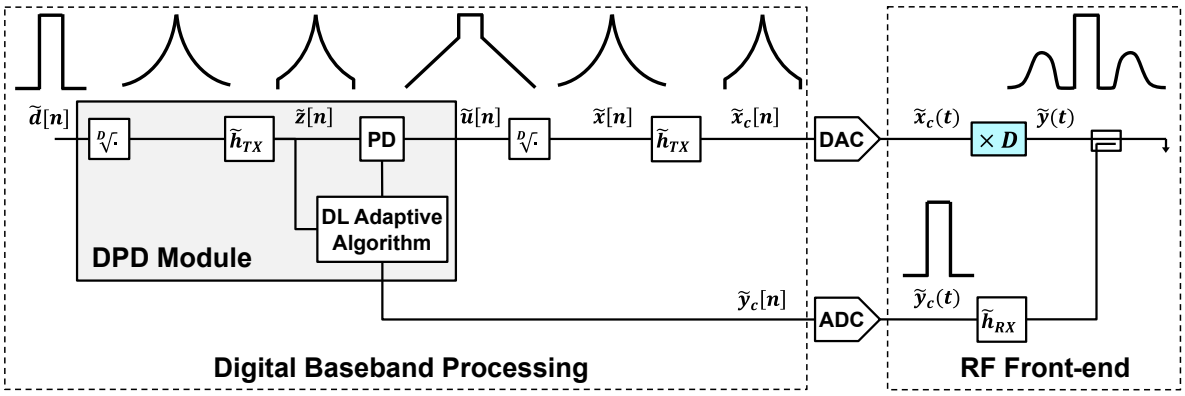


Figure 5.1: Block diagram of proposed direct learning DPD with constrained transmitter and observation bandwidths.

In this subsection, the expression of the proposed DPD scheme needed to linearize an FX with constrained transmitter and observation receiver bandwidths, as shown in Fig. 5.1, is derived. Let $\tilde{\mathbf{h}}_{\mathbf{TX}} = (\tilde{h}_{TX}[0], ..., \tilde{h}_{TX}[P])$ be the length $P+1$ impulse response of

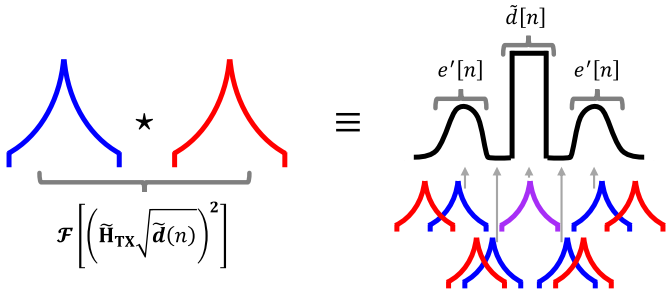


Figure 5.2: Illustration of the resulting error due to constraining the Dth root function bandwidth on the output of an ideal doubler.

the transmitter bandwidth limiting filter. The cascade of the Dth root function, $\tilde{h}_{TX}[n]$, and the non-ideal FX represents the nonlinear system to be linearized by the predistorter block DPD. In the following, the expression of the DPD function needed to linearize the aforementioned cascade will be developed.

Let $\tilde{u}[n]$ be the output of the predistortion (PD) function, $\tilde{x}[n]$ be the output of the Dth root function, $\tilde{x}_c[n]$ be the output of the transmitter bandwidth limiting filter, $\tilde{h}_{TX}[n]$, and $\tilde{y}[n]$ be the output of the multiplier. The bandwidth constrained input signal to the multiplier, $\tilde{x}_c[n]$, can hence be expressed as follows,

$$\tilde{x}_c[n] = \sum_{m=0}^{P} \tilde{x}[n-m]\tilde{h}_{TX}[m], \tag{5.1}$$

where $\tilde{x}[n] = \sqrt[D]{\tilde{u}[n]}$. Alternatively, using a block of $N+1$ samples, (5.1) can be expressed in matrix form as,

$$\tilde{x}_c[n] = \tilde{\mathbf{H}}^0_{\mathbf{TX}}\tilde{\mathbf{x}}(n) \tag{5.2}$$

$$= \tilde{\mathbf{H}}^0_{\mathbf{TX}}\sqrt[D]{\tilde{\mathbf{u}}(n)}, \tag{5.3}$$

where $\tilde{\mathbf{x}}(n) = (\tilde{x}[n], ..., \tilde{x}[n-N])^T$, $\tilde{\mathbf{H}}^i_{\mathbf{TX}}$ is a row vector defined as,

$$\tilde{\mathbf{H}}^i_{\mathbf{TX}} = \begin{cases} (\mathbf{0}_i, \tilde{\mathbf{h}}_{\mathbf{TX}}, \mathbf{0}_{N-P-i}) & 0 \le i \le N-P \\ (\mathbf{0}_i, \tilde{\mathbf{h}}_{\mathbf{TX}}(0:N-i)) & N-P < i \le N \end{cases} \tag{5.4}$$

$\sqrt[D]{\tilde{\mathbf{u}}(n)} = (\sqrt[D]{\tilde{u}[n]}, ..., \sqrt[D]{\tilde{u}[n-N]})^T$, and $\mathbf{0}_i$ is a $1 \times i$ zero vector.

Using the additive error model adopted in [7], the FX output $\tilde{y}[n]$ can be expressed as follows,

$$\tilde{y}[n] = \tilde{x}_c^D[n] + \tilde{e}(\tilde{\mathbf{x}}_\mathbf{c}(n)), \tag{5.5}$$

where the nonlinear error term, $\tilde{e}(\tilde{\mathbf{x}}_\mathbf{c}(n))$, takes the form of the FX forward model expressed in [7, eqn. (7)], and given by,

$$\tilde{e}(\tilde{\mathbf{x}}_\mathbf{c}(n)) = \tag{5.6}$$

$$\sum_{p=0}^{N_L} \sum_{\substack{(p_1,p_2)\in\mathcal{P}(p) \\ \mathbf{m}\in\mathcal{B}^{p_1},\hat{\mathbf{m}}\in\mathcal{B}^{p_2}}} \gamma_{\mathbf{m},\hat{\mathbf{m}}}^{p_1,p_2,\ell} \prod_{i=1}^{p_1} \tilde{x}_c[n-m_i] \prod_{j=1}^{p_2} \tilde{x}_c^*[n-\hat{m}_j], \tag{5.7}$$

where

$$\mathcal{P}(p) = \Big\{(p_1,p_2)\in\mathbb{Z}^2 \Big| p_1 \geq 0, p_2 \geq 0, \\ p_1+p_2 = p, p_1-p_2 = D\Big\}, \tag{5.8}$$

is the set of tuples (p_1, p_2) that results in a nonlinearity order of p, the set $\mathcal{B} = \{0, 1, 2, \ldots, M\}$, M is the maximum memory depth, N_L is the maximum nonlinearity order and $\gamma_{\mathbf{m},\hat{\mathbf{m}}}^{p_1,p_2,\ell}$ are the model coefficients.

Substituting (5.3) in (5.5) and assuming $\tilde{u}[n] = 0$ for $\ell < n - N$, the FX output $\tilde{y}[n]$ can be expressed as a function of the PD output, $\tilde{u}[n]$, as,

$$\tilde{y}[n] = \big(\tilde{\mathbf{H}}_{\mathbf{TX}}^0 \sqrt[D]{\tilde{\mathbf{u}}(n)}\big)^D + \tilde{e}\big(\tilde{\mathbf{H}}_{\mathbf{TX}}\sqrt[D]{\tilde{\mathbf{u}}(n)}\big), \tag{5.9}$$

where,

$$\tilde{\mathbf{H}}_{\mathbf{TX}} = \begin{bmatrix} \tilde{\mathbf{H}}_{\mathbf{TX}}^0 \\ \tilde{\mathbf{H}}_{\mathbf{TX}}^1 \\ \vdots \\ \tilde{\mathbf{H}}_{\mathbf{TX}}^N \end{bmatrix}, \tag{5.10}$$

is an upper triangular matrix with nonzero diagonal elements. Alternatively, (5.9) can be rewritten as follows,

$$\tilde{y}[n] = \tilde{u}[n] + \tilde{e}\big(\tilde{\mathbf{H}}_{\mathbf{TX}}\sqrt[D]{\tilde{\mathbf{u}}(n)}\big) + \tilde{e}'\big(\tilde{\mathbf{H}}_{\mathbf{TX}}\sqrt[D]{\tilde{\mathbf{u}}(n)}\big), \tag{5.11}$$

where,

$$\tilde{e}'\left(\tilde{\mathbf{H}}_{\mathbf{TX}}\sqrt[D]{\tilde{\mathbf{u}}(n)}\right) = \left(\tilde{\mathbf{H}}^{0}_{\mathbf{TX}}\sqrt[D]{\tilde{\mathbf{u}}(n)}\right)^{D} - \tilde{u}[n], \tag{5.12}$$

is the error due to the constrained bandwidth Dth root function. Note, the error $\tilde{e}'\left(\tilde{\mathbf{H}}_{\mathbf{TX}}\sqrt[D]{\tilde{\mathbf{u}}(n)}\right)$ cannot be corrected for by the DPD function and is mainly dominant in the out-of-band away from the signal bandwidth as shown in Fig. 5.2. Let the sampled complex envelop of the FX output signal after receiver bandwidth limiting be, $\tilde{y}_c[n]$, where

$$\tilde{y}_c[n] = \sum_{m=0}^{P'} \tilde{y}[n-m]\tilde{h}_{RX}[m], \tag{5.13}$$

and $\tilde{\mathbf{h}}_{\mathbf{RX}} = (\tilde{h}_{RX}[0], ..., \tilde{h}_{RX}[P'])$ is the impulse response of the receiver filter at the FX output with length equal $P'+1$. The bandwidth of $\tilde{h}_{RX}[n]$, denoted as $\mathrm{BW_{RX}}$, is used to reduce the required sampling speed for the receiver ADC and is assumed to filter out the out-of-band distortions that result from limiting the Dth root function bandwidth. Discussions on the choice of $\mathrm{BW_{RX}}$ that satisfy the aforementioned assumption are presented in the simulation section. Alternatively, (5.13) can be expressed in matrix form as follows,

$$\tilde{y}_c[n] = \tilde{\mathbf{H}}^{0}_{\mathbf{RX}}\tilde{\mathbf{y}}(n), \tag{5.14}$$

where $\tilde{\mathbf{y}}(n) = (\tilde{y}[n], ..., \tilde{y}[n-N])^T$, and

$$\tilde{\mathbf{H}}^{i}_{\mathbf{RX}} = \begin{cases} (\mathbf{0}_i, \tilde{\mathbf{h}}_{\mathbf{RX}}, \mathbf{0}_{N-P'-i}) & 0 \le i \le N-P' \\ (\mathbf{0}_i, \tilde{\mathbf{h}}_{\mathbf{RX}}(0:N-i)) & N-P' < i \le N \end{cases} \tag{5.15}$$

Substituting (5.11) in (5.14), we have,

$$\tilde{y}_c[n] = \tilde{\mathbf{H}}^{0}_{\mathbf{RX}}\left(\tilde{\mathbf{u}}(n) + \tilde{\mathbf{e}}\left(\tilde{\mathbf{H}}_{\mathbf{TX}}\sqrt[D]{\tilde{\mathbf{u}}(n)}\right) + \tilde{\mathbf{e}}'\left(\tilde{\mathbf{H}}_{\mathbf{TX}}\sqrt[D]{\tilde{\mathbf{u}}(n)}\right)\right), \tag{5.16}$$

where,

$$\tilde{\mathbf{e}}\left(\tilde{\mathbf{H}}_{\mathbf{TX}}\sqrt[D]{\tilde{\mathbf{u}}(n)}\right) = \begin{bmatrix} \tilde{e}\left(\tilde{\mathbf{H}}_{\mathbf{TX}}\sqrt[D]{\tilde{\mathbf{u}}(n)}\right) \\ \tilde{e}\left(\tilde{\mathbf{H}}_{\mathbf{TX}}\sqrt[D]{\tilde{\mathbf{u}}(n-1)}\right) \\ \vdots \\ \tilde{e}\left(\tilde{\mathbf{H}}_{\mathbf{TX}}\sqrt[D]{\tilde{\mathbf{u}}(n-N)}\right) \end{bmatrix}, \tag{5.17}$$

and,

$$\tilde{\mathbf{e}}'\left(\tilde{\mathbf{H}}_{\mathbf{TX}}\sqrt[D]{\tilde{\mathbf{u}}(n)}\right) = \begin{bmatrix} \tilde{e}'\left(\tilde{\mathbf{H}}_{\mathbf{TX}}\sqrt[D]{\tilde{\mathbf{u}}(n)}\right) \\ \tilde{e}'\left(\tilde{\mathbf{H}}_{\mathbf{TX}}\sqrt[D]{\tilde{\mathbf{u}}(n-1)}\right) \\ \vdots \\ \tilde{e}'\left(\tilde{\mathbf{H}}_{\mathbf{TX}}\sqrt[D]{\tilde{\mathbf{u}}(n-N)}\right) \end{bmatrix}. \tag{5.18}$$

Assuming that the out-of-band error due to limiting the Dth root function bandwidth is filtered by the receive filter, $\tilde{h}_{RX}[n]$, and is negligible within the passband of $\tilde{h}_{RX}[n]$, i.e,

$$\tilde{\mathbf{H}}^0_{\mathbf{RX}}\tilde{\mathbf{e}}'\left(\tilde{\mathbf{H}}_{\mathbf{TX}}\sqrt[D]{\tilde{\mathbf{u}}(n)}\right) \approx 0, \tag{5.19}$$

the following approximation can be made,

$$\tilde{y}_c[n] \approx \tilde{u}_c[n] + \tilde{\mathbf{H}}^0_{\mathbf{RX}}\tilde{\mathbf{e}}\left(\tilde{\mathbf{H}}_{\mathbf{TX}}\sqrt[D]{\tilde{\mathbf{u}}(n)}\right). \tag{5.20}$$

where,

$$\tilde{u}_c[n] = \tilde{\mathbf{H}}^0_{\mathbf{RX}}\tilde{\mathbf{u}}(n). \tag{5.21}$$

Then, if the DPD compensates for theFX nonlinearity, $\tilde{y}_c[n]$ in (5.20) will be equal to the desired input signal, $\tilde{d}[n]$, convolved with the impulse response of the receiver filter, $\tilde{h}_{RX}[n]$, i.e.,

$$\tilde{y}_c[n] = \tilde{\mathbf{H}}^0_{\mathbf{RX}}\tilde{\mathbf{d}}(n). \tag{5.22}$$

Consequently, from (5.20), the constrained bandwidth predistorted signal, $\tilde{u}_c[n]$, can be expressed as a function of the desired and error signals as follows,

$$\tilde{u}_c[n] = \tilde{\mathbf{H}}^0_{\mathbf{RX}}\tilde{\mathbf{d}}(n) - \tilde{\mathbf{H}}^0_{\mathbf{RX}}\tilde{\mathbf{e}}\left(\tilde{\mathbf{H}}_{\mathbf{TX}}\sqrt[D]{\tilde{\mathbf{u}}(n)}\right). \tag{5.23}$$

Alternatively, (5.23) can be expressed in vector form as follows,

$$\tilde{\mathbf{u}}_{\mathbf{c}}(n) = \tilde{\mathbf{H}}_{\mathbf{RX}}\tilde{\mathbf{d}}(n) - \tilde{\mathbf{H}}_{\mathbf{RX}}\tilde{\mathbf{e}}\left(\tilde{\mathbf{H}}_{\mathbf{TX}}\sqrt[D]{\tilde{\mathbf{u}}(n)}\right). \tag{5.24}$$

where,

$$\tilde{\mathbf{H}}_{\mathbf{RX}} = \begin{bmatrix} \tilde{\mathbf{H}}^0_{\mathbf{RX}} \\ \tilde{\mathbf{H}}^1_{\mathbf{RX}} \\ \vdots \\ \tilde{\mathbf{H}}^N_{\mathbf{RX}} \end{bmatrix}. \tag{5.25}$$

is an upper triangular matrix with nonzero diagonal elements and thus invertible, i.e., $\tilde{\mathbf{H}}_{\mathbf{RX}}\tilde{\mathbf{H}}_{\mathbf{RX}}^{-1} = \mathbf{I}$. Using (5.21) and the fact that $\tilde{\mathbf{H}}_{\mathbf{RX}}$ is invertible we have,

$$\tilde{\mathbf{u}}(n) = \tilde{\mathbf{H}}_{\mathbf{RX}}^{-1}\tilde{\mathbf{u}}_{\mathbf{c}}(n) \tag{5.26}$$

$$= \tilde{\mathbf{d}}(n) - \tilde{\mathbf{e}}\left(\tilde{\mathbf{H}}_{\mathbf{TX}}\sqrt[D]{\tilde{\mathbf{u}}(n)}\right). \tag{5.27}$$

Substituting (5.27) in (5.23), we get,

$$\tilde{u}_c[n] = \tilde{\mathbf{H}}_{\mathbf{RX}}^{0}\tilde{\mathbf{d}}(n) - \tilde{\mathbf{H}}_{\mathbf{RX}}^{0}\tilde{\mathbf{e}}\left(\tilde{\mathbf{H}}_{\mathbf{TX}}\sqrt[D]{\tilde{\mathbf{d}}(n) - \tilde{\mathbf{e}}\left(\tilde{\mathbf{H}}_{\mathbf{TX}}\sqrt[D]{\tilde{\mathbf{u}}(n)}\right)}\right). \tag{5.28}$$

Assuming that the contribution of the "error of the error" in (5.28) is negligible, the following approximation can be made,

$$\tilde{\mathbf{e}}\left(\tilde{\mathbf{H}}_{\mathbf{TX}}\sqrt[D]{\tilde{\mathbf{d}}(n) - \tilde{\mathbf{e}}\left(\tilde{\mathbf{H}}_{\mathbf{TX}}\sqrt[D]{\tilde{\mathbf{u}}(n)}\right)}\right) \approx \tilde{\mathbf{e}}\left(\tilde{\mathbf{H}}_{\mathbf{TX}}\sqrt[D]{\tilde{\mathbf{d}}(n)}\right). \tag{5.29}$$

Hence, (5.28) can be rewritten such that

$$\tilde{u}_c[n] = \tilde{\mathbf{H}}_{\mathbf{RX}}^{0}\tilde{\mathbf{d}}(n) - \tilde{\mathbf{H}}_{\mathbf{RX}}^{0}\tilde{\mathbf{e}}\left(\tilde{\mathbf{H}}_{\mathbf{TX}}\sqrt[D]{\tilde{\mathbf{d}}(n)}\right). \tag{5.30}$$

Let $\mathcal{A}$ denote the set of all forward model basis functions in (5.7) and $\tilde{\psi}_1, \tilde{\psi}_2, \ldots, \tilde{\psi}_{|\mathcal{A}|}$ enumerate the basis functions in $\mathcal{A}$. Then the error term, $\tilde{e}\left(\tilde{\mathbf{H}}_{\mathbf{TX}}\sqrt[D]{\tilde{\mathbf{d}}(n)}\right)$, in (5.30) can be rewritten compactly as,

$$\tilde{e}(\tilde{\mathbf{z}}(n)) = \sum_{\ell=1}^{|\mathcal{A}|} w_\ell \tilde{\psi}_\ell\left(\tilde{\mathbf{z}}(n)\right), \tag{5.31}$$

where w_ℓ is the model coefficient corresponding to the ℓth model basis, $\tilde{\psi}_\ell$, $\tilde{\mathbf{z}}(n) = (\tilde{z}[n], \tilde{z}[n-1], ..., \tilde{z}[n-N])^T$, and $\tilde{z}[n] = \tilde{\mathbf{H}}_{\mathbf{TX}}^{0}\sqrt[D]{\tilde{\mathbf{d}}(n)}$. Alternatively, (5.31) can be expressed in matrix form as,

$$\tilde{\mathbf{e}}(\tilde{\mathbf{z}}(n)) = \tilde{\mathbf{\Psi}}_n \mathbf{w} \tag{5.32}$$

where, $\mathbf{w} = (w_0, ..., w_L)^T$, $\tilde{\mathbf{\Psi}}_n$ is the basis matrix with ith column and jth row entry given by $\tilde{\psi}_i\left(\tilde{\mathbf{z}}(n-j)\right)$, and,

$$\tilde{\mathbf{e}}(\tilde{\mathbf{z}}(n)) = \begin{bmatrix} \tilde{e}(\tilde{\mathbf{z}}(n)) \\ \tilde{e}(\tilde{\mathbf{z}}(n-1)) \\ \vdots \\ \tilde{e}(\tilde{\mathbf{z}}(n-N)) \end{bmatrix}. \tag{5.33}$$

Substituting (5.32) in (5.30), we have,

$$\tilde{u}_c[n] = \tilde{\mathbf{H}}^0_{\mathbf{RX}}\tilde{\mathbf{d}}(n) - \tilde{\mathbf{H}}^0_{\mathbf{RX}}\tilde{\mathbf{\Psi}}_n\mathbf{w}. \tag{5.34}$$

Finally, using (5.12) and the approximation in (5.19), i.e.,

$$\tilde{\mathbf{H}}^0_{\mathbf{RX}}\tilde{\mathbf{d}}(n) \approx \tilde{\mathbf{H}}^0_{\mathbf{RX}}\big(\tilde{\mathbf{H}}_{\mathbf{TX}}\sqrt[D]{\tilde{\mathbf{d}}(n)}\big)^D, \tag{5.35}$$

then (5.34) can be rewritten more compactly as,

$$\tilde{u}_c[n] = \tilde{\mathbf{H}}^0_{\mathbf{RX}}\tilde{\mathbf{\Psi}}_n\mathbf{a}, \tag{5.36}$$

where $\mathbf{a} = (1 - w_0, ..., -a_L)$ are the predistorter coefficients and without loss of generality, it is assumed that $\tilde{\psi}_1\left(\tilde{\mathbf{z}}(n)\right) = \left(\tilde{\mathbf{z}}(n)\right)^D$.

The objective of DPD is to minimize the error between the DPD input signal $\tilde{d}[n]$ and the multiplier output $\tilde{y}[n]$. For this, the error between the DPD input signal $\tilde{d}[n]$ convoluted with $\tilde{h}_{RX}[n]$ and the multiplier constrained output $\tilde{y}_c[n]$ is minimized:

$$J(\mathbf{a}) = \sum_{n=M+1}^{L}\Big(\tilde{y}_c[n] - \tilde{\mathbf{H}}^0_{\mathbf{RX}}\tilde{\mathbf{d}}(n)\Big)\Big(\tilde{y}_c[n] - \tilde{\mathbf{H}}^0_{\mathbf{RX}}\tilde{\mathbf{d}}(n)\Big)^H, \tag{5.37}$$

where L is the length of the training data, and $\mathbf{a}$ is the vector of DPD coefficients that are to be optimized to minimize the cost function J. Using (5.36), and the direct learning algorithm, the optimal choice of $\mathbf{a}$ is iteratively calculated and the coefficients are obtained by the update equation,

$$\hat{\mathbf{a}}_{k+1} = \hat{\mathbf{a}}_k - \mu\big(\tilde{\mathbf{H}}_{\mathbf{RX}}\tilde{\mathbf{\Psi}}_{n_k}\big)^{\dagger}\big(\tilde{\mathbf{y}}_{\mathbf{c}}(n_k) - \tilde{\mathbf{H}}_{\mathbf{RX}}\tilde{\mathbf{d}}(n_k)\big), \tag{5.38}$$

where $\hat{\mathbf{a}}_k$ are the estimated DPD coefficients at the k^{th} iteration, $\mu > 0$ is the update step size, and $(.)^{\dagger}$ is the pseudo inverse operator such that,

$$\big(\tilde{\mathbf{H}}_{\mathbf{RX}}\tilde{\mathbf{\Psi}}_{n_k}\big)^{\dagger} = \Big(\big(\tilde{\mathbf{H}}_{\mathbf{RX}}\tilde{\mathbf{\Psi}}_{n_k}\big)^H\big(\tilde{\mathbf{H}}_{\mathbf{RX}}\tilde{\mathbf{\Psi}}_{n_k}\big)\Big)^{-1}\big(\tilde{\mathbf{H}}_{\mathbf{RX}}\tilde{\mathbf{\Psi}}_{n_k}\big)^H. \tag{5.39}$$

The updated PD output signal, $\tilde{u}[n_{k+1}]$, at time index n and in the $k+1$ iteration is then given as follows,

$$\tilde{u}[n_{k+1}] = \tilde{\mathbf{\Psi}}_{n_{k+1}}\mathbf{a}_{k+1}. \tag{5.40}$$

Hence, together (5.36), (5.39), and (5.40) comprise the iterative training process that identifies the predistortion coefficients. It is interesting to note that in the special case

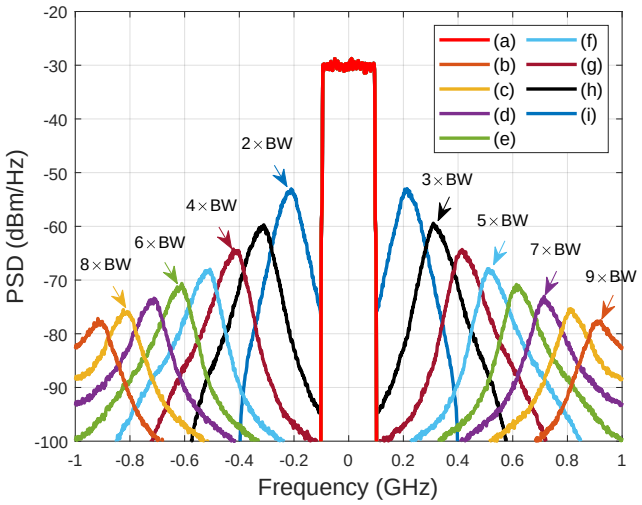


Figure 5.3: Simulated ideal doubler output spectrum with different constrained square-root function bandwidth input signals: (a) with ideal square-root function; (b)-(i) with square-root function bandwidth constrained from $\mathrm{BW_{TX}} = 9 \times \mathrm{BW}$ down to $\mathrm{BW_{TX}} = 2 \times \mathrm{BW}$ with a step of $1 \times \mathrm{BW}$. The inset in the figure denotes the bandwidth of the transmitter limiting filter.

of $D = 1$ (i.e., PA case), the above formulation simplifies to the result in [163]. The effectiveness of the proposed DPD to linearize FXs with different transmitter Dth root function and observation receiver bandwidths are presented next.

In the proposed DPD scheme, the theoretical formulation indicates that the bandwidth limiting filter used to restrict the bandwidth of the Dth root function output signal must be considered when generating the DPD bases and identifying the DPD coefficients. This filter, along with the PD function, is critical in emulating the nonlinearity resulting from constraining the bandwidth of the Dth root function output signal. Indeed, the absence of this filter within the DPD module depicted in Fig. 5.1 would hinder the generation of essential nonlinear bases necessary for the linearization of the FX in the presence of constrained bandwidth Dth root function.

5.1.2 Numerical Analysis

In this subsection, the effect of constraining the bandwidth of the Dth root function on the output spectrum of an idea FX is discussed. The linearization performance of the presented DPD on an EM-simulated frequency doubler is also discussed in this section. In

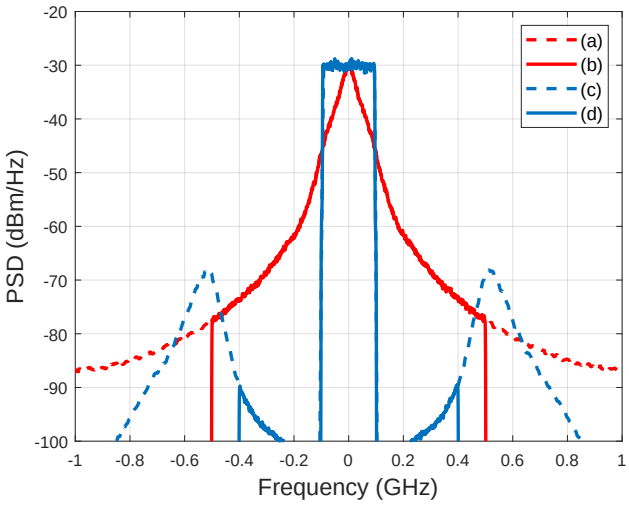


Figure 5.4: Simulated ideal doubler spectrum plots: (a) ideal square-root function; (b) square-root function constrained to a bandwidth of $5 \times \text{BW}$; (c) doubler output when the input is (a); (d) doubler output when the input is (b) and with receiver filter applied with bandwidth $4 \times \text{BW}$.

the next subsection, the ability of the proposed DPD to linearize FXs will be validated experimentally using two distinct frequency doublers.

Effect of Constraining the Bandwidth of the Dth Root Function on Ideal Frequency Multipliers

Denote the bandwidth of the transmitter filter, $\tilde{h}_{TX}[n]$, used for constraining the Dth root function, as BW_{TX}, while the ideal signal bandwidth (i.e., the bandwidth of the signal inputted to the Dth root function) is represented as BW. Fig. 5.3 illustrates the simulated output spectra of an ideal doubler; (a) with ideal square-root function input signal and (b)-(i) with constrained bandwidth square-root function where the bandwidth is swept from $9 \times \text{BW}$ down to $2 \times \text{BW}$, with a step on $1 \times \text{BW}$. From Fig. 5.3 it is clear that constraining the Dth root function bandwidth results in spectrum regrowth in the signal adjacent bands. Furthermore, the maximum magnitude of the generated distortions is inversely proportional to the constrained Dth root function bandwidth, BW_{TX}. These distortions are the result of the time-domain power function characteristic of FXs, which manifest as a convolution in the frequency domain and is illustrated in Fig. 5.2.

Fig. 5.4 further explores the effects of limiting the square-root function's bandwidth on

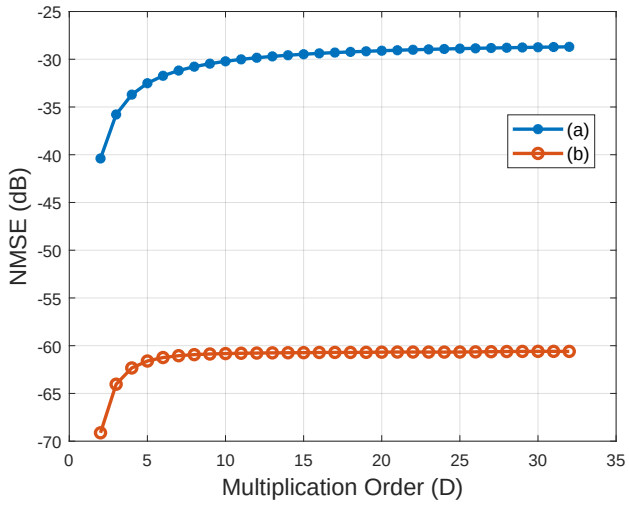


Figure 5.5: Simulated NMSE at an ideal multiplier output with Dth root function bandwidth constrained to $\mathrm{BW_{TX}} = 5\times\mathrm{BW}$ versus different multiplier multiplication orders: (a) before and (b) after receiver filter applied with $\mathrm{BW_{RX}} = 4\times\mathrm{BW}$.

the output spectrum of an ideal frequency doubler: (a) shows the spectrum of the ideal square-root function, (b) depicts the spectrum of the square-root function constrained to 5×BW, and (c) shows the output spectrum of an ideal multiplier when driven by the 5×BW constrained square-root function. As evident from Fig. 5.4 the most substantial distortions resulting from constraining the square-root function bandwidth appear at $\pm\frac{\mathrm{BW_{TX}}}{2}$. In order to filter out the out-of-band error, $\tilde{e}'\left(\tilde{\mathbf{H}}_{\mathbf{TX}}\sqrt[D]{\tilde{\mathbf{u}}(n)}\right)$, relax the constraints on the receiver ADC sampling rate, and satisfy the assumption in (5.19), a filter with bandwidth $\mathrm{BW_{RX}}$ is used. The value of $\mathrm{BW_{RX}}$ used in this manuscript was selected to be,

$$\mathrm{BW_{RX}} = \mathrm{BW_{TX}} - \mathrm{BW}. \tag{5.41}$$

Subsequently, Fig. 5.4 (d) illustrates the output spectra of an ideal doubler when driven with square-root function constrained to a bandwidth of $5\times\mathrm{BW}$ shown in (b) and after applying the receive filter with bandwidth, $\mathrm{BW_{RX}} = 4\times\mathrm{BW}$. This filtering operation significantly reduces the out-of-band error due to the constrained square-root root function bandwidth. Comparing the filtered spectrum with the unfiltered case, the residual error, quantified in terms of normalized NMSE, is greatly reduced from −40.4 dB to −69.1 dB. This result provides robust support for the assumption made in (5.20), affirming that distortions originating from transmitter bandwidth constraints predominantly manifest in the out-of-band spectrum, specifically around $\pm\frac{\mathrm{BW_{TX}}}{2}$, with negligible impact on the

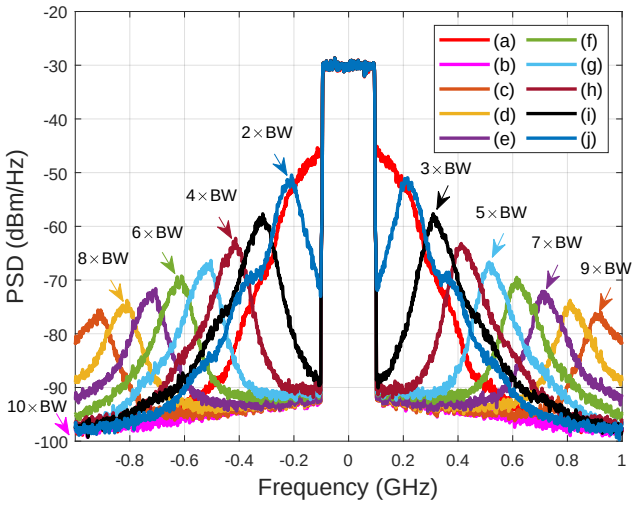


Figure 5.6: Output spectra of a simulated frequency-doubler driven with 200 MHz OFDM signal: (a) before DPD with ideal square-root function applied; (b)-(j) After proposed DPD with $\mathrm{BW_{TX}}$ and $\mathrm{BW_{RX}}$ varied from $\mathrm{BW_{TX}} = 10 \times \mathrm{BW}$ and $\mathrm{BW_{RX}} = 9 \times \mathrm{BW}$ down to $\mathrm{BW_{TX}} = 2 \times \mathrm{BW}$ and $\mathrm{BW_{RX}} = 1 \times \mathrm{BW}$, respectively with a step of $1 \times \mathrm{BW}$. The inset in the figure denotes the bandwidth of the transmitter limiting filter.

in-band portion of the signal. It's noteworthy that these conclusions also apply to FXs when $D > 2$. Fig. 5.5 shows, for different multiplication orders, the NMSE between the ideal signal and the output of the FX (a) before and (b) after applying receiver filtering ($\mathrm{BW_{RX}} = 4 \times \mathrm{BW}$). For this, the Dth root output signal bandwidth is limited to $\mathrm{BW_{TX}} = 5 \times \mathrm{BW}$. From Fig .5.5, it is evident that the application of the filter significantly reduces the NMSE, highlighting that the distortions attributed to limiting the bandwidth at the output of the Dth root function are predominantly in the out-of-band spectrum. This validates the assumption made in (5.20) across different D.

Linearization Results of the Proposed DPD on an EM Simulated 60 GHz-Output Frequency Doubler

The FX used in this subsection is a 60 GHz-output frequency doubler in a stacked push-push configuration. The doubler is designed using 45-nm CMOS SOI technology. The design is simulated in ADS software. The simulated AM-AM and AM-PM are used to generate a LUT based forward model for the doubler which is then used to train the DPD function. The test signal used in the simulation is a 200 MHz OFDM signal with

subcarriers modulated using 256-QAM and a PAPR of 9 dB.

Fig. 5.6 shows the simulatedPSD at the doubler output: (a) before DPD with ideal square-root function applied, (b)-(j) after the proposed DPD with constrained square-root function and observation receiver bandwidths swept from $\mathrm{BW_{TX}} = 10 \times \mathrm{BW}$ and $\mathrm{BW_{RX}} = 9 \times \mathrm{BW}$ in (b), down to $\mathrm{BW_{TX}} = 2 \times \mathrm{BW}$ and $\mathrm{BW_{RX}} = 1 \times \mathrm{BW}$ in (j), respectively, with a step of $1 \times \mathrm{BW}$. Using the proposed DPD, the EVM improved from 20.7% before DPD in (a) to 0.4% in (b)-(i), and to 0.6% in (j). Similarly, the ACPR after DPD improved from 21.3/21.5 dBc in (a), to better than 60 dBc in (b)-(g), 58.2/58.2 dBc in (h), 36.9/37.4 dBc in (i), and 25.8/25.9 dBc in (j). The DPD coefficients used in the simulation were obtained using the direct learning algorithm in (5.39) and a total of 30 coefficients were used. Note, the deterioration in the ACPR results reported in (i) and (j), are attributed to the out-of-band error, $\tilde{e}'[n]$, caused by the constrained bandwidth square-root function, leading to peak distortion at $\pm\frac{3}{2}\mathrm{BW}$ in (i) and $\pm\mathrm{BW}$ in (j). However, it's worth emphasizing that this error does not significantly impact the in-band signal quality, as evidenced by the EVM after DPD remaining at 0.4% in (i) and slightly increasing to 0.6% in (j).

5.1.3 Experimental Validation

In this subsection the effectiveness of the proposed DPD method to linearize FXs with constrained TX and RX bandwidths is experimentally validated.

Measurement Setup

To that end, the experimental setup, shown in Fig. 5.17, was developed. Two different frequency doublers ($D = 2$) were used in these experiments; i) a frequency doubler with output centered at 25 GHz from SpaceK Labs (A2510-2x-20) and ii) a frequency doubler with output centered at 28 GHz from Analog Devices (HMC-578). The vector-modulated test signals used in the experiment were generated using a 12-bit, 12 GS/s AWG (M8121A from Keysight Technologies), with output centered at an IF of 1.75 GHz. A custom up-converter constituted of a variable attenuator (HMC-624), a driver amplifier (HMC-788A), a hybrid-90° (IPP-4120) and an IQ-mixer (MMIQ 1037H from Marki Microwave) is used to up-convert the IF signal to a center frequency of 12.5 GHz for the first frequency doubler and 14 GHz for the second frequency doubler case. The signal was then amplified using a driver amplifier (MAAM-011109 from MACOM). Afterward, a LPF (FLP-1250 from Marki Microwave) for the first frequency doubler and a custom filter for the second frequency doubler are used to reject the residual image and LO leakage before being fed

Table 5.1: Linearization results for the frequency doubler (SpaceK) with output frequency centered around 25 GHz

		(a)	(b)	(c)	(d)	(e)	(f)	(g)	(h)	(i)	(j)
200 MHz	**TX BW**	10×	10×	9×	8×	7×	6×	5×	4×	3×	2×
	RX BW	10×	9×	8×	7×	6×	5×	4×	3×	2×	1×
	EVM (%)	13.6	1.6	1.2	1	1	1	1	1	1	1.1
	ACPR (dBc)	24./24.5	51.1/51.2	51.4/51.3	52.6/52.2	52.5/52.7	52.6/52.6	52.6/52.6	51.9/52.0	36.4/37.1	26.0/26.1
400 MHz	**TX BW**	8×	8×	7×	6×	5×	4×	3×	2×	-	-
	RX BW	8×	7×	6×	5×	4×	3×	2×	1×	-	-
	EVM (%)	15.9	1.5	1.4	1.38	1.38	1.37	1.38	1.46	-	-
	ACPR (dBc)	23.7/23.3	45.8/46.7	46.7/47.3	46.5/47.2	46.5/47.1	46.5/46.8	36.1/37.2	25.6/26.2	-	-

to the doubler under test. The output of the frequency doubler is then fed to a directional coupler, followed by a receiver (N9040B from Keysight) connected to its coupled port. The through signal from the directional coupler is then down-converted to an IF frequency of 3.025 GHz using a heterodyne-mixer (MM-11140H) and captured using a 10-bit, 20 Gsps, 8 GHz analog bandwidth oscilloscope (MSOS804A from Keysight Technologies). LO sources (MXG-N5183B from Keysight Technologies) are used to drive the up-conversion and down-conversion mixers used in the setup.

The measurements are performed using 200 MHz, 400 MHz, and 800 MHz modulation bandwidth OFDM signals conforming to 3GPP 5G NR downlink specifications, with sub-carriers modulated using 256-QAM, sub-carrier spacing of 120 kHz, total data sub-carriers K_{D} of 1584, 3168, and 6336, and fast Fourier transform sizes K_{FFT} of 2048, 4096, and 8192, for the 200 MHz, 400 MHz, and 800 MHz signals respectively. The used test signals are characterized by a PAPR (after crest factor reduction using clipping and filtering) of 9 dB. The 200 MHz, 400 MHz, and 800 MHz test signals are complex sampled at 2 Gsps, 4 Gsps, and 4 Gsps, respectively. For the DPD function, the nonlinearity order, nonlinear memory depth, linear memory depth, memory step, and pruning parameter were set to 20, 5, 5, 8, and 2 respectively, resulting in a total of 30 coefficients. The number of iterations used to train the DPD function was fixed to 10, and 1.5×10^4 samples were used per iteration for DPD training.

Linearization Results of the 25 GHz Frequency Doubler

Fig. 5.7 shows the PSD at the SpaceK doubler output when driven with a 200 MHz signal: (a) before DPD with square-root function applied $\mathrm{BW_{TX}}$ = 10×BW, and $\mathrm{BW_{RX}}$ = 10×BW, (b)-(j) after the proposed DPD with constrained square-root function and observation receiver bandwidths swept from $\mathrm{BW_{TX}} = 10 \times \mathrm{BW}$ and $\mathrm{BW_{RX}} = 9 \times \mathrm{BW}$ in (b), down to $\mathrm{BW_{TX}} = 2 \times \mathrm{BW}$ and $\mathrm{BW_{RX}} = 1 \times \mathrm{BW}$ in (j), respectively, with a step of $1 \times \mathrm{BW}$. Using

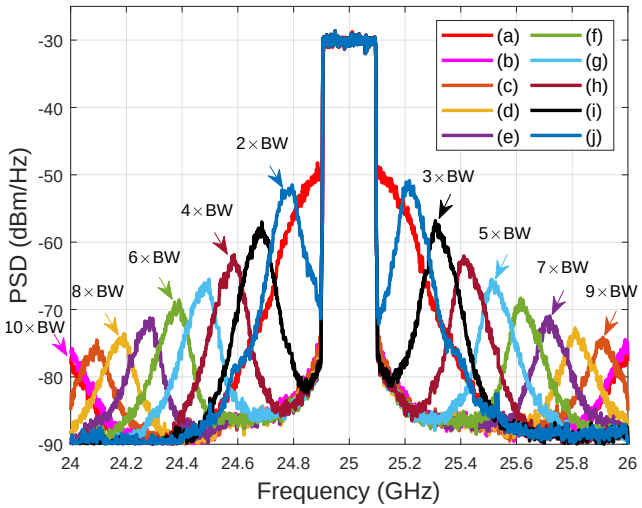


Figure 5.7: Measured output spectra of frequency-doubler (SpaceK) driven with 200 MHz OFDM signal: (a) before DPD with square-root function applied, $BW_{TX} = 10 \times BW$, and $BW_{RX} = 10 \times BW$; (b)-(j) After proposed DPD with BW_{TX} and BW_{RX} varied from $10 \times BW$ and $9 \times BW$ down to $2 \times BW$ and $1 \times BW$, respectively with a step of $1 \times BW$. The inset in the figure denotes the bandwidth of the transmitter limiting filter.

the proposed DPD scheme, the EVM improved from 13.6% before DPD in (a) to 1% in (d)-(i), and to 1.1% in (j). Similarly, the ACPR after DPD improved from 24.4/24.5 dBc in (a), to better than 50 dBc in (b)-(h), 36.4/37.1 dBc in (i), and 26.0/26.3 dBc in (j).

Similar linearization results were reported for the 400 MHz case. Fig. 5.8 shows the PSD at the SpaceK doubler output when driven with a 256-QAM 400 MHz OFDM signal: (a) before DPD with square-root function applied, $BW_{TX} = 8 \times BW$, and $BW_{RX} = 8 \times BW$; (b)-(h) after the proposed DPD with constrained square-root function and receiver bandwidths swept from $BW_{TX} = 8 \times BW$ and $BW_{RX} = 7 \times BW$ in (b), down to $BW_{TX} = 2 \times BW$ and $BW_{RX} = 1 \times BW$ in (h), respectively, with a step of one. Fig. 5.9 shows the AM-AM (Left) and AM-PM (Right) distortion characteristics, respectively, at the SpaceK doubler output corresponding to the measurements presented in Fig. 5.8 (a) and (h). The measurement results for the SpaceK doubler are summarized in Table 5.1.

Using the proposed DPD scheme, the EVM improved from 15.9% before DPD in (a) to below 1.4% in (c)-(g), and to 1.46% in (h). Similarly, the ACPR after DPD exhibited substantial enhancement, decreasing from 23.7/23.3 dBc in (a), to as low as 46.7/47.3 in (c). It is worth noting that minor deterioration in EVM and ACPR results were reported in (b), compared to (d)-(h), for both the 200 MHz and 400 MHz test signal cases, respectively.

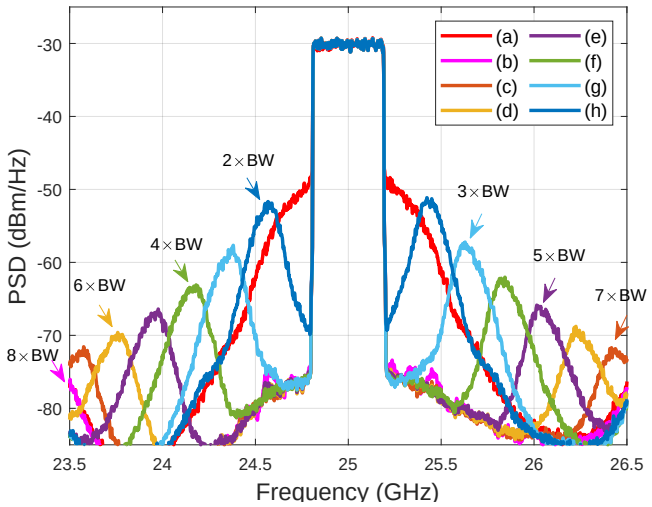


Figure 5.8: Measured output spectra of frequency-doubler (SpaceK) driven with 400 MHz OFDM signal: (a) before DPD with square-root function applied, $\mathrm{BW_{TX}} = 8 \times \mathrm{BW}$, and $\mathrm{BW_{RX}} = 8 \times \mathrm{BW}$; (b)-(h) After proposed DPD with $\mathrm{BW_{TX}}$ and $\mathrm{BW_{RX}}$ varied from $8 \times \mathrm{BW}$ and $7 \times \mathrm{BW}$ down to $2 \times \mathrm{BW}$ and $1 \times \mathrm{BW}$, respectively with a step of $1 \times \mathrm{BW}$. The inset in the figure denotes the bandwidth of the transmitter limiting filter.

These are attributed to transmitter calibration errors. Specifically, in the 200 MHz test case, when using a $\mathrm{BW_{TX}} = 10 \times \mathrm{BW}$ and $\mathrm{BW_{RX}} = 9 \times \mathrm{BW}$ in (b), transmitter calibration at the doubler input would necessitate ensuring error-free signal over a wider bandwidth, i.e., $\mathrm{BW_{TX}} = 10 \times \mathrm{BW}$, compared to when the transmitter bandwidth is constrained to $\mathrm{BW_{TX}} < 10 \times \mathrm{BW}$. Achieving such wideband calibration is challenging in practice. Consequently, in addition to reducing the transmitter and observation receiver data converters sampling rates, constraining the Dth root function bandwidth has the added benefit of relaxing the transmitter calibration requirements where the calibration bandwidth needs to match $\mathrm{BW_{TX}}$. Moreover, the deterioration in the ACPR results reported when $\mathrm{BW_{TX}}$ and $\mathrm{BW_{RX}}$ were set to less than $3 \times \mathrm{BW}$ and $2 \times \mathrm{BW}$, respectively, is attributed to the out-of-band error, $\tilde{e}'[n]$, due to the constrained bandwidth square-root function, leading to peak distortion at $\pm\frac{3}{2}\mathrm{BW}$ and $\pm\mathrm{BW}$, respectively. While this error cannot be rectified by the DPD, its impact on in-band signal quality remains negligible. This is exemplified in the EVM after DPD being maintained at 1% in (i) and 1.38% in (g) for the 200 MHz and 400 MHz test signals respective when $\mathrm{BW_{TX}} = 3 \times \mathrm{BW}$ and $\mathrm{BW_{RX}} = 2 \times \mathrm{BW}$. Additionally, there is a marginal increase in EVM to 1.1% in (i) and 1.46% in (h) for the 200 MHz and 400 MHz signals respective, when $\mathrm{BW_{TX}} = 2 \times \mathrm{BW}$ and $\mathrm{BW_{RX}} = 1 \times \mathrm{BW}$. Despite this marginal

Table 5.2: Linearization results for the frequency doubler (HMC578) with output frequency centered around 28 GHz

		(a)	(b)	(c)	(d)	(e)	(f)	(g)	(h)	(i)	(j)
200 MHz	**TX BW**	10×	10×	9×	8×	7×	6×	5×	4×	3×	2×
	RX BW	10×	9×	8×	7×	6×	5×	4×	3×	2×	1×
	EVM (%)	21.1	2.3	1.6	1	1	1	1	1	1	1.1
	ACPR (dBc)	20.5/21.0	49.8/49.3	50.8/50.0	52.2/51.4	52.4/51.6	51.8/51.7	51.9/51.5	51.4/51.0	36.2/36.4	26.2/25.7
400 MHz	**TX BW**	8×	8×	7×	6×	5×	4×	3×	2×	-	-
	RX BW	8×	7×	6×	5×	4×	3×	2×	1×	-	-
	EVM (%)	17.9	1.8	1.4	1.4	1.4	1.4	1.4	1.4	-	-
	ACPR (dBc)	21.7/22.0	47.3/47.2	47.9/47.7	47.9/47.9	48.0/47.6	47.8/47.7	36.6/36.7	25.9/25.9	-	-
800 MHz	**TX BW**	3.75×	3.75×	3.5×	3×	2.5×	2.25×	2×	-	-	-
	RX BW	3.75×	2.75×	2.5×	2×	1.5×	1.25×	1×	-	-	-
	EVM (%)	21	1.4	1.4	1.6	1.4	1.4	1.5	-	-	-
	ACPR (dBc)	22.0/22.1	44.1/40.2	43.4/39.8	36.9/35.8	30.3/29.8	28.4/27.8	26.6/26.0	-	-	-

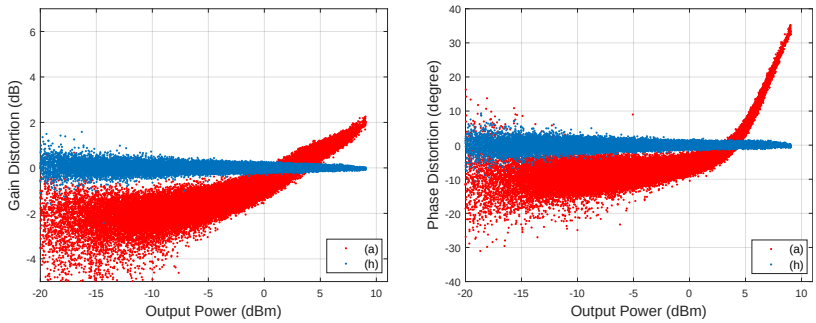


Figure 5.9: Measured gain distortion (Left) and phase distortion (Right) of the frequency-doubler (SpaceK) driven with 400 MHz OFDM signal: (a) before linearization with square-root applied, $BW_{TX} = 8\times BW$, and $BW_{RX} = 8\times BW$; (h) After proposed DPD with BW_{TX} and BW_{RX} set to $2 \times BW$ and $1 \times BW$, respectively.

increase in EVM, the proposed DPD was able to mitigate the FX's nonlinear distortion as illustrated by the flat AM-AM and AM-PM curves in Fig. 5.9 (h). Furthermore, it is interesting to note that for $BW_{TX} >= 3 \times BW$ and $BW_{RX} >= 2 \times BW$ the achieved ACPR and EVM remained compliant with the 3GPP requirements for FR2 frequencies operating in the n257 band for 256 QAM OFDM signals which specify a maximum EVM of 3.5% and a maximum ACPR of 28 dBc for 256 QAM OFDM signals [69, p. 144-147]. Moreover, for $BW_{TX} >= 2 \times BW$ and $BW_{RX} >= 1 \times BW$ the achieved ACPR and EVM remained compliant with the 3GPP requirements for FR2 frequencies operating in the n260 band for 256 QAM OFDM signals which specify a maximum EVM of 3.5% and a maximum ACPR of 26 dBc for 256 QAM OFDM signals [69, p. 144-147]. These results align with

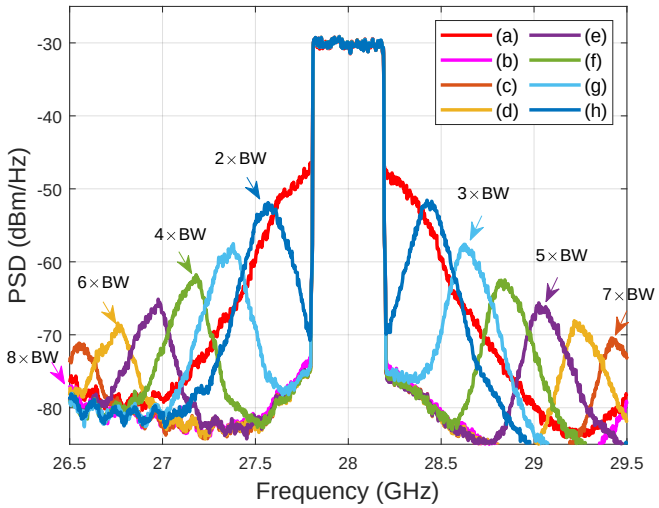


Figure 5.10: Measured output spectra of frequency-doubler (HMC-578) driven with 400 MHz OFDM signal: (a) before DPD with square-root function applied, BW_{TX} = 8×BW, and BW_{RX} = 8×BW; (b)-(h) After proposed DPD with BW_{TX} and BW_{RX} varied from 8×BW and 7×BW down to 2×BW and 1×BW, respectively with a step of 1×BW. The inset in the figure denotes the bandwidth of the transmitter limiting filter.

the simulation results presented in Section. 5.1.2.

Linearization Results of the 28 GHz Frequency Doubler

To verify the generality of the proposed DPD scheme for linearizing frequency doublers with contained transmitter and observation receiver bandwidths, a second doubler (HMC578 from Analog Devices) driven in higher compression, i.e., worse starting ACPR and EVM, was used as DUT. The measurement results for the HMC578 doubler are summarized in Table 5.2.

Similar to the first frequency doubler case, excellent linearization results were achieved using the proposed DPD across different transmitter and observation receiver bandwidth configurations. Fig. 5.10 shows the PSD at the HMC578 doubler output when driven with a 400 MHz signal: (a) before DPD with square-root function applied BW_{TX} = 8×BW, and BW_{RX} = 8 × BW, (b)-(h) after the proposed DPD with constrained square-root function and observation receiver bandwidths ranging from BW_{TX} = 8 × BW and BW_{RX} = 7 × BW in (b), down to BW_{TX} = 2×BW and BW_{RX} = 1×BW in (h), respectively, with a step size of 1 × BW. Using the proposed DPD scheme, the EVM improved significantly, reducing

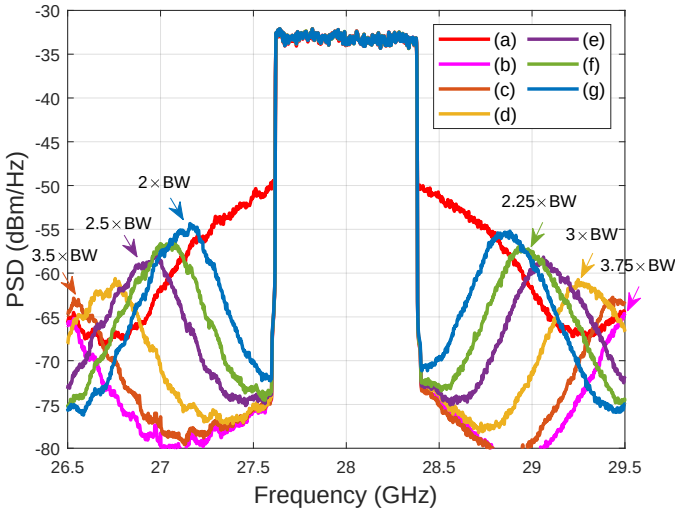


Figure 5.11: Measured output spectra of frequency-doubler (HMC-578) driven with 800 MHz OFDM signal: (a) before DPD with square-root function applied, $BW_{TX} = 3.75 \times BW$, and $BW_{RX} = 3.75 \times BW$; (b)-(g) After proposed DPD with BW_{TX} and BW_{RX} varied from $3.75 \times BW$ and $2.75 \times BW$ down to $2 \times BW$ and $1 \times BW$, respectively. The inset in the figure denotes the bandwidth of the transmitter limiting filter.

from 17.9% before DPD in (a) to 1.8% in (b) and 1.4% in (c)-(h). Likewise, the ACPR after DPD improved from 21.0/22.0 dBc in (a), to better than 47 dBc in (b)-(f) and as reaching as low as 47.9/47.9 dBc in (d). The measurement results clearly show the effectiveness of the proposed DPD in linearizing FXs with constrained transmitters and observation receiver bandwidths.

In addition to the capacity of the proposed DPD to reduce the transmitter and observation receive required bandwidths for linearizing FXs, it also enables the generation of wider bandwidth signals without compromising the linearizability of the device under test. Fig. 5.11 shows the PSD at the HMC578 doubler output when driven with a 800 MHz signal: (a) before DPD with square-root function applied $BW_{TX} = 3.75 \times BW$, and $BW_{RX} = 3.75 \times BW$, (b)-(g) after the proposed DPD with constrained square-root function and observation receiver bandwidths swept from $BW_{TX} = 3.75 \times BW$ and $BW_{RX} = 2.75 \times BW$ in (b), down to $BW_{TX} = 2 \times BW$ and $BW_{RX} = 1 \times BW$ in (g), respectively. Fig. 5.12 shows the AM-AM (Left) and AM-PM (Right) at the HMC578 doubler output corresponding to the measurements presented in Fig. 5.11 (a) and (g). Furthermore, the constellation plot corresponding to the results in Fig. 5.11 (a) and (g) is shown in Fig. 5.13. Using the proposed DPD scheme, the EVM significantly improved from 21% before DPD in (a) to 1.4%

Table 5.3: Summary of state-of-the-art DPD schemes for FXs

	[146]	[142]	[164]	[67]		[5]	[7]		[165]	[148]	This work	
RF (GHz)	78.6	2.46	99.6	3.56		25	25	28	24	48.6	25	28
Signal bandwidth	1 GHz	1.2 MHz	162.5 MHz	10 MHz	20 MHz	400 MHz	400 MHz		20 MHz	24 MHz	400 MHz	800 MHz
Modulation scheme	8-PSK	QPSK, CDMA	4-QAM	256-QAM		256-QAM, OFDM	256-QAM, OFDM		64-QAM, OFDM	16-QAM	256-QAM, OFDM	
Data rate (Mbps)	3000	0.0144	625	69.1	138.2	2844	2844		120	96	2844	5689
Multiplication factor	6	3	6	4		2	2		4	4	2	
Bandwidth constrained DPD formulation	No	No	No	No		No	No		No	Yes (@ RX)	Yes (@ TX and RX)	
Transmitter bandwidth (BW)	6×	–	–	5×	5×	10×	10×		7.5×	10×	10-2×	
Receiver bandwidth (BW)	6×	–	–	10×	5×	5×	10×		7.2×	3.75×	10-1×	
Number of coefficients	–	–	–	79	–	56	39	44	858	92	30	
EVM after DPD (%)	8.5	7.3	–	1.6	2.4	3.6	1.3	1.8	3.1	1.94	1.4-1.5	

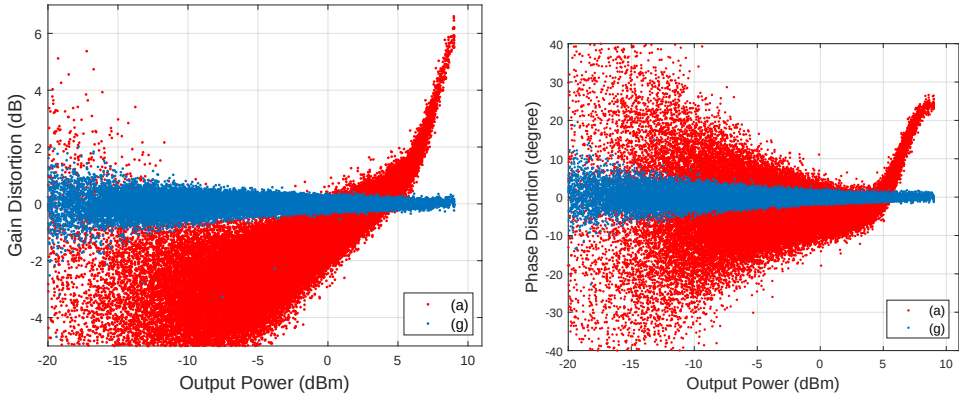


Figure 5.12: Measured gain distortion (Left) and phase distortion (Right) frequency-doubler (HMC-578) driven 800 MHz OFDM signal: (a) before linearization with square-root applied, $BW_{TX} = 3.75 \times BW$, and $BW_{RX} = 3.75 \times BW$; (g) After proposed DPD with BW_{TX} and BW_{RX} set to $2 \times BW$ and $1 \times BW$, respectively.

in (b), (c), (e), (f), and to 1.5% in (g). Similarly, the ACPR after DPD improved from 22.7/22.1 dBc in (a), to as good as 44.0/40.2 dBc in (b). Furthermore, when the transmitter and observation receiver bandwidths are limited to $BW_{TX} = 2 \times BW$ and $BW_{RX} = 1 \times BW$, respectively, the proposed DPD is still effective in mitigating the FX's nonlinearity. This is highlighted by the flat AM-AM and AM-PM plots in Fig. 5.12 (g) and the negligible distortion in the constellation plot in Fig. 5.13 (Blue). Note, when employing transmitter and observation receiver bandwidths as low as $BW_{TX} = 2.25 \times BW$ and $BW_{RX} = 1.25 \times BW$, respectively, the achieved ACPR and EVM remained compliant with the 3GPP requirements for FR2 frequencies operating in the n257 band for 256 QAM OFDM signals which

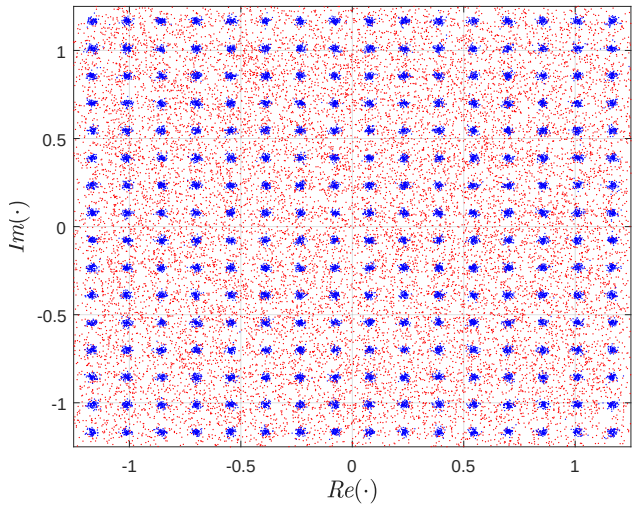


Figure 5.13: Measured constellation at the frequency-doubler (HMC-578) output driven with 800 MHz OFDM signal: (Red) before DPD with square-root function applied, $\mathrm{BW_{TX}} = 3.75 \times \mathrm{BW}$, and $\mathrm{BW_{RX}} = 3.75 \times \mathrm{BW}$; (Blue) After proposed DPD with $\mathrm{BW_{TX}}$ and $\mathrm{BW_{RX}}$ set to $2 \times \mathrm{BW}$ and $1 \times \mathrm{BW}$, respectively.

specify a maximum EVM of 3.5% and a maximum ACPR of 28 dBc for 256 QAM OFDM signals [69, p. 144-147]. Moreover, for $\mathrm{BW_{TX}} = 2 \times \mathrm{BW}$ and $\mathrm{BW_{RX}} = 1 \times \mathrm{BW}$ the achieved ACPR and EVM remained compliant with the 3GPP requirements for FR2 frequencies operating in the n260 band for 256 QAM OFDM signals which specify a maximum EVM of 3.5% and a maximum ACPR of 26 dBc for 256 QAM OFDM signals [69, p. 144-147].

The measurement results presented in Sections 5.1.3 and 5.1.3, summarized in Tables 5.1 and 5.2, demonstrate the effectiveness of the proposed DPD in linearizing frequency doublers with constrained transmitter and observation receiver bandwidths. Furthermore, Table 5.3 provides a summary of state-of-the-art DPDs for FXs. From Table 5.3, the proposed scheme yielded excellent linearization capacity while using the lowest ratio of transmitter and receiver bandwidths to modulation bandwidth. Furthermore, this work reports the largest linearization bandwidth and data rate in the literature at 5.7 Gbps.

5.2 Linearization of Frequency Multipliers based on Nonlinear Deviations in Frequency Multipliers from the Ideal Power Function

To overcome the limitations of current DPD methods in linearizing FXs [3–5, 7, 142, 148, 164–168], which demonstrate reduced effectiveness with wider bandwidth signals and higher FX multiplication orders, this section introduces a novel DPD method to linearizing high-order FXs driven by wideband vector-modulated signals. Unlike existing DPD methods discussed in the literature [3, 4, 7, 142, 164–168], which primarily focus on mitigating the deviation of the cascade comprised of the Dth root function and the FX from an ideal gain block (as shown in Fig. 5.14 (a)), this work rethinks the DPD problem formulation and presents an alternative DPD method tailored to mitigate the deviation of the FX's response from an ideal power function.

Central to the proposed method, this section introduces a novel DPD cost function that triggered a shift in the placement of the DPD module within the overall signal generation/transmission chain (as depicted in Fig. 5.14 (b)) along with a novel DPD coefficient update equation. The strategic repositioning in the DPD module reduces the susceptibility of linearization performance to hardware non-idealities, which commonly compromise the effectiveness of DPD methods aimed at linearizing the cascade of the Dth root function and FX response. Moreover, this section derives the DPD bases required by the proposed method to linearize FXs, revealing a notable departure from the reliance on fractional power bases utilized in previous state-of-the-art methodologies. This aspect contributes significantly to reducing the hardware implementation complexity of the proposed DPD method compared to existing methods. Detailed theoretical analysis and extensive simulation experimental validations are presented.

5.2.1 Problem Formulation

In this subsection, the proposed DPD scheme for linearizing FX-based transmitters, as shown in Fig. 5.15, is formulated. Let $\tilde{z}(t)$ and $\tilde{y}(t)$ be the continuous-time CBBE input and output signals, respectively, to the FX with multiplication order D. Let $\tilde{z}[n] = \tilde{z}(n/F_s)$ and $\tilde{y}[n] = \tilde{y}(n/F_s)$ be the discrete-time CBBE signals of $\tilde{z}(t)$ and $\tilde{y}(t)$, respectively, where F_s is the sampling rate. Using the additive error model adopted in [7], the FX output $\tilde{y}[n]$ can be expressed as follows,

$$\tilde{y}[n] = (\tilde{z}[n])^D + \tilde{e}(\tilde{\mathbf{z}}(n)), \tag{5.42}$$

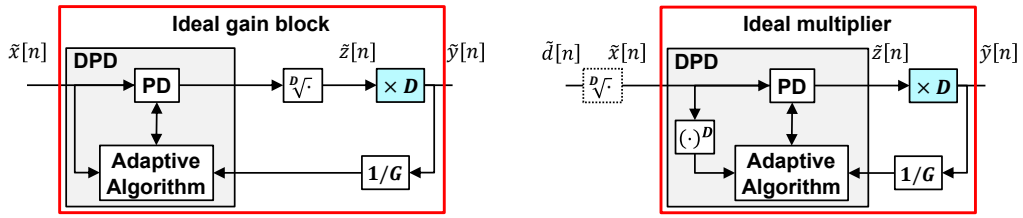


Figure 5.14: Functional block diagrams illustrating: (a) DPD method of [7]; (b) proposed DPD method.

where the nonlinear error term, $\tilde{e}(\tilde{\mathbf{z}}(n))$, takes the form of the FX forward model expressed in [7, eqn. (7)], and given by,

$$\tilde{e}(\tilde{\mathbf{z}}(n)) = \tag{5.43}$$

$$\sum_{p=0}^{N_L} \sum_{\substack{(p_1,p_2)\in\mathcal{P}(p) \\ \mathbf{m}\in\mathcal{B}^{p_1},\hat{\mathbf{m}}\in\mathcal{B}^{p_2}}} \gamma_{\mathbf{m},\hat{\mathbf{m}}}^{p_1,p_2,\ell} \prod_{i=1}^{p_1} \tilde{z}[n-m_i] \prod_{j=1}^{p_2} \tilde{z}^*[n-\hat{m}_j], \tag{5.44}$$

where

$$\mathcal{P}(p) = \Big\{(p_1,p_2)\in\mathbb{Z}^2 \Big| p_1\geq 0, p_2\geq 0, \\ p_1+p_2=p, p_1-p_2=D\Big\}, \tag{5.45}$$

is the set of tuples (p_1, p_2) that results in a nonlinearity order of p, the set $\mathcal{B} = \{0,\ldots,M\}$, M is the maximum memory depth, N_L is the maximum nonlinearity order and $\gamma_{\mathbf{m},\hat{\mathbf{m}}}^{p_1,p_2,\ell}$ are the model coefficients.

The predistorter (DPD) function is responsible for correcting the deviation of the FX from the ideal power operation. Accordingly, the DPD model coefficients can be obtained by minimizing the following quadratic cost function,

$$J(\mathbf{a}) = \sum_{n=1}^{L} \Big(\tilde{y}[n] - (\tilde{x}[n])^D\Big)\Big(\tilde{y}[n] - (\tilde{x}[n])^D\Big)^*, \tag{5.46}$$

where L is the length of the training data, and $\mathbf{a}$ is the vector of DPD coefficients that are to be optimized to minimize the cost function J. The optimal DPD coefficients can be

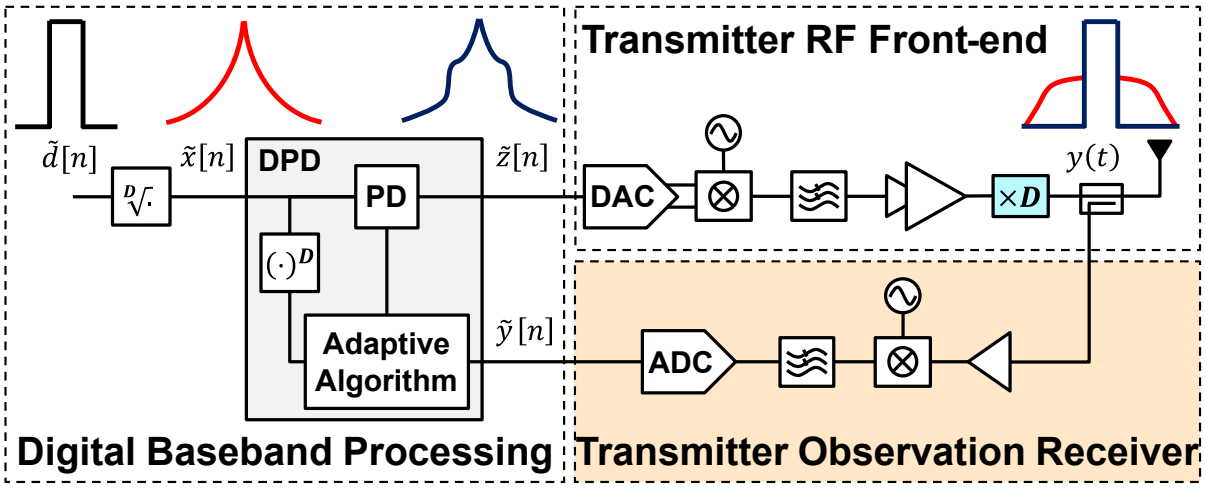


Figure 5.15: Detailed system block diagram of an FX-based transmitter equipped with the proposed DPD scheme.

iteratively computed using the Quasi-Newton method for a real-valued cost function with complex-valued arguments using the following update equation,

$$\hat{\mathbf{a}}_{k+1} = \hat{\mathbf{a}}_k - \mu \left[\left(\frac{\partial^2 J}{\partial \mathbf{a}^* \partial \mathbf{a}^T} \right)^{-1} \left(\frac{\partial J}{\partial \mathbf{a}} \right) \right] \tag{5.47}$$

where $\mathbf{a}_k$ denote the DPD coefficient vector at the k'th iteration, and $\mu \in (0, 1]$ is the learning step size.

To solve the update equation in (5.47) a weakly nonlinear system is assumed, i.e., the multiplier weakly deviates from an ideal multiplier. Consequently, the DPD signal, $\tilde{z}[n]$, can be obtained as a small perturbation of $\tilde{x}[n]$, i.e.,

$$\tilde{z}[n] = \tilde{x}[n] + \beta[n]. \tag{5.48}$$

where β is a high-order nonlinearity term assumed to be much smaller than $\tilde{x}[n]$, i.e.,

$$\mathrm{E}\left[|\tilde{x}\,[n]|^2\right] \gg \mathrm{E}\left[|\beta\,[n]|^2\right]. \tag{5.49}$$

Substituting, (5.48) in (5.42), we have

$$\tilde{y}[n] = \left(\tilde{x}[n] + \beta[n]\right)^D + \tilde{e}\left(\tilde{\mathbf{z}}(n)\right). \tag{5.50}$$

Using the binomial expansion (5.50) can be rewritten as follows,

$$\tilde{y}[n] = \sum_{k=0}^{D} \binom{D}{k} (\tilde{x}[n])^{D-k} (\beta[n])^{k} + \tilde{e}\left(\tilde{\mathbf{z}}(n)\right). \tag{5.51}$$

Using the approximation in (5.49), (5.51) can be approximated as follows,

$$\tilde{y}[n] \approx (\tilde{x}[n])^{D} + D\beta[n](\tilde{x}[n])^{D-1} + \tilde{e}\left(\tilde{\mathbf{z}}(n)\right), \tag{5.52}$$

where higher powers of $\beta[n]$ are neglected. Subsequently substituting the expression of $\beta[n]$ from (5.48), i.e., $\beta[n] = \tilde{z}[n] - \tilde{x}[n]$, into (5.52), we get,

$$\tilde{y}[n] \approx (\tilde{x}[n])^{D} + D(\tilde{z}[n] - \tilde{x}[n])(\tilde{x}[n])^{D-1} + \tilde{e}\left(\tilde{\mathbf{z}}(n)\right), \tag{5.53}$$

Finally, rearranging the terms in (5.53), we have,

$$\tilde{y}[n] \approx D\tilde{z}[n]\left(\tilde{x}\left[n\right]\right)^{D-1} - (D-1)\left(\tilde{x}\left[n\right]\right)^{D} + \tilde{e}\left(\tilde{\mathbf{z}}(n)\right). \tag{5.54}$$

Moreover, the DPD signal in (5.48) is expressed as a function of nonlinear bases, $\tilde{\psi}_q(\cdot)$, as follows,

$$\tilde{z}[n] = \sum_{q=1}^{Q} a_q \tilde{\psi}_q\left(\tilde{\mathbf{x}}(n)\right), \tag{5.55}$$

where Q is the total number of DPD bases and the basis functions, $\left\{\tilde{\psi}_q\left(\cdot\right)\right\}$, are yet to be determined. Using (5.54) and (5.55) the update equation in (5.47) can be solved. Specifically, assuming $(\partial\tilde{e}(\tilde{\mathbf{z}}(n))/(\partial a_j) = 0$, we get,

$$\frac{\partial J}{\partial a_j} \approx \sum_{n=1}^{L} \left(\tilde{y}[n] - \left(\tilde{x}\left[n\right]\right)^{D}\right)^{*} D\left(\tilde{x}\left[n\right]\right)^{D-1} \tilde{\psi}_j\left(\tilde{\mathbf{x}}(n)\right), \tag{5.56}$$

and,

$$\frac{\partial^2 J}{\partial a_i^* \partial a_j} \approx \sum_{n=M+1}^{L} D^2\left(\tilde{x}^*\left[n\right]\right)^{D-1} \tilde{\psi}_i^*\left(\tilde{\mathbf{x}}(n)\right) \times \left(\tilde{x}\left[n\right]\right)^{D-1} \tilde{\psi}_j\left(\tilde{\mathbf{x}}(n)\right). \tag{5.57}$$

Finally, substituting (5.56) and (5.57) in (5.47), we have,

$$\hat{\mathbf{a}}_{k+1} = \hat{\mathbf{a}}_k - \mu\left(\tilde{\mathbf{\Phi}}\left(\tilde{\mathbf{x}}(n_k)\right)\right)^{\dagger}\left(\tilde{\mathbf{y}}(n_k) - \left(\tilde{\mathbf{x}}(n_k)\right)^{D}\right), \tag{5.58}$$

where,

$$\left(\tilde{\mathbf{\Phi}}\left(\tilde{\mathbf{x}}(n_k)\right)\right)^{\dagger} = \left(\tilde{\mathbf{\Phi}}^H\left(\tilde{\mathbf{x}}(n_k)\right)\,\tilde{\mathbf{\Phi}}\left(\tilde{\mathbf{x}}(n_k)\right)\right)^{-1}\tilde{\mathbf{\Phi}}^H(\tilde{\mathbf{x}}(n_k))\,, \tag{5.59}$$

$\tilde{\mathbf{\Phi}}\left(\tilde{\mathbf{x}}(n_k)\right)$ is the basis matrix with ith row and jth column entry, $\left[\tilde{\mathbf{\Phi}}\left(\tilde{\mathbf{x}}(n_k)\right)\right]_{i,j}$, given by,

$$\left[\tilde{\mathbf{\Phi}}\left(\tilde{\mathbf{x}}\left(n_k\right)\right)\right]_{i,j} = \left(\tilde{x}[n_k - i]\right)^{D-1} \times \tilde{\psi}_j\left(\tilde{\mathbf{x}}\left[n_k - i\right]\right). \tag{5.60}$$

Hence, together (5.55), (5.58), and (5.60) comprise the iterative training process that identifies the DPD coefficients.

We next derive the bases used for the DPD. When the DPD converges, the multiplier output, $\tilde{y}[n]$, is equal to $(\tilde{x}[n])^D$. Consequently, (5.54) can be rewritten as follows,

$$(\tilde{x}[n])^D = D\tilde{z}[n]\left(\tilde{x}\left[n\right]\right)^{D-1} - (D-1)\left(\tilde{x}\left[n\right]\right)^D + \tilde{e}\left(\tilde{\mathbf{z}}(n)\right). \tag{5.61}$$

Rearranging the terms in (5.61) and solving for $\tilde{z}[n]$, we have,

$$\tilde{z}[n] = \tilde{x}[n] - \frac{\tilde{e}\left(\tilde{\mathbf{z}}(n)\right)}{D(\tilde{x}[n])^{D-1}} \tag{5.62}$$

$$= \tilde{x}[n] - \frac{\tilde{e}\left(\tilde{\mathbf{x}}(n) - \frac{1}{D}\tilde{\mathbf{e}}\left(\tilde{\mathbf{z}}(n)\right) \oslash \left(\tilde{\mathbf{x}}(n)\right)^{D-1}\right)}{D(\tilde{x}[n])^{D-1}}, \tag{5.63}$$

where $\oslash$ is the Hadamard division (element by element). Assuming that the contribution of the "error of the error" in (5.63) is negligible, the following approximation can be made,

$$\tilde{e}\left(\tilde{\mathbf{x}}(n) - \frac{1}{D}\tilde{\mathbf{e}}\left(\tilde{\mathbf{z}}(n)\right) \oslash \left(\tilde{\mathbf{x}}(n)\right)^{D-1}\right) \approx \tilde{e}\left(\tilde{\mathbf{x}}(n)\right). \tag{5.64}$$

Consequently, (5.63) can be rewritten, such that,

$$\tilde{z}[n] = \tilde{x}[n] - \frac{\tilde{e}\left(\tilde{\mathbf{x}}(n)\right)}{D(\tilde{x}[n])^{D-1}}. \tag{5.65}$$

The DPD bases can then be obtained by substituting (5.65) in (5.44) resulting in,

$$\tilde{z}[n] = \tag{5.66}$$

$$\sum_{p=0}^{N'_L} \sum_{\substack{(p_1,p_2)\in\mathcal{P}(p) \\ \mathbf{m}\in\mathcal{B}^{p_1},\hat{\mathbf{m}}\in\mathcal{B}^{p_2}}} \frac{a_{\mathbf{m},\hat{\mathbf{m}}}^{p_1,p_2,\ell}}{D(\tilde{x}[n])^{D-1}} \prod_{i=1}^{p_1} \tilde{x}[n-m_i] \prod_{j=1}^{p_2} \tilde{x}^*[n-\hat{m}_j], \tag{5.67}$$

where N'_L is the model's maximum nonlinearity order.

In summary, this subsection has presented the proposed DPD method aimed at mitigating nonlinear distortions in non-ideal FXs. The method leverages a newly formulated cost function, shown in (5.37), that is minimized using the Quasi-Newton method. This process yields the update equation for the PD function coefficients, as detailed in (5.58). Additionally, the section derived the optimal PD function model bases employed within the proposed DPD method as shown in (5.67). Notably, these bases do not incorporate fractional power bases, significantly reducing their hardware implementation complexity compared to the state-of-the-art method in [7].

The block diagram depicted in Fig. 5.15 illustrates the proposed DPD method in an FX-based transmitter. A key outcome of the derivations in this work is the repositioning of the DPD module within the signal generation/transmission chain. As shown in Fig. 5.15, the proposed DPD method places the DPD module after the Dth root function. This repositioning stems from the proposed cost function formulation, where the DPD module compensates for the deviation of the FX's response from an ideal power function. By relocating the DPD module directly before the FX in the digital domain signal generation path, the proposed DPD method mitigates the susceptibility of the FX linearization performance to hardware non-idealities.

To illustrate this, consider a scenario where the multiplier is modeled as a Wiener model, comprising linear memory terms cascaded with an ideal FX. If the method in [7] is employed, the Dth root function, as perceived by the ideal FX, is distorted by the linear memory preceding the ideal FX. Since the PD signal in [7] operates from within the Dth root function, compensating for this linear memory acting on the Dth root function becomes challenging, potentially leading to a breakdown of the weakly nonlinear assumption. In contrast, the proposed method directly links the DPD module output to the FX input, facilitating easier compensation for this linear memory, which is often unavoidable in practical transmitters that exhibit residual linear distortion even after calibration.

Another critical distinction of the proposed DPD method from previous literature lies in the proposed derivations not assuming the pth order post and pre-inversion equivalency. Consequently, implementing the proposed method through indirect learning is not feasible in its current form. Nonetheless, the reduced complexity and enhanced linearization performance of the proposed method, as demonstrated subsequently, position it as an attractive solution for linearizing FXs and facilitating the generation of wideband, high-integrity vector-modulated signals.

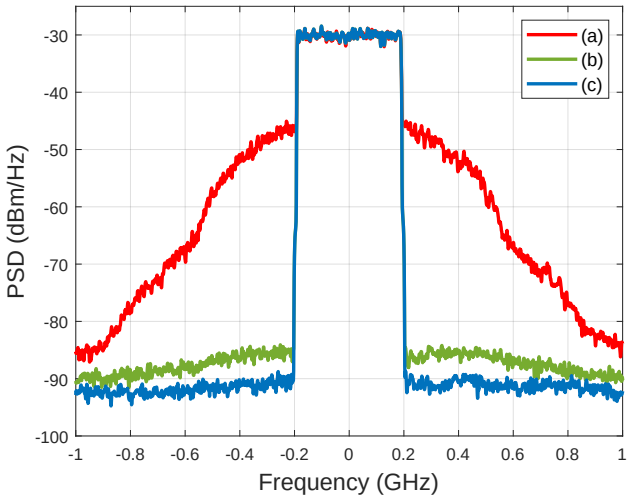


Figure 5.16: Simulated output spectra of the 60 GHz frequency-doubler driven with 400 MHz OFDM signal: (a) before DPD with square-root function applied; (b) after DPD in [7]; (c) after proposed DPD.

5.2.2 Numerical Analysis

In this subsection, simulations are carried out on a 60 GHz-output frequency doubler in a stacked push-push configuration. The doubler is designed using 45-nm CMOS SOI technology. The design is simulated in ADS software. The simulated AM-AM and AM-PM are used to generate a LUT based forward model for the doubler. Additionally, a finite impulse response filler emulating a non-ideal transmitter frequency response is incorporated into the simulation, positioned before the doubler forward model. The test signal used in the simulation is a 400 MHz OFDM signal with subcarriers modulated using 256-QAM.

Fig. 5.16 shows the simulated output spectra of the frequency-doubler when driven with the 400 MHz OFDM signal: (a) before DPD with square-root function applied; (b) after DPD in [7]; (c) after proposed DPD. Using DPD, the EVM improved from 25.7% before DPD in (a) to 0.4% in (b), and to 0.3% in (c). Similarly, the ACPR after DPD improved from 20.1/20.5 dBc in (a), to 55.7/55.6 dBc in (b), and 60.7/60.4 dBc in (c). The DPD coefficients used in the simulation result reported in (c) were obtained using the learning algorithm in (5.58). Furthermore, both the DPD in (b) and the proposed DPD scheme in (c) used a total of 30 coefficients. For the DPD in (b), the nonlinearity order, linear memory, and nonlinear memory were set to 15, 10, and 1, respectively, incorporating even and odd power bases as well as fraction power bases. In contrast, for the proposed DPD in (c), these parameters were set to 10, 10, and 1, respectively, and included even and odd

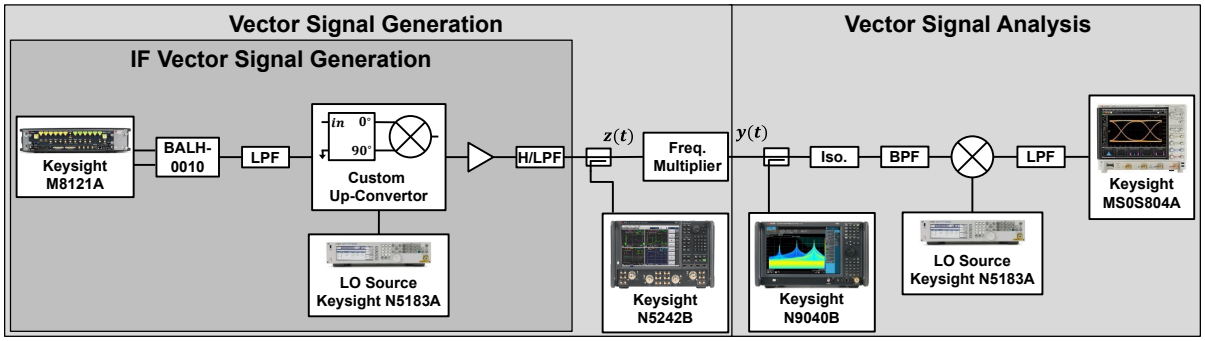


Figure 5.17: Test and measurement setup to validate the proposed DPD scheme for a frequency doubler-based vector signal generation system

power bases. From Fig. 5.16, the proposed DPD scheme outperformed the state-of-the-art DPD in [7] by 5 dB in ACPR, all while eliminating the need for fraction power bases, thus significantly reducing DPD implementation complexity.

5.2.3 Experimental Validation

In this subsection the effectiveness of the proposed DPD method to linearize the deviation of FXs from ideal power functions is experimentally validated.

Measurement Setup

In order to demonstrate the effectiveness of the proposed DPD scheme, an experimental setup as shown in Fig. 5.17 was developed. Different DUT with different multiplication orders were used in these experiments: i) a frequency doubler with output centered at 14 GHz from Analog devices (HMC-573), ii) a frequency doubler with output centered at 25 GHz from SpaceK Labs (A2510-2x-20), iii) a custom built frequency doubler with output centered at 62 GHz, iv) a frequency quadrupled consisting of the DUT in (i) and doubler from ADI (HMC-578), and v) an octupler with output centered at 58 GHz from QUINSTAR Technology composed of a cascade of frequency-doubler (QMM-16-06-10-02) and frequency-quadrupler (QMM-63-25-14-04).

The measurements are performed using 200 MHz, 400 MHz, and 800 MHz modulation bandwidth OFDM signals conforming to 3GPP 5G NR downlink specifications, with sub-carriers modulated using 256-QAM, sub-carrier spacing of 120 kHz, total data sub-carriers

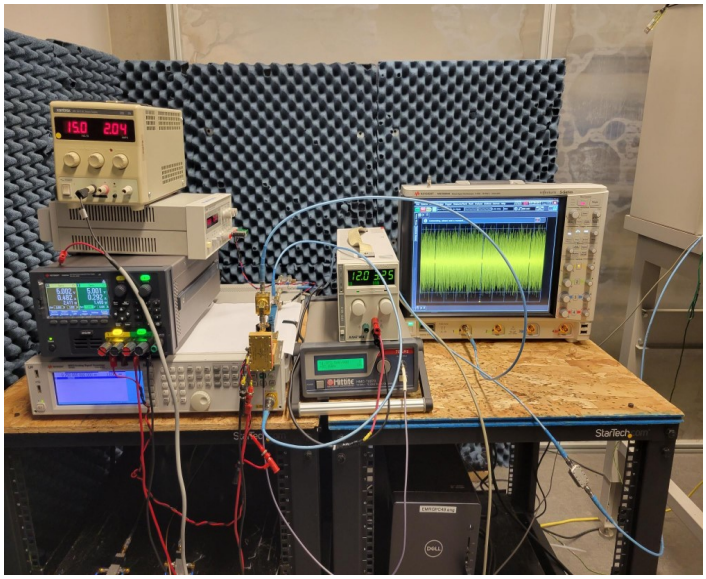


Figure 5.18: Picture of the measurement setup conducted on an octupler with output frequency centered around 58 GHz.

K_{D} of 1584, 3168, and 6336, and fast Fourier transform sizes K_{FFT} of 2048, 4096, and 8192, for the 200 MHz, 400 MHz, and 800 MHz signals respectively. The used test signals are characterized by a PAPR (after crest factor reduction using clipping and filtering) of 9 dB. The 200 MHz, 400 MHz, and 800 MHz test signals are complex sampled at 2 Gsps, 4 Gsps, and 4 Gsps, respectively. The DPD model parameters were meticulously tuned for each measurement and for the various reported DPD schemes to guarantee optimal performance. Additionally, to maintain a fair and consistent comparison across the different DPD schemes, the total number of coefficients used by the proposed scheme was set to equal or less than the total number of coefficients used by the state-of-the-art scheme in [7]. Furthermore, the number of iterations employed for training the DPD functions was set at 10, with each iteration utilizing 1.5×10^4 samples for DPD coefficient training.

Linearization Results of the 14 GHz Frequency Doubler

we first discuss the measurement results conducted on the 14 GHz output frequency doubler from ADI (HMC-573). The vector-modulated test signals used in the experiment were generated using a 12-bit, 12 GSps AWG (M8121A from Keysight Technologies), with output centered at an IF of 2 GHz. A low pass filter from mini circuits was used at the

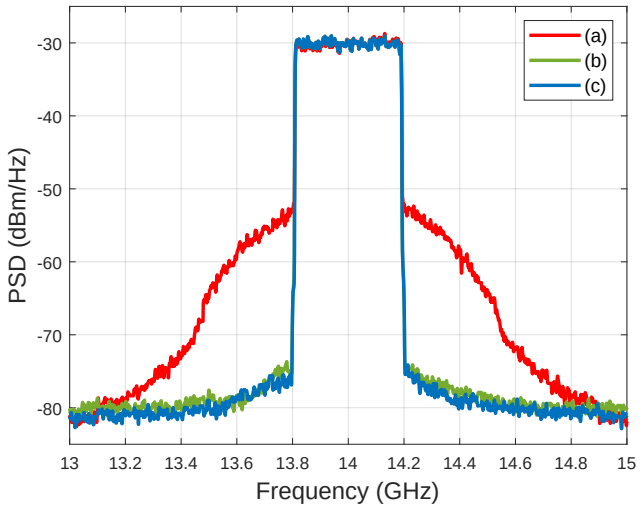


Figure 5.19: Measured output spectra of the 14 GHz frequency-doubler driven with 400 MHz OFDM signal: (a) before DPD with square-root function applied; (b) after DPD in [7]; (c) after proposed DPD.

output of the AWG with a cutoff frequency of 7.2 GHz to filter the AWG's higher Nyquist signals. The IF signal was subsequently up-converted using a cascade of a hybrid-90° (IPP-4120) and an IQ-mixer (MLIQ-0416L from Marki Microwave) to a second IF of 7 GHz. A bandpass filter was used at the output of the mixer to filter the residual image signal and the LO leakage before being amplified using a driver amplifier (MAAM-011109 from MACOM) and fed to the DUT through a direction coupler. The output of the frequency doubler was down-converted to an IF frequency of 3.025 GHz using a heterodyne-mixer (MM-11140H), and captured using a 10-bit, 20 GS/s, 8 GHz analog bandwidth oscilloscope (MSOS804A from Keysight Technologies). The coupler's coupled port was captured using a VNA (5245B from Keysight Technologies) equipped with a spectrum vector stitching option and was used to celebrate the transmitter up to the DUT's input. The LO sources (MXG-N5183B from Keysight Technologies) are used to drive the up-conversion and down-conversion mixers used in the setup. The DPD model parameters for the DPD method in [7] were tuned and selected to a total of 43 coefficients. The proposed DPD parameters were set to a total of 30 coefficients.

Fig. 5.19 shows the PSD at the HMC-573 doubler output when driven with a 256-QAM 400 MHz OFDM signal: (a) before DPD with square-root function applied; (b) after DPD in [7]; (c) after proposed DPD. Using the proposed DPD, the EVM and ACPR improved from 10% and 27.8/27.3 dBc before DPD in (a), to 1% and 50.6/50.3 dBc in (c). In

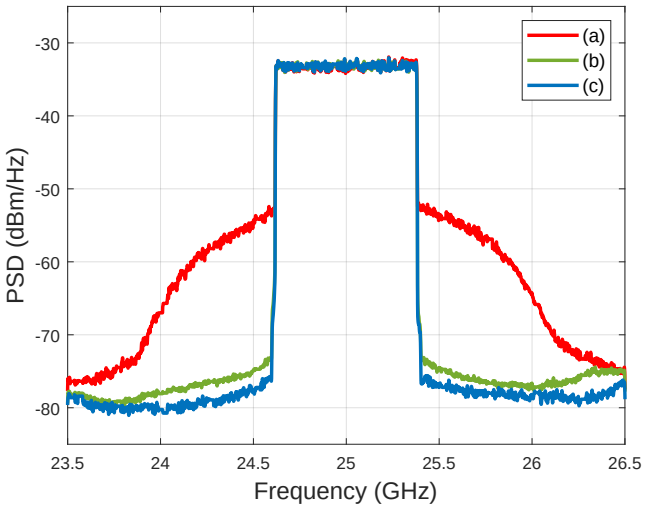


Figure 5.20: Measured output spectra of 25 GHz frequency-doubler driven with 800 MHz OFDM signal: (a) before DPD with square-root function applied; (b) after DPD in [7]; (c) after proposed DPD.

comparison, the state-of-the-art DPD scheme in [7] yielded an EVM of 1.1% and ACPR of 49.5/48.8 dBc. The proposed DPD scheme exhibited enhanced linearization performance, achieving approximately $1-2$ dB improvement in ACPR while avoiding the need for fractional power bases and using fewer DPD basis terms. Subsequently, we investigate the performance of the proposed scheme on two distinct doublers when subjected to signals with bandwidths of up to 800 MHz.

Linearization Results of the 25 GHz Frequency Doubler

we now discuss the measurement results conducted on the 25 GHz output frequency doubler from SpaceK. In order to generate the IF signal to the DUT input, the AWG IF output was up-converted from 2 GHz to an IF of 12.5 GHz using a hybrid-90° (IPP-4120) and an IQ-mixer (MMIQ-1037H from Marki Microwave). A low-pass filter with cutoff frequency of 12.5 GHz was used to filter out the image signal and the LO leakage at the output of the mixer before being amplified using a driver amplifier (MAAM-011109 from MACOM) and fed the DUT through a directional coupler. The output of the directional coupler at the DUT input and the DUT output were connected to a switch with its output connected to a down-converter and captured using the heterodyne-mixer and scope presented in Section 5.2.3. The DPD parameters for the DPD method in [7] were tuned and selected

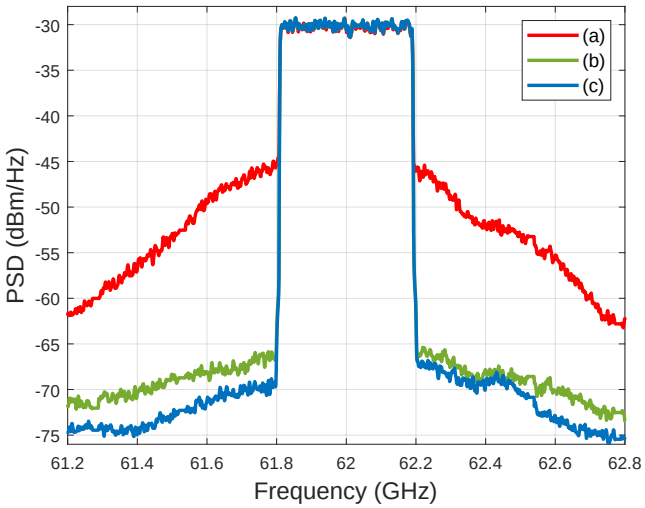


Figure 5.21: Measured output spectra of the 62 GHz frequency-doubler driven with 400 MHz OFDM signal: (a) before DPD with square-root function applied; (b) after DPD in [7]; (c) after proposed DPD.

to a total of 54 coefficients. The proposed method DPD parameters were set to a total of 40 coefficients.

Fig. 5.20 shows the PSD at the SpaceK doubler output when driven with a 256-QAM 800 MHz OFDM signal: (a) before DPD with square-root function applied; (b) after DPD in [7]; (c) after proposed DPD. Using the proposed DPD, the EVM and ACPR improved from 14.1% and 25.0/23.7 dBc before DPD in (a), to 1.4% and 46.3/46.2 dBc in (c). In comparison, the state-of-the-art DPD scheme in [7] yielded an EVM of 1.9% and ACPR of 43.9/43.7 dBc. Notably, in this particular test case, the proposed DPD scheme demonstrated an approximately 3 dB improvement in linearization, specifically in terms of ACPR, compared to the state-of-the-art DPD scheme in [7].

Linearization Results of the 62 GHz Frequency Doubler

In the following, we discuss the measurement results conducted on the custom design 62 GHz output frequency doubler. The DUT is a custom-designed push-push deep class C doubler operating at an output frequency of 62 GHz. The doubler is designed with 45-nm CMOS SOI transistor technology. In order to generate the IF signal to the DUT input, the AWG IF output was up-converted from 2 GHz to an IF of 31 GHz using a cascade of a hybrid-90° (IPP-4120) and an up-converter board (ADMV-1013 from ADI). A bandpass

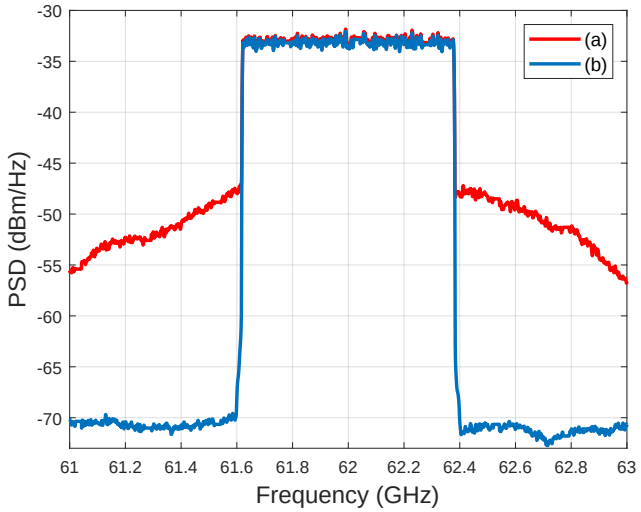


Figure 5.22: Measured output spectra of the 62 GHz frequency-doubler driven with 800 MHz OFDM signal: (a) before DPD with square-root function applied; (b) after proposed DPD.

filter was used to filter out the image signal and the LO leakage at the output of the up-converter before being amplified using a driver amplifier (HMC-1131 from ADI). The driver output was connected to an isolated and subsequently fed to the DUT through a directional coupler. The DUT was mounted on a probe station and 67 GHz ground-signal-ground RF probes were used to access the DUT's input and output ports. The directional coupler coupled port was down-converter and captured using the heterodyne-mixer and scope in Section 5.2.3. The DUT output was connected to a wave-guide heterodyne balanced mixer (SFB-15-N1-M from Sage Millimeter) and digitized using a high-speed (MSOS804A from Keysight Technologies). A high-frequency LO source (HMC-T2270 from Hittite Microwave) was used to drive the mixer's LO port needed to down-convert the DUT' output signal.

Fig. 5.21 shows the PSD at the custom-designed doubler output when driven with a 256-QAM 400 MHz OFDM signal: (a) before DPD with square-root function applied; (b) after DPD in [7]; (c) after proposed DPD. Using the proposed DPD, the EVM and ACPR improved from 22.8% and 18.4/19.6 dBc before DPD in (a), to 1.8% and 41.7/39.6 dBc in (c). In comparison, the state-of-the-art DPD scheme in [7] yielded an EVM of 2.3% and ACPR of 38.1/38.1 dBc. Similarly to the results presented for the 25 GHz doubler shown in Fig. 5.20, using the proposed scheme the linearization performance was around 3 dB better interns of ACPR.

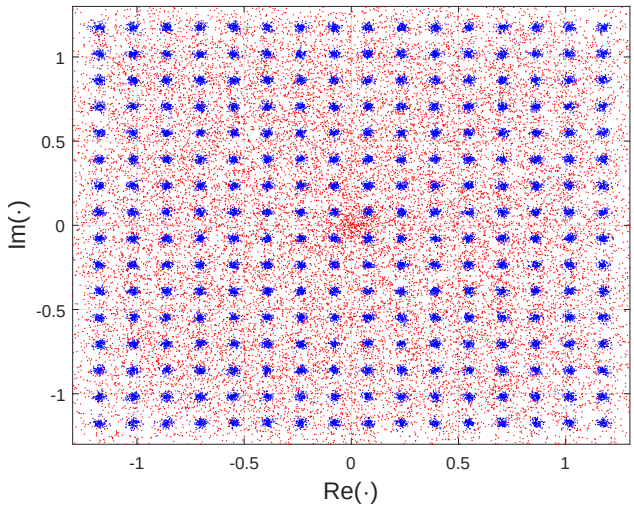


Figure 5.23: Measured constellation of the 62 GHz frequency-doubler driven with 800 MHz OFDM signal: (a) before DPD with square-root function applied; (b) after proposed DPD.

Fig. 5.22 shows the PSD at the custom-designed doubler output when driven with a 256-QAM 800 MHz OFDM signal: (a) before DPD with square-root function applied; (b) after proposed DPD. With the proposed DPD, the EVM and ACPR improved from 24.1% and 18.6/18.0 dBc before DPD in (a), to 2% and 37.0/38.2 dBc in (b). The constellation results before and after employing the proposed DPD scheme are depicted in Fig.5.23, highlighting the cleaner constellation and superior signal quality achieved with the proposed DPD scheme. It is noteworthy that when the DPD method from [7] was applied in this scenario using such wide excitation bandwidth, the DPD failed to converge. This is attributed to the source's inability to synthesize an ideal Dth root function at the DUT input, influenced by residual source linear distortion and the inherent band-limitation of the transmitter chain's components.

Linearization Results of the 28 GHz Frequency Quadrupler

we next discuss the measurement results conducted on the 28 GHz output frequency quadrupled constituted of the cascade of two doublers from ADI (HMC-573 and HMC-578). The AWG IF signal output was up-converted using a cascade of a hybrid-90° (IPP-4120) and an IQ-mixer (MLIQ-0416L from Marki Microwave) to a second IF of 7 GHz. A bandpass filter was used at the output of the mixer to filter the residual image signal and the LO leakage before being amplified using a driver amplifier (MAAM-011109 from MA-

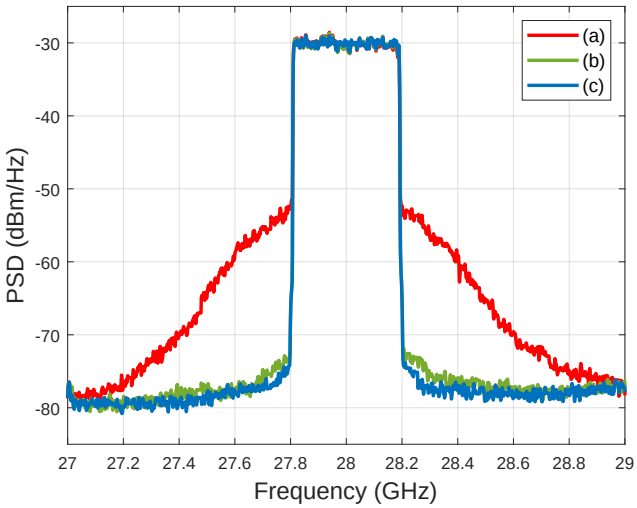


Figure 5.24: Measured output spectra of the 28 GHz frequency-quadrupler driven with 400 MHz OFDM signal: (a) before DPD with square-root function applied; (b) after DPD in [7]; (c) after proposed DPD.

COM) and fed to the DUT through a direction coupler. The directional coupler coupled port and the DUT output were captured using the receiver setup discussed in section 5.2.3. The DPD parameters for the DPD method in [7] were tuned and selected to a total of 42 coefficients. The proposed method DPD parameters were set to a total of 30 coefficients.

Fig. 5.24 shows the PSD at the 28 GHz quadrupler when driven with a 256-QAM 400 MHz OFDM signal: (a) before DPD with fourth-root function applied; (b) after DPD in [7]; (c) after proposed DPD. Using the proposed DPD, the EVM and ACPR improved from 8.8% and 27.6/27.9 dBc before DPD in (a), to 1.2% and 49.8/49.1 dBc in (c). In comparison, the state-of-the-art DPD scheme in [7] yielded an EVM of 1.3% and ACPR of 47.9/46.7 dBc. Fig. 5.24 shows that the proposed DPD method achieves approximately 2 dB better ACPR performance compared to the method in [7], while requiring 20% fewer DPD coefficients.

Linearization Results of the 58 GHz Frequency Octupler

In the following, the measurement results conducted on the 58 GHz output frequency octupler are presented. In order to generate the IF signal centered at 7.25 GHz to the DUT input, the signal generation portion of the setup presented in Section 5.2.3 was used. To capture the octupler output, the waveguide-based receiver used in Section 5.2.3 was

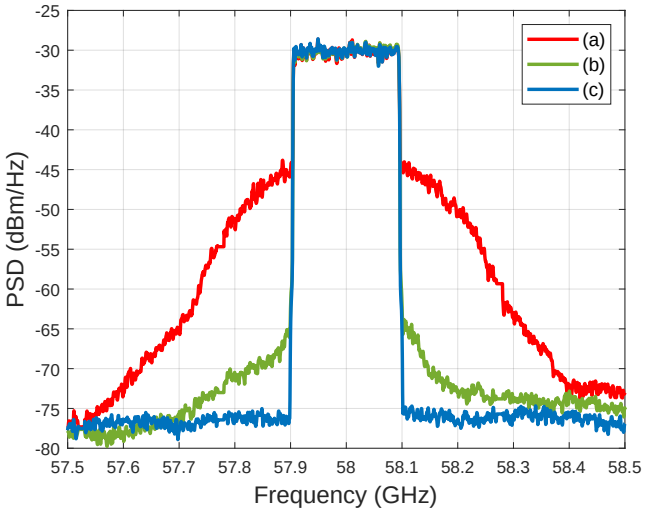


Figure 5.25: Measured output spectra of the 58 GHz frequency-octupler driven with 200 MHz OFDM signal: (a) before DPD with eighth-root function applied; (b) after DPD in [7]; (c) after proposed DPD.

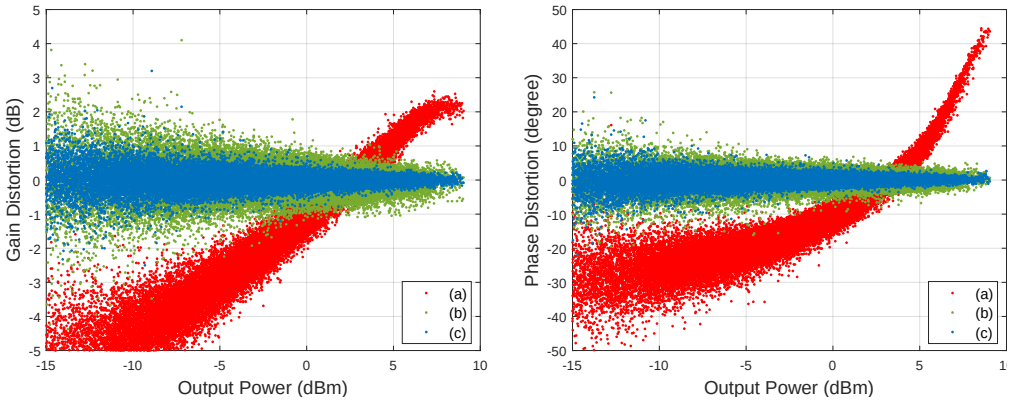


Figure 5.26: Measured gain distortion (Left) and phase distortion (Right) of the 58 GHz frequency-octupler driven with 256-QAM 200 MHz OFDM signal: a) before linearization with eighth-root applied; (b) after DPD in [7]; (c) after proposed DPD.

used. The DPD parameters for the DPD method in [7] were tuned and selected to a total of 64 coefficients. The proposed method DPD parameters were set to a total of 47 coefficients.

Fig. 5.25 shows the PSD at the 58 GHz octupler output when driven with a 256-QAM 200 MHz OFDM signal: (a) before DPD with eighth-root function applied; (b) after DPD in [7]; (c) after proposed DPD. Using the proposed DPD, the EVM and ACPR improved from 23.4% and 19.7/19.3 dBc before DPD in (a), to 0.8% and 48.0/47.8 dBc in (c). In comparison, the state-of-the-art DPD scheme in [7] yielded an EVM of 3.1% and ACPR of 41.0/40.8 dBc. Notably, in this particular test case, the proposed DPD scheme demonstrated an approximately 8 dB improvement in linearization, in terms of ACPR, compared to the state-of-the-art DPD scheme in [7]. Fig.5.26 presents the gain (left) and phase (right) distortion plots corresponding to the measurements in Fig.5.25. From Fig.5.26, it is evident that the state-of-the-art DPD in [7] exhibits non-negligible residual nonlinearity compared to the proposed scheme, as highlighted by the dispersive gain and phase distortion plots. These results highlight that previous state-of-the-art DPD linearization performance may be affected when the multiplication order is increased. In contrast, the proposed DPD scheme was able to maintain excellent linearization results. Unfortunately, wider bandwidth measurements for the frequency octupler case were not possible due to a lack of filters capable of removing unwanted leakage signals from the IF stage mixers.

5.3 Device Characterization Under Wideband Modulated Signals using Vector Network Analyzer Frequency Extenders

The rapid evolution of wireless communication systems has spurred a growing demand for higher data rates and superior signal quality. Critical to this evolution are measurement instruments capable of precisely characterizing RF components under CW and wideband modulated signal excitation conditions. At MMW frequencies, this precise characterization is enabled through the use of VNA frequency extenders to enable CW characterization and through the use of wideband up and down-converters for the modulated signal testing. In this section, a measurement system that leverages VNA frequency extenders for component/system testing under both CW and modulated signal excitation is presented along with the enabling signal processing algorithms and experimental validation on an OML VNA frequency extender operating at 58 GHz and on a custom-built doubler operating 120 GHz. The proposed measurement system builds on the promising results achieved in linearizing FXs highlighted in the previous sections. Particularly, this section proposes a novel linearizer based on ILC that can mitigate the nonlinear distortions exhibited by FXs

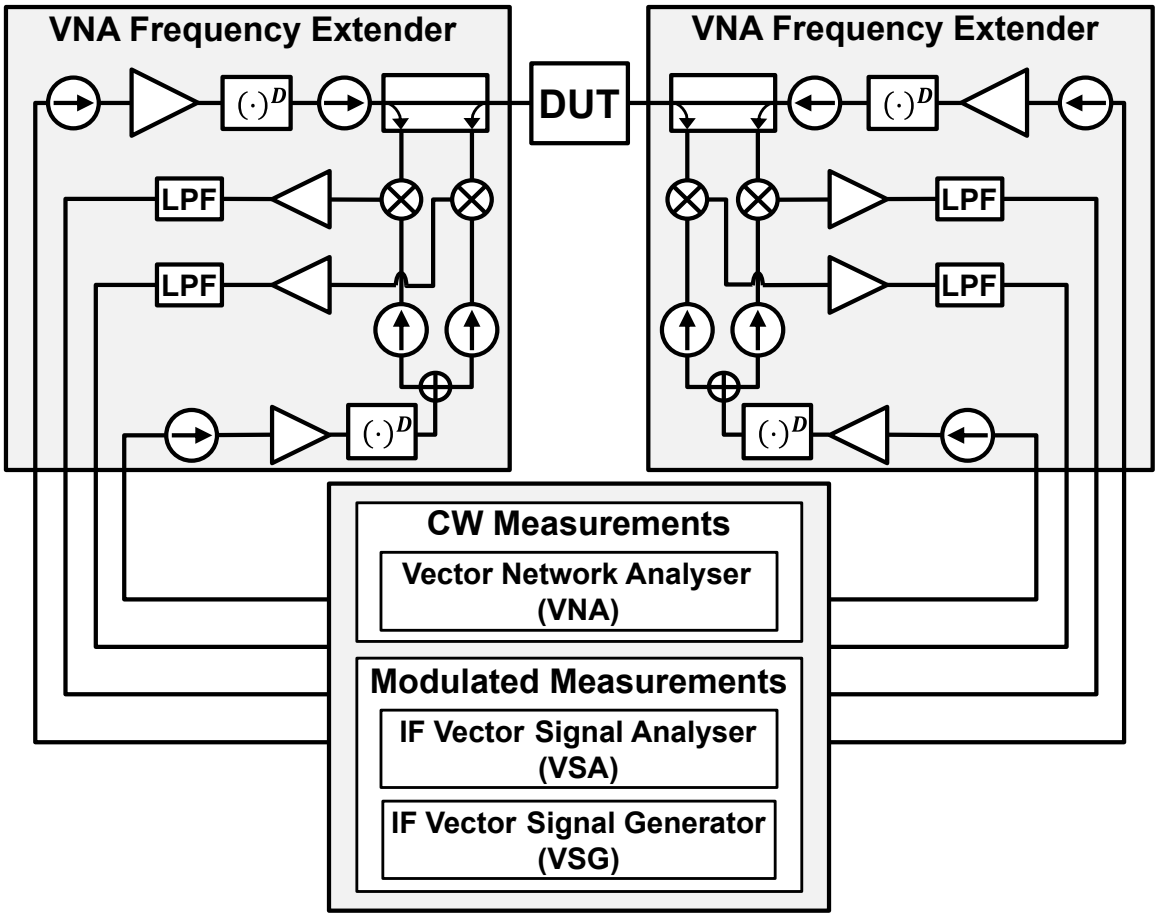


Figure 5.27: System block diagram of the proposed measurement system for component level characterization under CW and modulated signal excitation.

in the VNA frequency extenders, hence enabling wideband signal generation. Furthermore, the proposed system uses a frequency stitching-based receiver to enable the application of VNA frequency extenders to receive wideband modulated signals. Of note, the proposed ILC linearizer introduced in this section operates on a fundamentally different principle compared to DPD. Unlike DPD, ILC may not always yield a closed-form analytical solution and relies on the assumption that the generated signal is periodic. However, ILC offers a distinct advantage: it can potentially achieve optimal linearization of the DUT without limitations imposed by model accuracy. As a result, ILC is often used in PA-based systems as a benchmark for the ideal linearization that DPD solutions aim to achieve.

the proposed ILC linearizer in this section is fundamentally different from DPD. ILC may not result in an analytical solution and relies on the periodicity assumption of the generated signal. Nevertheless ILC has the advantage over DPD to yield an optimal linearization of the DUT without being hindered by modeling accuracy and is commonly used at the benchmark linearization to be targeted by the DPD solution.

5.3.1 Problem Formulation

In this subsection, the proposed unified measurement system, shown in Fig. 5.27, designed to facilitate the comprehensive characterization of DUTs under both CW and modulated signal excitations is formulated. The system leverages VNA frequency extenders to enable RF-modulated signal generation and analysis. To realize this capability, a novel ILC linearization scheme, specifically designed for FXs, is formulated and applied to linearize the FXs within VNA frequency extenders thus enabling the mixer-less generation of wideband modulated signals at RF frequencies with exceptional signal integrity. To enable this linearization, the TOR in the VNA frequency extenders is used to serve as feedback. Nevertheless, these TORs are typically narrowband given that they are designed for CW operation. To mitigate this limitation, a receiver stitching method that leverage the period nature of test signals to enable the capture of wideband signals using narrowband receivers is presented.

Wideband Signal Analysis Algorithm Using Narrow-band Receivers

To enable the capture of the wideband periodic signal $\tilde{x}[n]$, the signal $\tilde{x}[n]$ is partitioned into P sections, each section having a length of $S+1$ and containing L frequency component overlap. These partitions are then captured sequentially or in parallel using low-speed high-resolution receivers. The pth partition of $\tilde{x}[n]$, denoted as $\tilde{x}_p[n]$, can be expressed as follows,

$$\tilde{x}_p[n] = \sum_{k \in \mathcal{A}_p} \tilde{X}[k] e^{j2\pi nk/N}, \tag{5.68}$$

where the set $\mathcal{A}_p = \{p \times (S-L), ..., p \times (S-L)+S\}$. In order to avoid the image challenge in frequency-stitching-based receivers arising from the down-converting stage, in the following, the proposed digital image rejection approach is presented. Let the $x(t)$, be the wideband periodic RF continuous-time signal to be captured such that,

$$x(t) = \Re\left\{\tilde{x}(t) e^{j\omega_{RF} t}\right\}, \tag{5.69}$$

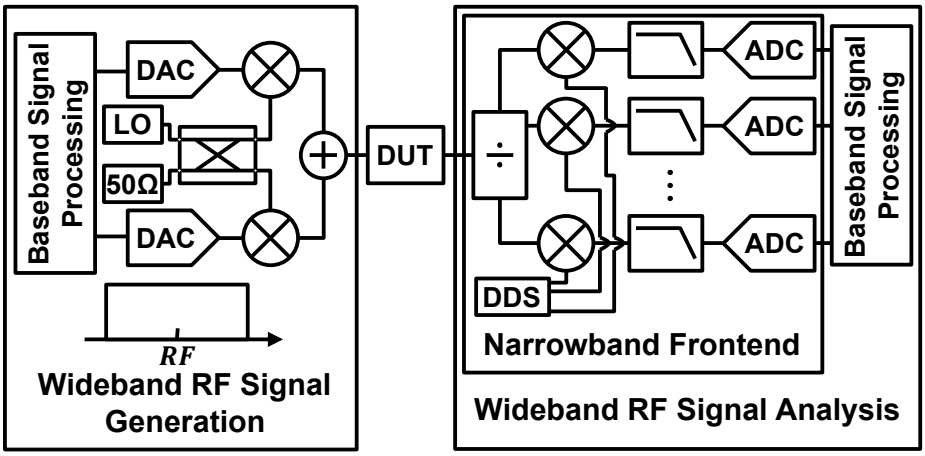


Figure 5.28: Proposed system block diagram.

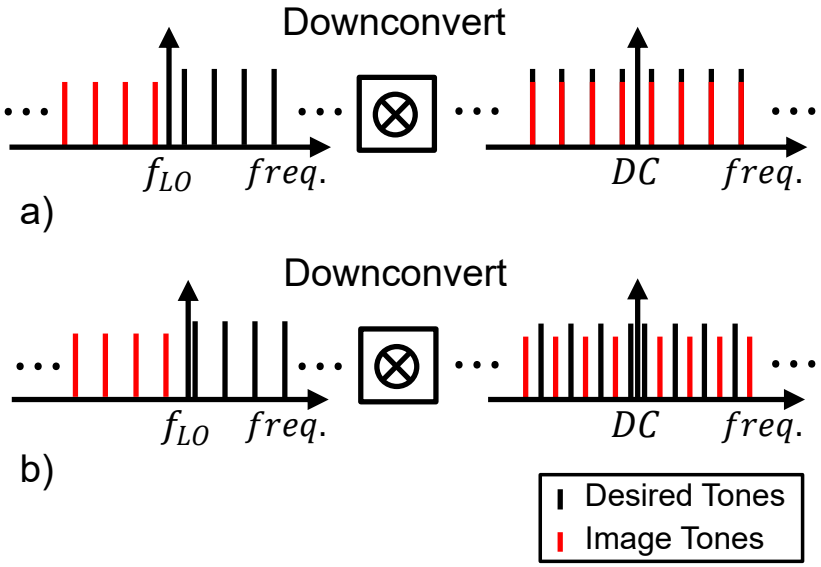


Figure 5.29: a) Image signal overlapping onto the desired signal. b) Select LO at 3/4 of the signal tones, the image signal tones will fall in between the desired signal tones.

where ω_{RF} is the RF angular frequency. Substituting (5.68) in (5.69) we then have,

$$x(t) = \Re\left\{\sum_{k=0}^{N-1} \tilde{X}[k] e^{j\omega_0 kt} e^{j\omega_{RF} t}\right\}. \tag{5.70}$$

When digitizing the p'th partition of the signal $x(t)$, i.e.,

$$x_p(t) = \Re\left\{\sum_{k\in\mathcal{A}_p} \tilde{X}[k]e^{j\omega_0 kt}e^{j\omega_{RF}t}\right\}, \tag{5.71}$$

using a heterodyne receiver, the RF signal $x(t)$ is down-converted to an IF frequency where the LO angular frequency, ω'_p, is selected to be,

$$\omega'_p = \omega_p - \omega_{RF} + \Delta\omega_p, \tag{5.72}$$

where $\omega_p = 2\pi \times p \times (S-L) \times \mathrm{Fs}/N$ is the angular frequency of the partition $x_p(t)$ first signal tone of interest and $\Delta\omega_p$ is an arbitrary offset. Accordingly, we have

$$x_p(t) = \Re\left\{\sum_{k=0}^{N-1} \tilde{X}[k]e^{j\omega_0 kt}e^{-j2\pi(\mathcal{A}_p(1)+\Delta\omega_p)t}\right\}, \tag{5.73}$$

For simplicity, the receiver bandwidths are assumed to have a bandwidth equal to the signal's partition bandwidth, consequently, the bandwidth-limited version of the above can be expressed as follows,

$$\bar{x}_p(t) = \sum_{k\in\mathcal{A}_p} \tilde{X}[k]e^{j\omega_0 kt}e^{-i2\pi(\mathcal{A}_p(1)+\Delta\omega_p)t} + \tag{5.74}$$

$$\sum_{k\in\mathcal{A}'_p} \tilde{X}^*[k]e^{-j\omega_0 kt}e^{j2\pi(\mathcal{A}_p(1)+\Delta\omega_p)t}. \tag{5.75}$$

where $\mathcal{A}'_p = \{p\times(S-L)-S, ..., p\times(S-L)\}$. The above can be further simplified to,

$$x_p(t) = \sum_{k\in\mathcal{A}_p} \tilde{X}[k]e^{j\omega_0 kt}e^{-j2\pi(\mathcal{A}_p(1)+\Delta\omega_p)t} + \tag{5.76}$$

$$\tilde{X}^*[2\mathcal{A}_p(0)-k]e^{j\omega_0 kt}e^{-j2\pi(\mathcal{A}_p(1)-\Delta\omega_p)t}. \tag{5.77}$$

Note, when $\Delta\omega_p = 0$, the above simplifies to

$$x_p(t) = \sum_{k\in\mathcal{A}_p} \left(\tilde{X}[k] + \tilde{X}^*[2\mathcal{A}_p(0)-k]\right)e^{j\omega_0 kt}e^{-j2\pi\mathcal{A}_p(1)t}, \tag{5.78}$$

where the image terms are folded on top of the desired tones. In order to avoid this from happening, a clever choice of $\Delta\omega_p$ needs to be considered. In this work we select

$$\Delta\omega_p = \frac{\omega_0}{Q}, \tag{5.79}$$

where Q is an arbitrary integer and $Q > 2$. Consequently, (5.73) can be rewritten as follows,

$$x_p(t) = \sum_{k \in \mathcal{A}_p} \tilde{X}[k] e^{j\omega_0 kt} e^{-j2\pi(\mathcal{A}_p(1)+\frac{\omega_0}{Q})t} + \tag{5.80}$$

$$\tilde{X}^*[2\mathcal{A}_p(0) - k] e^{j\omega_0 kt} e^{-j2\pi(\mathcal{A}_p(1)-\frac{\omega_0}{Q})t}, \tag{5.81}$$

where the first desired tone appears at $\frac{\omega_0}{Q}$ and the desired tone spacing are ω_0. Lets assume that the receiver capture Q periods of the signal $x_p(t)$, i.e., $Q \times N$ samples, then the CBBE signal $\tilde{x}_p[n]$ can be expressed as follows,

$$\tilde{x}_p[n] = x_p[n] e^{j2\pi/N(\mathcal{A}_p(1)+\frac{1}{Q})n} \tag{5.82}$$

$$= \Re \left\{ \sum_{k'=0}^{Q\times N-1} \tilde{X}_p[k'] e^{j2\pi nk'/(Q\times N)} \right\}, \tag{5.83}$$

where

$$\tilde{X}_p[k'] = \begin{cases} \tilde{X}[(k'-1)/Q] & k' \in \mathcal{A}_p \times Q + 1 \\ \tilde{X}^*[2\mathcal{A}_p(0) - (k'+1)/Q] & k' \in \mathcal{A}_p \times Q - 1 \\ 0 & \text{Otherwise} \end{cases} \tag{5.84}$$

Finally, the anti-aliasing can be achieved by zeroing their terms for which $k \notin \mathcal{A}_p \times Q + 1$ and then translating the signal to a length of N, (33) simplifies to (5.68) and the aforementioned steps can be used to stitch the signal.

Iterative Learning Control Algorithm

In the following, the proposed ILC algorithm used to linearize the FXs within VNA frequency extenders in the proposed measurement system in Fig. 5.27, is formulated. Let $\tilde{d}[n]$, $\tilde{z}[n]$, and $\tilde{y}[n]$ be the desired FX output, the FX input and the measured FX output, respectively.

We begin by applying the additive error model, as established in [7], where the FX output $\tilde{y}[n]$ is expressed as,

$$\tilde{y}[n] = G\left(\tilde{z}\left[n\right]\right)^D + \tilde{e}\left(\tilde{\mathbf{z}}(n)\right). \tag{5.85}$$

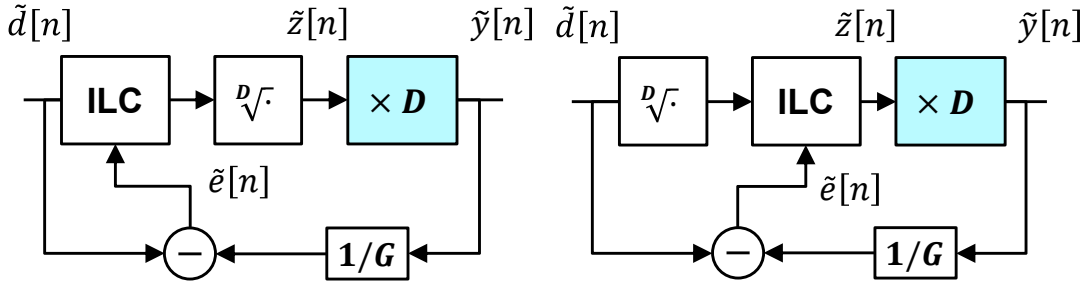


Figure 5.30: Block diagram illustrating; (Left) the PA-based ILC algorithm extended to FXs; (Right) the proposed FX-based ILC algorithm.

Here, G denotes the FX's conversion gain, D is multiplication factor, $\tilde{e}(\tilde{\mathbf{z}}(n))$ represents the FX's nonlinearity, $\tilde{\mathbf{z}}(n) = (\tilde{z}[n], ..., \tilde{z}[n-M])^T$, and M is the system's memory depth.

PA-based ILC formulation:: To linearize the FX output, an extension of the ILC solution commonly applied to PAs, as shown in Fig. 5.30 (Left), can be employed. Accordingly, if the linearizer effectively compensates for the FX nonlinearity, $\tilde{y}[n]$ in (5.85) simplifies to the desired input signal $\tilde{d}[n]$ scaled by the FX conversion gain. Assuming the existence of such a solution, $\tilde{z}[n]$ in (5.85) can be expressed as a function of the desired and error signals as follows,

$$\tilde{z}[n] = \sqrt[D]{\tilde{d}[n] - \frac{\tilde{e}(\tilde{\mathbf{z}}(n))}{G}}. \tag{5.86}$$

Considering a weakly nonlinear scenario, (5.86) can be solved iteratively to yield a sequence of predistorted signals, $\tilde{z}_k[n]$ for $k = 1, 2, ...$, as follows,

$$\tilde{z}_{k+1}[n] = \sqrt[D]{\tilde{d}[n] - \frac{\tilde{e}(\tilde{\mathbf{z}}_k(n))}{G}}, \tag{5.87}$$

where the initial condition is set as $\tilde{z}_1[n] = \sqrt[D]{\tilde{d}[n]}$. If $\tilde{y}_k[n]$ is taken to be $G\left(\tilde{z}_k[n]\right)^D + \tilde{e}_k\left(\tilde{\mathbf{z}}_k(n)\right)$, (5.87) simplifies to,

$$\tilde{z}_{k+1}[n] = \sqrt[D]{(\tilde{z}_k[n])^D - \mu\frac{\tilde{y}_k[n] - G\tilde{d}[n]}{G}}, \tag{5.88}$$

where $\mu \in (0, 1]$ is a learning parameter introduced to help with convergence. Therefore, (5.88) encapsulates the iterative training process of the PA-based ILC linearizer.

Proposed FX-based ILC: formulation: As an alternative to the PA-based ILC solution discussed above, in this work, we propose a novel ILC algorithm, as shown in Fig. 5.30 (Right), that is tailored to linearize the FXs within VNA frequency extenders. To that end, let us first assume that the optimal linearization signal can be expressed using an additive model such that,

$$\tilde{z}[n] = \sqrt[D]{\tilde{d}[n]} + \tilde{e}'[n]. \tag{5.89}$$

where $\tilde{e}'[n]$ is a high-order nonlinearity term assumed to be much smaller than $\sqrt[D]{\tilde{d}[n]}$. Substituting, (5.89) in (5.85), we have

$$\tilde{y}[n] = G\left(\sqrt[D]{\tilde{d}[n]} + \tilde{e}'[n]\right)^D + \tilde{e}\left(\tilde{\mathbf{z}}(n)\right). \tag{5.90}$$

Using binomial approximation, (5.90) can be simplified to,

$$\tilde{y}[n] \approx GD\tilde{z}[n]\left(\sqrt[D]{\tilde{d}\,[n]}\right)^{D-1} - G\left(D-1\right)\tilde{d}\,[n] + \tilde{e}\left(\tilde{\mathbf{z}}(n)\right). \tag{5.91}$$

Furthermore, if $\tilde{z}[n]$ is taken to be the optimal linearizer solution, $\tilde{y}[n]$ in (5.91) simplifies to the desired input signal $\tilde{d}[n]$ scaled by the FX conversion gain. Consequently, $\tilde{z}[n]$ in (5.91), can be expressed as follows,

$$\tilde{z}[n] = \sqrt[D]{\tilde{d}\,[n]} - \frac{\tilde{e}\left(\tilde{\mathbf{z}}(n)\right)}{GD\left(\sqrt[D]{\tilde{d}\,[n]}\right)^{D-1}}. \tag{5.92}$$

Considering a weakly nonlinear scenario, the recursive function (5.92) can be solved iteratively as follows,

$$\tilde{z}_{k+1}[n] = \sqrt[D]{\tilde{d}\,[n]} - \frac{\tilde{e}\left(\tilde{\mathbf{z}}_k(n)\right)}{GD\left(\sqrt[D]{\tilde{d}\,[n]}\right)^{D-1}}. \tag{5.93}$$

where the initial condition is set as $\tilde{z}_1[n] = \sqrt[D]{\tilde{d}[n]}$. If $\tilde{y}_k[n]$ is taken to be the FX output at the kth iteration, from (5.91), (5.93) can be rewritten as follows,

$$\tilde{z}_{k+1}[n] = \tilde{z}_k\,[n] - \mu\frac{\tilde{y}_k[n] - G\tilde{d}[n]}{GD\left(\sqrt[D]{\tilde{d}\,[n]}\right)^{D-1}}, \tag{5.94}$$

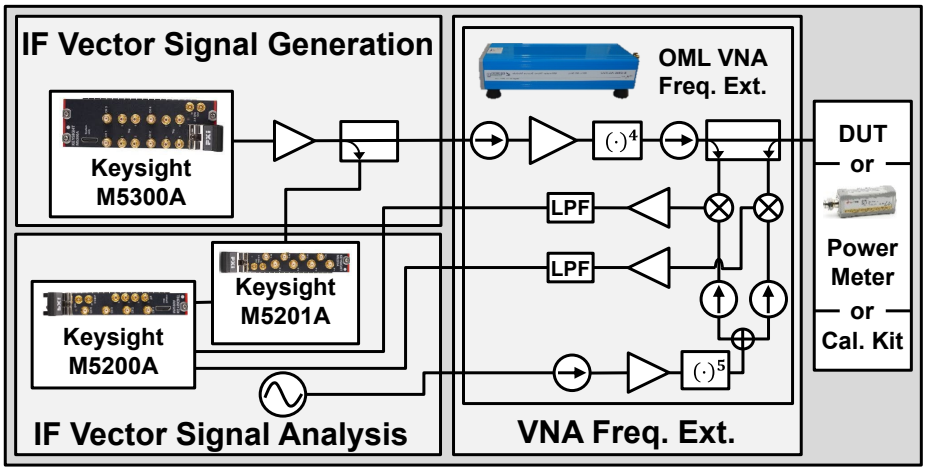


Figure 5.31: Measurement setup using the OML VNA extenders.

where $\mu \in (0, 1]$ is a learning parameter introduced to help with convergence. Therefore, (5.94) encapsulates the iterative training process of the proposed FX-based ILC linearizer. Note, for PAs ($D = 1$), both (5.88) and (5.94) simplify to the same solution. This demonstrates continuity in the solution between the proposed ILC algorithm and those previously established in the literature for PAs.

5.3.2 Experimental Validation

In this subsection, experimental validation of the proposed measurement system and enabling algorithms are presented using an OML VNA frequency extender operating at 58 GHz and a D-band custom-built frequency doubler operating at 120 GHz.

Measurement Setup OML

To validate the proposed measurement system, and demonstrate the effectiveness of the proposed ILC and receiver stitching algorithms to linearize the FX within VNA frequency extenders, an experimental setup, shown in Fig. 5.31, was developed. A picture of the measurement setup is shown in Fig. 5.32. The FX to be linearized is a quadrupler ($D=4$) within an OML V-band VNA frequency extender. The modulated test signals used in the experiment were generated using two 14-bit, 2 GHz bandwidth, 2.4 Gsps RF-AWGs (M5300A from Keysight) with their outputs frequency-stitched to generate up to 4 GHz

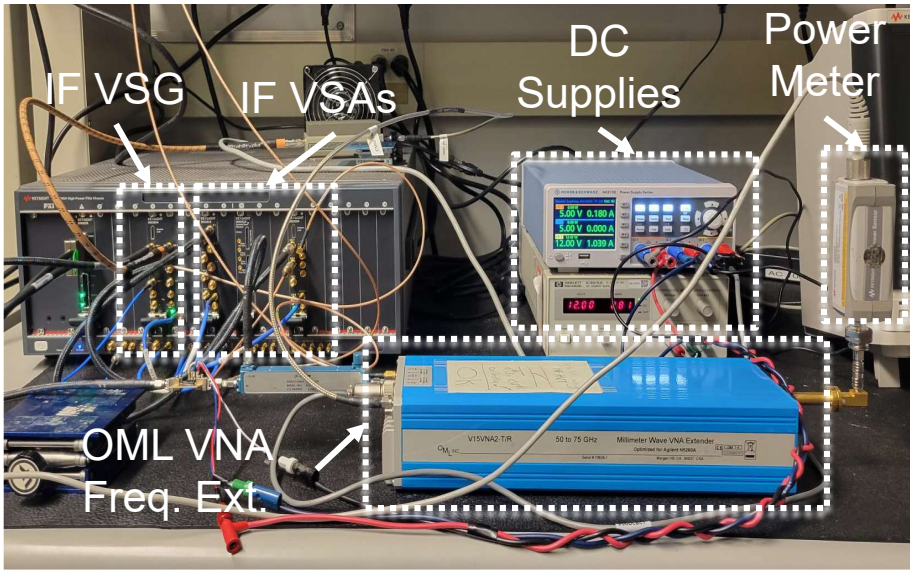


Figure 5.32: Picture of the measurement setup using the OML VNA extenders.

of modulated bandwidth centered around an IF of 14.4 GHz. A driver amplifier was then used to amplify the RF-AWG IF signal output before being fed to the OML IF input port through a directional coupler. The coupler-coupled port was used for transmitter calibration. The output of the OML's frequency quadrupled centered at 57.6 GHz was then sampled and down-converted using the OML's built-in directional coupler and down-converter mixer and was then captured using a 12-bits, 2 GHz bandwidth and 4.8 Gsps digitizer (M5200A from Keysight). To accommodate for the OML's feedback path limited modulation bandwidth of 300 MHz, a frequency stitching receiver-based approach was adopted where the OML's mixer LO signal was swept, and the wideband spectrum at the FX output was captured sequentially, and reconstructed digitally using the proposed receiver stitching algorithm discussed in the previous section. The OML's waveguide output was connected to a power meter for power calibration.

Measurement Results OML

Fig. 5.33 shows the PSD (Left) and constellation (Right) at the OML's frequency quadrupler output when driven with a 256-QAM 400 MHz OFDM signal. Using the ILC algorithms, the EVM and ACPR improved from 44.8% and 17.1/17.0 dBc, before linearization and with Dth-root applied in (a), to 1.6% and 49.2/49.3 dBc in (b) using the PA-based ILC,

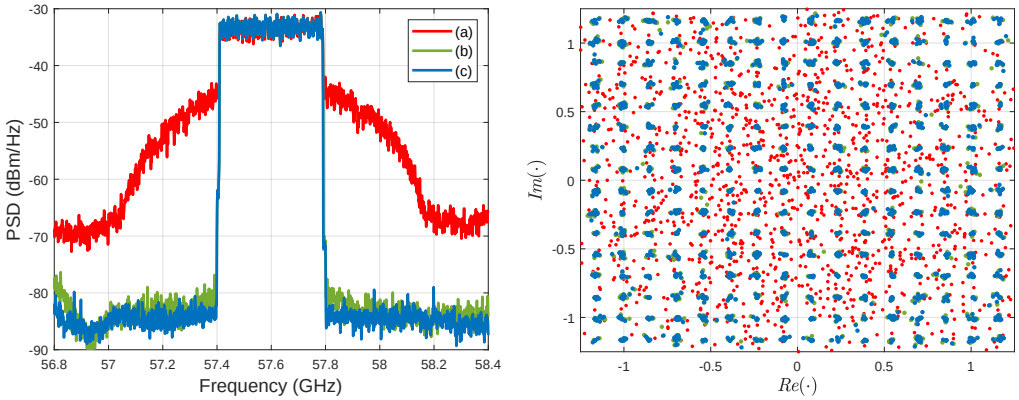


Figure 5.33: Measured PSD (Left) and constellation (Right) at OML's frequency quadrupled output when driven with 256-QAM 400 MHz OFDM signal: a) before linearization with $\boldsymbol{D}$th-root applied; b) with PA-based ILC applied; c) with proposed FX-based applied.

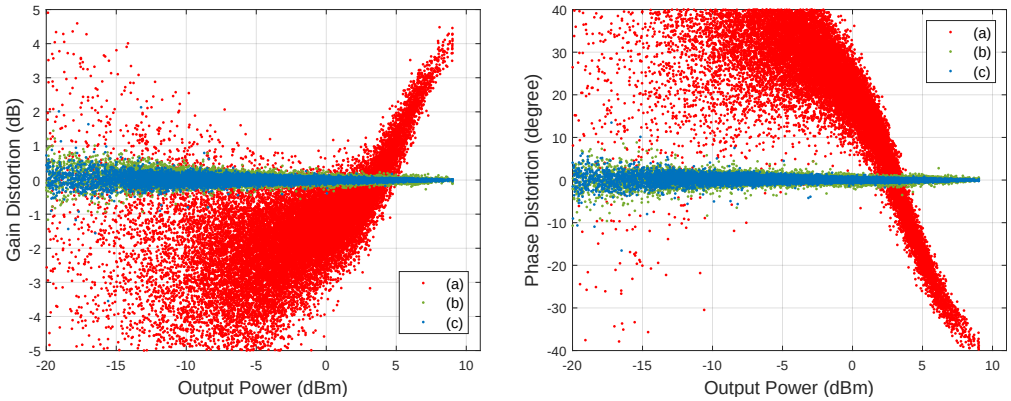


Figure 5.34: Measured gain distortion (Left) and phase distortion (Right) at OML's frequency quadrupled output when driven with 256-QAM 400 MHz OFDM signal: a) before linearization with $\boldsymbol{D}$th-root applied; b) with PA-based ILC applied; c) with proposed FX-based applied.

and to 1.45% and 50.7/51.0 dBc in (c) using the proposed FX-based ILC. It is interesting to note that both ILC algorithms were able to achieve excellent linearization performance at the quadrupler output as illustrated by the flat gain (Left) and phase (Right) distortion plots shown in Fig. 5.34 (b) and (c).

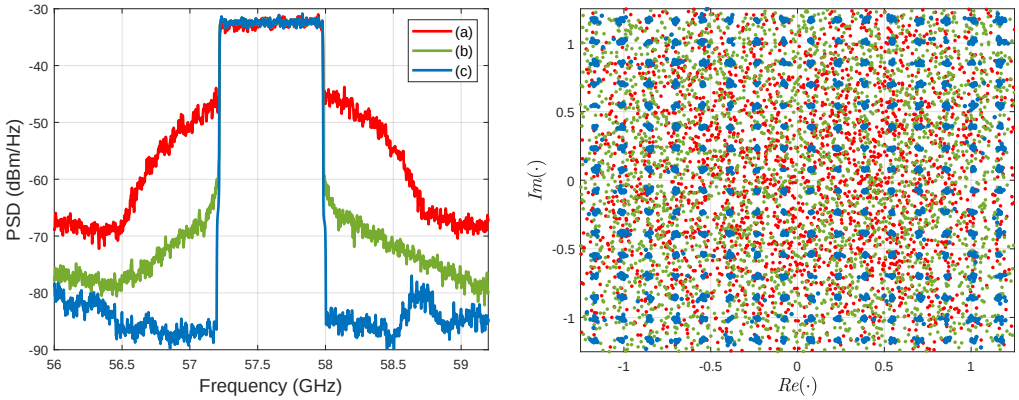


Figure 5.35: Measured PSD (Left) and constellation (Right) at OML's frequency quadrupled output when driven with 256-QAM 800 MHz OFDM signal: a) before linearization with Dth-root applied; b) with PA-based ILC applied; c) with proposed FX-based applied.

Fig. 5.35 shows the PSD (Left) and constellation (Right) at the OML's frequency quadrupler output when driven with a 256-QAM 800 MHz OFDM signal. Using the ILC algorithms, the EVM and ACPR improved from 49.4% and 17.9/15.7 dBc, before linearization and with Dth-root applied in (a), to 13.9% and 36.2/34.8 dBc in (b) using the PA-based ILC, and to 1.17% and 51.6/48.7 dBc in (c) using the proposed FX-based ILC. Note, the reported deterioration in linearization results by the PA-based ILC, compared to the proposed FX-based ILC, is attributed to linear memory at the OML's frequency quadrupler input, leading to strong nonlinear memory at the FX output. This phenomenon is evident in the gain (Left) and phase distortion (Right) plots before linearization and with Dth-root applied, as shown in Fig. 5.36 (a), exhibiting pronounced dispersion. This strong nonlinear memory adversely impacted the accuracy of the weakly nonlinear assumption made in Section 5.3.1, causing the PA-based ILC algorithm to exhibit non-convergence, as evidenced by the PSD in Fig. 5.35 (b) and the gain (Left) and phase (Right) distortion plots in Fig. 5.36 (b). In contrast, the proposed FX-based ILC algorithm in Section 5.3.1 remained unaffected, demonstrating successful convergence and excellent linearization results, as indicated by the flat gain (Left) and phase (Right) distortion plots in Fig. 5.36 (c).

Measurement Setup D-Band

In the following, additional experiments conducted at D-band on a custom-built doubler are presented to further validate the capacity of the proposed FX-based ILC algorithm

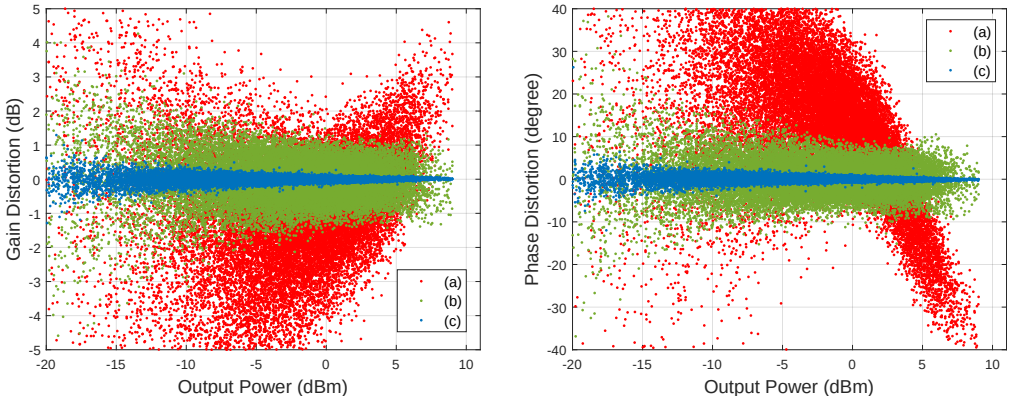


Figure 5.36: Measured gain distortion (Left) and phase distortion (Right) at OML's frequency quadrupled output when driven with 256-QAM 800 MHz OFDM signal: a) before linearization with Dth-root applied; b) with PA-based ILC applied; c) with proposed FX-based applied.

to linearize FXs. The block diagram and picture of the D-band measurement setup are shown in Fig. 5.37 and Fig. 5.38 respectively. An AWG (Keysight M8190A) was utilized to generate an OFDM signal centered at 2 GHz. This signal was up-converted to a center frequency of 14 GHz using an IQ mixer, amplified by a driver amplifier, and fed to a heterodyne mixer to further up-convert the signal to 60 GHz before being fed to the DUT through a series of a driver amplifier, an isolator, and a directional coupler. The DUT was mounted on a probe station, and GSG RF probes were employed to access the DUT's input and output ports. The DUT output was connected to a waveguide variable attenuator, and the RF signal was down-converted using a WR-6 down-converter from Eravant. The DUT's output signals was then sampled using a 10-bit, 20 Gsps, 8 GHz analog bandwidth oscilloscope (Keysight MSOS804A). LO sources (Keysight MXG-N5183B and Hittite Microwave HMC-T2270) were employed to drive the up-conversion and down-conversion mixers in the setup.

Measurement Results D-Band

Fig. 5.39 illustrates the PSD (Left) and constellation (Right) at the output of the D-band doubler when driven by a 256-QAM 800 MHz OFDM signal. Leveraging the proposed FX-based ILC algorithm, substantial enhancements were observed in both EVM and ACPR, improving from 14.8% and 22.5/23.1 dBc, respectively, prior to linearization and with Dth-

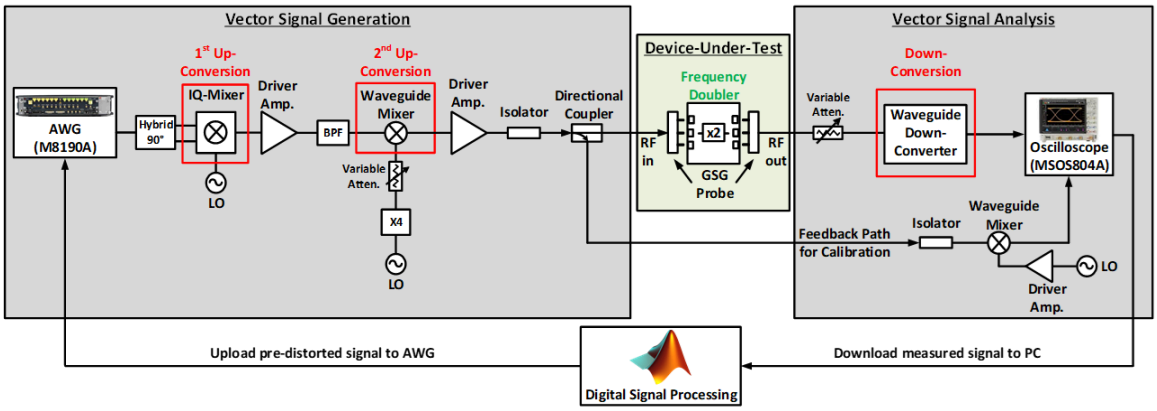


Figure 5.37: Measurement setup for the D-Band doubler.

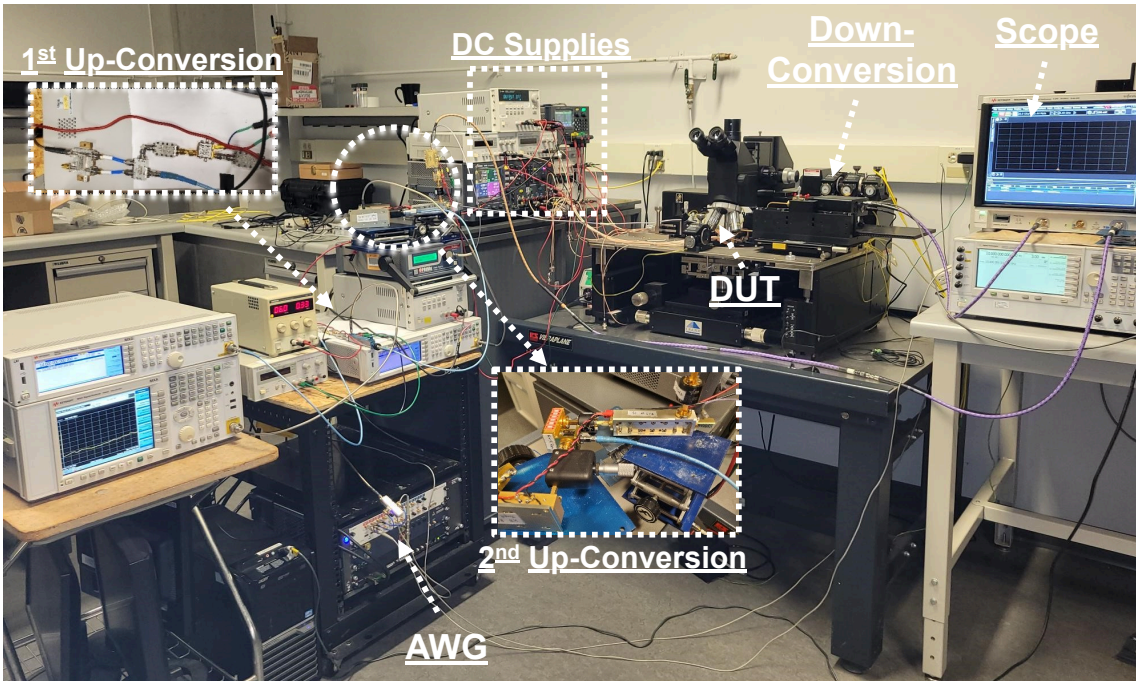


Figure 5.38: Picture of the measurement setup for the D-Band doubler.

root applied (a), to 0.8% and 49.8/50.7 dBc in (b), showcasing the efficacy of the FX-based ILC algorithm.

Similarly, Fig. 5.40 displays the PSD (Left) and constellation (Right) at the output of

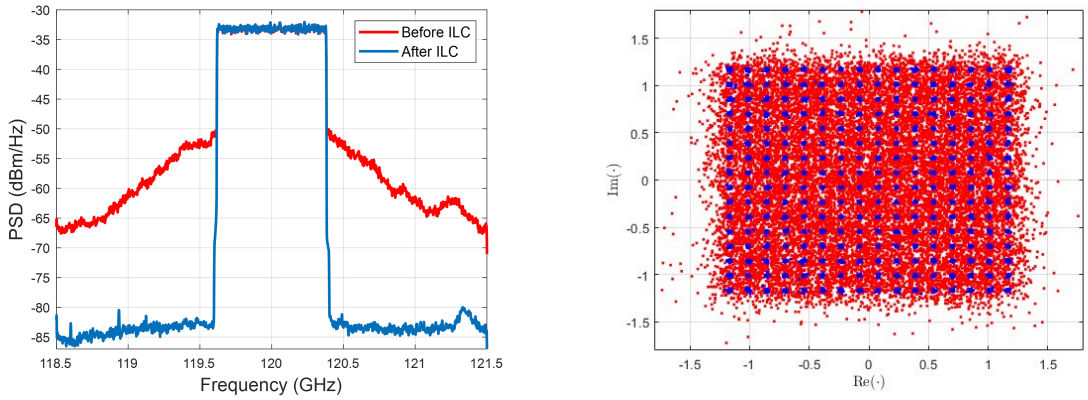


Figure 5.39: Measured PSD (Left) and constellation (Right) at the D-band frequency doubler output when driven with 256-QAM 800 MHz OFDM signal: a) before linearization with Dth-root applied; b) with PA-based ILC applied; c) with proposed FX-based applied.

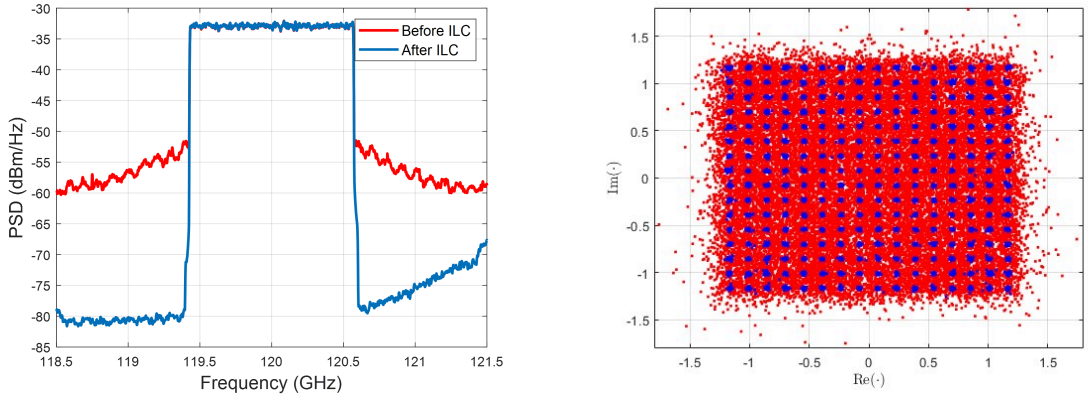


Figure 5.40: Measured PSD (Left) and constellation (Right) at the D-band frequency doubler output when driven with 256-QAM 1200 MHz OFDM signal: a) before linearization with Dth-root applied; b) with PA-based ILC applied; c) with proposed FX-based applied.

the D-band doubler when stimulated with a 256-QAM 1200 MHz OFDM signal. Employing the same FX-based ILC algorithm, notable improvements were achieved, with EVM and ACPR enhancing from 15.6% and 24.0/24.1 dBc, pre-linearization and with Dth-root applied (a), to 1.5% and 47.1/37.5dBc in (b). The imbalance observed in Fig.5.40 (Left) is attributed to LO leakage in the transmitter, resulting in distortions close to the signal center frequency, a phenomenon that can be mitigated through the implementation of filters

at the doubler input to eliminate the LO leakage.

These results underscore the capability of the proposed approach to generate wideband modulated signals with exceptional signal quality, as evidenced by the minimal distortion depicted in the constellation plots in Fig.5.39 (Right) and Fig.5.40 (Right) for the 800 MHz and 1200 MHz test signals, respectively. It is noteworthy that the reported outcomes utilizing 1200 MHz represent the first instance in the literature achieving linearization over such a wide bandwidth, achieving a remarkable data rate of 10.7 Gbps. These measurement results further advocate for the utilization of FXs and, specifically, VNA frequency extenders for component and system testing at higher frequencies.

Chapter 6

Thesis Summary and Future Work

6.1 Thesis Summary

This thesis has been dedicated to enhancing the performance of wireless communication systems operating in the MMW and sub-THz frequency bands through a combination of system-level innovations and advanced signal processing techniques. The key findings and contributions of this thesis are summarized as follows:

In **Publications I**, a comprehensive theoretical analysis was conducted to investigate the intricate dependencies among array nonlinearity, antenna mutual coupling, and steering angles. This analysis led to the derivation of a closed-form equation capturing these relationships. Notably, the study highlighted the significant impact of tapering on antenna mutual coupling and array nonlinear behavior. Building upon this, an optimization algorithm was developed to synthesize tapering coefficients aimed at mitigating the array's nonlinear behavior dependency on beam-steering, particularly in the presence of antenna mutual coupling. Experimental validation on a 64-element RF beamforming array operating at 28 GHz confirmed the effectiveness of this approach. By applying these tapering coefficients, the array's nonlinear behavior ceased to vary with steering angles, enabling linearization of RF beamforming arrays at any specific steering angle without the need for adaptive retraining of the linearization function during beam-steering.

In **Publications II**, the impact of antenna mutual coupling on the nonlinear behavior of FX-based beamforming transmitters was investigated. Through a circuit-inspired analysis, it was revealed that FX-based beamforming transmitters exhibit resilience to antenna mutual coupling. These findings were validated through simulations and experiments conducted on a developed multiplier-based array prototype. This research underscores the

attractiveness of FX-based architectures for high-frequency ultra-wideband vector-signal generation and their scalability to array systems.

In **Publications III**, a TOR utilizing NF probes for integration within beamforming arrays was proposed. The associated signal processing algorithms that enable the use of NF captured signals using the TOR for DPD training were presented. The formation assumed a flat coupling between the NF probes and the array radiating antenna elements. Experimental validation on a 16-element RF beamforming array, including four NF probes, demonstrated that the proposed NF-based DPD achieved similar linearization performance to FF-based DPD techniques while only using information available at the transmitter.

In **Publications IV**, the NF-based DPD algorithm was extended to account for the frequency-selective coupling between the NF probes and the radiating antenna elements in the array. Additionally, an active calibration algorithm combining the advantages of element-wise and FF-based active calibration schemes was introduced. Experimental validation on a 16-element RF beamforming array showcased improved calibration performance compared to state-of-the-art techniques and enhanced linearization performance compared to the NF-based DPD algorithm developed in **Publications III**.

In **Publications V**, a DPD scheme for linearizing FXs driven with wideband modulated signals under constrained transmitter TOR feedback bandwidths was proposed. The impact of limiting the bandwidth of the $\boldsymbol{D}$th root function on DPD linearization performance was investigated. Furthermore, the DPD training was derived to account for the constrained transmitter and TOR bandwidths. Experimental validation demonstrated excellent linearization performance, outperforming previous state-of-the-art techniques and enabling the generation of 800 MHz OFDM signals using FXs.

In **Publications VI**, a reformulation of the approach to linearizing FXs was developed. Instead of training the DPD function to linearize the cascade of the $\boldsymbol{D}$th root function and FX nonlinearity, the proposed DPD linearizes the deviation of FXs from an ideal power function. Experimental results showed significant improvements in linearization performance compared to state-of-the-art DPDs, with better resilience to residual calibration errors in the transmitter and reduced complexity as the formulation does not require factional power bases. These experiments were conducted on different FXs with multiplication orders ranging from two to eight and operating at out frequencies ranging from 14 GHz to 58 GHz.

In **Publications VII**, a novel measurement system for accurate and calibrated measurements at MMW and sub-THz frequencies was proposed. This system enables both CW and modulated signal measurements with a single setup, streamlining testing and characterization processes. The development of this measurement system required the creation

of two distinct algorithms, facilitating ultra-wideband signal acquisition using narrowband receivers, and linearization of VNA frequency extenders. This innovative approach to modulated signal measurements holds significant potential to advance high-frequency component/system testing and characterization in RF front-end development. Experimental validations were conducted on a VNA frequency extender driven with up to 800 MHz with 256-QAM OFDM modulation at 58 GHz and a custom-built frequency doubler operating at 120 GHz, driven with up to 1200 MHz 256-QAM OFDM signals. These experiments showcased the effectiveness of the proposed ILC-based linearizer and frequency stitching receivers in enabling the generation of distortion-free wideband vector-modulated signals and validated the effectiveness of using VNA frequency extenders for modulated signal testing at higher frequencies.

6.2 Future Work

This thesis has presented significant contributions toward enhancing the performance of MMW/sub-THz wireless communication systems. However, the field of high-frequency communication is constantly evolving, and there are exciting avenues for future research that build upon the work presented here.

6.2.1 Extending the Framework to Advanced Array Architectures

- **Dual-Polarization and Multi-Beam Arrays**: The current work focused on single-polarization arrays. Future investigations can extend the proposed modeling and optimization techniques to dual-polarization and multi-beam array configurations. These arrays offer improved flexibility and capacity but introduce additional complexities. Research is needed to understand the impact of mutual coupling on the nonlinear behavior of these arrays and develop optimization algorithms for mitigating these effects.
- **NF-based DPD for Advanced Array Architectures**: This thesis demonstrated the effectiveness of NF-based TORs for DPD training in single-beam arrays. Future work can explore the extension of this concept to dual-polarization and multi-beam arrays. Investigating the challenges and potential benefits of NF-based DPD in these more complex architectures is a promising area of research.

6.2.2 DPD for Frequency Multipliers

- **Multi-Band DPD for FXs**: The proposed formulated DPD schemes for FXs focused on single-band operation. Future research can explore the development of multi-band DPD algorithms specifically tailored for FXs. This would be particularly beneficial for applications requiring operation across multiple frequency bands within the MMW/sub-THz regime.

6.2.3 Additional Areas of Exploration

- **Hardware Implementation and System Integration**: While the work presented in this thesis focused on simulations and proof-of-concept experiments, future efforts can explore the hardware implementation of the proposed designs and algorithms. This would involve integrating the developed circuits and functionalities into complete communication transceiver systems, allowing for real-world validation and performance characterization.
- **Machine Learning for Hardware Optimization**: Machine learning techniques have shown promise in various areas of communication system design. Future research can investigate the application of machine learning algorithms to optimize hardware components or system parameters within the context of MMW/sub-THz communication systems.

By pursuing these areas of future work, researchers can build upon the foundation established in this thesis and further advance the development of high-performance, reliable, and efficient wireless communication systems operating in the MMW/sub-THz spectrum.

References

[1] "Ericsson mobility report," Ericssin, Stockholm, Sweeden, Tech. Rep., 2023. [Online]. Available: https://www.ericsson.com/4ae12c/assets/local/reports-papers/mobility-report/documents/2023/ericsson-mobility-report-november-2023.pdf

[2] Q. Wu and et al., "Digital predistortion for dual linearly-polarized millimeter wave transmitters with cross-polarization interference," in *IEEE MTT-S Int. Wir. Symp. (IWS)*, Nanjing, China, Aug. 2021, pp. 1–3.

[3] Y. Park, K. M. Low, and J. Kenney, "Digital predistortion linearization of frequency multipliers," in *IEEE MTT-S Int. Microw. Symp. Dig.*, vol. 3, July 2003, pp. 1695–1698 vol.3.

[4] L. Liu, W. Chen, L. Ma, and H. Sun, "Single-PA-Feedback Digital Predistortion for Beamforming MIMO Transmitter," in *Proc. IEEE Int. Conf. Microw. Millim. Wave Technol. (ICMMT)*, Beijing, China, Jun. 2016, pp. 573–575.

[5] A. Chung, A. M. Darwish, E. Viveiros, H. A. Hung, P. Mitran, and S. Boumaiza, "Analysis and Compensation of Nonidealities in Frequency Multiplier-Based High-Frequency Vector Signal Generators," *IEEE Trans. Microw. Theory Tech.*, vol. 67, no. 6, pp. 2270–2283, 2019.

[6] I. Jaffri, A. Ben Ayed, A. M. Darwish, P. Mitran, and S. Boumaiza, "Novel baseband equivalent model for digital predistortion of wideband frequency-multiplier-based millimeter wave sources," *IEEE Trans. Microw. Theory Tech.*, vol. 68, no. 9, pp. 3942–3957, 2020.

[7] I. Jaffri, A. B. Ayed, A. M. Darwish, P. Mitran, and S. Boumaiza, "Novel baseband equivalent model for digital predistortion of wideband frequency-multiplier-based millimeter wave sources," *IEEE Trans. Microw. Theory Techn.*, vol. 68, no. 9, pp. 3942–3957, 2020.

[8] K. Katayama, K. Takano, S. Amakawa, S. Hara, A. Kasamatsu, K. Mizuno, K. Takahashi, T. Yoshida, and M. Fujishima, "A 300 GHz CMOS transmitter with 32-QAM 17.5 Gb/s/ch capability over six channels," *IEEE J. Solid-State Circuits*, vol. 51, no. 12, pp. 3037–3048, 2016.

[9] K. Takano, S. Amakawa, K. Katayama, S. Hara, R. Dong, A. Kasamatsu, I. Hosako, K. Mizuno, K. Takahashi, T. Yoshida, and M. Fujishima, "17.9 a 105Gb/s 300GHz CMOS transmitter," in *IEEE Int. Solid-State Circuits Conf.*, Feb. 2017, pp. 308–309.

[10] C. Wang, H. Herdian, W. Zheng, C. Liu, J. Mayeda, Y. Liu, O. A. Yong, W. Wang, Y. Zhang, C. D. Gomez, A. Shehata, S. Kato, I. Abdo, T. Jyo, H. Hamada, H. Takahashi, H. Sakai, A. Shirane, and K. Okada, "24.3 a 236-to-266ghz 4-element amplifier-last phased-array transmitter in 65nm cmos," in *2024 IEEE Int. Solid-State Circuits Conf. (ISSCC)*, vol. 67, 2024, pp. 415–417.

[11] H.-J. Song, J.-Y. Kim, K. Ajito, N. Kukutsu, and M. Yaita, "50-Gb/s direct conversion QPSK modulator and demodulator MMICs for terahertz communications at 300 GHz," *IEEE Trans. Microw. Theory Tech.*, vol. 62, no. 3, pp. 600–609, 2014.

[12] N. Sarmah, P. R. Vazquez, J. Grzyb, W. Foerster, B. Heinemann, and U. R. Pfeiffer, "A wideband fully integrated sige chipset for high data rate communication at 240 GHz," in *11th Eur. Microw. Integr. Circuits Conf.*, Oct. 2016, pp. 181–184.

[13] K. K. Tokgoz, S. Maki, J. Pang, N. Nagashima, I. Abdo, S. Kawai, T. Fujimura, Y. Kawano, T. Suzuki, T. Iwai, K. Okada, and A. Matsuzawa, "A 120Gb/s 16QAM CMOS millimeter-wave wireless transceiver," in *IEEE Int. Solid-State Circuits Conf.*, Feb. 2018, pp. 168–170.

[14] I. M. Milosavljevic, D. P. Krcum, D. P. Glavonjic, S. P. Jovanovic, V. R. Mihajlovic, D. M. Tasovac, and V. M. Milovanovic, "A SiGe highly integrated FMCW transmitter module with a 59.5–70.5-GHz single sweep cover," *IEEE Trans. Microw. Theory Tech.*, vol. 66, no. 9, pp. 4121–4133, 2018.

[15] P. Rodríguez-Vazquez, J. Grzyb, N. Sarmah, B. Heinemann, and U. R. Pfeiffer, "A 65 Gbps QPSK one meter wireless link operating at a 225–255 GHz tunable carrier in a sige hbt technology," in *2018 IEEE Radio Wirel. Symp. RWS*, Jan. 2018, pp. 146–149.

[16] M. H. Eissa, A. Malignaggi, R. Wang, M. Elkhouly, K. Schmalz, A. C. Ulusoy, and D. Kissinger, "Wideband 240-GHz transmitter and receiver in BiCMOS technology

with 25-Gbit/s data rate," *IEEE J. Solid-State Circuits*, vol. 53, no. 9, pp. 2532–2542, 2018.

[17] Q. Zhong, Z. Chen, N. Sharma, S. Kshattry, W. Choi, and K. O. Kenneth, "300-GHz CMOS QPSK transmitter for 30-Gbps dielectric waveguide communication," in *Proc. Cust. Integr. Circuits Conf.*, Apr. 2018, pp. 1–4.

[18] K. K. Tokgoz and K. Okada, "Millimeter-wave CMOS transceiver toward 1Tbps wireless communication," in *IEEE Int. Symp. Circuits Syst.*, May 2019, pp. 1–4.

[19] C. M. Grotsch, S. Wagner, and I. Kallfass, "An active gate-pumped transconductance upconverter for terahertz frequencies," in *Ger. Microw. Conf.*, Apr. 2019, pp. 236–239.

[20] P. Rodríguez-VAzquez, J. Grzyb, B. Heinemann, and U. R. Pfeiffer, "A 16-QAM 100-Gb/s 1-M wireless link with an evm of 17% at 230 GHz in an SiGe technology," *IEEE Microw. Wirel. Compon. Lett.*, vol. 29, no. 4, pp. 297–299, 2019.

[21] F. M. Barradas, L. C. Nunes, T. R. Cunha, P. M. Lavrador, P. M. Cabral, and J. C. Pedro, "Compensation of long-term memory effects on gan hemt-based power amplifiers," *IEEE Trans. Microw. Theory Techn.*, vol. 65, no. 9, pp. 3379–3388, 2017.

[22] V. Raghavan and J. Li, "Deembedding Static Nonlinearities and Accurately Identifying and Modeling Memory Effects in Wide-Band RF Transmitters," *IEEE Access*, vol. 7, pp. 10 392–10 401, 2019.

[23] T. Liu, S. Boumaiza, and F. M. Ghannouchi, "Deembedding static nonlinearities and accurately identifying and modeling memory effects in wide-band RF transmitters," *IEEE Trans. Microw. Theory Techn.*, vol. 53, no. 11, pp. 3578–3587, 2005.

[24] A. Darwish, J. Qiu, E. Viveiros, H. A. Hung, and J. Hesler, "Efficient linear transmission of complex waveforms at 216 ghz using nonlinear multiplier chains," in *2016 IEEE MTT-S Int Microw. Symp.*, 2016, pp. 1–3.

[25] A. Chung, M. B. Rejeb, A. Darwish, H. A. Hung, and S. Boumaiza, "Frequency doubler based outphasing system for millimeter wave vector signal generation," in *2018 48th European Microwave Conference (EuMC)*, 2018, pp. 1469–1472.

[26] T.-Y. Yang and H.-K. Chiou, "A 25–75 GHz miniature double balanced frequency doubler in 0.18-μm CMOS technology," *IEEE Microw. Wirel. Compon. Lett.*, vol. 18, no. 4, pp. 275–277, Mar. 2008.

[27] J. Deng, Y. Yang, Z. Zhu, and X. Luo, "A 140–220-GHz balanced doubler with 8.7%–12.7% efficiency," *IEEE Microw. Wirel. Compon. Lett.*, vol. 28, no. 6, pp. 515–517, Apr. 2018.

[28] A. Y.-K. Chen, Y. Baeyens, Y.-K. Chen, and J. Lin, "A 36–80 GHz high gain millimeter-wave double-balanced active frequency doubler in SiGe BiCMOS," *IEEE Microw. Wirel. Compon. Lett.*, vol. 19, no. 9, pp. 572–574, Aug. 2009.

[29] Y. Zhu, H. Ghaleb, V. Rieß, N. Joram, and F. Ellinger, "A 60 GHz frequency doubler with 3.4-dBm output power and 4.4% DC-to-RF-efficiency in 130-nm SiGe BiCMOS," in *2021 16th Europ. Microw. Integrated Circuits Conf. (EuMIC)*, London, UK, Apr. 2022, pp. 100–103.

[30] F. Ellinger and H. Jackel, "Ultracompact SOI CMOS frequency doubler for low power applications at 26.5-28.5 GHz," *IEEE Microw. Wirel. Compon. Lett.*, vol. 14, no. 2, pp. 53–55, Feb. 2004.

[31] Y. Ye, B. Yu, A. Tang, B. Drouin, and Q. J. Gu, "A high efficiency E-band CMOS frequency doubler with a compensated transformer-based balun for matching enhancement," *IEEE Microw. Wirel. Compon. Lett.*, vol. 26, no. 1, pp. 40–42, Dec. 2016.

[32] G. Liu, J. Jayamon, J. Buckwalter, and P. Asbeck, "Frequency doublers with 10.2/5.2 dBm peak power at 100/202 GHz in 45nm SOI CMOS," in *2015 IEEE Radio Freq. Integr. Circuits Symp. (RFIC) Dig.*, Phoenix, USA, May 2015, pp. 271–274.

[33] Z. Chen, Y. Yu, Y. Wu, H. Liu, C. Zhao, and K. Kang, "A 19.5% efficiency 51–73-GHz high-output power frequency doubler in 65-nm CMOS," *IEEE Microw. Wirel. Compon. Lett.*, vol. 29, no. 12, pp. 818–821, Nov. 2019.

[34] C. So and S. Hong, "A V-band differential push–push frequency doubler with a current-reuse gm-boosted buffer," *IEEE Microw. Wirel. Compon. Lett.*, vol. 33, no. 3, pp. 299–302, 2023.

[35] H. Fu, H. Wang, and K. Ma, "A high conversion gain frequency doubler using transformer-based second harmonic feedback technique in 28-nm CMOS," *IEEE Microw. Wirel. Compon. Lett.*, vol. 32, no. 9, pp. 1071–1074, Apr. 2022.

[36] J. Oh, J. Jang, C.-Y. Kim, and S. Hong, "A W-band high-efficiency CMOS differential current-reused frequency doubler," *IEEE Microw. Wirel. Compon. Lett.*, vol. 25, no. 5, pp. 307–309, Mar. 2015.

[37] W. Lee and A. Valdes-Garcia, "W-band SiGe frequency doubler with optimum harmonic termination for 14% efficiency," *IEEE Microw. Wirel. Compon. Lett.*, vol. 31, no. 3, pp. 272–275, Jan. 2021.

[38] X. Wu, Z. Kang, Y. Wang, and L. Wu, "A 53–78 GHz complementary push–push frequency doubler with implicit dual resonance for output power combining," *IEEE Trans. Circuits Syst. I: Regul. Pap.*, vol. 70, no. 3, pp. 1202–1213, Feb. 2023.

[39] J. Jang, H. Lim, and T. W. Kim, "A CMOS complementary common gate capacitive cross-coupled frequency doubler," *IEEE Trans. Circuits Syst. II: Express Br.*, vol. 69, no. 9, pp. 3694–3698, May 2022.

[40] S. Li, T. Chi, T.-Y. Huang, M.-Y. Huang, D. Jung, and H. Wang, "A buffer-less wideband frequency doubler in 45-nm CMOS-SOI with transistor multiport waveform shaping achieving 25% drain efficiency and 46–89 GHz instantaneous bandwidth," *IEEE Solid-State Circuits Lett.*, vol. 2, no. 4, pp. 25–28, Apr. 2019.

[41] S. Maas, *Nonlinear Microwave and RF Circuits, Second Edition.* Artech, 2003.

[42] M. Eladwy, A. Ben Ayed, and S. Boumaiza, "Vna-based characterization of frequency multipliers phase-distortions under continuous-wave and modulated signal excitation," in *101st ARFTG Microw. Meas. Conf.*, June 2023, pp. 1–4.

[43] T. L. Marzetta, "Noncooperative cellular wireless with unlimited numbers of base station antennas," *IEEE Wirel. Commun.*, vol. 9, no. 11, pp. 3590–3600, 2010.

[44] X. Jiang, A. Decurninge, K. Gopala, F. Kaltenberger, M. Guillaud, D. Slock, and L. Deneire, "A framework for over-the-air reciprocity calibration for tdd massive mimo systems," *IEEE Wirel. Commun.*, vol. 17, no. 9, pp. 5975–5990, 2018.

[45] J. Jose, A. Ashikhmin, T. L. Marzetta, and S. Vishwanath, "Pilot contamination and precoding in multi-cell tdd systems," *IEEE Wirel. Commun.*, vol. 10, no. 8, pp. 2640–2651, 2011.

[46] V. Venkateswaran and A.-J. van der Veen, "Analog beamforming in mimo communications with phase shift networks and online channel estimation," *IEEE Trans. Signal Process.*, vol. 58, no. 8, pp. 4131–4143, 2010.

[47] W. Zhang, X. Xia, Y. Fu, and X. Bao, "Hybrid and full-digital beamforming in mmwave massive mimo systems: A comparison considering low-resolution adcs," *China Commun.*, vol. 16, no. 6, pp. 91–102, 2019.

[48] W. Roh, J.-Y. Seol, J. Park, B. Lee, J. Lee, Y. Kim, J. Cho, K. Cheun, and F. Aryanfar, "Millimeter-wave beamforming as an enabling technology for 5g cellular communications: theoretical feasibility and prototype results," *IEEE Commun. Mag.*, vol. 52, no. 2, pp. 106–113, 2014.

[49] S. Li, Z. Zhang, B. Rupakula, and G. M. Rebeiz, "An eight-element 140-ghz wafer-scale if beamforming phased-array receiver with 64-qam operation in cmos rfsoi," *IEEE J. Solid-State Circuits*, vol. 57, no. 2, pp. 385–399, 2022.

[50] J. Pang, R. Wu, Y. Wang, M. Dome, H. Kato, H. Huang, A. Tharayil Narayanan, H. Liu, B. Liu, T. Nakamura, T. Fujimura, M. Kawabuchi, R. Kubozoe, T. Miura, D. Matsumoto, Z. Li, N. Oshima, K. Motoi, S. Hori, K. Kunihiro, T. Kaneko, A. Shirane, and K. Okada, "A 28-ghz cmos phased-array transceiver based on lo phase-shifting architecture with gain invariant phase tuning for 5g new radio," *IEEE J. Solid-State Circuits*, vol. 54, no. 5, pp. 1228–1242, 2019.

[51] O. E. Ayach, S. Rajagopal, S. Abu-Surra, Z. Pi, and R. W. Heath, "Spatially sparse precoding in millimeter wave mimo systems," *IEEE Wirel. Commun.*, vol. 13, no. 3, pp. 1499–1513, 2014.

[52] B.-H. Ku, P. Schmalenberg, O. Inac, O. D. Gurbuz, J. S. Lee, K. Shiozaki, and G. M. Rebeiz, "A 77–81-ghz 16-element phased-array receiver with ±50° beam scanning for advanced automotive radars," *IEEE Trans. Microw. Theory Techn.*, vol. 62, no. 11, pp. 2823–2832, 2014.

[53] K. Kibaroglu, M. Sayginer, and G. M. Rebeiz, "A low-cost scalable 32-element 28-ghz phased array transceiver for 5g communication links based on a 2×2 beamformer flip-chip unit cell," *IEEE J. Solid-State Circuits*, vol. 53, no. 5, pp. 1260–1274, 2018.

[54] K. Kibaroglu, M. Sayginer, T. Phelps, and G. M. Rebeiz, "A 64-element 28-ghz phased-array transceiver with 52-dbm eirp and 8–12-gb/s 5g link at 300 meters without any calibration," *IEEE Trans. Microw. Theory Techn.*, vol. 66, no. 12, pp. 5796–5811, 2018.

[55] K. Hausmair, S. Gustafsson, C. Sánchez-Pérez, P. N. Landin, U. Gustavsson, T. Eriksson, and C. Fager, "Prediction of nonlinear distortion in wideband active antenna arrays," *IEEE Trans. Microw. Theory Techn.*, vol. 65, no. 11, pp. 4550–4563, 2017.

[56] T. E. Bogale, L. B. Le, A. Haghighat, and L. Vandendorpe, "On the number of rf chains and phase shifters, and scheduling design with hybrid analog–digital beamforming," *IEEE Wirel. Commun.*, vol. 15, no. 5, pp. 3311–3326, 2016.

[57] F. Sohrabi and W. Yu, "Hybrid digital and analog beamforming design for large-scale antenna arrays," *IEEE J. of Selected Topics in Signal Processing*, vol. 10, no. 3, pp. 501–513, 2016.

[58] W. Ni and X. Dong, "Hybrid block diagonalization for massive multiuser mimo systems," *IEEE Trans. Commun.*, vol. 64, no. 1, pp. 201–211, 2016.

[59] O. El Ayach, R. W. Heath, S. Rajagopal, and Z. Pi, "Multimode precoding in millimeter wave mimo transmitters with multiple antenna sub-arrays," in *IEEE Global Commun. Conf. (GLOBECOM2013)*, 2013, pp. 3476–3480.

[60] L. Dai, X. Gao, J. Quan, S. Han, and C.-L. I, "Near-optimal hybrid analog and digital precoding for downlink mmwave massive mimo systems," in *IEEE Int. Conf. Commun. (ICC2015)*, 2015, pp. 1334–1339.

[61] X. Gao, L. Dai, S. Han, C.-L. I, and R. W. Heath, "Energy-efficient hybrid analog and digital precoding for mmwave mimo systems with large antenna arrays," *IEEE J. Sel. Areas Commun.*, vol. 34, no. 4, pp. 998–1009, 2016.

[62] R. Méndez-Rial, C. Rusu, N. González-Prelcic, A. Alkhateeb, and R. W. Heath, "Hybrid mimo architectures for millimeter wave communications: Phase shifters or switches?" *IEEE Access*, vol. 4, pp. 247–267, 2016.

[63] A. Chung, M. B. Rejeb, Y. Beltagy, A. M. Darwish, H. A. Hung, and S. Boumaiza, "IQ Imbalance Compensation and Digital Predistortion for Millimeter-wave Transmitters Using Reduced Sampling Rate Observations," *IEEE Trans. Microw. Theory Techn.*, vol. 66, no. 7, pp. 3433–3442, 2018.

[64] F. Mkadem, M. C. Fares, S. Boumaiza, and J. Wood, "Complexity-reduced volterra series model for power amplifier digital predistortion," *Analog Integr. Circuits Signal Process.*, vol. 79, no. 2, p. 331–343, 2014.

[65] D. Morgan, Z. Ma, J. Kim, M. Zierdt, and J. Pastalan, "A generalized memory polynomial model for digital predistortion of rf power amplifiers," *IEEE Trans. Signal Process.*, vol. 54, no. 10, pp. 3852–3860, 2006.

[66] A. Zhu, J. C. Pedro, and T. J. Brazil, "Dynamic deviation reduction-based volterra behavioral modeling of rf power amplifiers," *IEEE Trans. Microw. Theory Techn.*, vol. 54, no. 12, pp. 4323–4332, 2006.

[67] Y. Liu, G. Liu, and P. M. Asbeck, "High-order modulation transmission through frequency quadrupler using digital predistortion," *IEEE Trans. Microw. Theory Techn.*, vol. 64, no. 6, pp. 1896–1910, 2016.

[68] A. Zhu, P. J. Draxler, J. J. Yan, T. J. Brazil, D. F. Kimball, and P. M. Asbeck, "Open-loop digital predistorter for rf power amplifiers using dynamic deviation reduction-based volterra series," *IEEE Trans. Microw. Theory Techn.*, vol. 56, no. 7, pp. 1524–1534, 2008.

[69] 3GPP, "5G; NR; Base Station (BS) Radio Transmission and Reception (3GPP TS 38.104 version 15.9.0 Release 15)," Jan. 2024.

[70] S. Lee, M. Kim, Y. Sirl, E.-R. Jeong, S. Hong, S. Kim, and Y. H. Lee, "Digital Predistortion for Power Amplifiers in Hybrid MIMO Systems with Antenna Subarrays," in *Proc. IEEE Veh. Tech. Conf. (VTC)*, Glasgow, UK, May 2015, pp. 1–5.

[71] B. Khan, N. Tervo, M. Jokinen, A. Pärssinen, and M. Juntti, "Statistical digital predistortion of 5g millimeter-wave rf beamforming transmitter under random amplitude variations," *IEEE Trans. Microw. Theory Tech.*, vol. 70, no. 9, pp. 4284–4296, July 2022.

[72] W. Chen, G. Lv, X. Liu, and Z. Feng, "Energy-Efficient Doherty Power Amplifier MMIC and Beamforming-Oriented Digital Predistortion for 5G Massive MIMO Applicationtervo2017digital," in *IEEE Asia Pacific Microw. Conf. (APMC)*, Kuala Lumpur, Malaysia, Nov. 2017, pp. 391–394.

[73] N. Tervo, J. Aikio, T. Tuovinen, T. Rahkonen, and A. Parssinen, "Digital Predistortion of Amplitude Varying Phased Array Utilising Over-the-Air Combining," in *IEEE MTT-S Int. Microw. Symp. (IMS)*, Honololu, HI, USA, Jun. 2017, pp. 1165–1168.

[74] E. Ng, Y. Beltagy, P. Mitran, and S. Boumaiza, "Single-input single-output digital predistortion of power amplifier arrays in millimeter wave RF beamforming transmitters," in *2018 MTT-S Int Microw. Symp. (IMS)*. IEEE, 2018, pp. 481–484.

[75] X. Liu, Q. Zhang, W. Chen, H. Feng, L. Chen, F. M. Ghannouchi, and Z. Feng, "Beam-Oriented Digital Predistortion for 5G Massive MIMO Hybrid Beamforming

Transmitters," *IEEE Trans. Microw. Theory Tech.*, vol. 66, no. 7, pp. 3419–3432, May 2018.

[76] M. Abdelaziz, L. Anttila, A. Brihuega, F. Tufvesson, and M. Valkama, "Digital Predistortion for Hybrid MIMO Transmitters," *IEEE J. Sel. Top. Signal Process.*, vol. 12, no. 3, pp. 445–454, Apr. 2018.

[77] E. Ng, Y. Beltagy, G. Scarlato, A. Ben Ayed, P. Mitran, and S. Boumaiza, "Digital Predistortion of Millimeter-Wave RF Beamforming Arrays Using Low Number of Steering Angle-Dependent Coefficient Sets," *IEEE Trans. Microw. Theory Tech.*, vol. 67, no. 11, pp. 481–484, Nov 2019.

[78] Yu, Chao and Jing, Jianxin and Shao, Han and Jiang, Zhi Hao and Yan, Pinpin and Zhu, Xiao-Wei and Hong, Wei and Zhu, Anding, "Full-Angle Digital Predistortion of 5G Millimeter-Wave Massive MIMO Transmitters," *IEEE Trans. Microw. Theory Tech.*, vol. 67, no. 7, pp. 2847–2860, 2019.

[79] X. Liu, W. Chen, L. Chen, F. M. Ghannouchi, and Z. Feng, "Power Scalable Beam-Oriented Digital Predistortion for Compact Hybrid Massive MIMO Transmitters," *IEEE Trans. Circuits Syst. I Regul. Pap.*, vol. 67, no. 12, pp. 4994–5006, Aug. 2020.

[80] A. Brihuega, M. Abdelaziz, L. Anttila, M. Turunen, M. Allén, T. Eriksson, and M. Valkama, "Piecewise Digital Predistortion for MmWave Active Antenna Arrays: Algorithms and Measurements," *IEEE Trans. Microw. Theory Tech.*, vol. 68, no. 9, pp. 4000–4017, Jun. 2020.

[81] A. Brihuega, L. Anttila, and M. Valkama, "Neural-Network-Based Digital Predistortion for Active Antenna Arrays Under Load Modulation," *IEEE Microw. Wirel. Compon. Lett.*, vol. 30, no. 8, pp. 843–846, July 2020.

[82] F. Jalili, F. F. Tafuri, O. K. Jensen, Q. Chen, M. Shen, and G. F. Pedersen, "Bandwidth-scalable digital predistortion of active phased array using transfer learning neural network," *IEEE Access*, vol. 11, pp. 13 877–13 888, 2023.

[83] X. Wang, Y. Li, C. Yu, W. Hong, and A. Zhu, "Digital Predistortion of 5G Massive MIMO Wireless Transmitters Based on Indirect Identification of Power Amplifier Behavior With OTA Tests," *IEEE Trans. Microw. Theory Tech*, vol. 68, no. 1, pp. 316–328, Nov. 2020.

[84] R. R. Zhao, Y. Zhu, X.-W. Zhu, P. Chen, J. Zhai, and C. Yu, "Stable-sample-level-based digital predistortion for 2-d millimeter-wave phased array steering," *Microw. Wirel. Compon. Lett.*., pp. 1–4, 2022.

[85] J. Zhao, P. Liu, L. Zhai, and F. Yang, "Real-time optimization of dynamic predistortion model for 5g massive mimo broadband rf power amplifier," *Microw. Wirel. Compon. Lett.*., vol. 34, no. 1, pp. 99–102, 2024.

[86] X. Liu, W. Chen, L. Chen, F. M. Ghannouchi, and Z. Feng, "Linearization for Hybrid Beamforming Array Utilizing Embedded Over-the-Air Diversity Feedbacks," *IEEE Trans. Microw. Theory Tech*, vol. 67, no. 12, pp. 5235–5248, Oct. 2019.

[87] R. Murugesu, M. Holyoak, H. Chow, and S. Shahramian, "Linearization of mm-Wave Large-Scale Phased Arrays Using Near-Field Coupling Feedback for > 10Gb/s Wireless Communication," in *IEEE MTT-S Int. Microw. Symp. Dig. (IMS)*, Los Angeles, CA, USA, Aug. 2020, pp. 1271–1274.

[88] A. Ben Ayed, G. Scarlato, P. Mitran, and S. Boumaiza, "On the Effectiveness of Near-Field Feedback for Digital Pre-Distortion of Millimeter-Wave RF Beamforming Arrays," in *IEEE MTT-S Int. Microw. Symp. Dig. (IMS)*, Los Angeles, CA, USA, Aug. 2020, pp. 1165–1168.

[89] A. Ben Ayed, Y. Cao, P. Mitran, and S. Boumaiza, "Digital Predistortion of Millimeter-Wave Arrays Using Near-Field Based Transmitter Observation Receivers," *IEEE Trans. Microw. Theory Tech.*, pp. 3713 – 3723, May 2022.

[90] M. Romier, A. Barka, H. Aubert, J.-P. Martinaud, and M. Soiron, "Load-Pull Effect on Radiation Characteristics of Active Antennas," *IEEE Antennas Wirel. Propag. Lett.*, vol. 7, pp. 550–552, Sept. 2008.

[91] T. Sadeghpour, R. Alhameed, N. T. Ali, I. T. Elfergani, Y. Dama, and O. O. Anoh, "Linear and Nonlinear Crosstalk in MIMO OFDM Transceivers," in *IEEE Int. Symp. Circuits Syst.*, Beirut, Lebanon, Dec. 2011, pp. 504–507.

[92] F. M. Barradas, T. R. Cunha, and J. C. Pedro, "Digital Predistortion of RF PAs for MIMO Transmitters Based on the Equivalent Load," in *Proc. Integr. Nonlinear Microw. Millimetre-Wave Circuits Workshop,*, Apr. 2017, pp. 1–4.

[93] H. Yin, Z. Yu, C. Yu, J. Jing, X. W. Zhu, W. Hong, and A. Zhu, "Data-Clustering-Assisted Digital Predistortion for 5G Millimeter-Wave Beamforming Transmitters

With Multiple Dynamic Configurations," *IEEE Trans. Microw. Theory Tech.*, vol. 69, no. 3, pp. 1805–1816, Dec. 2021.

[94] S. K. Dhar, A. Abdelhafiz, M. Aziz, M. Helaoui, and F. M. Ghannouchi, "A Reflection-Aware Unified Modeling and Linearization Approach for Power Amplifier Under Mismatch and Mutual Coupling," *IEEE Trans. Microw. Theory Tech.*, vol. 66, no. 9, pp. 4147–4157, Aig. 2018.

[95] X. Wang, Y. Li, H. Yin, C. Yu, Z. Yu, W. Hong, and A. Zhu, "Digital Predistortion of 5G Multiuser MIMO Transmitters Using Low-Dimensional Feature-Based Model Generation," *IEEE Trans. Microw. Theory Tech.*, vol. 70, no. 3, pp. 1509–1520, Dec. 2022.

[96] M. Mengozzi, G. P. Gibiino, A. M. Angelotti, C. Florian, and A. Santarelli, "Beam-dependent active array linearization by global feature-based machine learning," *Microw. Wirel. Compon. Lett.*., vol. 33, no. 6, pp. 895–898, 2023.

[97] Y. Li, X. Wang, and A. Zhu, "Complexity-reduced model adaptation for digital predistortion of rf power amplifiers with pretraining-based feature extraction," *IEEE Trans. Microw. Theory Techn.*, vol. 69, no. 3, pp. 1780–1790, 2021.

[98] Y. Li, Y. Huang, Q. Chen, F. Jalili, K. B. Olesen, J. G. Brask, L. F. Dyring, G. F. Pedersen, and M. Shen, "Hybrid digital pre-distortion for active phased arrays subject to varied power and steering angle," *IEEE Microw. Wirel. Compon. Lett.*, vol. 32, no. 10, pp. 1243–1246, 2022.

[99] W. Lee, J.-O. Plouchart, C. Ozdag, Y. Aydogan, M. Yeck, A. Cabuk, A. Kepkep, S. K. Reynolds, E. Apaydin, and A. Valdes-Garcia, "Fully integrated 94-ghz dual-polarized tx and rx phased array chipset in sige bicmos operating up to 105 °c," *IEEE J. Solid-State Circuits*, vol. 53, no. 9, pp. 2512–2531, 2018.

[100] A. G. Roy, O. Inac, A. Singh, T. Mukatel, O. Brandelstein, T. W. Brown, S. Abughazaleh, J. S. Hayden, B. Park, G. Bachmanek, T.-Y. J. Kao, J. Hagn, S. Dalmia, D. Shoham, B. Davis, I. Fisher, R. Sover, A. Freiman, B. Xiao, B. Singh, and J. Jensen, "A 37-40 ghz phased array front-end with dual polarization for 5g mimo beamforming applications," in *2019 IEEE Radio Frequency Integrated Circuits Symposium (RFIC)*, 2019, pp. 251–254.

[101] U. Kodak, B. Rupakula, S. Zihir, and G. M. Rebeiz, "60-ghz 64- and 256-element dual-polarized dual-beam wafer-scale phased-array transceivers with reticle-to-reticle stitching," *IEEE Trans. Microw. Theory Techn.*, vol. 68, no. 7, pp. 2745–2767, 2020.

[102] Q. Wu and et al., "Digital predistortion for dual-linearly polarized millimeter-wave phased array user equipment," *IEEE Trans. Microw. Theory Techn.*, vol. 70, no. 11, pp. 5248–5258, 2022.

[103] E. Ng, A. B. Ayed, P. Mitran, and S. Boumaiza, "Single-input single-output digital predistortion of multi-user rf beamforming arrays," in *2019 IEEE MTT-S Int Microw. Symp. (IMS)*, 2019, pp. 472–475.

[104] A. Ben Ayed, E. Ng, P. Mitran, and S. Boumaiza, "Digital predistortion of millimeter-wave hybrid beamforming transmitters using observation receivers with low-bit resolution analog-to-digital converter," *IEEE Access*, vol. 9, pp. 100 627–100 636, 2021.

[105] Q. Luo, X.-W. Zhu, C. Yu, and W. Hong, "Single-Receiver Over-the-Air Digital Predistortion for Massive MIMO Transmitters With Antenna Crosstalk," *IEEE Trans. Microw. Theory Tech.*, vol. 68, no. 1, pp. 301–315, 2020.

[106] X. Liu, W. Chen, and J. Chu, "Behavioral Modeling and Digital Predistortion for Fully-Connected Hybrid Beamforming Massive MIMO Transmitters," in *2020 IEEE Asia-Pacific Microwave Conference (APMC)*, 2020, pp. 463–465.

[107] X. Liu, W. Chen, J. Chu, F. M. Ghannouchi, and Z. Feng, "Multi-stream spatial digital predistortion for fully-connected hybrid beamforming massive mimo transmitters," *IEEE Trans. Circuits Syst. I: Regul.*, vol. 68, no. 7, pp. 2998–3011, 2021.

[108] L. Zhao, S. Wan, K. Kang, W. Feng, and H. Qian, "A General Digital Predistortion Linearization Scheme for Hybrid Beamforming System," *IEEE Trans. Veh. Technol.*, vol. 72, no. 1, pp. 654–663, 2023.

[109] H. Yu, E. Traore, M. Almoneer, J. G. Lim, J. Xia, and S. Boumaiza, "Experimental study of the effects of antenna crosstalk on the linearity and efficiency of 5g sub-6 ghz wideband 2×2 transmitter arrays," in *2021 IEEE MTT-S Int Microw. Symp. (IMS)*, 2021, pp. 869–872.

[110] J. G. Lim, H. Barkhordar-Pour, A. B. Ayed, P. Mitran, and S. Boumaiza, "On the viability of using a subset of transmitter- observation receivers for training a common dpd in fully digital mimo transmitters," *Microw. Wirel. Compon. Lett.*., vol. 33, no. 6, pp. 907–910, 2023.

[111] S. A. Bassam, M. Helaoui, and F. M. Ghannouchi, "Crossover digital predistorter for the compensation of crosstalk and nonlinearity in mimo transmitters," *IEEE Trans. Microw. Theory Techn.*, vol. 57, no. 5, pp. 1119–1128, 2009.

[112] P. Jaraut, M. Rawat, and F. M. Ghannouchi, "Composite neural network digital predistortion model for joint mitigation of crosstalk, i/q imbalance, nonlinearity in mimo transmitters," *IEEE Trans. Microw. Theory Techn.*, vol. 66, no. 11, pp. 5011–5020, 2018.

[113] D. López-Bueno, G. Montoro, and P. L. Gilabert, "Training data selection and dimensionality reduction for polynomial and artificial neural network mimo adaptive digital predistortion," *IEEE Trans. Microw. Theory Techn.*, vol. 70, no. 11, pp. 4940–4954, 2022.

[114] M. Tanio, N. Ishii, and N. Kamiya, "A sparse neural network-based power adaptive dpd design and its hardware implementation," *IEEE Access*, vol. 10, pp. 114 673–114 682, 2022.

[115] K. Hausmair, P. N. Landin, U. Gustavsson, C. Fager, and T. Eriksson, "Digital predistortion for multi-antenna transmitters affected by antenna crosstalk," *IEEE Trans. Microw. Theory Techn.*, vol. 66, no. 3, pp. 1524–1535, 2017.

[116] H. Barkhordar-Pour, J. G. Lim, M. Almoneer, P. Mitran, and S. Boumaiza, "Real-time fpga-based implementation of digital predistorters for fully digital mimo transmitters," in *2023 IEEE MTT-S Int. Microw. Symp.*, 2023, pp. 263–266.

[117] M. Almoneer, J. G. Lim, H. Yu, P. Mitran, and S. Boumaiza, "Massive mimo precoding methods that minimize the variation in average power and active impedance with channel conditions," *IEEE Trans. Microw. Theory Tech.*, vol. 70, no. 8, pp. 4002–4016, 2022.

[118] J. Jang, S.-W. Jeon, H. Chae, H.-S. Cha, and D. K. Kim, "Low complexity zeroforcing precoder design under per-antenna power constraints," *IEEE Communications Letters*, vol. 19, no. 9, pp. 1556–1559, 2015.

[119] M. Almoneer, P. Mitran, and S. Boumaiza, "Load and power indexed predistortion for improved robusteness to mimo channel conditions," *Microw. Wirel. Compon. Lett.*., pp. 1–4, 2022.

[120] A. Wiesel, Y. C. Eldar, and S. Shamai, "Zero-forcing precoding and generalized inverses," *IEEE Trans. Signal Process.*, vol. 56, no. 9, pp. 4409–4418, 2008.

[121] M. Yao, M. Sohul, R. Nealy, V. Marojevic, and J. Reed, "A digital predistortion scheme exploiting degrees-of-freedom for massive mimo systems," in *2018 EEE Int. Conf. Commun.*, 2018, pp. 1–5.

[122] C. Tarver, A. Balalsoukas-Slimining, C. Studer, and J. R. Cavallaro, "Virtual dpd neural network predistortion for ofdm-based mu-massive mimo," in *2021 55th Asilomar Conference on Signals, Systems, and Computers*, 2021, pp. 376–380.

[123] A. Brihuega, L. Anttila, and M. Valkama, "Beam-level frequency-domain digital predistortion for ofdm massive mimo transmitters," *IEEE Trans. Microw. Theory Techn.*, pp. 1–16, 2022.

[124] C. Hemmi, "Pattern characteristics of harmonic and intermodulation products in broadband active transmit arrays," *IEEE Trans. Antennas Propag.*, vol. 50, no. 6, pp. 858–865, 2002.

[125] N. Kolomvakis, M. Bavand, I. Bahceci, and U. Gustavsson, "A distortion nullforming precoder in massive mimo systems with nonlinear hardware," *IEEE Wirel. Commun.*, vol. 11, no. 9, pp. 1775–1779, 2022.

[126] T. Feys, G. Callebaut, L. Van der Perre, and F. Rottenberg, "Measurement-based validation of z3ro precoder to prevent nonlinear amplifier distortion in massive mimo systems," in *2022 IEEE 95th Vehicular Technology Conference: (VTC2022-Spring)*, 2022, pp. 1–5.

[127] F. Rottenberg, G. Callebaut, and L. Van der Perre, "The z3ro family of precoders cancelling nonlinear power amplification distortion in large array systems," *IEEE Wirel. Commun.*, vol. 22, no. 3, pp. 2036–2047, 2023.

[128] S. R. Aghdam, S. Jacobsson, U. Gustavsson, G. Durisi, C. Studer, and T. Eriksson, "Distortion-aware linear precoding for massive MIMO downlink systems with nonlinear power amplifiers," *CoRR*, vol. abs/2012.13337, 2020. [Online]. Available: https://arxiv.org/abs/2012.13337

[129] W. Patton and L. Yorinks, "Near-field Alignment of Phased-Array Antennas," *IEEE Trans. Antennas Propag.*, vol. 47, no. 3, pp. 584–591, 1999.

[130] S. Mano and T. Katagi, "A method for measuring amplitude and phase of each radiating element of a phased array antenna," *Electronics and Communications in Japan (Part I: Communications)*, vol. 65, no. 5, pp. 58–64, 1982. [Online]. Available: https://onlinelibrary.wiley.com/doi/abs/10.1002/ecja.4410650508

[131] R. Long, J. Ouyang, F. Yang, W. Han, and L. Zhou, "Fast amplitude-only measurement method for phased array calibration," *IEEE Trans. Antennas Propag.*, vol. 65, no. 4, pp. 1815–1822, 2017.

[132] H. Aumann, A. Fenn, and F. Willwerth, "Phased array antenna calibration and pattern prediction using mutual coupling measurements," *IEEE Trans. Antennas Propag.*, vol. 37, no. 7, pp. 844–850, 1989.

[133] J. A. Haimerl, B. Hudson, G. P. Fonder, and D. K. Lee, "Overview of the Large Digital Arrays of the Space Fence Radar," in *IEEE Int. Symp. on Phased Array Systems and Technology (PAST)*, Waltham, MA, USA, Oct. 2016, pp. 1–8.

[134] Y. Cao, A. B. Ayed, J. Xia, and S. Boumaiza, "Uniformly Distributed Near-Field Probing Array for Enhancing the Performance of 5G Millimetre-wave Beamforming Transmitters," *IEEE Microw. Wirel. Compon. Lett.*, vol. 31, no. 6, pp. 823 – 826, June 2021.

[135] S.-C. Chae, H.-W. Jo, J.-I. Oh, G. Kim, and J.-W. Yu, "Coupler Integrated Microstrip Patch Linear Phased Array for Self-Calibration," *IEEE Antennas Wirel. Propag. Lett.*, vol. 19, no. 9, pp. 1615–1619, 2020.

[136] C. Guo, L. Tian, Z. H. Jiang, and W. Hong, "A Self-Calibration Method for 5G Full-Digital TDD Beamforming Systems Using an Embedded Transmission Line," *IEEE Trans. Antennas Propag.*, vol. 69, no. 5, pp. 2648–2659, 2021.

[137] B. Brautigam, M. Schwerdt, M. Bachmann, and M. Stangl, "Individual T/R Module Characterisation of the TerraSAR-X Active Phased Array Antenna by Calibration Pulse Sequences with Orthogonal Codes," in *IEEE Int. Geosci. Remote Sens. Symp.,*, Barcelona, Spain, Jul. 2007, pp. 5202–5205.

[138] R. Long, J. Ouyang, F. Yang, W. Han, and L. Zhou, "Multi-Element Phased Array Calibration Method by Solving Linear Equations," *IEEE Trans. Antennas Propag.*, vol. 65, no. 6, pp. 2931–2939, 2017.

[139] Y. Aoki, Y. Kim, Y. Hwang, H. Kang, S. Kim, A.-S. Ryu, and S.-G. Yang, "An Intermodulation Distortion Oriented 256-Element Phased-Array Calibration for 5G Base Station," in *IEEE MTT-S Int. Microw. Symp. Dig. (IMS)*, Denver, CO, USA, Jun. 2022, pp. 518–521.

[140] Y. Aoki, Y. Kim, Y. Hwang, H. Kang, S. Kim, A.-S. Ryu, M. T. Dao, K. Min, D. Kang, D. Minn, H.-C. Park, S. Jeon, and S.-G. Yang, "Fast Characterization of Phased-Array Elements Using Orthogonal Codes," *IEEE Trans. Microw. Theory Tech.*, vol. 71, no. 1, pp. 263–273, 2023.

[141] H. Li, X. Hao, Z. Liu, Z. Zhang, Z. Shen, J. Liu, and H. Liao, "A 2.9 GHz variable inductor-based DCO with 1.3 khz frequency resolution for FMCW radar applications," *IEEE Trans. Circuits Syst. II Express Briefs*, vol. 66, no. 5, pp. 813–817, 2019.

[142] Y. Park and J. S. Kenney, "Adaptive digital predistortion linearization of frequency multipliers," *IEEE Trans. Microw. Theory Techn.*, vol. 51, no. 12, pp. 2516–2522, Dec. 2003.

[143] Y. Park, R. Melville, R. C. Frye, M. Chen, and J. S. Kenney, "Dual-band transmitters using digitally predistorted frequency multipliers for reconfigurable radios," *IEEE Trans. Microw. Theory Techn.*, vol. 53, no. 1, pp. 115–122, Jan. 2005.

[144] J. H. Choi, S. M. Kang, and K. H. Koo, "Digital predistortion of frequency multiplier for dual band wireless LAN transmitter," in *IEEE MTT-S Int. Microw. Symp. Dig.*, June 2005, pp. 1998–2001.

[145] S. M. Kang, S. W. Nam, and K. H. Koo, "Adaptive linearization of frequency doubler using DGS," in *IEEE MTT-S Int. Microw. Symp.*, July 2007, pp. 1225–1228.

[146] D. Nopchinda, Z. He, G. Granstrom, M. Gavell, and H. Zirath, "8-PSK upconverting transmitter using E-band frequency sextupler," *IEEE Microw. Wireless Compon. Lett.*, vol. 28, no. 2, pp. 177–179, Feb. 2018.

[147] D. Nopchinda, "OFDM upconverting transmitter using a frequency multiplier," in *52nd Eur. Microw. Conf.*, Sept. 2022, pp. 20–23.

[148] T. Cao, Y.-J. Liu, J. Jiang, Q. Zhang, C. Lin, D. Yang, G. Zhang, C. Yang, and J. Zhou, "Frequency multiplier-based millimeter-wave vector signal transmitter using digital predistortion with constrained feedback bandwidth," *IEEE Trans. Microw. Theory Techn.*, vol. 68, no. 5, pp. 1819–1829, 2020.

[149] "AWMF-0162 Silicon Core BFIC." [Online]. Available: https://www.anokiwave.com/products/awmf-0162/index.html

[150] M. Gupta, R. Laton, and T. Lee, "Performance and Design of Microwave FET Harmonic Generators," *IEEE Tran. Microw. Theory Tech.*, vol. 29, no. 3, pp. 261–262, 1981.

[151] A. Gopinath and J. Rankin, "Single-Gate MESFET Frequency Doublers," *IEEE Tran. Microw. Theory Tech.*, vol. 30, no. 6, pp. 869–875, 1982.

[152] S. A. Maas, *Nonlinear microwave and RF circuits.* Artech House, 2003.

[153] F. Giannini and G. Leuzzi, *Nonlinear microwave circuit design.* Wiley, 2004.

[154] A. Zhu, J. C. Pedro, and T. R. Cunha, "Pruning the Volterra Series for Behavioral Modeling of Power Amplifiers Using Physical Knowledge," *IEEE Tran. Microw. Theory Tech.*, vol. 55, no. 5, pp. 813–821, 2007.

[155] M. Eladwy, J. Xia, A. B. Ayed, and S. Boumaiza, "A 60 GHz CMOS-SOI Stacked Push-Push Frequency Doubler with 12 dBm Output Power and 20% Efficiency," in *IEEE MTT-S Int. Microw. Symp.*, Atlanta, GA, USA, June 2021, pp. 297–300.

[156] F. Mkadem, M. C. Fares, S. Boumaiza, and J. Wood, "Complexity-Reduced Volterra Series Model for Power Amplifier Digital Predistortion," *Analog Integr. Circuits Signal Process.*, vol. 79, no. 2, pp. 331–343, May 2014.

[157] D. R. Morgan and et al., "A Generalized Memory Polynomial Model for Digital Predistortion of RF Power Amplifiers," *IEEE Trans. Signal Process.*, vol. 54, no. 10, pp. 3852–3860, oct. 2006.

[158] R. N. Braithwaite, "Memory Correction of a Doherty Power Amplifier with a WCDMA Input using Digital Predistortion," in *IEEE MTT-S Int. Microw. Symp. Dig. (IMS)*, San Francisco, CA, USA, Jun. 2006, pp. 1526–1529.

[159] L. Ding, F. Mujica, and Z. Yang, "Digital Predistortion Using Direct Learning with Reduced Bandwidth Feedback," in *IEEE MTT-S Int. Microw. Symp. Dig. (IMS)*, Seattle, WA, USA, Jun. 2013, pp. 1–3.

[160] F. Jalili, F. F. Tafuri, O. K. Jensen, Y. Li, M. Shen, and G. F. Pedersen, "Linearization Trade-Offs in a 5G MM-Wave Active Phased Array OTA Setup," *IEEE Access*, vol. 8, pp. 110 669–110 677, 2020.

[161] P. P. Campo, A. Brihuega, L. Anttila, M. Turunen, D. Korpi, M. Allén, and M. Valkama, "Reduced-Complexity Digital Predistortion: Adaptive Spline-Based Hammerstein Approach," *arXiv preprint arXiv:1907.02350*, 2019.

[162] H. Jin, A. Ben Ayed, B. Tung, P. Mitran, and S. Boumaiza, "Embedded Near-Field Probing Antenna for Enhancing the Performance of 37-41 GHz Linear and Dual - Polarized Phased Antenna Arrays," in *IEEE MTT-S Int. Microw. Symp. Dig. (IMS)*, San Diego, CA, USA, 2023.

[163] Y. Liu, W. Pan, S. Shao, and Y. Tang, "A new digital predistortion for wideband power amplifiers with constrained feedback bandwidth," *IEEE Microw. Wirel. Compon. Lett.*, vol. 23, no. 12, pp. 683–685, 2013.

[164] Y. Zhao, X. Pang, L. Deng, X. Yu, X. Zheng, H. Zhang, and I. T. Monroy, "Digital predistortion of 75-110 GHz W-band frequency multiplier for fiber wireless short range access systems," *Opt. Express*, vol. 19, no. 26, pp. B18–B25, Dec. 2011.

[165] G. C. Tripathi and M. Rawat, "High-frequency signal generator using cascaded frequency multiplier," *IEEE Access*, vol. 11, pp. 74 559–74 568, 2023.

[166] A. Ben Ayed, I. Jaffri, A. M. Darwish, P. Mitran, and S. Boumaiza, "Proof-of-concept of millimeter-wave RF beamforming transmitter architecture employing frequency-multiplier-based up-converters," *IEEE Microw. Wirel. Compon. Lett.*, vol. 32, no. 6, pp. 776–779, 2022.

[167] A. Ben Ayed, I. Jaffri, M. ElAdwy, A. M. Darwish, P. Mitran, and S. Boumaiza, "Analysis and linearization of frequency-multiplier-based RF beamforming transmitters over a wide steering range," *IEEE Trans. Microw. Theory Tech.*, vol. 70, no. 8, pp. 3987–4001, 2022.

[168] M. Almoneer, P. Mitran, and S. Boumaiza, "Wideband digital predistortion for frequency multipliers driven by nonideal upconverters," *IEEE Microw. Wirel. Compon. Lett.*, vol. 33, no. 1, pp. 82–85, 2023.

[169] "Ericsson mobility report," Ericssin, Stockholm, Sweeden, Tech. Rep., 2022. [Online]. Available: https://www.ericsson.com/4ae28d/assets/local/reports-papers/mobility-report/documents/2022/ericsson-mobility-report-november-2022.pdf

[170] "F6121." [Online]. Available: https://www.renesas.com/us/en/products/rf-products/phased-array-beamformers/f6121-16-channel-dual-beam-rx-active-beamforming-ic-ku-band-satcomoverview

[171] "Adar3001," Feb 2022. [Online]. Available: https://www.analog.com/en/products/adar3001.html

[172] D. Zhang, Y. Wang, X. Li, and W. Xiang, "Hybridly connected structure for hybrid beamforming in mmwave massive mimo systems," *IEEE Trans. Commun.*, vol. 66, no. 2, pp. 662–674, 2018.

[173] L. Ding, G. Zhou, D. Morgan, Z. Ma, J. Kenney, J. Kim, and C. Giardina, "A robust digital baseband predistorter constructed using memory polynomials," *IEEE Trans. Commun.*, vol. 52, no. 1, pp. 159–165, 2004.

[174] F. Wang, D. F. Kimball, J. D. Popp, A. H. Yang, D. Y. Lie, P. M. Asbeck, and L. E. Larson, "An improved power-added efficiency 19-dbm hybrid envelope elimination and restoration power amplifier for 802.11g wlan applications," *IEEE Trans. Microw. Theory Techn.*, vol. 54, no. 12, pp. 4086–4099, 2006.

[175] D. Kimball, J. Jeong, C. Hsia, P. Draxler, S. Lanfranco, W. Nagy, K. Linthicum, L. Larson, and P. Asbeck, "High-efficiency envelope-tracking w-cdma base-station amplifier using gan hfets," *IEEE Trans. Microw. Theory Techn.*, vol. 54, no. 11, pp. 3848–3856, 2006.

[176] F. M. Ghannouchi and O. Hammi, "Behavioral modeling and predistortion," *IEEE Microw. Mag.*, vol. 10, no. 7, pp. 52–64, 2009.

[177] V. Raghavan and J. Li, "Evolution of Physical-Layer Communications Research in the Post-5G Era," *IEEE Access*, vol. 7, pp. 10 392–10 401, 2019.

[178] G. Z. El Nashef, F. Torres, S. Mons, T. Reveyrand, T. Monédière, E. Ngoya, and R. Quéré, "EM/circuit mixed simulation technique for an active antenna," *IEEE Antennas Wirel. Propag. Lett.*, vol. 10, pp. 354–357, 2011.

[179] F. M. Barradas, P. M. Tomé, J. M. Gomes, T. R. Cunha, P. M. Cabral, and J. C. Pedro, "Power, linearity, and efficiency prediction for MIMO arrays with antenna coupling," *IEEE Trans. Microw. Theory Techn.*, vol. 65, no. 12, pp. 5284–5297, 2017.

[180] H. Yan and D. Cabric, "Digital predistortion for hybrid precoding architecture in millimeter-wave massive MIMO systems," in *2017 IEEE Int Conf Acoust Speech Signal Process (ICASSP)*. IEEE, 2017, pp. 3479–3483.

[181] Y. Liu, J. J. Yan, H.-T. Dabag, and P. M. Asbeck, "Novel technique for wideband digital predistortion of power amplifiers with an under-sampling ADC," *IEEE Trans. Microw. Theory Tech.*, vol. 62, no. 11, pp. 2604–2617, 2014.

[182] C. Yu, L. Guan, E. Zhu, and A. Zhu, "Band-limited Volterra series-based digital predistortion for wideband RF power amplifiers," *IEEE Trans. Microw. Theory Tech.*, vol. 60, no. 12, pp. 4198–4208, 2012.

[183] S. Deb, M. Tanio, S. Hori, N. Tawa, Y. Wada, and K. Kunihiro, "Band-Limited Digital Predistortion with Band-Switching Feedback Architecture for 5G mmWave Power Amplifiers," in *2018 48th European Microwave Conference (EuMC)*. IEEE, 2018, pp. 9–12.

[184] Y. Li, J. Zhai, C. Yu, Z. Jiang, and L. Zhang, "A band-limited CPWL-based memory polynomial model for digital predistortion," in *2017 Sixth Asia-Pacific Conference on Antennas and Propagation (APCAP)*. IEEE, 2017, pp. 1–3.

[185] S. Bensmida, O. Hammi, A. Kwan, M. S. Sharawi, K. A. Morris, and F. M. Ghannouchi, "Extending the characterization bandwidth of dynamic nonlinear transmitters with application to digital predistortion," *IEEE Trans. Microw. Theory Tech.*, vol. 64, no. 8, pp. 2640–2651, 2016.

[186] H. Wang, G. Li, C. Zhou, W. Tao, F. Liu, and A. Zhu, "1-bit Observation for Direct-Learning-Based Digital Predistortion of RF Power Amplifiers," *IEEE Trans. Microw. Theory Tech.*, vol. 65, no. 7, pp. 2465–2475, 2017.

[187] P. Singerl, A. Agrawal, A. Garg, G. Kubin, H. Eul *et al.*, "Complex baseband predistorters for nonlinear wideband RF power amplifiers," in *2006 49th IEEE International Midwest Symposium on Circuits and Systems*, vol. 2. IEEE, 2006, pp. 675–678.

[188] "Anokiwave AWMF-0134 5G 28 GHz Active Antenna Innovator's Kit." [Online]. Available: https://www.anokiwave.com/products/awa-0134/index.html

[189] "Anokiwave AWMF-0128 5G 28 GHz Active Antenna Innovator's Kit." [Online]. Available: https://www.anokiwave.com/products/awmf-0129/index.html

[190] T.-H. Yu and S. Mitra, "A new two-dimensional window," *IEEE Transactions on Acoustics, Speech, and Signal Processing*, vol. 33, no. 4, pp. 1058–1061, 1985.

[191] H. Kato and T. Furukawa, "Two-dimensional type-preserving circular windows," *IEEE Transactions on Acoustics, Speech, and Signal Processing*, vol. 29, no. 4, pp. 926–928, 1981.

[192] C. Yu, J. Jing, H. Shao, Z. H. Jiang, P. Yan, X.-W. Zhu, W. Hong, and A. Zhu, "Full-Angle Digital Predistortion of 5G Millimeter-Wave Massive MIMO Transmitters," *IEEE Trans. Microw. Theory Techn.*, vol. 67, no. 7, pp. 2847–2860, June 2019.

[193] D. R. Morgan, Z. Ma, J. Kim, M. G. Zierdt, and J. Pastalan, "A generalized memory polynomial model for digital predistortion of RF power amplifiers," *IEEE Trans. Signal Process.*, vol. 54, no. 10, pp. 3852–3860, 2006.

[194] J. Vieira, F. Rusek, O. Edfors, S. Malkowsky, L. Liu, and F. Tufvesson, "Reciprocity Calibration for Massive MIMO: Proposal, Modeling, and Validation," *IEEE Wirel. Commun.*, vol. 16, no. 5, pp. 3042–3056, May 2017.

[195] R. N. Braithwaite, "Memory Correction of a Doherty Power Amplifier with a WCDMA Input using Digital Predistortion," in *2006 IEEE MTT-S Int. Microw. Symp. Dig. (IMS)*, June 2006, pp. 1526–1529.

[196] Scarlato, Giovanni, "Design of 28 GHz 4x4 RF Beamforming Array for 5G Radio Front-Ends," 2019. [Online]. Available: http://hdl.handle.net/10012/14995

[197] Y. Qin, R. Li, and Y. Cui, "Embeddable Structure for Reducing Mutual Coupling in Massive MIMO Antennas," *IEEE Access*, vol. 8, pp. 195 102–195 112, 2020.

[198] A. Ben Ayed, I. Jaffri, M. ElAdwy, A. M. Darwish, P. Mitran, and S. Boumaiza, "Analysis and Linearization of Frequency-Multiplier-Based RF Beamforming Transmitters Over a Wide Steering Range," *IEEE Trans. Microw. Theory Tech.*, vol. 70, no. 8, pp. 3987–4001, July 2022.

[199] N. Sarmah, P. R. Vazquez, J. Grzyb, W. Foerster, B. Heinemann, and U. R. Pfeiffer, "A wideband fully integrated sige chipset for high data rate communication at 240 ghz," in *2016 11th European Microwave Integrated Circuits Conference (EuMIC)*, 2016, pp. 181–184.

[200] K. K. Tokgoz, S. Maki, J. Pang, N. Nagashima, I. Abdo, S. Kawai, T. Fujimura, Y. Kawano, T. Suzuki, T. Iwai, K. Okada, and A. Matsuzawa, "A 120gb/s 16qam cmos millimeter-wave wireless transceiver," in *2018 IEEE Int. Solid-State Circuits Conf. - (ISSCC)*, 2018, pp. 168–170.

[201] H.-J. Song, J.-Y. Kim, K. Ajito, N. Kukutsu, and M. Yaita, "50-gb/s direct conversion qpsk modulator and demodulator mmics for terahertz communications at 300 ghz," *IEEE Trans. Microw. Theory Techn.*, vol. 62, no. 3, pp. 600–609, 2014.

[202] Y. Beltagy, P. Mitran, and S. Boumaiza, "Direct learning algorithm for digital predistortion training using sub-nyquist intermediate frequency feedback signal," *IEEE Trans. Microw. Theory Techn.*, vol. 67, no. 1, pp. 267–277, 2019.

[203] C. Yu, L. Guan, E. Zhu, and A. Zhu, "Band-limited volterra series-based digital predistortion for wideband rf power amplifiers," *IEEE Trans. Microw. Theory Techn.*, vol. 60, no. 12, pp. 4198–4208, 2012.

[204] A. Chung, M. B. Rejeb, Y. Beltagy, A. Darwish, H. Hung, and S. Boumaiza, "High frequency and wideband modulated signal generation using frequency doublers," in *IEEE MTT-S Int. Microw. Symp. Dig.*, Jun. 2018, pp. 156–159.

[205] A. Mostajeran, S. M. Naghavi, M. Emadi, S. Samala, B. P. Ginsburg, M. Aseeri, and E. Afshari, "A high-resolution 220-ghz ultra-wideband fully integrated isar imaging system," *IEEE Trans. Microw. Theory Techn.*, vol. 67, no. 1, pp. 429–442, 2019.

[206] D. Simic, K. Guo, and P. Reynaert, "A 420-GHz Sub-5-μm Range Resolution TX-RX Phase Imaging System in 40-nm CMOS Technology," *IEEE J. Solid-State Circuits*, pp. 1–1, 2021.

[207] S. Kang, S. V. Thyagarajan, and A. M. Niknejad, "A 240 ghz fully integrated wideband qpsk transmitter in 65 nm cmos," *IEEE J. Solid-State Circuits*, vol. 50, no. 10, pp. 2256–2267, 2015.

[208] J. Treuttel, A. Maestrini, J. Sarrazin, and F. Joint, "330 ghz and 600 ghz schottky heterodyne systems for qpsk terahertz telecommunication," in *2018 25th International Conference on Telecommunications (ICT)*, 2018, pp. 291–294.

[209] A. Standaert and P. Reynaert, "A 390-ghz outphasing transmitter in 28-nm cmos," *IEEE J. Solid-State Circuits*, vol. 55, no. 10, pp. 2703–2713, 2020.

[210] M. Almoneer, P. Mitran, and S. Boumaiza, "I/q imbalance compensation in wideband millimeter-wave transmitters using a single undersampling adc," *IEEE Trans. Circuits Syst. I: Regul.*, vol. 67, no. 8, pp. 2730–2738, 2020.

[211] H. Rashidzadeh, M. Almoneer, P. Mitran, and S. Boumaiza, "Compensation of transmitter i/q imbalance in millimeter-wave mimo systems using a single transmitter observation receiver," *IEEE Trans. Microw. Theory Techn.*, vol. 68, no. 7, pp. 2920–2929, 2020.

[212] M. Pashaeifar, L. C. N. de Vreede, and M. S. Alavi, "14.4 a 24-to-30ghz double-quadrature direct-upconversion transmitter with mutual-coupling-resilient series-doherty balanced pa for 5g mimo arrays," in *2021 IEEE Int. Solid-State Circuits Conf. (ISSCC)*, vol. 64, 2021, pp. 223–225.

[213] R. Quaglia, J. Powell, K. Chaudhry, and S. Cripps, "Effect of hemt output characteristics on the load mismatch resilience in balanced power amplifiers," in *2022 International Workshop on Integrated Nonlinear Microwave and Millimetre-Wave Circuits (INMMiC)*, 2022, pp. 1–3.

[214] F. Mkadem and S. Boumaiza, "Physically inspired neural network model for rf power amplifier behavioral modeling and digital predistortion," *IEEE Trans. Microw. Theory Techn.*, vol. 59, no. 4, pp. 913–923, 2011.

[215] J. Sun, W. Shi, Z. Yang, J. Yang, and G. Gui, "Behavioral modeling and linearization of wideband rf power amplifiers using bilstm networks for 5g wireless systems," *IEEE Trans. Veh. Technol.*, vol. 68, no. 11, pp. 10 348–10 356, 2019.

[216] T. Kobal and A. Zhu, "Digital predistortion of rf power amplifiers with decomposed vector rotation-based recurrent neural networks," *IEEE Trans. Microw. Theory Techn.*, vol. 70, no. 11, pp. 4900–4909, 2022.

[217] A. Vaicaitis and J. Dooley, "Segmented spline curve neural network for low latency digital predistortion of rf power amplifiers," *IEEE Trans. Microw. Theory Techn.*, vol. 70, no. 11, pp. 4910–4915, 2022.

[218] P. Jaraut, A. Abdelhafiz, H. Chenini, X. Hu, M. Helaoui, M. Rawat, W. Chen, N. Boulejfen, and F. M. Ghannouchi, "Augmented convolutional neural network for behavioral modeling and digital predistortion of concurrent multiband power amplifiers," *IEEE Trans. Microw. Theory Techn.*, vol. 69, no. 9, pp. 4142–4156, 2021.

[219] C. Cuccia and E. Matthews, "PSK and QPSK modulators for gigabit data rates," in *IEEE MTT-S Int. Microw. Symp. Dig.*, June 1977, pp. 208–211.

[220] K. B. Cooper, R. J. Dengler, G. Chattopadhyay, E. Schlecht, J. Gill, A. Skalare, I. Mehdi, and P. H. Siegel, "Submillimeter-wave active radar imager," in *2007 Joint 32nd International Conference on Infrared and Millimeter Waves and the 15th International Conference on Terahertz Electronics*, 2007, pp. 922–923.

[221] J. Park, H. Ryu, K.-W. Ha, J.-G. Kim, and D. Baek, "76–81-GHz CMOS transmitter with a phase-locked-loop-based multichirp modulator for automotive radar," *IEEE Trans. Microw. Theory Tech.*, vol. 63, no. 4, pp. 1399–1408, 2015.

[222] J.-H. Song, C. Cui, S.-K. Kim, B.-S. Kim, and S. Nam, "A low-phase-noise 77-GHz FMCW radar transmitter with a 12.8-GHz PLL and a ×6 frequency multiplier," *IEEE Microw. Wirel. Compon. Lett.*, vol. 26, no. 7, pp. 540–542, 2016.

[223] C. Mangiavillano, A. Kaineder, K. Aufinger, and A. Stelzer, "A terahertz monostatic transceiver in 90-nm SiGe BiCMOS," *IEEE Trans. Terahertz Sci. Technol.*, vol. 14, no. 1, pp. 126–129, 2024.

[224] A. Fawzy, S. Sun, T. J. Lim, Y. Yu, C. Yu, and Y. Guo, "Iterative learning control based digital pre-distortion for mitigating impairments in mimo wireless transmitters," *IEEE Trans. Veh. Technol.*, vol. 72, no. 6, pp. 6933–6947, 2023.

[225] J. Chani-Cahuana, P. N. Landin, C. Fager, and T. Eriksson, "Iterative learning control for RF power amplifier linearization," *IEEE Trans. Microw. Theory Tech.*, vol. 64, no. 9, pp. 2778–2789, 2016.

[226] W. Hong, Z. H. Jiang, C. Yu, D. Hou, H. Wang, C. Guo, Y. Hu, L. Kuai, Y. Yu, Z. Jiang, Z. Chen, J. Chen, Z. Yu, J. Zhai, N. Zhang, L. Tian, F. Wu, G. Yang, Z.-C. Hao, and J. Y. Zhou, "The role of millimeter-wave technologies in 5G/6G wireless communications," *IEEE j. microw.*, vol. 1, no. 1, pp. 101–122, Jan. 2021.

[227] M. Elkhouly, J. Ha, M. J. Holyoak, D. Hendry, M. Sayginer, R. Enright, I. Kimionis, Y. Baeyens, and S. Shahramian, "Fully integrated 2D scalable TX/RX chipset for D-band phased-array-on-glass modules," in *2022 IEEE Int. Solid-State Circuits Conf. (ISSCC)*, vol. 65, San Francisco, USA, Feb. 2022, pp. 76–78.

[228] K. Kibaroglu, M. Sayginer, and G. M. Rebeiz, "A low-cost scalable 32-element 28-GHz phased array transceiver for 5G communication links based on a 2 x 2 beamformer flip-chip unit cell," *IEEE J. Solid-State Circuits*, vol. 53, no. 5, pp. 1260–1274, Jan. 2018.

[229] J. Pang, Z. Li, X. Luo, J. Alvin, R. Saengchan, A. A. Fadila, K. Yanagisawa, Y. Zhang, Z. Chen, Z. Huang, X. Gu, R. Wu, Y. Wang, D. You, B. Liu, Z. Sun, Y. Zhang, H. Huang, N. Oshima, K. Motoi, S. Hori, K. Kunihiro, T. Kaneko, A. Shirane, and K. Okada, "A CMOS dual-polarized phased-array beamformer utilizing cross-polarization leakage cancellation for 5G MIMO systems," *IEEE J. Solid-State Circuits*, vol. 56, no. 4, pp. 1310–1326, Jan. 2021.

[230] K. K. W. Low, S. Zihir, T. Kanar, and G. M. Rebeiz, "A 27–31-GHz 1024-element Ka-band SATCOM phased-array transmitter with 49.5-dBW peak EIRP, 1-db AR,

and ±70° beam scanning," *IEEE Trans. Microw. Theory Tech.*, vol. 70, no. 3, pp. 1757–1768, Mar. 2022.

[231] S. Li, Z. Zhang, and G. M. Rebeiz, "An eight-element 136–147 GHz wafer-scale phased-array transmitter with 32 dBm peak EIRP and ¿16 Gbps 16QAM and 64QAM operation," *IEEE J. Solid-State Circuits*, vol. 57, no. 6, pp. 1635–1648, Jun. 2022.

[232] Y. Yang, O. Gurbuz, and G. M. Rebeiz, "An eight-element 370–410-GHz phased-array transmitter in 45-nm CMOS SOI with peak EIRP of 8–8.5 dBm," *IEEE Trans. Microw. Theory Tech.*, vol. 64, no. 12, pp. 4241–4249, Oct. 2016.

[233] Y. Yang, O. D. Gurbuz, and G. M. Rebeiz, "An eight-element 370–410-GHz phased-array transmitter in 45-nm CMOS SOI with peak EIRP of 8–8.5 dBm," *IEEE Trans. Microw. Theory Tech.*, vol. 64, no. 12, pp. 4241–4249, Dec. 2016.

[234] K. Wu, B. Fahs, and M. Hella, "A 220 GHz OOK outphasing transmitter in 130-nm BiCMOS technology," in *2018 IEEE BiCMOS and Compound Semiconductor Integrated Circuits and Technology Symposium (BCICTS)*, San Diego, USA, Oct. 2018, pp. 227–230.

[235] A. Standaert and P. Reynaert, "A 390-GHz outphasing transmitter in 28-nm CMOS," *IEEE J. Solid-State Circuits*, vol. 55, no. 10, pp. 2703–2713, Oct. 2020.

[236] I. Jaffri, A. B. Ayed, A. M. Darwish, and S. Boumaiza, "High-frequency vector-modulated signal generation using frequency-multiplier-based RF beamforming architecture," in *2020 IEEE MTT-S Int. Microw. Symp. (IMS) Dig.*, Los Angeles, USA, Aug. 2020, pp. 551–554.

[237] Y. Liu, G. Liu, and P. M. Asbeck, "High-order modulation transmission through frequency quadrupler using digital predistortion," *IEEE Trans. Microw. Theory Tech.*, vol. 64, no. 6, pp. 1896–1910, Jun. 2016.

[238] A. Chung, A. M. Darwish, E. Viveiros, H. A. Hung, P. Mitran, and S. Boumaiza, "Analysis and compensation of nonidealities in frequency multiplier-based high-frequency vector signal generators," *IEEE Trans. Microw. Theory Tech.*, vol. 67, no. 6, pp. 2270–2283, Jun. 2019.

[239] T. Cao, Y.-J. Liu, J. Jiang, Q. Zhang, C. Lin, D. Yang, G. Zhang, C. Yang, and J. Zhou, "Frequency multiplier-based millimeter-wave vector signal transmitter using

digital predistortion with constrained feedback bandwidth," *IEEE Trans. Microw. Theory Tech.*, vol. 68, no. 5, pp. 1819–1829, May 2020.

[240] I. Jaffri, A. B. Ayed, A. M. Darwish, P. Mitran, and S. Boumaiza, "Novel baseband equivalent model for digital predistortion of wideband frequency-multiplier-based millimeter wave sources," *IEEE Trans. Microw. Theory Tech.*, vol. 68, no. 9, pp. 3942–3957, Sept. 2020.

[241] A. B. Ayed, I. Jaffri, M. Eladwy, A. M. Darwish, P. Mitran, and S. Boumaiza, "Analysis and linearization of frequency-multiplier-based RF beamforming transmitters over a wide steering range," *IEEE Trans. Microw. Theory Tech.*, vol. 70, no. 8, pp. 3987–4001, 2022.

[242] J. Xia, M. Farouk, and S. Boumaiza, "Digitally-assisted 27-33 GHz reflection-type phase shifter with enhanced accuracy and low il-variation," in *2019 IEEE Radio Freq. Integr. Circuits Symp. (RFIC) Dig.*, Boston, USA, Jun. 2019, pp. 63–66.

[243] M. Eladwy, J. Xia, A. B. Ayed, and S. Boumaiza, "A 60 GHz CMOS-SOI stacked push-push frequency doubler with 12 dBm output power and 20% efficiency," in *2021 IEEE MTT-S Int. Microw. Symp. (IMS) Dig.*, Atlanta, USA, Jun. 2021, pp. 297–300.

[244] N. Messaoudi, A. Ben Ayed, J.-P. Teyssier, and S. Boumaiza, "VNA-based testbed for accurate linearizability testing of power amplifiers under modulated signals," in *2022 99th ARFTG Microw. Meas. Conf.*, Denver, USA, Jun. 2022, pp. 1–4.

[245] M. Frounchi, S. G. Rao, and J. D. Cressler, "A Ka-band SiGe bootstrapped gilbert frequency doubler with 26.2% PAE," *IEEE Microw. Wirel. Compon. Lett.*, vol. 28, no. 12, pp. 1122–1124, Nov. 2018.

[246] M. Eladwy, A. Ben Ayed, and S. Boumaiza, "VNA-based characterization of frequency multipliers phase-distortions under continuous-wave and modulated signal excitation," in *2023 101th ARFTG Microw. Meas. Conf.*, San Diego, USA, Jun. 2023, pp. 1–4.